이학박사 학위논문

# The Radio/Gamma-Ray Connection of Blazars

## 블레이저들의 전파/감마선 상관관계

**2021년 8월**

서울대학교 대학원

물리·천문학부 천문학전공

김 대 원

# The Radio/Gamma-Ray Connection of Blazars

## 블레이저들의 전파/감마선 상관관계

지도교수 Sascha Trippe

이 논문을 이학박사 학위논문으로 제출함
2021년 6월

서울대학교 대학원
물리·천문학부 천문학전공
김 대 원

김 대 원 의 이학박사 학위논문을 인준함
2021년 8월

| | |
|---|---|
| 위 원 장 | 구 본 철 |
| 부위원장 | SASCHA TRIPPE |
| 위 원 | 임 명 신 |
| 위 원 | 이 상 성 |
| 위 원 | 변 도 영 |

# The Radio/Gamma-Ray Connection of Blazars

by

Daewon Kim
(dwkim@astro.snu.ac.kr)

A dissertation submitted in partial fulfillment of the requirements for
the degree of

**Doctor of Philosophy**

in
Astronomy

in
Astronomy Program
Department of Physics and Astronomy
Seoul National University

Committee:

| | |
|---|---|
| Professor | Bon-Chul Koo |
| Professor | Sascha Trippe |
| Professor | Myungshin Im |
| Professor | Sang-Sung Lee |
| Professor | Do-Young Byun |

# ABSTRACT

Relativistic jets in Active Galactic Nuclei (AGN) are one of the most powerful, persistent sources of energy in the Universe. Investigation of AGN jets is valuable and promising as they play an important role in not only the fields of high-energy astrophysics, but also the evolution of galaxies and clusters. Radio-loud AGNs with their relativistic jets directed toward us (e.g., with a viewing angle of ~5°), are classified as **blazars**. One of the well-known characteristics of blazars is strong $\gamma$-ray emission originating from their relativistic jets. Because the spatial resolution of high-energy telescopes is inadequate, however, our understanding of the high-energy emission is limited and thus the production site of blazar $\gamma$-ray flares is a matter of active debate. To explore the high-energy emission processes and its origin, I studied several individual blazars that recently showed strong $\gamma$-ray emission: BL Lacertae, OT 081 (1749+096), 3C 273, and 0716+714. In these studies, I analyzed their multi-wavelength (radio-to-$\gamma$-ray) light curves and Very Long Baseline Interferometry (VLBI) datasets on both the time-domain and image-plane to investigate the variations in emission, structure, and kinematics of the jets during a number of $\gamma$-ray flaring periods.

The blazar BL Lacertae which is the prototypical BL Lac object (a subclass of blazar), was explored using VLBI datasets obtained from the Korean VLBI Network (KVN). Properties of the radio jet are presented with light curves of the radio core (i.e., the VLBI core seen by the KVN) at 22, 43, 86, and 129 GHz. Our observations covered the decaying part of a strong radio flare. The timescales ($\tau$) of the exponential decays show the following relationship: $\tau \propto \nu^{-0.2}$, with $\nu$ being observing frequency. This is much shallower than the one expected from opacity effects (i.e., the core shift). Simultanous multi-frequency observations of the KVN allow us to perform spectral analysis of the radio emission. The spectral indices versus time and radio frequency, support the models of recollimation shocks (Marscher et al. 2008) and the generalized shock evolution (Valtaoja et al. 1992).

OT 081 is a blazar with a compact radio jet. In many VLBI images, the source shows a simple point-like feature without any notable extended structures. It had been consistently bright at radio wavelengths (e.g., a few Jy), but without noteworthy strong $\gamma$-ray outbursts.

However, there was a historically strong $\gamma$-ray outburst in 2016 in this source. To investigate this phenomenon, multi-waveband data were used: KVN and OVRO (radio), ASAS-SN (optical), Swift-XRT (X-ray), and *Fermi*-LAT ($\gamma$-ray). It was revealed that the 2016 $\gamma$-ray outburst is highly correlated with emission at lower frequencies from radio to X-ray. By using VLBA observations, we found that this $\gamma$-ray event was accompanied by the emergence of a moving polarized knot from the radio core which propagates further downstream of the flow. Combining all the evidence, we conclude that the radio core is the origin of the $\gamma$-ray outburst.

Blazars can be divided into two subclasses: flat-spectrum radio quasars (FSRQ) and BL Lac objects, based on the presence/absence of broad optical emission lines. Recent studies supported that $\gamma$-rays of FSRQs originate from a region beyond the broad-line region (BLR), suggesting distances of a few parsecs from the central engine where the radio core is thought to be located. Motivated by this, I investigated two recent $\gamma$-ray outbursts of the FSRQ 3C 273 which is one of the most powerful and famous blazars. Analysis were done with data obtained from the ALMA, VLBA, and *Fermi*-LAT. In order to check the correlation between radio and $\gamma$-ray emission, the discrete correlation function (DCF) was employed. Our results indicate that the compact features (i.e., multiple standing shocks) are responsible for the observed $\gamma$-ray outbursts in the jet of 3C 273.

0716+714 is known to have extreme variability over the entire electromagnetic spectrum. Our preliminary findings of an unusual anti-correlation between radio and $\gamma$-ray emission in this source, lead us to start a detailed study of the radio/$\gamma$-ray connection in the jet of 0716+714. Archival multi-frequency data (i.e., SMA, Metsähovi, OVRO, *Fermi*-LAT, and VLBA) were employed and the correlation analysis between the datasets was performed using the techniques of modeling and simulating the light curves. As a result, we found three significant radio-to-$\gamma$-ray correlations: two anti-correlations and one positive correlation. We also analyzed VLBA datasets to investigate the parsec-scale jet activity during the $\gamma$-ray flares. With all the evidence, we constrain the origin of the $\gamma$-ray flares in the jet and suggest internal-shock interactions induced by the passage of a moving disturbance through the radio core as the mechanism behind the observed correlated behaviors.

Physics of the relativistic jets in blazars is tricky and complicated due to the extreme physical conditions and various scenarios/possibilities. More detailed observations of the jets with high-resolution VLBI arrays, are currently the best way to resolve the issues of the jet physics. This thesis presents new observational data and results on the nature of blazar $\gamma$-ray flares and contributes to the scientific community by supplying the wealth of information for the cases of four remarkable blazars. The individual studies presented in this thesis, conclude as follow: (1) blazar $\gamma$-ray flares have multiple emission regions in the jets (i.e., subpc/pc-scales distances from the central black hole) and (2) the propagation of shocks/disturbances along the jet in the subpc/pc-scale regions, causes $\gamma$-ray flares (particularly when they pass through the standing shock features; e.g., the radio core).

**Keywords:** galaxies: active – galaxies: jets – radio continuum: galaxies – individual: BL Lacertae, 1749+096, 3C 273, 0716+714 – techniques: interferometric – instrumentation: interferometers – gamma-rays: galaxies

***Student Number:*** 2014-21383

# Contents

# List of Figures

# List of Tables

# Chapter 1

# Introduction

## 1.1 Radio jets in Active Galactic Nuclei (AGN)

### 1.1.1 Active Galactic Nuclei

Active Galactic Nucleus (AGN) is a central region of a galaxy with strong, nonthermal emission. After the first manifestation of AGN by Fath (1909), more detailed observations of AGNs were performed and reported their information in the middle of the 20th century (e.g., Seyfert 1943; Shklovsky 1955; Hazard et al. 1963). AGNs are characterized by broad-band (radio to $\gamma$-ray) emission, nonthermal emission, strong polarization, rapid variability (typically days to years, but even down to minute-scales at $\gamma$-rays) at the entire electromagnetic spectrum, and powerful jet with superluminal motion. However, most of these characteristics can be observed in radio-loud AGNs (i.e., quasars and radio galaxies). Quasars are compact and outshine their host galaxy. Based on the radio power (i.e., $L_{\rm rad} = dL/dln\,\nu\,(6\,{\rm GHz})$; with $L$ being the luminosity), quasars can be divided by two types: $L_{\rm rad} \sim 10^{40}$–$10^{46}\,{\rm erg\,s^{-1}}$ for radio-loud quasar and $L_{\rm rad} \sim 10^{38}$–$10^{40}\,{\rm erg\,s^{-1}}$ for radio-quiet quasar (Blandford et al. 2019). Here the radio-loud quasars are also called 'blazar'. Figure 1.1 shows a schematic diagram of the unified model of AGN. The AGN model can also be described in the following dimensions: (1) Type-I/II based on the obscuration of the central emitting source (e.g., Type-I for a face-on orientation and Type-II for an edge-on orientation) and (2) radio-loud/quiet based on the radio loudness parameter $R$ defined by the ratio of radio to optical monochromatic luminosity ($L_\nu$) as below;

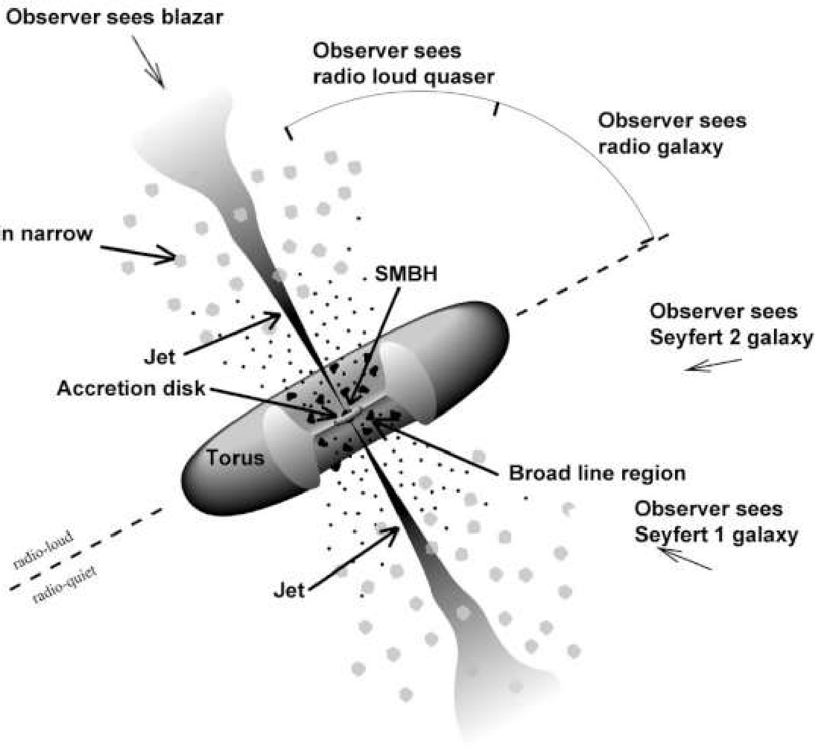

**Figure 1.1.** Diagram of AGN classification. In general, AGN classification depends on the viewing angle and radio-loudness. Image credit: *Fermi* Gamma-ray Space Telescope, NASA.

a fiducial point is $R = 10$.

$$R = \frac{L_\nu\,(5\,\mathrm{GHz})}{L_\nu\,(4400\,\text{Å})} \tag{1.1}$$

Basically, AGN consist of supermassive black holes (SMBHs) that spin rapidly with mass of $10^6$–$10^{10}\,M_\odot$, accretion disk ($< 10^2\,\mathrm{R_s}$; $\mathrm{R_s}$ being Schwarzschild radii), broad line region ($\sim 10^3\,\mathrm{R_s}$), dusty torus ($\sim 10^5\,\mathrm{R_s}$), narrow line region ($\sim 10^6\,\mathrm{R_s}$) and relativistic jet ($\sim 10^{11}\,\mathrm{R_s}$). AGN jets usually appear in radio-loud AGNs; recent studies have reported some narrow-line Seyfert 1 galaxies (NLS1) that have the radio jet and even notable $\gamma$-ray flaring events (e.g., Foschini et al. 2011; D‘Ammando et al. 2015; Yang et al. 2018). These unexpected findings are a matter of active debate and it might be an indication of a evolutionary connection between blazar and NLS1. More detailed classification of AGNs depends on the characteristics of emission lines. Seyfert galaxies ($L_{\rm bol} > 10^{42}$; $L_{\rm bol}$, the bolometric luminosity in $\rm erg\,s^{-1}$) can be divided into type 1 (broad lines) and type 2 (narrow lines). Radio galaxies ($L_{\rm bol} > 10^{42}\,\rm erg\,s^{-1}$) have also such classification, narrow-line radio galaxy (NLRG) and broad-line radio galaxy (BLRG); however, there is weak-line radio galaxy (WLRG), with $L_{\rm bol} < 10^{42}\,\rm erg\,s^{-1}$. Blazars can also be divided spectroscopically: BL Lac objects (very weak or no emission lines, plus low power source) and flat-spectrum radio quasars (FSRQ; strong and broad lines, plus high power source). FSRQs tend to have larger accretion rate than BL Lac objects; the disk is supposed to emit $\geq 1\,\%$ of the Eddington luminosity ($L_{\rm Edd}$) for FSRQs, whereas it is below this value for BL Lac objects (Ghisellini et al. 2011). Furthermore, there is other important element in the AGN classification that determines source characteristics. As can be seen in Figure 1.1, AGN subclasses depend on the inclination of AGNs that is a viewpoint between edge-on and face-on. Such an effect comes from the presence of the jet. Depending on the so-called viewing angle ($\theta_{\rm jet}$) that is an angle between the jet axis and our line of sight, a blazar-like feature (e.g., rapid variability, strong $\gamma$-ray emission, and superluminal motion) can be observed; typically from a face-on view ($\theta_{\rm jet} \sim 0^\circ$) of radio-loud quasars.

### 1.1.2 Formation of AGN jets

Jet formation is one of the long-standing questions in the jet physics. In general, It is assumed that the black hole spin (B-Z mechanism, Blandford & Znajek 1977) or the rotation of the accretion disk (B-P mechanism, Blandford & Payne 1982) powers the jets. In addition, the presence of an accreting process around the central, compact objects (e.g., black holes, neutron stars, and white dwarfs) is essential to launch jets. Ghisellini et al. (2014) reported that jet powers are larger than accretion powers (i.e., the gravitational power of the falling matter). This indicates that the accretion disk amplifies the magnetic field which extracts the rotational energy of the central black holes, thus implying the black hole rotation as the source of jet energetics. Either way, magnetic field plays a key role in the formation of the jets (e.g., Davis & Tchekhovskoy 2020).

Figure 1.2 explains the conception of jet formation. A perfectly conducting and spinning sphere (e.g., black hole) can be seen in the first panel *a*. The sphere is connected with its surroundings (i.e., ambient medium) by a magnetic field line. Owing to the rotation of the sphere, the field line is coiled up and turn into a magnetic spring (*b*). These toroidal loops produce a gradient in field strength, thus exerting magnetic pressure ($\rho_{\rm m}$) on its surroundings (*c*). This accelerate and push the ambient medium away (*d*). The rotation continues to turn the initially vertical field line into the toroidal field emanating from the sphere. Although black holes do not have their physical surface, their rotation can drag the inertial frames near them. This results in the magnetic field lines to rotate like the case of the perfectly conducting sphere.

There is an obvious relation between the jet power and the black hole spin. However, the spin changes very slowly. This indicates that the magnetic flux ($\Phi$) threading the central black hole is only responsible for the variations in the jet power. Hence, deeper information of the accretion physics would be necessary to understand the $\Phi$ value. As mentioned earlier, our understanding of the formation of AGN jets is poorly understood. Future works will provide a

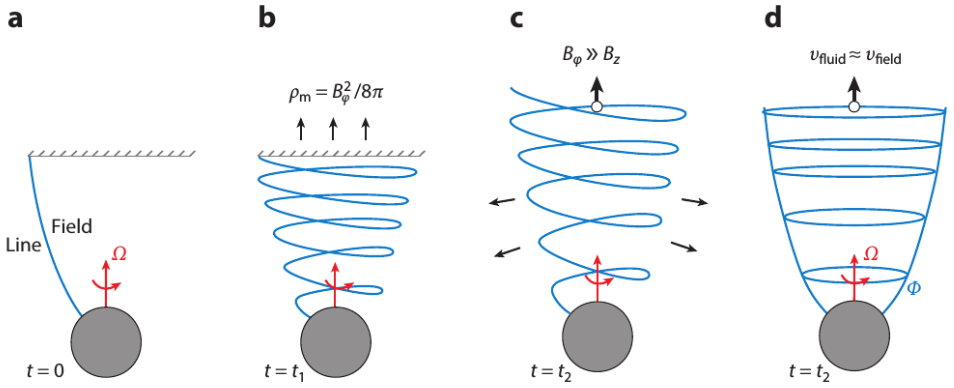

**Figure 1.2.** Illustration of jet formation by magnetic fields, taken from Davis & Tchekhovskoy (2020). (*a*) A poloidal field line ($B_\varphi = 0$; toroidal field) connect a stationary, ambient medium (a hashed horizontal line) to the central black hole (a black filled circle). $\Omega$ is the angular frequency. (*b*) At t = $t_1$, the magnetic spring with $N$ toroidal loops appears and pushes the medium. (*c*) With increasing the pressure, it accelerates the medium (or plasma) along the rotation axis. (*d*) The jet can be considered as a collection of toroidal field loops. $\Phi$ is the radial magnetic flux.

wealth of information on the following issues: (1) the origin of the magnetic flux (e.g., ISM or the disk), (2) the acceleration process that makes AGN jets relativistic, (3) the role of the jets in the galaxy evolution, and (4) the physics near the supermassive black holes (e.g., general relativity and the field of extreme gravity). Recent EHT observations of M 87 (e.g., The EHT Collaboration et al. 2019) support the B-Z mechanism for the jet, plus magnetically arrested accretion disk.

As the jets form and develop, they will expand spatially with a decrease in pressure inside the jets. This requires other elements that constrain the jets to be confined and collimated as many previous studies suggest (e.g., Sadowski et al. 2013; Nakamura et al. 2018). A recent

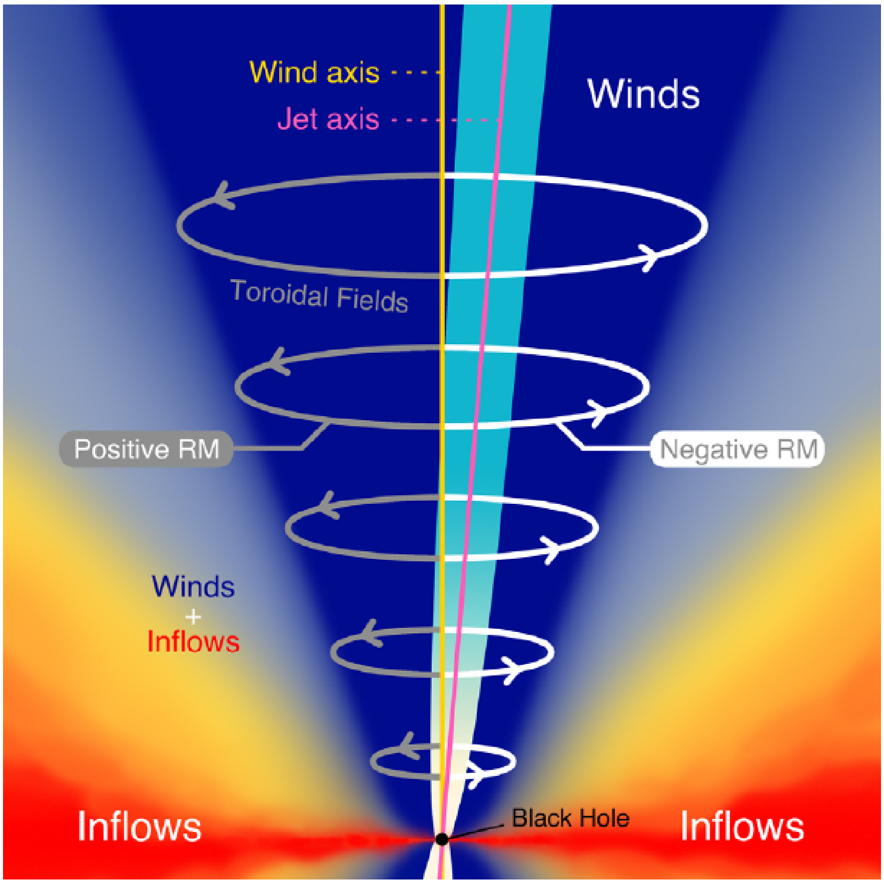

**Figure 1.3.** Schematic picture of the inflow-outflow system. Substantial winds (dark blue) surround the jet (cyan) which lead to the jet confinement. The jet axis is tilted by about ~5°, away from the wind axis. Image credit: Park et al. (2019a).

study Park et al. (2019a), found rotation measure (RM) dominated by a single (negative) sign in the jet of the radio galaxy M 87. Based on the model of hot accretion flows, nonrelativistic and uncollimated winds (or gas outflow) surround the jet and become a primary source of the observed RM. It is assumed that a misalignment in the axis between the jet and winds, results in the one-sided jet respect to the toroidal fields, thus leading such single RM signature (see Figure 1.3). This result demonstrates observationally the presence of the winds surrounding the jet.

### 1.1.3 Jet structures and evolution

At present, it is known that there are $\sim 10^9$ extragalactic sources in the sky with a strong radiative power (i.e., $L_{\rm rad} \geq 10^{38}\,{\rm erg\,s^{-1}}$) at low radio frequencies (Blandford et al. 2019). Most of these bright sources have the jet-like features: the core, jet, and lobes. Observations of AGN jets have been performed at not only radio, but also optical and X-rays. These observations provided information on the global structures of the jets. Owing to the unprecedented high angular resolution of radio interferometric observations (i.e., reaching to sub-milliarcseconds scales), however, radio interferometers like very-long baseline interferometer (VLBI) are currently the only way that can provide the images of more detailed jet structures. Figure 1.4 shows one of the most famous radio-loud AGNs, M 87 seen by various interferometric arrays at different radio frequencies: the very large array (VLA), very long baseline array (VLBA), global mm-VLBI array (GMVA), and event horizon telescope (EHT). This radio galaxy is one of the nearest radio-loud AGNs to us (i.e., the redshift, $z$ of 0.00436; McConnell & Ma 2013), and show the remarkable features over the small and large distance scales from its central black hole.

With bolometric luminosities occasionally exceeding those of galaxies by orders of magnitude, relativistic jets in AGNs are one of the most powerful, persistent sources of energy in the Universe. As mentioned in Section 1.1.2, the plasma outflows are thought to be powered by an accreting central supermassive black hole and launched from a region close to the central black hole (e.g., $\leq 100\,R_{\rm s}$). During its journey to kiloparsec- or sometimes megaparsec-scales from the central engine, they form various confined morphologies over the wide distance

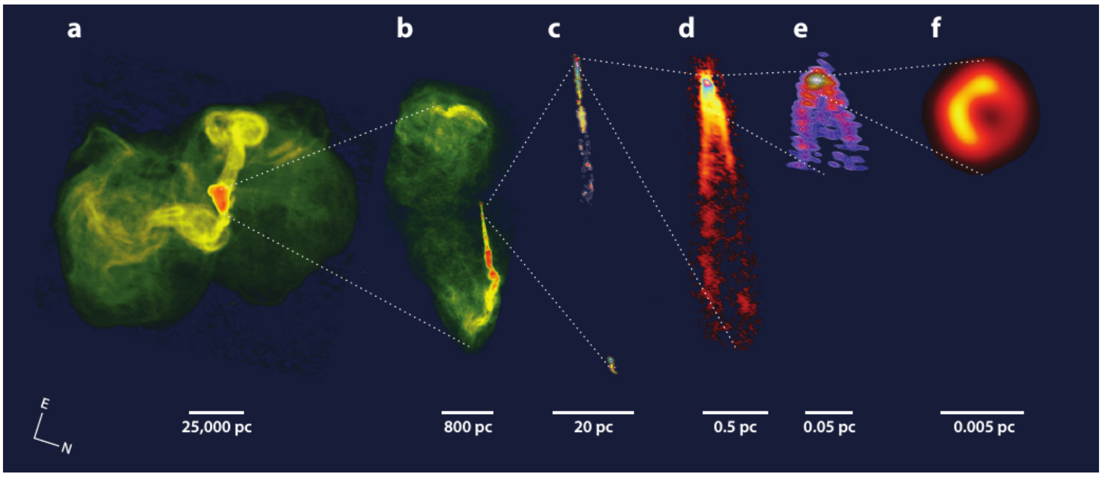

**Figure 1.4.** Example images of the radio galaxy M 87 with its relativistic jet (or radio jet) seen by different arrays and observing frequencies. (*a*) Jet and outer lobes observed by the VLA at 90 cm, (*b*) jet and inner lobes observed by the VLA at 20 cm, (*c*) & (*d*) parsec-scale jet observed by the VLBA at 20 cm and 7 mm, respectively, (*e*) jet base near the central black hole observed by the GMVA at 3 mm, and (*f*) the black hole shadow observed by the EHT at 1.3 mm. Image credit: Blandford et al. (2019).

scales. FR I/FR II dichotomy (Fanaroff & Riley 1974) is widely considered to categorize their kiloparsec radio morphologies: jet-dominated emission dimming with distance from the core (FR I) and lobe-dominated emission brightening with distance from the core (FR II). FR I jets show large-scale plumes or tails with complicated bent structures, whereas FR II jets are simply straight with very bright lobes (hotspot) where the jet is terminated (see e.g., Figure 1.5). Many previous theoritical studies found that the formation of such jet morphologies strongly depend on the energy dissipation processes, ambient medium density profile, and the jet power (e.g., Perucho et al. 2010; Massaglia et al. 2016; Tchekhovskoy & Bromberg 2016; van der Westhuizen et al. 2019).

The different morphology of the jet is thought to be determined by how the jets lose their energy. During the propagation from parsec- to kiloparsec-scales, the jets interact with the interstellar/intergalactic medium (ISM/IGM) and this causes plasma instabilities (e.g., Kelvin-Helmholtz and/or kink instability) which is assumed to be the main process responsible for

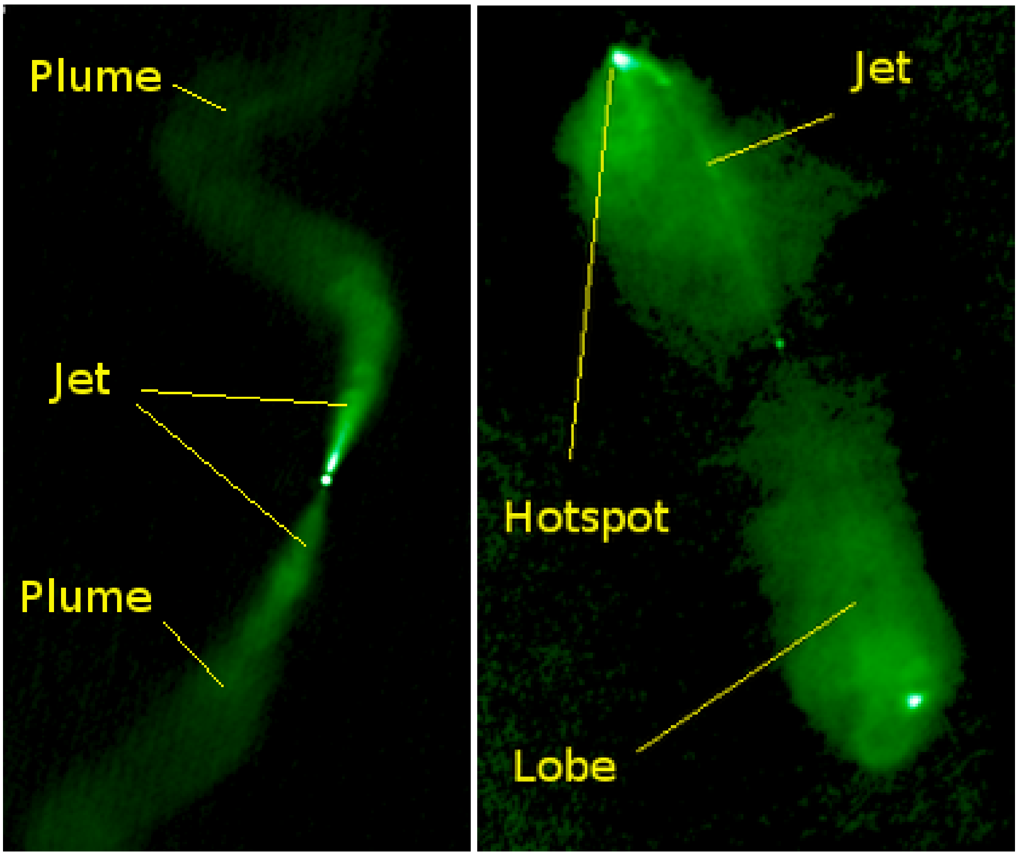

**Figure 1.5.** FR I/FR II dichotomy is described visually with radio interferometric images of the jets 3C 31 (FR I; *left*) and 3C 98 (FR II; *right*). The specific structures of the jets are indicated by the yellow names.

the complicated jet structures. As the balance in pressure between the jet and ambient medium varies, a series of recollimation shocks (e.g., the radio/VLBI core) could be produced and affect the jet dynamics. Furthermore, one may expect the mass entrainment from the ambient medium or stellar winds that causes the deceleration and/or decollimation of the jets. On the distant scales (e.g., >10 kiloparsec), buoyancy effects might also be an important factor, considering the galaxy gravitational potential. In addition, it has been found that the jets are a strong X-ray emitter (e.g., Jimenez-Gallardo et al. 2020). The bright X-rays coincide with the knots, hotspots, and nuclei of the jets spatially, thus meaning the presence of hot gas in the surrounding IGM (e.g., Massaro et al. 2018). Such environmental conditions could be affecting the jet morphology.

The evolution of the jet can be described in three stages after it launched near the central black hole: (1) acceleration and collimation up to $10^5\,R_\mathrm{s}$ ($\sim$10 parsec; pc) where the jet dynamics is dominated by the magnetic field, (2) kinetic-flux dominated dynamics up to $10^9\,R_\mathrm{s}$ ($\sim$100 kiloparsec; kpc) with the energy loss being dominated by radiative cooling, and finally (3) a dissipation-dominated region where the jet forms radio lobes from the conversion of kinetic energy into radiation (e.g., Boccardi et al. 2017). Figure 1.6 shows a picture of the evolution of AGN jets. Considering the current paradigm, VLBI observations at mm-radio wavelengths are the key to reveal the physics of the jet phenomena near the central black hole, which is the origin of the jet evolution.

As explained above, the typical morphology of AGN jets comprises a compact, bright and unresolved core at the upstream end of the VLBI jets, a continuous downstream jet flow, and lobes with hotspots at the end. In general, temporal variations in structure and variability are more dramatic in the parsec-scale region close to the radio core and are associated with the emergence of new plasma blobs (e.g., Jorstad et al. 2013). Relativistic light travel time and projection effects, as well as Doppler boosting, are much stronger than the kiloparsec-scale regions of the jets that are smoother, extended morphologies. Hence, the physical processes in inner jet regions (e.g., $\leq 10^5\,R_\mathrm{s}$), are very dynamic and strong. Based on many previous studies on the (sub-)parsec-scale jets, now we have the most probable picture of the inner jet regions. Figure 1.7 shows the model of the jets. The plasma outflow ejected from the central SMBH with a mass of $10^{8-9}\,M_\odot$ (*left*), propagates outwards (*right*), emitting strong nonthermal emission at the entire electromagnetic spectrum (radio to $\gamma$-ray). This picture present more detailed structure of the inner jet regions which corresponds to the launching, acceleration and collimation regimes described in Figure 1.6. Magnetic fields is ordered with helical structures, and then become disordered or partially ordered with passing through the standing conical shock (or the radio core). As a moving shock (or superluminal knot) passes through the first region (i.e., acceleration and collimation zone; ACZ), the shock is accelerated in this poynting flux dominated region. Then, the moving shocks can be detected via VLBI observations as it passes through the radio core. Turbulence plays an important role beyond the radio core (i.e., parsec-scales).

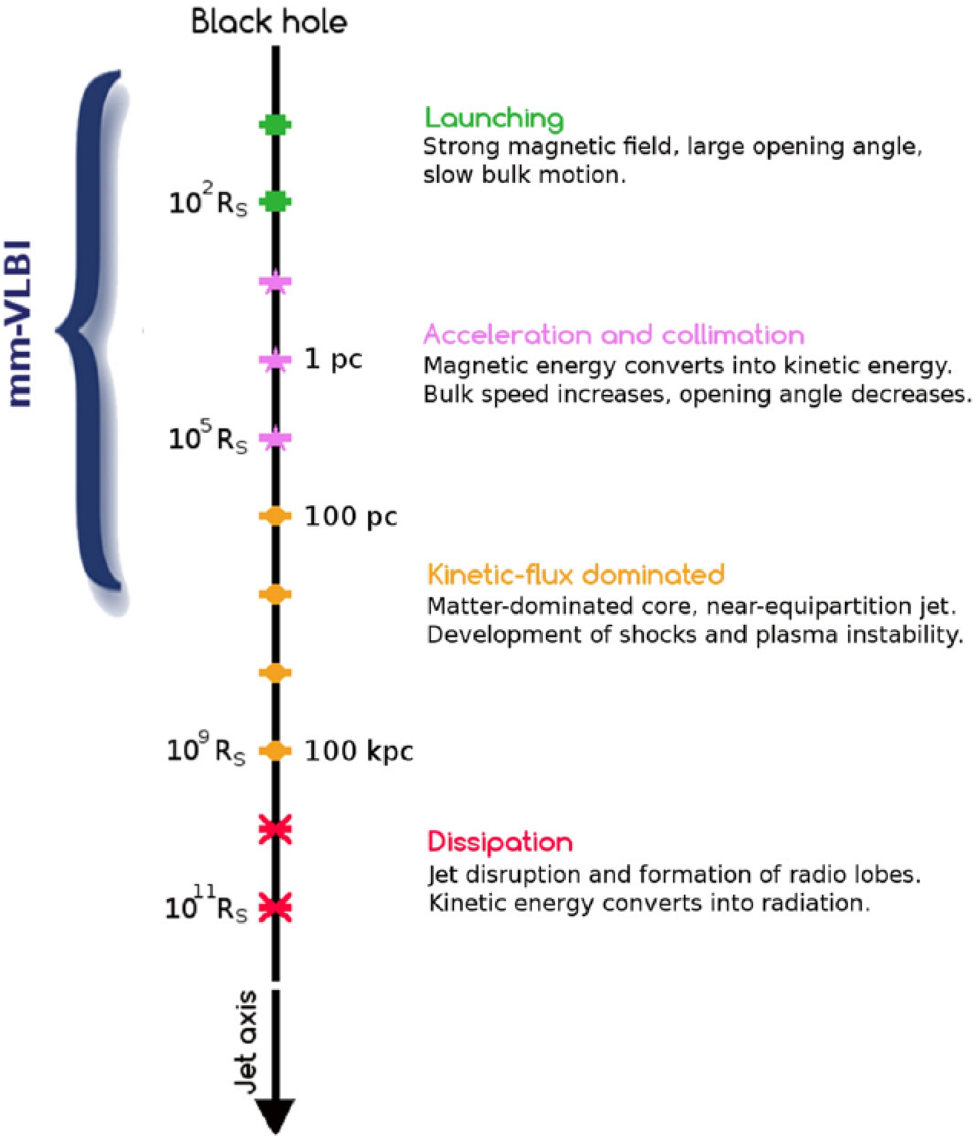

**Figure 1.6.** Schematic view of the jet regions at different distance scales. $R_s$ is Schwarzschild radii and the distance is on the logarithmic scale. A black hole mass of $10^9\ M_\odot$ is considered in this picture. Image credit: Boccardi et al. (2017).

The region with turbulent fields is supposed to accelerate electrons via second-order *Fermi* acceleration and magnetic reconnection, thus leading to a power-law distribution of electron energy.

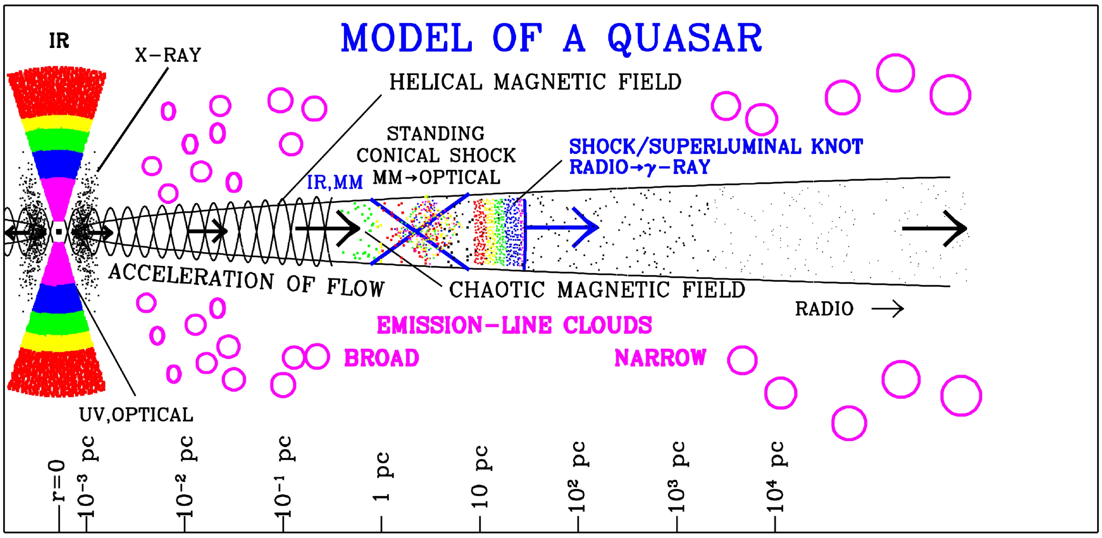

**Figure 1.7.** A model of the jet structure and primary emitting regions, created by Prof. A. Marscher (image from `https://www.bu.edu/blazars/research.html`). The central SMBH and accretion disk are shown on the left. The colors indicate the stratification in the frequency of emission.

Opacity effects are crucial to explain the jet structure. The ACZ region is opaque at radio wavelengths due to strong synchrotron self-absorption (SSA). As this region ends, the jets become transparent at radio wavelengths. This is the main definition of the radio (or VLBI) core. The radio core usually appear at the upstream end of the jets as the brightest, compact feature in VLBI images (e.g., Figure 1.10). As optical depth ($\tau_\nu$) of the radio core becomes unity, however, it appears at different distances. Figure 1.9 describes this phenomenon which is so-called ‘core shift’. The surface (i.e., $\tau_\nu = 1$) of the core appears at inner jet regions with higher radio frequencies. In these days, such compact, bright and stationary features in the parsec-scale jets are thought to be a recollimation shock (RCS; Marscher et al. 2008). The RCS can be produced by an imbalance in pressure between the jet and ambient medium at the jet boundary. This implies that the jets are confined by external gas pressure in ACZ, then the external gas pressure profile changes suddenly at the Bondi radius (e.g., a few $10^5\,R_\mathrm{S}$) resulting in a RCS. Such circumstances lead to a transition in the jet structure (see e.g., Figure 1.8). In the jet of M 87, Asada & Nakamura (2012) discovered that the shape of the jet varies from

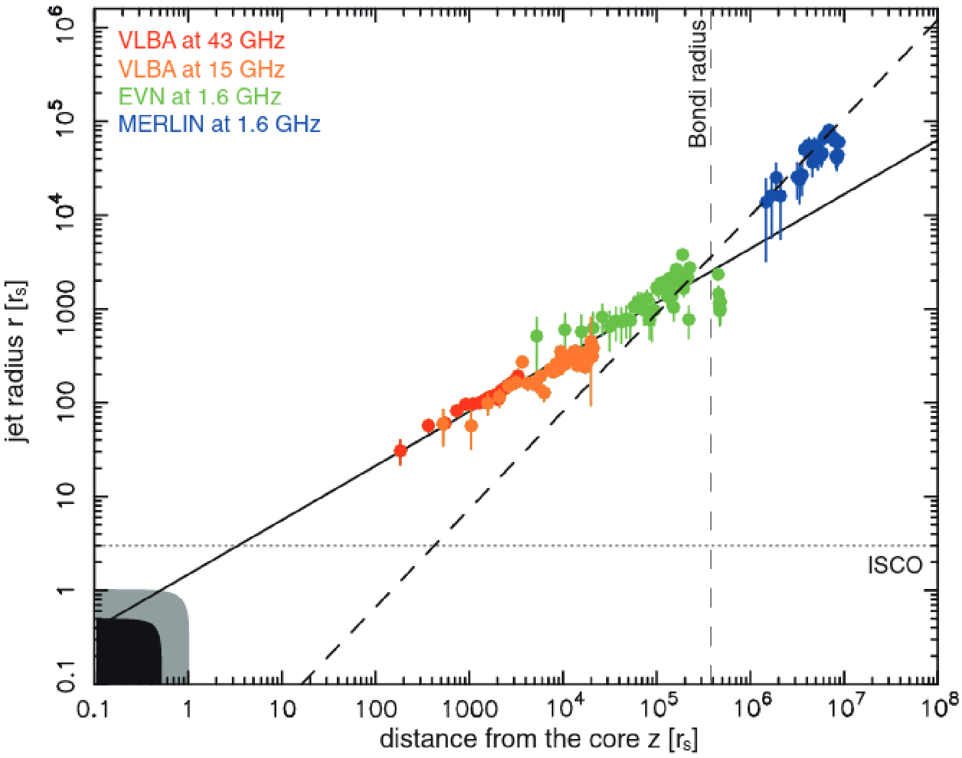

**Figure 1.8.** The jet radius as a function of the deprojected distance from the core; image taken from Asada & Nakamura (2012). Two shapes of the jet are described with the black solid and dashed lines: a parabolic structure (solid) and a conical structure (dashed). The black and gray areas show the minor and major axis of the event horizon size of the central black hole, respectively.

parabolic to conical at around the Bondi radius. This further proves a connection between RCS and the collimation in AGN jets.

Contrary to the conventional concept of the core with the frequency-dependent shift, the RCS predicts no core shift at mm-wavelengths. This indicates that the core shift is severe at cm-wavelengths, but it becomes weaker above e.g., 30 GHz (see also Kim et al. 2018a, for illustration of the central engine and mm-wave cores). Indeed, recent studies (e.g., Dodson et al. 2017) have presented a similar result to Marscher et al. (2008). In the view of radio spectrum, one can expect the source to be optically thick at cm-wavelengths, while optically

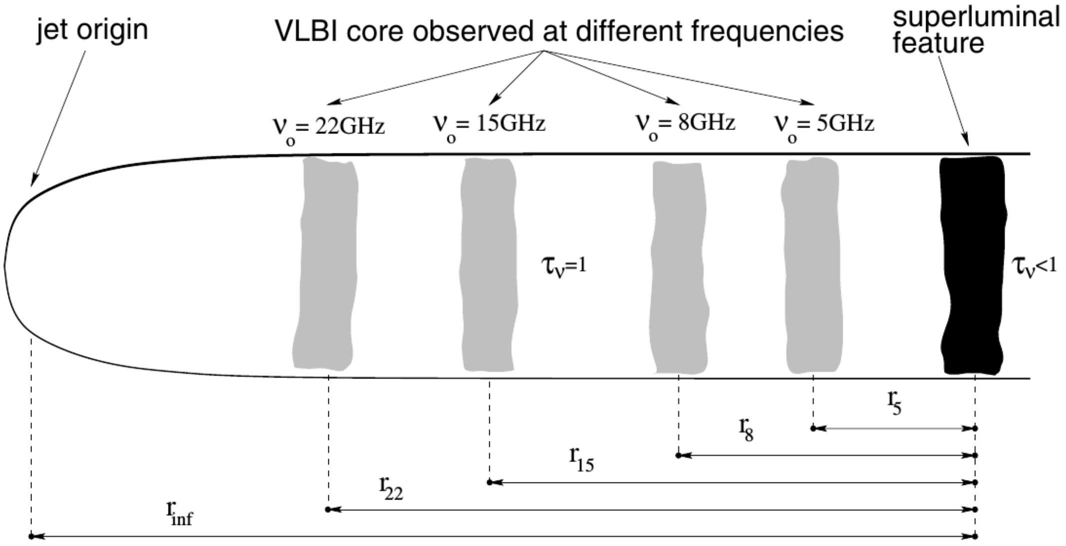

**Figure 1.9.** The frequency dependent locations of the radio core (so-called 'core shift'). Each surface of the radio core that becomes transparent ($\tau_\nu = 1$ with $\tau_\nu$ being optical depth) at different frequencies, is shown as gray thin regions. Image credit: Lobanov (1996); Kovalev et al. (2008).

thin at mm-wavelengths. As many theoretical studies predicted (Gómez et al. 1995; Mizuno et al. 2015), multiple RCSs have been now observed in many AGN jets (e.g., Wehrle et al. 2016). These standing shocked regions are assumed to be dense in magnetic field and particle density. Such circumstances produce remarkable phenomena (e.g., strong radio-to-$\gamma$-ray flares) in these regions. Owing to their compact sizes (e.g., less than 0.1 milliarcsecond; mas), mm-VLBI observations are important to resolve them and explore the nature of the upstream regions of the jets.

### 1.1.4 Beaming effects

So far, VLBI have observed more than 10,000 AGNs (Blandford et al. 2019) and the parsec-scale jets of ~500 AGNs have been monitored by the MOJAVE project[1]. The most interesting feature of the jets found by previous studies, is the superluminal motion (i.e., the apparent

---

[1] `https://www.physics.purdue.edu/MOJAVE/`

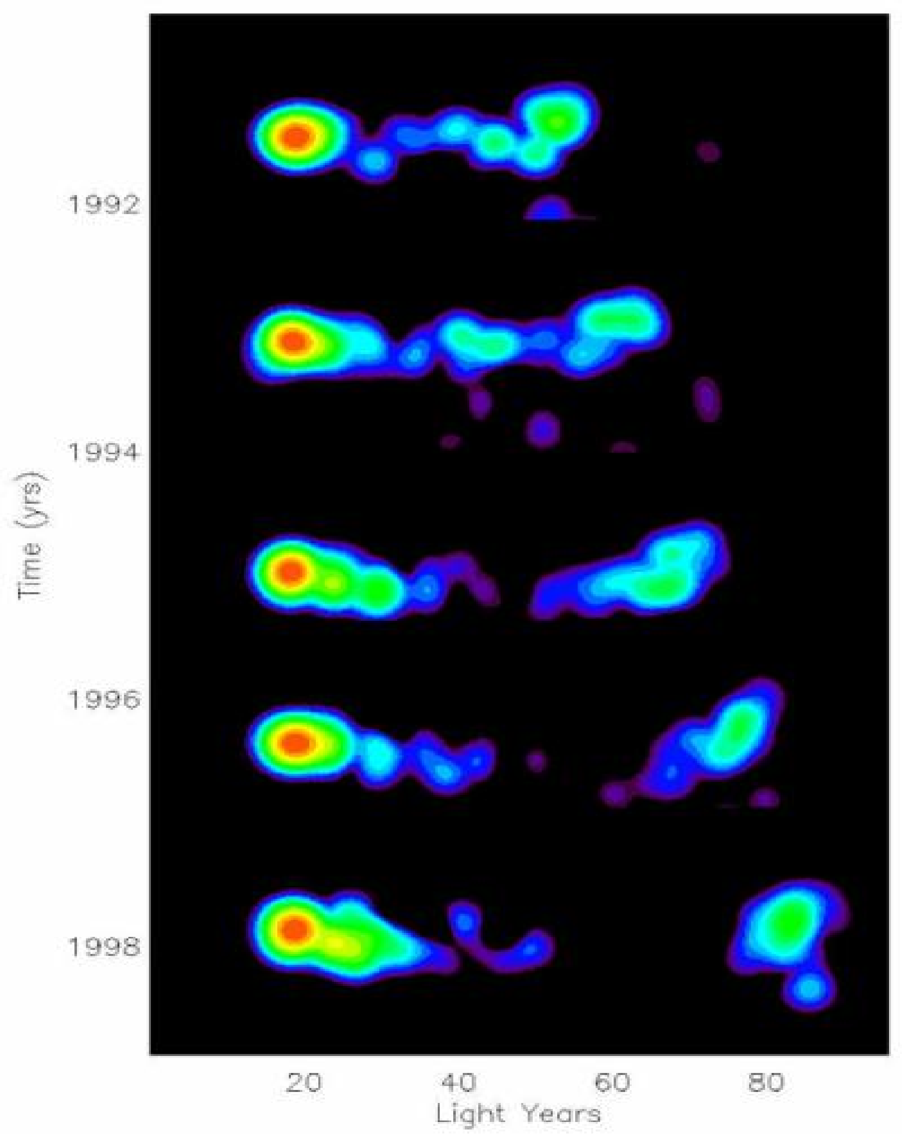

**Figure 1.10.** Superluminal motion of the quasar 3C 279. The jet is on mas-scale seen by VLBI. Image credit: NRAO/AUI.

motions of > 1 *c* with *c* being the speed of light). Figure 1.10 shows the superluminal motion of the quasar 3C 279 at mas scales. As can be seen, a bright blob on the right moves toward the right with time. In the observer's frame, this motion is superluminal given the physical distance of this source (i.e., about 6.3 pc/mas[2]). We can interpret the superluminal motion geometrically.

---

[2] `http://www.physics.purdue.edu/astro/MOJAVE/sourcepages/1253-055.shtml`

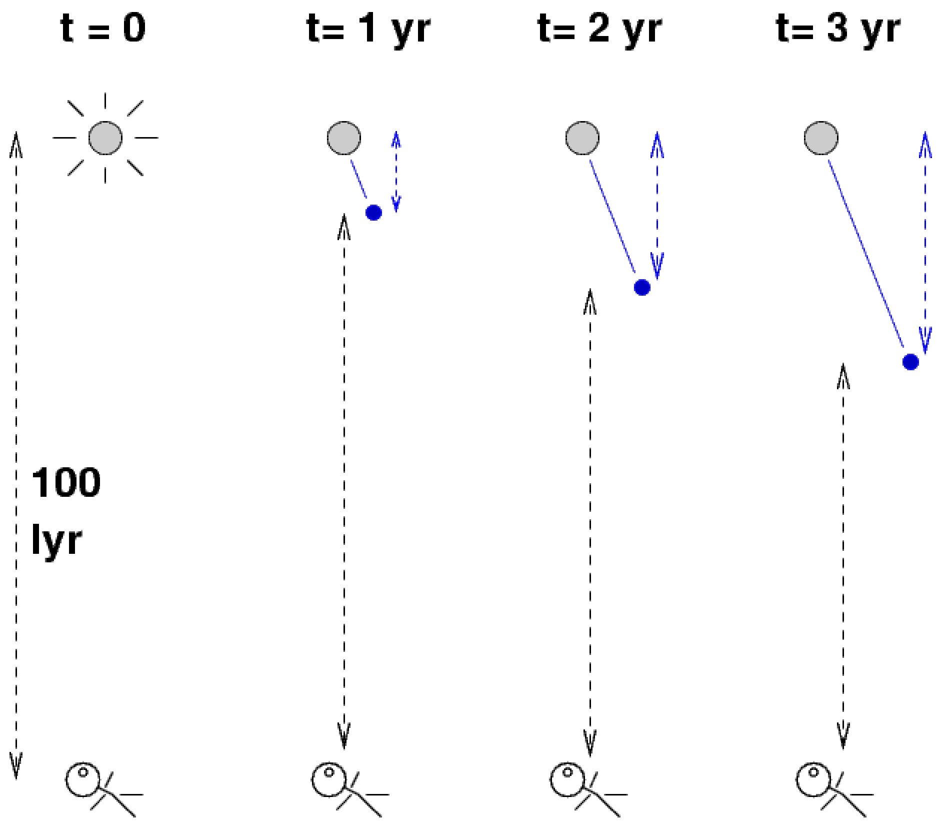

**Figure 1.11.** Illustration of the superluminal motion of the blob (blue small circle) emerged from the source (gray large circle); image taken from: http://spiff.rit.edu/classes/phys200/lectures/superlum/superlum.html. An observer is described at the bottom with a human-like symbol.

Imagine there is a source outflowing plasma blobs. This source is located very far away from us ($d$ = 100 light years; lyr) and the motion of a blob is relativistic ($v$, close to the speed of light $c$) with a centain angle of $\theta_{\text{jet}}$ (see Figure 1.11). Suppose the blob emerges from the source at $t = t_0$. Emission of the blob will need some amount of time (i.e., 100 lyr/$c$) to arrive at us. Now, things are more complicated at $t = t_{1\,\text{yr}}$. At $t = t_{1\,\text{yr}}$, the blob have traveled for 1 yr since it left the source (i.e., $t = t_0$). For us, however, the blob will be observed after the following time: $[100\ \text{lyr}/c - 1\ \text{yr} \times v \cos\theta_{\text{jet}}/c] + 1\ \text{yr}$. This means that now the emission need to travel $d_1$ decreased by the displacement of the blob's motion. Hence, the time interval between $t = t_0$

and $t = t_{1\,\mathrm{yr}}$ will be 1 yr × $[1 - v\cos\theta_{\mathrm{jet}}/c]$. During this time, the blob will move the following projected distance in the image plane: 1 yr × $v\sin\theta_{\mathrm{jet}}$. Thus, the apparent speed ($v_{\mathrm{app}}$) can be calculated by the projected distance over the time interval: $v_{\mathrm{app}} = v\sin\theta_{\mathrm{jet}}/[1 - (v/c)\cos\theta_{\mathrm{jet}}]$. In general, the apparent speed ranges from $0.03\,c$ to $40\,c$, but it can reach $\sim 50\,c$ in some of AGN jets (Blandford et al. 2019).

Emission from such a relativistically moving blob, will be highly enhanced by Doppler boosting. If the blob moving toward us, then the observed flux density ($S_{\nu,\,\mathrm{obs}}$) will be increased by about $\delta^{2-3}$ times the intrinsic one ($S_{\nu,\,\mathrm{int}}$), where $\delta$ being Doppler factor. The Doppler factor is often described as $\delta = 1/[\Gamma(1 - \beta\cos\theta_{\mathrm{jet}})]$, with the speed of the jet flow $\beta = v/c$, the bulk Lorentz factor $\Gamma = 1/\sqrt{(1 - \beta^2)}$, and the viewing angle $\theta_{\mathrm{jet}}$. Jorstad et al. (2017) reported that Doppler factor of a blazar jet can be as high as ~60 with the averages of 13 and 11 for FSRQs and BL Lac objects, respectively. For the Lorentz factor, it was ~38 with the averages of 12 and 7 for FSRQs and BL Lac objects, respectively. In the case of the viewing angle, both subclasses have a range of 0° to 5° with an average of ~1.5°. Thus, one can easily expect a huge amplification of the observed flux density of AGN jets through Doppler boosting.

### 1.1.5 Importance in astrophysics

Studies of AGN jets are relevant for other astrophysical systems. An important example is offered by the scaling relation (i.e., Nemmen et al. 2012) between gamma-ray luminosity and jet power which spans over about 10 orders of magnitude in both parameters and covers both BL Lac objects and gamma-ray bursts (GRBs), after correcting for viewing angle effects (see also Woosley & Bloom 2006; Hjorth 2013; Coppejans et al. 2018, for discussion of astrophysical jets in supernovae). Hence, the gamma-ray activity and radio/gamma connection in blazars offer a wealth of information in astrophysics widely.

Furthermore, AGN jets have a great impact on their galactic surroundings such as the giant radio bubbles, the formation of new galaxies, star formation, cosmic-ray acceleration, and the intergalactic magnetic field (Blandford et al. 2019). Hence, AGN jets play an important role in the evolution of galaxies and clusters (see also Hardcastle & Croston 2020). For instance, Russell et al. (2017) reported that the jets are stimulating star formation by producing cold

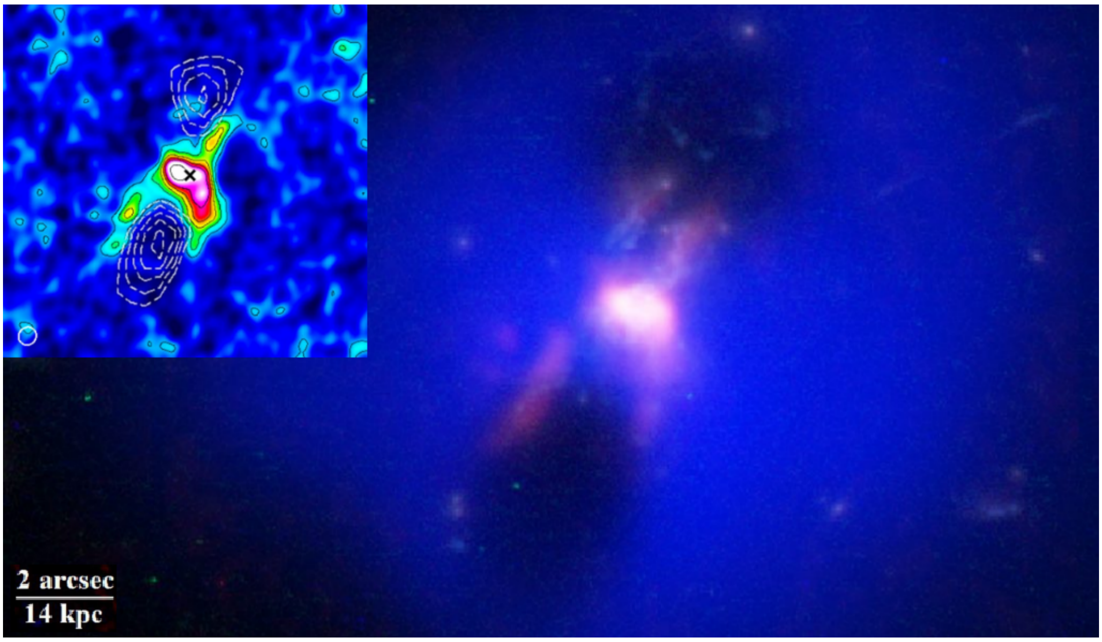

**Figure 1.12.** *Backgound*: a HST image of the Phoenix Cluster. The X-ray cavities (i.e., radio bubbles) are imaged by NASA's Chandra X-ray observation (two black empty regions). A powerful jet and filaments can be seen at the center of the image. The diffusive, hot plasma (blue) surrounds the galaxy. *Inset*: same as the background map, but observed by ALMA. Intensity map of the CO(3-2) line is presented (0 to 0.7 Jy/beam km $s^{-1}$). The ALMA beam is indicated at the bottom-left (0.60 × 0.56 arcsec). The dashed white contours represent the X-ray cavities. Long filaments of cold molecular gas surround the outer edges of the radio bubbles. Image credit: the inset (Russell et al. 2017) and the background image (ALMA – ESO/NAOJ/NRAO H.Russell, et al.; NASA/ESA Hubble; NASA/CXC/MIT/M.McDonald et al.; B. Saxton – NRAO/AUI/NSF).

gas in the halo of massive galaxies (see Figure 1.12). This observation suggests a connection between radio bubbles, the long filaments of cold molecular gas, and the powerful radio jet launched by a SMBH of the central galaxy. In addition to this, AGN jets can also be used to investigate the pressure and density profile of the surrounding medium (e.g., Lara et al. 2004; Liodakis 2018; Park et al. 2021).

As mentioned earlier, the jets propagate through the ambient medium extensively (e.g., up

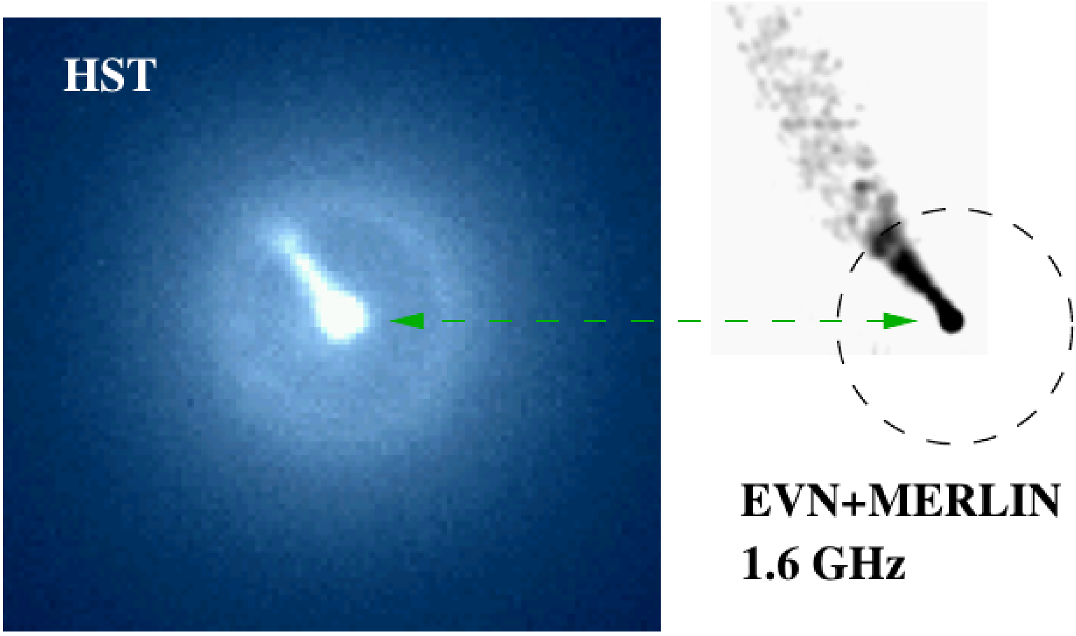

**Figure 1.13.** The jet of the radio galaxy 3C 264 seen by the HST (*left*) and a combined (EVN+MERLIN) VLBI array (*right*). A circumnuclear ring-like feature in the optical image, is overlaid with the 1.6 GHz image of the radio jet. Image credit: Lara et al. (2004).

to megaparsec-scales in some AGNs). In the radio galaxy 3C 264, Lara et al. (2004) found a notable change in the jet structure at around 200 milliarcseconds from the VLBI core. This could hint to a transition in the jet environment as in, e.g., the bubble scenario (e.g., Hutchings+ 1998): the jet evacuates a spherical region centering the black hole and experinces a sudden transition in ambient gas pressure when leaving the bubble. Intrinsic factors (e.g., binary black holes) affecting the jet dynamics need to be considered, too (Kharb+ 2010).

## 1.2 Multi-waveband observations of AGN

### 1.2.1 Very Long Baseline Interferometry

In order to obtain more detailed information of the nature of astrophysical objects, observations with high angular resolution are essential. Very long baseline interferometry (VLBI) is a technique providing extremely high resolution and now being the most powerful, promis-

**Figure 1.14.** The Very Long Baseline Array (VLBA) is a VLBI system of 10 single-dishes (radio telescopes) located over the USA.

ing method in astronomy. Previously, single-dish observations offered a typical resolution of ~1 arcmin at radio wavelengths (0.1 mm–100 m). In the case of the largest single-dish (i.e., FAST, China), the resolution reaches ~0.3 arcmin with a diameter of 500 m. Using VLBI, this can be improved dramatically (e.g., sub-mas scales), and thus one can directly observe detailed structures of the objects and monitor their variations (see e.g., Figure 1.14).

In 1950s, radio interferometers were constructed by connecting multiple antennas each other (i.e., radio array) with cable (e.g., VLA, NOEMA, SMA, etc.); the antennas of VLBI arrays are too far from each other for physical connection (via cable or radio link). The length ($d$) of a pair of the antennas, so-called 'baseline', ranges kilometer scales; typically higher than 100 km or 1000 km for VLBI arrays. VLBI observations are performed with all the element antennas simultaneously aiming at the same target source (or a field). Figure 1.15 describes how it works. Incoming radiation from an astronomical object is received by the antenna pairs. As it comes from the Universe which is a very long distance, we observe a plane wave from the source with a time delay ($\tau$). The signals are then multiplied, combined in a correlator to

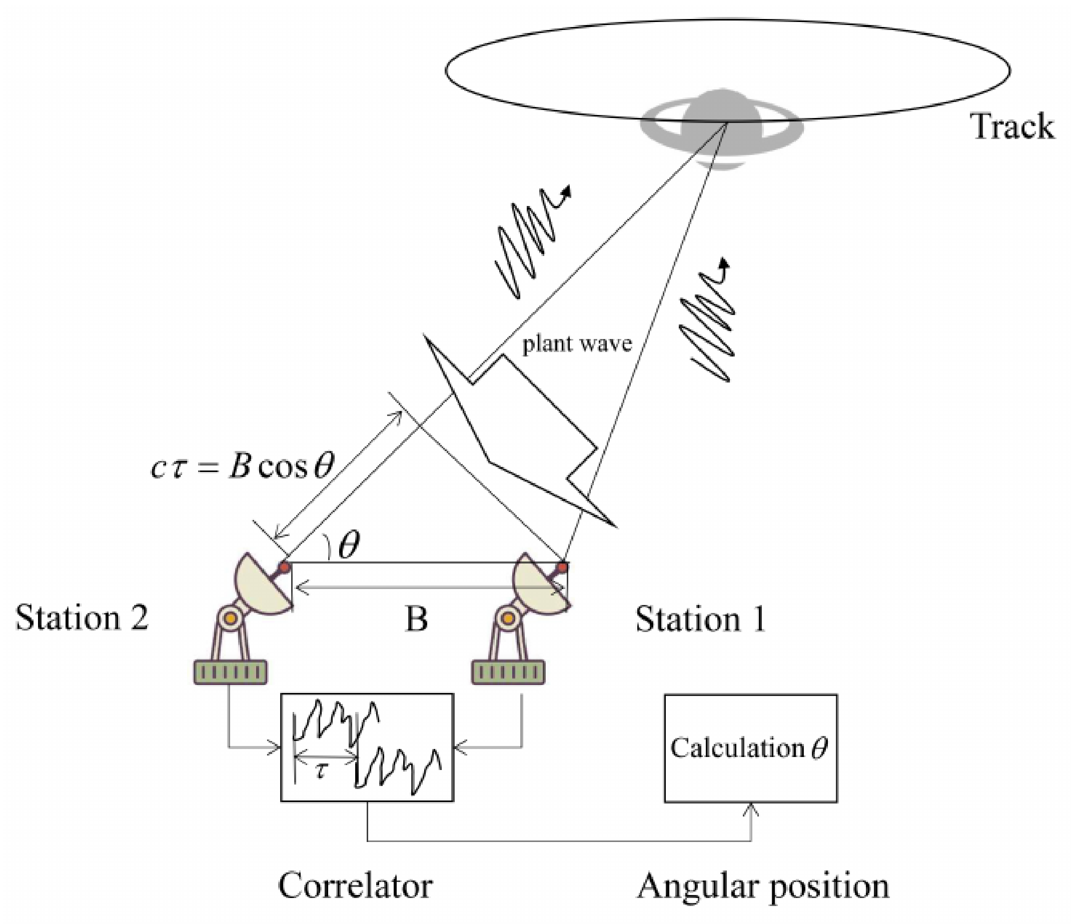

**Figure 1.15.** Schematic picture of Very Long Baseline Interferometry system; image taken from Zhang et al. (2021). A pair of two VLBI-element antennas is receiving a plane wave emitted from a celestial object. Here $B$ indicates the baseline length that is the length between two antennas. $c$ is the speed of light.

make a peak-valley pattern (i.e., so-called 'fringe'). At an observing frequency ($\lambda$), the angular resolution ($\theta_{\mathrm{res}}$) becomes: $\theta_{\mathrm{res}} \sim \lambda/d$. Successful VLBI observations depend on the detection of the fringes. This requires that the signals obtained from a pair of the antennas, are coherent with each other. Path lengths of the light received by two antennas have $\tau$ as the antennas are located at different location. This quantity should be corrected during the data reduction. 'Visibility' is the amplitude of the coherence between the observed signals. The visibility is a complex quantity in the Fourier plane $R(u, v)$ and contain the brightness distribution of the source $B(x, y)$. The relationship between the brightness distribution of the source and the visibility can be expressed by the van Cittert-Zernike theorem: the Fourier transform of the visibility is the brightness distribution of the sky. The following equation 1.2 defines the visibility function $V(u, v)$ normalized by the integral of the source brightness over solid angle (i.e., total flux of the source).

$$V(u, v) \equiv \frac{R(u, v)}{R(0, 0)} = \frac{\iint B(x, y) e^{2\pi i(ux+vy)} dxdy}{\iint B(x, y) dxdy} \tag{1.2}$$

The width of the fringes is proportional to $\theta_{\rm res}$. If the size of the target source is larger than the fringe width, then the source structure becomes removed from the resultant image (i.e., ‘resolve out’). This means that large-scale structures of the sources need shorter baseline lengths to be recovered, otherwise the positive and negative peaks of the fringes will be cancelled out with each other. VLBI observations of a faint source requires good sensitivity. The key factors which determine the sensitivity, are system equivalent flux density (SEFD), bandwidth, and on-source time. SEFD can be considered as the system noise in units of Jansky. On-source time is the observing time on a source. A better sensitivity can be achieved with low SEFD, large bandwidth (in Hz) and on-source time (in seconds). As the Earth rotates, tracking of VLBI arrays on a target source is recorded on the Fourier plane; the $uv$-coordinates of the antennas (baseline length) perpendicular to the vector of the line of sight in wavelengths. The $u$ and $v$ axis correspond to the East-to-West direction and the North-to-South direction, respectively. Sampling of the visibilities measured by all the pairs of the VLBI antennas (i.e., the $uv$-coverage) can be considered as point spread function (PSF) or the beam. The $uv$-coverage acts like a single-dish with a diameter of the maximum baseline length of a VLBI array; in the case of the very long baseline array (VLBA), it becomes a length of the Earth’s diameter. An example of the $uv$-coverage of a VLBI array can be found in Figure 1.16. The beam pattern of a VLBI observation can be obtained from the inverse Fourier transform of the $uv$-coverage.

The Astronomical Image Processing System[3] (AIPS) has been the standard software for the calibration of VLBI data. The calibration of raw VLBI data obtained from the correlator

---

[3] `http://www.aips.nrao.edu/index.shtml`

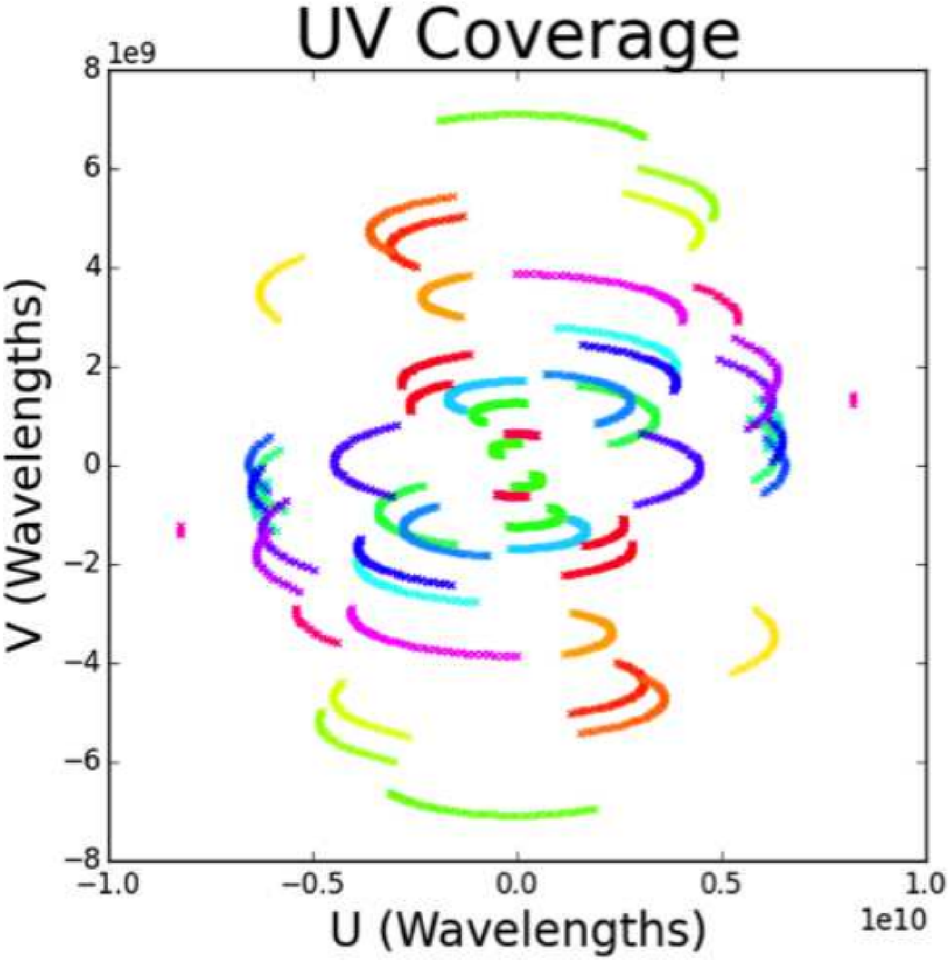

**Figure 1.16.** *uv*-coverage of the Event Horizon Telescope (EHT). The projected baseline lengths can be seen as the EHT antennas track the target source M 87. Each color corresponds to the same antenna pair. Image credit: Bouman et al. (2016).

centers (e.g., NRAO, Soccoro in the USA), includes the phase correction (i.e., delays) caused by the ionosphere, time-dependent positions of the antennas (the Earth Orientation Parameters; EOPs), an amplitude correction with the information of the gain curve (the source elevation) and system temperature of each antenna related to the receiver and weather conditions, the conversion of the visibility amplitude to the physical unit (Jansky) and the correction for the visibility phase (e.g., the parallactic angle of the antennas, the geometric delays, and the phase

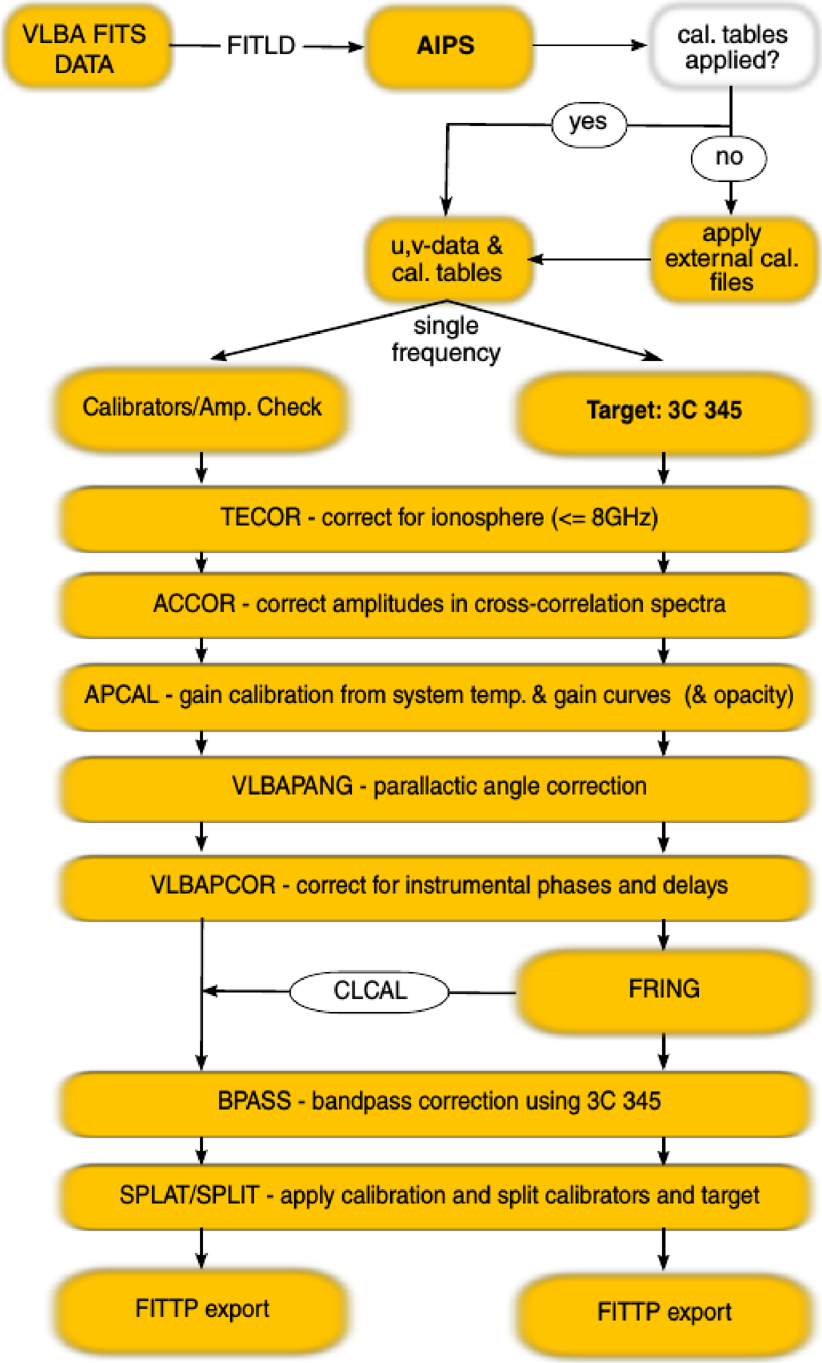

**Figure 1.17.** Calibration steps and reduction procedure in AIPS for VLBA observations. An overview of various AIPS tasks is presented. Image credit: Schinzel (2011).

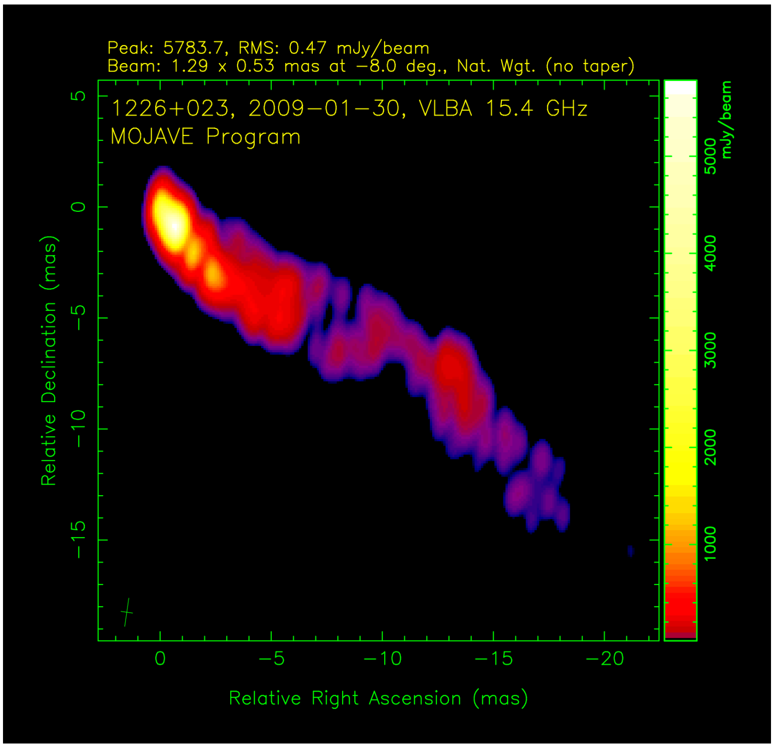

**Figure 1.18.** The relativistic jet of the blazar 3C 273 (the redshift of ~0.16) observed by the VLBA on 30 January 2009. Strong radio emission (15 GHz) can be seen throughout the parsec-scale jet regions. The image scale is 2.71 pc/mas. Image credit: MOJAVE program[4].

variations along the frequency bandwidth). Lastly, the global fringe fitting identifies the significant fringes (i.e., peaks) based on the amplitude and phase of the corrected signals. The higher integration time we have in this process (e.g., 5 minutes, depending on the observing frequency), the better for signal to noise ratio (S/N), owing to the interference by the atmosphere (ionosphere and troposphere). In AIPS, the above steps can be performed with various tasks. An overview of them can be found in Figure 1.17.

Once the calibration in AIPS is finished, the calibrated *uv* data can be imaged in the software DIFMAP[5]. The initial data shows a residual map (so-called 'dirty map'). The true source structure is buried in this dirty map. This map is produced by convolving the brightness distribution of the sky with the dirty beam. This beam has a lot of sidelobes that are caused by incom-

---

[5] `https://www.cv.nrao.edu/adass/adassVI/shepherdm.html`

plete *uv*-coverage due to limited number of the antennas, observing time, and bandwidth. Thus, care should be taken in the imaging process as many artifacts (e.g., bright knots) will appear in the residual map. In general, CLEAN (Högbom 1974) is the most commonly used method for the image construction. The CLEAN extracts and removes bright regions (i.e., intensity peaks) in the residual map by deconvolving the beam. One can iterate the CLEAN process until the residual map becomes noisy without any significant, notable emission. With these CLEANed components, the phase and amplitude of the visibilities can be further corrected by the self-calibration; at least three antennas are required for the phase only self-calibration, whereas four antennas for the amplitude+phase self-calibration. Once the above processes are done, the final image can be obtained from this fully calibrated *uv* data. Figure 1.18 shows a final image of the jet of 3C 273. The image construction of this VLBA data can be done with both AIPS and DIFMAP.

### 1.2.2 *Fermi*-LAT

The *Fermi* Gamma-ray Space Telescope (*Fermi*), is a $\gamma$-ray telescope which is operated in space (see Figure 1.19). This satellite was launched on 11 June 2008 and orbits the Earth every 96 minutes in the inclination angle of 26° at an altitude of 535 km[6]. The GLAST covers the photon energy range of 8 keV–300 GeV. The observing mode of the telescope is a survey mode, thus scanning the entire $\gamma$-ray sky every two orbits. The GLAST is a powerful tool in $\gamma$-ray astronomy and one can study the following astronomical objects with this telescope: supernova remnants, $\gamma$-ray bursts, pulsar nebulae, AGNs, binary sources, pulsars, diffuse $\gamma$-rays, and extragalactic background. There are two instruments that the GLAST carries: the Large Area Telescope (LAT) and Gamma-ray Burst Monitor (GBM). $\gamma$-ray emission of AGN jets has been monitored[7] and studied by the LAT. The LAT is a pair-production instrument with the energy coverage of 20 MeV–300 GeV. The thin tungsten foils in the LAT instrument, produce an electron-positron pair by interacting with an incoming $\gamma$-ray. The field of view (FOV) reaches 2.4 steradians and the spatial resolution is less than 1° at 1 GeV; smaller resolutions with higher

---

[6] `https://fermi.gsfc.nasa.gov/science/eteu/about/`

[7] `https://fermi.gsfc.nasa.gov/ssc/data/access/lat/msl_lc/`

**Figure 1.19.** A picture of the *Fermi* Large Area Telescope (LAT).

energy bands.

The $\gamma$-ray detection is performed with the detectors in the same manner as particle accelerators. $\gamma$-rays coming from the Universe, pass through the LAT instrument (see Figure 1.20). The first entrance into the LAT is the thin plastic anticoincidence detector. This 1st detector filters out any charged cosmic rays which cause a flash of light. Then, the $\gamma$-rays enter the 2nd consecutive detectors: a lot of sets of the conversion foils + silicon strip detectors. Once the $\gamma$-rays produce two charged particles (electron and positron) by interacting with the atom in one of the foils, the silicon strips can track further the propagation of the particles which leads to the direction of the incoming $\gamma$-rays. Lastly, a thick calorimeter measures the total

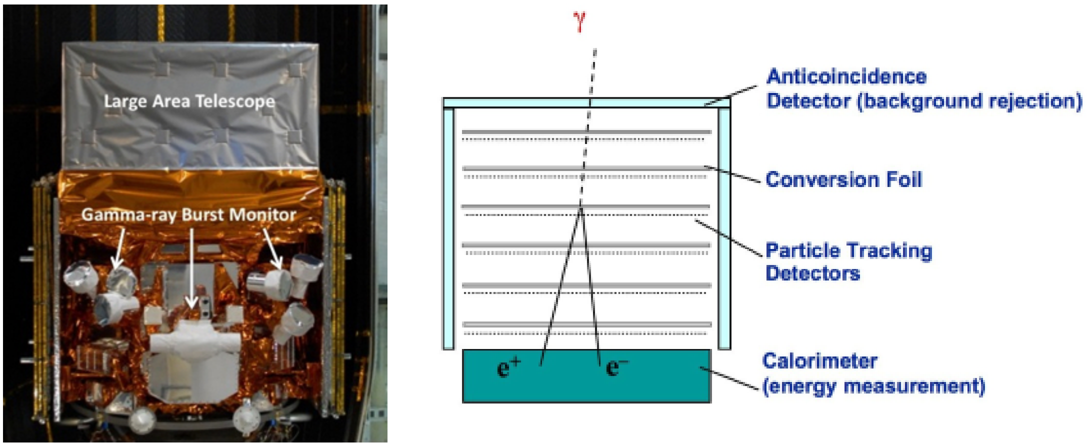

**Figure 1.20.** *left* (a): two instruments of the GLAST. *right* (b): internal structure of the LAT instrument.

energy of the pairs received in the energy band of the LAT. From all these detectors, the energy and direction of the incoming $\gamma$-rays can be estimated. Background emission which is charged cosmic particles, can disrupt the estimation of the $\gamma$-rays. Such events are prevented by the anti-coincidence detector (ACD): numbers of scintillator tiles surround the LAT. The presence of the ACD improves the sensitivity of the LAT instrument dramatically. More details about an overview of the LAT can be found in the NASA website[8].

Raw LAT data needs to be fully calibrated with the software Fermitools[9] which is developed by the *Fermi* group. It was initially operated in a stand-alone way (i.e., *Fermi* Science-Tools). However, the software has recently been combined, merged into a Python-based way (i.e., the Fermitools). The Fermitools has various tasks and one can perform data analysis, calibration, and the evaluation of the significance of the detected $\gamma$-ray emission with them. So far, observations of the LAT have reported lots of bright $\gamma$-ray emitting sources in the sky. A recent catalog (i.e., *Fermi*-LAT Fourth Source Catalog Paper; 4FGL) with more than 5000 of the *Fermi* $\gamma$-ray sources can be found in The Fermi-LAT Collaboration et al. (2019). The most recent *Fermi* catalog (4FGL-DR2) has now been published (The Fermi-LAT Collaboration et

---

[8] https://fermi.gsfc.nasa.gov/ssc/data/analysis/documentation/Cicerone/Cicerone_Introduction/LAT_overview.html

[9] https://fermi.gsfc.nasa.gov/ssc/data/analysis/software

al. 2021).

## 1.3 High energy $\gamma$-ray emission in blazars

### 1.3.1 Nonthermal emission

AGN jets are a strong synchrotron emitter as it has both relativistic electrons and magnetic fields. Synchrotron is a radiative process that produces nonthermal emission. Suppose a relativistic electron (or positron) with energy $\gamma m_e c^2$ where $\gamma$ is Lorentz factor, revolving round a static magnetic field line. This electron will emit synchrotron radiation which is linearly polarized about 70%. Figure 1.21 describes the emitting mechanism. Owing to the relativistic motion of the electron, the radiation becomes highly beamed, focused into the angular cone. The characteristic frequency $\nu_c$ is $\sim \gamma^2 B$ MHz and the cooling timescale is $t_{\rm syn} \sim 8 \times 10^8 B^{-2} \gamma^{-1}$ s, where $B$ is the magnetic field strength in units of Gauss (e.g., Rybicki & Lightman 1997). In AGN jets, emission from radio to UV (or up to X-rays) is assumed to be synchrotron emission. In the case of $\gamma$-rays, it is expected to be produced via inverse Compton process. This is due to

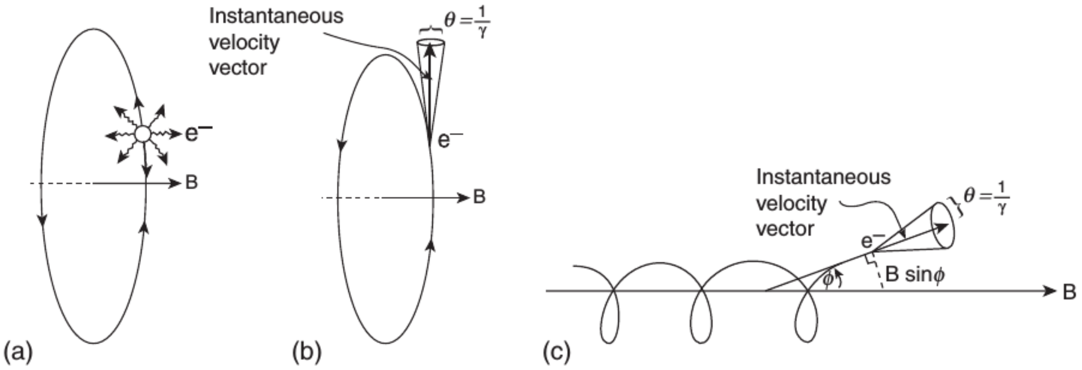

**Figure 1.21.** A picture of nonthermal emission produced by an electron ($e^-$) encircling magnetic field line $B$; image taken from Irwin (2007). (a) Non-relativistic electron produces *cyclotron radiation* in all directions. (b) Relativistic electron produces *synchrotron radiation* in the direction of half-opening angle $\theta = 1/\gamma$. (c) Relativistic electrons practically have both velocity components parallel and perpendicular to $B$. $\phi$ is the pitch angle of the electron.

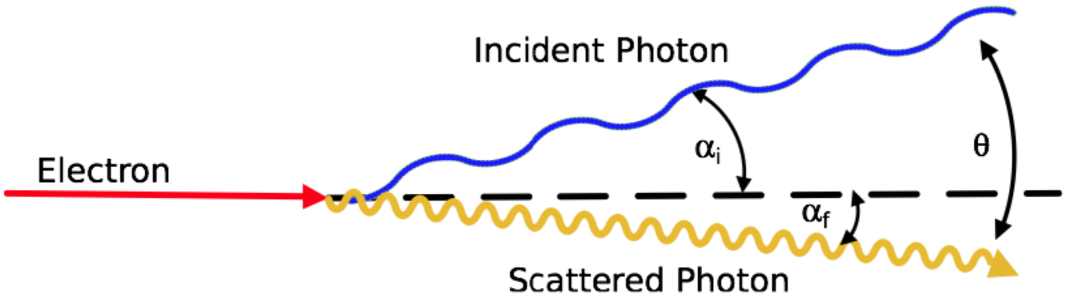

**Figure 1.22.** Schematic view of inverse Compton scattering; image taken from Ertley (2014). Each component is shown in different color s: high energy electron (red), incoming soft seed photon (blue), and up-scattered high frequency photon (yellow).

a radiation reaction limit (i.e., ~70 MeV). However, there is a possibility of synchrotron $\gamma$-ray emission which requires large electric field components along the magnetic field (e.g., Blandford et al. 2019; Meyer et al. 2019). This predicts synchrotron $\gamma$-rays of ~0.5 MeV in the frame of AGN jets that are emitted from high-energy electrons of reaching ~300 GeV accelerated by the electric fields (Meyer et al. 2019).

In general, X-rays and $\gamma$-rays from AGN jets are assumed to be produced via inverse Compton scattering (IC). An interaction between photons and particles (e.g., electron or positron) causes the IC process. Figure 1.22 shows a picture that describes how this process occur: an incoming photon (seed photon) collides inelastically with a high energy electron. As a result, the electron loses its kinetic energy, whereas the seed photon gains energy and become higher-frequency radiation. Such process requires a condition that energy of the electron is larger than energy of the seed photon. For the $\gamma$-rays of AGN jets, soft (e.g., infrared) seed photons are up-scattered by highly relativisitic electrons in the jets. Then, the frequency ($\nu$) of the seed photons becomes Doppler-boosted by an average factor of $\sim \gamma^2$ in the observer's frame, because the electron motion is relativistic with a Lorentz factor. Seed photons may originates from the jet itself, dusty torus, broad-line region, and the accretion disk. Thus, the properties of these sources (e.g., size, location, and radiation field) are one of the important elements that determine the nature of the IC $\gamma$-ray emission in AGN jets.

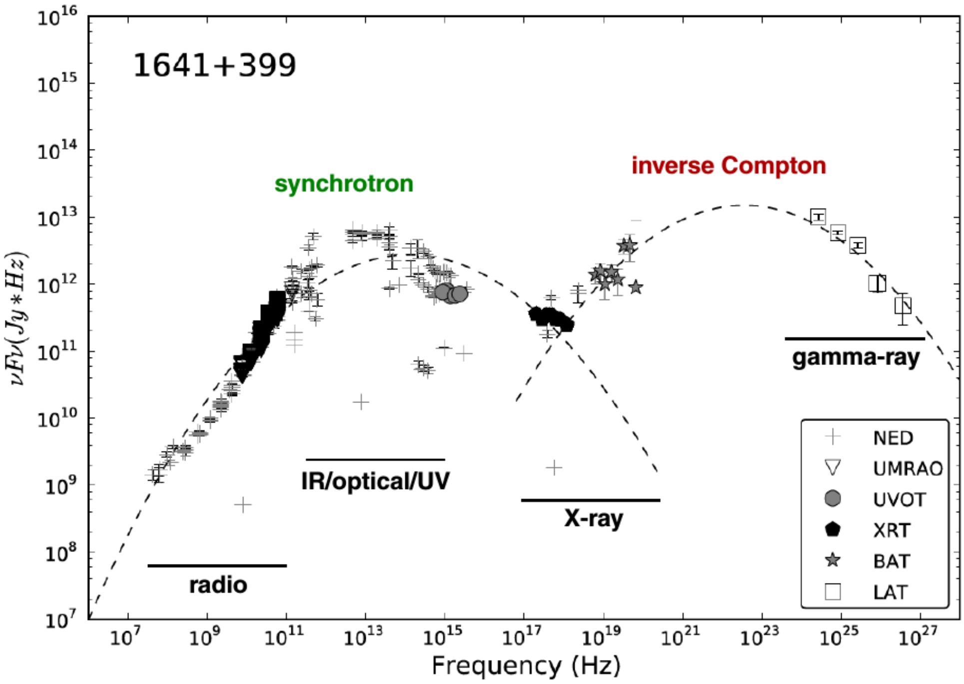

**Figure 1.23.** SED of the blazar 3C 345; image taken from Schinzel (2011). The two main mechanisms of the emission are displayed.

Typically, blazars radiate non-thermal emission over the wide spectral range from radio to $\gamma$-rays. The spectral energy distributions (SED) of blazars are supposedly dominated by the emission from relativistic jets (Lewis et al. 2018). The relativistic jets are responsible for the formation of the observed spectral energy distributions (SEDs) of blazars (Chen 2018; Lewis et al. 2018; Meyer et al. 2019). In general, blazar SEDs consist of two ‘humps’ (see e.g., Figure 1.23): one which is located at relatively low frequencies from radio to UV/X-ray which is attributed to synchrotron radiation; one at higher frequencies from X-rays, all the way up to $\gamma$-rays which is attributed to IC radiation (e.g., Potter & Cotter 2013; Ramakrishnan et al. 2015; Piano et al. 2018; Liodakis et al. 2019). To date, the physical processes of blazar jets, such as the acceleration of relativistic electrons, the structure of the inner jet region, the magnetic field structure, the origin of the seed photons for the IC process, and multi-waveband correlations are still unclear. However, these processes play a key role in the flaring activities of the jets and lead to changes in the SEDs (e.g., Figure 1.24).

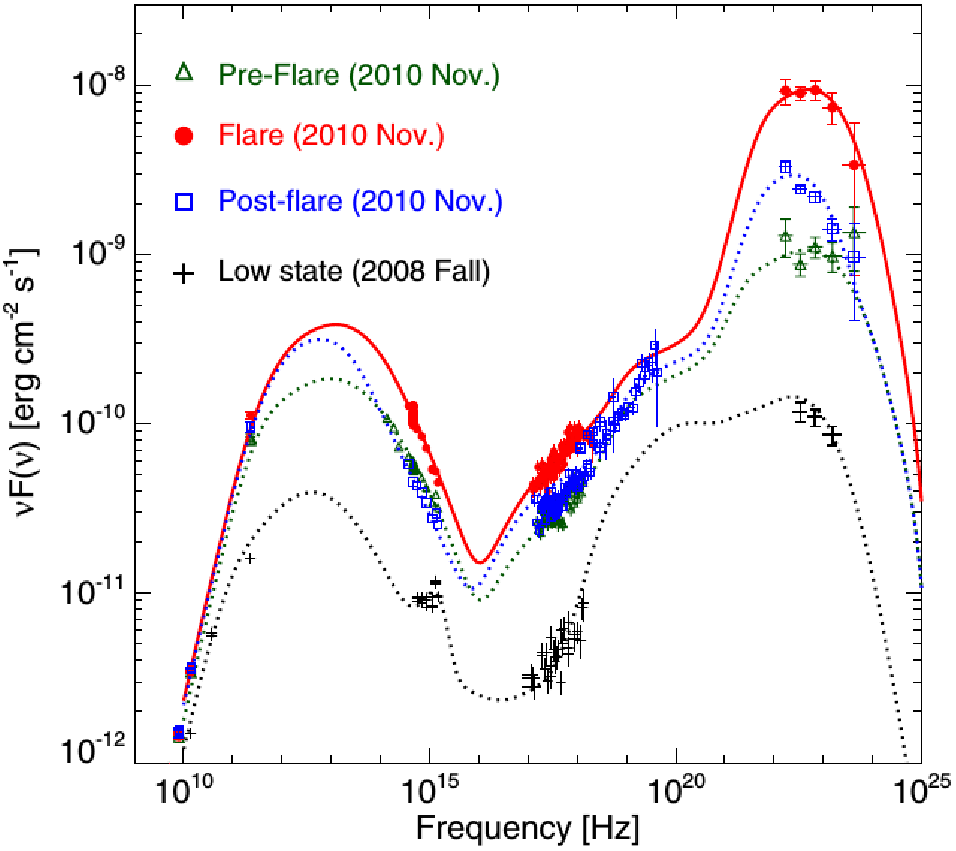

**Figure 1.24.** SED of the blazar 3C 454.3; image taken from Vercellone (2019). The SEDs of the 2010 November flare are presented in different color.

Furthermore, blazars can be divided based on the frequency of the synchrotron peak in the SEDs: low-synchrotron peaked (LSP) for $\nu_{\rm sy}^{\rm peak} < 10^{14}$ Hz, intermediate-synchrotron peaked (ISP) for $10^{14} \leq \nu_{\rm sy}^{\rm peak} \leq 10^{15}$ Hz, and high-synchrotron peaked (HSP) blazars for $\nu_{\rm sy}^{\rm peak} > 10^{15}$ Hz. In addition to this, Fossati et al. (1998) found a correlation (the ‘blazar sequence’) in blazar SEDs between the synchrotron hump and the IC hump which implies a tight connection between the powerful radio jet and $\gamma$-ray emission in blazars (e.g., Hughes et al. 2011; Jorstad et al. 2013). Indeed, several studies suggest a strong correlation between the radio and $\gamma$-ray emission (León-Tavares et al. 2012; Lico et al. 2017).

As mentioned above, the standard model of blazar SEDs is the leptonic models: the radiative output of synchrotron + synchrotron-self Compton (SSC). This indicates that the $\gamma$-ray emission of blazar jets is dominated by the leptonic processes (e.g., Liodakis et al. 2019; but see also H.E.S.S Collaboration et al. 2019, for discussion of its limitations and alternative models). As an alternative, however, the hadronic models (e.g., proton synchrotron) cannot be ruled out (e.g., Böttcher et al. 2013). In this scenario, both electrons and protons are actively radiate in the jets. However, the hadronic processes are responsible for the high-energy emission (e.g., $\gamma$-rays), whereas the low-energy emission is still produced mainly by the synchrotron process (e.g., Böttcher et al. 2013; Cerruti et al. 2015). Recently, a combined model of the leptonic and hadronic processes (i.e., a lepto-hadronic radiative model) has been developed by many researchers (e.g., Paliya et al. 2018). Such approaches will provide more detailed information on the processes of the observed blazar SEDs.

### 1.3.2 The radio/$\gamma$-ray connection

Since the dawn of the *Fermi*-LAT era it has became clear that blazars are the dominant source type (~75% of sources, excluding unknown blazar types) in the extragalactic $\gamma$-ray sky above 10 GeV (Ajello et al. 2017). As can be seen in Figure 1.25, it has been revealed that the $\gamma$-ray bright blazars have powerful radio jets.

Blazars are arguably the most energetic persistent objects in the Universe. As mentioned in Section 1.1.1, they are characterized by various extreme phenomena, such as powerful non-thermal emission, rapid variability, superluminal motion, and strong polarization (Trippe et al. 2012). This phenomenology can be explained by the presence of a relativistic jet whose emission is subject to substantial Doppler boosting that is the result of a small viewing angle between the jet axis and the line of sight (e.g., Blandford et al. 2019). $\gamma$-ray emission from blazars is known to vary on short timescales ranging from minutes to days (e.g., Nalewajko 2013; Petropoulou & Dimitrakoudis 2015; Meyer et al. 2019). However, the origin and physical radiation mechanisms of the high energy ($\gamma$-rays) emission in blazar jets are still unknown due to the spatial resolution of high energy telescopes is inadequate (Chatterjee et al. 2012; Fuhrmann et al. 2014; Max-Moerbeck et al. 2014a; Jorstad & Marscher 2016; Lewis et al. 2018). The connection between radio and $\gamma$-ray emission in blazars is now a matter of active debate (Jorstad et al. 2001a; Marscher et al. 2010, 2011; Chatterjee et al. 2012; Raiteri et al. 2013; Marscher 2014; Ramakrishnan et al. 2016; Wehrle et al. 2016). The most plausible scenario suggests that the bulk of the gamma-ray emission is produced within the parsec-scale jet (Ramakrishnan et al. 2014; Kravchenko et al. 2016; Lisakov et al. 2017), and may be associated with the stationary structures (e.g. Pushkarev et al. 2019; Kim et al. 2020).

Emission regions located within relativistic jets (e.g., Marscher et al. 2008; Boccardi et al. 2017) are thought to be the production site of $\gamma$-radiation – notably, of $\gamma$-ray flares – in blazars. Models of the location of $\gamma$-ray flares broadly suggest two potential locations (e.g., Dotson et al. 2012): the broad line region (BLR) and the radio core which is the surface of unity optical depth. At sub-parsec scale distances from the black hole (BH), optical–UV photons from the BLR can be up-scattered by electrons accelerated in a relativistic shock (Sikora et al. 1994). Such shocks are supposed to occur when a disturbance moving along the jet passes through the acceleration and collimation zone (ACZ) (see also Marscher et al. 2008, for the canonical model of a blazar jet). In opposition to this scenario, many observations which found concurrence of

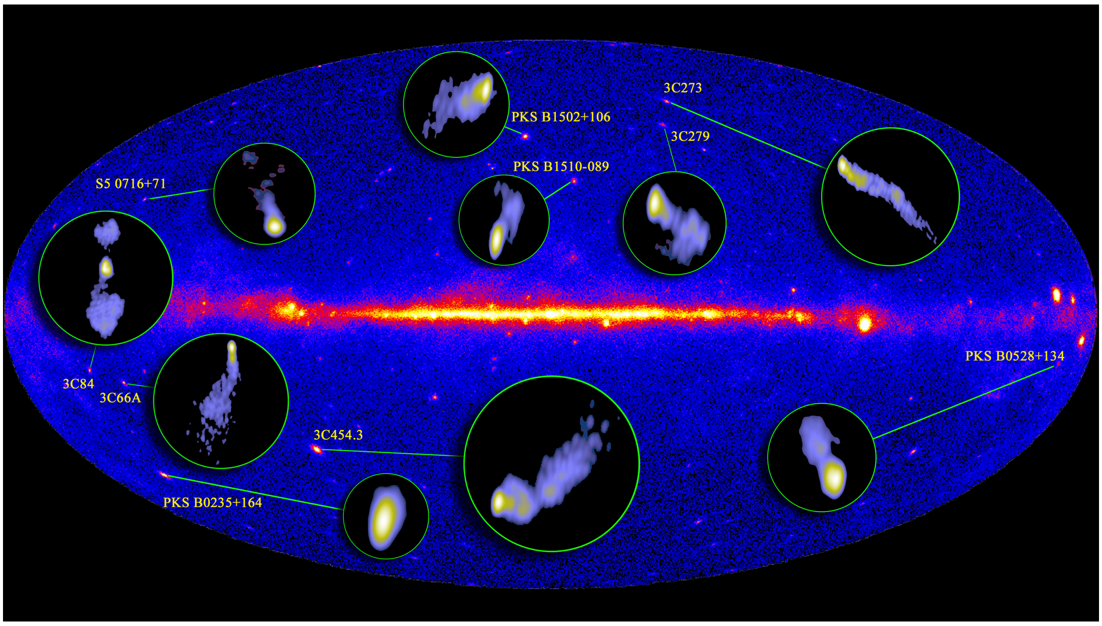

**Figure 1.25.** *Fermi*-LAT $\gamma$-ray sky. $\gamma$-ray bright AGNs (mostly blazars) in the sky, are indicated with their relativistic jets. Image credit: NASA/DOE/*Fermi* LAT Collaboration and MOJAVE.

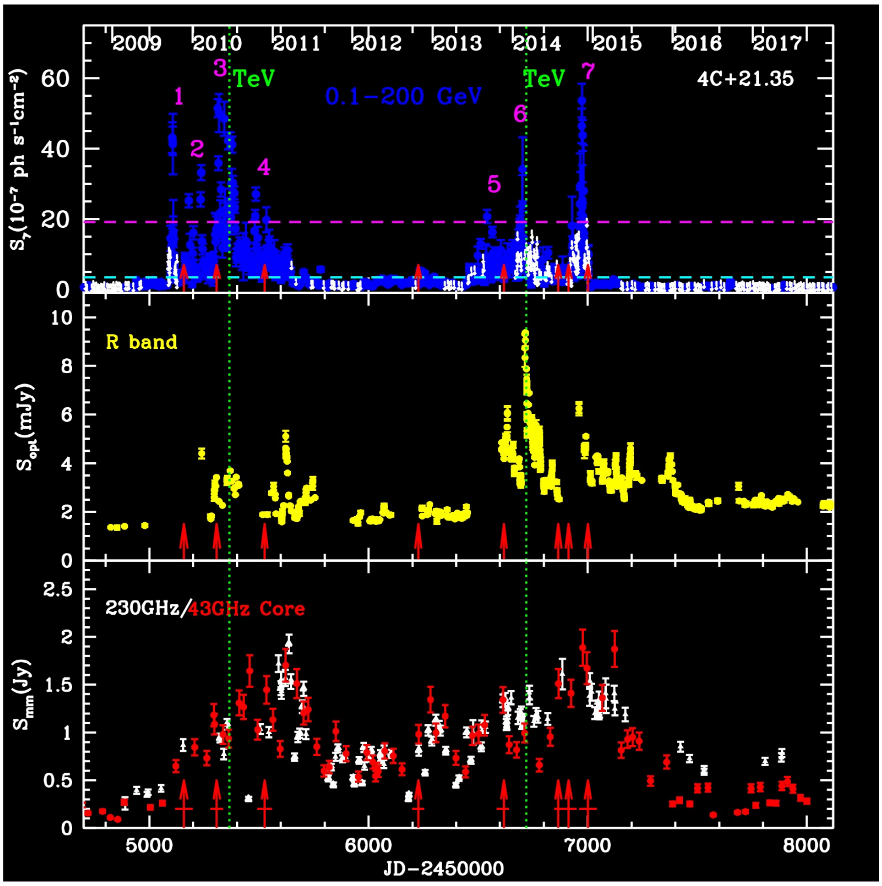

**Figure 1.26.** Radio (*bottom*), optical (*middle*), and $\gamma$-ray (*top*) light curves (i.e., brightness vs. time) of the blazar 4C 21.35. The green vertical lines indicate the detection of bright TeV $\gamma$-rays. The red upward arrows denote the ejection times of new moving blobs in VLBI image. Flux densities of the 43 GHz core are measured with the VLBA. Image credit: BU group[10] (Boston University Blazar Group).

events at different wavebands (including $\gamma$-rays) point to the radio core (i.e., $\geq 10^4$ $R_\mathrm{s}$) as the place of origin of $\gamma$-ray events. In this scenario, $\gamma$-radiation is produced via inverse Compton scattering of radio-to-IR seed photons from the jet itself (e.g., Marscher et al. 2010) or from the dusty torus located a few parsecs from the black hole (León-Tavares et al. 2011). In addition, the absence of $\gamma$-ray absorption by the BLR photons further supports a location of the $\gamma$-ray dissipation zone downstream of the relativistic jet, where the parsec-scale radio core appears (e.g., Harris et al. 2012; Costamante et al. 2018; Meyer et al. 2019; see also Jorstad et al. 2013;

Kravchenko et al. 2016; Kim et al. 2018b, for VLBI studies consistent with the idea). However, the $\gamma$-ray origin with the BLR photons which is closer to the central black hole, still cannot be ruled out as the $\gamma$-ray production site (e.g., Rani et al. 2013b; Berton et al. 2018; but see also Hodgson et al. 2018; Rani et al. 2018, for discussion of multiple $\gamma$-ray sites).

The parsec-scale scenario has been supported by Jorstad et al. (2001a,b) who observed a connection of the $\gamma$-ray emission with the ejection of (apparently) superluminal jet components and the flux density of the VLBI core. Further insights are provided multi-waveband photometry plus polarimetry VLBI campaigns. Agudo et al. (2011b) reported that a disturbance propagating through the 7-mm core caused a very strong $\gamma$-ray outburst with counterparts at frequencies from radio to $\gamma$-rays in the blazar AO 0235+164 in 2008. The disturbance showed strong linear polarization, corresponding to the signature of a moving shock (Marscher et al. 2010; Wehrle et al. 2012; Jorstad et al. 2013). Such scenario expects the presence of $\gamma$-ray outbursts when a radio flare (i.e., the “radio counterparts”) is rising or peaking (Valtaoja & Teräsranta 1995; León-Tavares et al. 2011). It occasionally shows distinct spectral variations at $\gamma$-rays such as hardening or softening (e.g., Rani et al. 2013b; Kim et al. 2018b; Shah et al. 2019; but see also Nalewajko 2013; Paliya 2015, for limitations in the spectral analysis). Thus, the ejection of new jet components and $\gamma$-ray outbursts are correlated in the jets and tend to cause an increase in core opacity (e.g., Jorstad et al. 2001b, 2013).

Multiwaveband studies have reported strong positive correlations between $\gamma$-ray emission and the emission at lower frequencies (e.g., Algaba et al. 2018; Prince 2019). Figure 1.26 shows typical multi-waveband light curves of a blazar. Significant $\gamma$-ray outbursts are marked by the magenta numbers. The observations provide indications for the emission physics: a small or narrow emission region, variations in acceleration or cooling processes, and spatial separation between emitting regions at different observing frequencies. The $\gamma$-ray-to-radio correlations (e.g., Pushkarev et al. 2010; León-Tavares et al. 2012; Ramakrishnan et al. 2015; Lico et al. 2017) in particular played an important role in linking the $\gamma$-ray production site to the VLBI radio core (see e.g., Figure 1.27). Lico et al. (2014) also found a correlation between the flux of the radio core (at 15, 24, and 43 GHz) and $\gamma$-ray emission in the blazar Mrk 421 throughout 2011, albeit with substantial scatter (with Pearson correlation coefficients of 0.42 to 0.46).

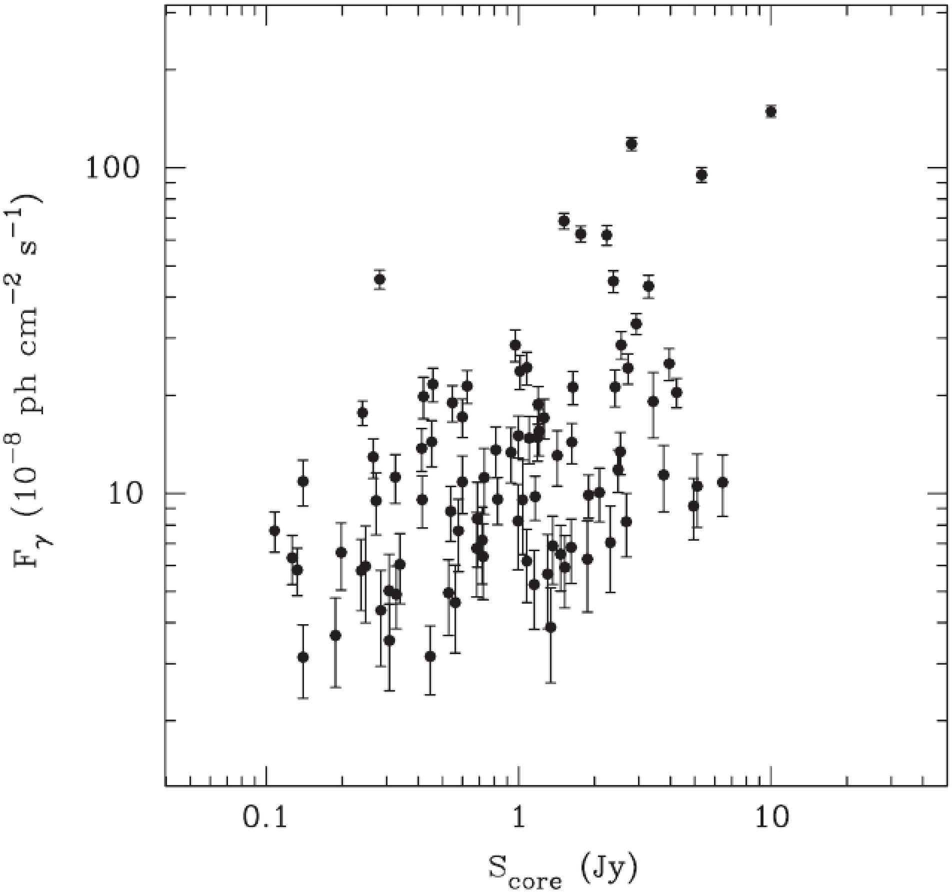

**Figure 1.27.** Correlation between Radio and $\gamma$-ray (0.1–100 GeV) emission of more than 100 $\gamma$-ray bright AGNs; image taken from Pushkarev et al. (2010). The radio core fluxes are obtained from the VLBA at 15 GHz.

During their observations, only the first $\gamma$-ray peak (on MJD 55627) had a radio counterpart (on MJD 55621) in the 7-mm core flux. Given the sampling interval of the radio observations, it is unclear where the radio counterpart peaked. They also reported no spectral hardening in the $\gamma$-ray spectrum during the enhanced $\gamma$-ray state in Mrk 421, which is a rare feature in blazars. In addition to this, Jorstad et al. (2001a) also found a positive correlation between radio core flux and $\gamma$-ray flux in 42 $\gamma$-ray bright blazars, thus suggesting that the $\gamma$-ray emission site is located near the core. On the other hand, several studies do not find significant correlations between radio and $\gamma$-ray emission from BL Lac objects (e.g., León-Tavares et al. 2011) and blazars (e.g., Max-Moerbeck et al. 2014a). Hence, the connection between radio and $\gamma$-ray emission from blazar jets is rather obscure because of the complicated and dynamic processes of the emission. More detailed studies with many samples are further required.

Moreover, the picture could be complicated further by 'orphan' $\gamma$-ray flares that have no counterparts at lower frequencies (Krawczynski et al. 2004; Böttcher 2005; MacDonald et al. 2015; Banasiński et al. 2016). Orphan $\gamma$-ray flares are thought to occur occasionally in BL Lac objects and a few FSRQs (Banasiński et al. 2016). A number of studies suggests possible origins of orphan flares: (i) a sudden enhancement of an external radiation field (e.g., from the accretion disk) (Krawczynski et al. 2004); (ii) a slow jet sheath (the 'ring of fire') in front of the radio core provides localized seed photons to a relativistic plasma cloud during its passage through the ring (MacDonald et al. 2015); (iii) an interaction of relativistic jet particles with a dense radiation field or stellar wind from a luminous star located around the central engine (Banasiński et al. 2016).

## 1.4 Thesis outline

This thesis aims to present all works I have done throughout the whole time of my integrated MS + PhD course. Thus, the contents of the thesis are focused on four journal papers written by me; three of them (i.e., Chapter 2 to 4) are already published by the journals JKAS, MNRAS, and A&A and the other one (Chapter 5) is currently under review by ApJ. Throughout Chapter 1, an overview on the relativistic jets of radio-loud AGNs, data/observations, $\gamma$-ray emission in blazar jets is given for better understanding of the works. From Chapter 2 to 5 (i.e., studies of the blazars: BL Lacertae, 1749+096, 3C 273, and 0716+714), I present the four papers that are my previous/ongoing studies of the radio/$\gamma$-ray connection of blazars. Each of these Chapters has a structure of introduction to the target source (i.e., blazars), data/observations, results, discussion, and summary. Then, the last Chapter 6 presents a conclusion that is what I have learned from the four works.

The four works provide the wealth of information in the relevant research field by reporting either new data or results/interpretations. In Chapter 2, I focused on the profiles of radio emission of BL Lacertae obtained from KVN observations. The KVN is kind of a new VLBI array and is able to perform multi-frequency (22/43/86/129 GHz) simultaneous observation. Using the KVN, we showed this new VLBI data and a science case that can be done with the KVN; physical conditions of the jet were measured by using the timescales and spectral properties of the radio emission. In Chapter 3, I studied a huge $\gamma$-ray flare occurred in 2016 in the blazar 1749+096 by using the KVN, VLBA, and multi-waveband light curves (from radio to $\gamma$-ray). There are only a handful of studies on the jet of this blazar and the 2016 $\gamma$-ray outburst was investigated in this work for the first time. Multi-waveband correlations and linearly polarized emission in the core region were explored intensively at the time of the 2016 $\gamma$-ray outburst. In Chapter 4, one of the most famous blazar 3C 273 was studied by using the VLBA, ALMA, and *Fermi*-LAT. In this study, I focused on two intermediate-level $\gamma$-ray flares occurred between 2015 and 2018. Given their relatively low flux levels and the absence of previous studies on these two $\gamma$-ray events, I checked these two $\gamma$-ray events carefully. The radio/$\gamma$-ray correlation, inner jet structures, and pc-scale jet activity were investigated at the time of the two $\gamma$-ray flares. The analysis revealed that multiple stationary components located near the radio core, play an important role in both radio and $\gamma$-ray emission. This is a new result, considering the general expectation that the radio core is the production site of $\gamma$-ray flares in the pc-scale regions. In Chapter 5, more detailed analysis on the radio/$\gamma$-ray connection was performed in the blazar 0716+714. This blazar is known to have a rapid variability even at radio wavelengths (e.g., scales of months). Thus, I focused on making an appropriate analysis to identify any significant radio/$\gamma$-ray correlations. Multi-frequency radio light curves and *Fermi*-LAT were used for the analysis. Jet kinematics with the VLBA, was further provided to interpret the observed radio/$\gamma$-ray correlations. In this study, we found an anti-correlation between the radio and $\gamma$-ray light curves. To explain this unusual phenomenon, we suggest a new interpretation.

# Chapter 2

# The Millimeter-Radio Emission of BL Lacertae During Two $\gamma$-Ray Outbursts[1]

## Abstract

We present a study of the inexplicit connection between radio jet activity and $\gamma$-ray emission of BL Lacertae (BL Lac; 2200+420). We analyze the long-term millimeter activity of BL Lac via interferometric observations with the Korean VLBI Network (KVN) obtained at 22, 43, 86, and 129 GHz simultaneously over three years (from January 2013 to March 2016); during this time, two $\gamma$-ray outbursts (in November 2013 and March 2015) can be seen in $\gamma$-ray light curves obtained from *Fermi* observations. The KVN radio core is optically thick at least up to 86 GHz; there is indication that it might be optically thin at higher frequencies. To first order, the radio light curves decay exponentially over the time span covered by our observations, with decay timescales of 411±85 days, 352±79 days, 310±57 days, and 283±55 days at 22, 43, 86, and 129 GHz, respectively. Assuming synchrotron cooling, a cooling time of around one year is consistent with magnetic field strengths $B \sim 2\,\mu\mathrm{T}$ and electron Lorentz factors $\gamma \sim 10\,000$. Taking into account that our formal measurement errors include intrinsic variability

---

[1] Published in the *Journal of the Korean Astronomical Society*: Kim et al. 2017, JKAS, 50, 167

and thus over-estimate the statistical uncertainties, we find that the decay timescale $\tau$ scales with frequency $\nu$ like $\tau \propto \nu^{-0.2}$. This relation is much shallower than the one expected from opacity effects (core shift), but in agreement with the (sub-)mm radio core being a standing recollimation shock. We do not find convincing radio flux counterparts to the $\gamma$-ray outbursts. The spectral evolution is consistent with the 'generalized shock model' of Valtaoja et al. (1992). A temporary increase in the core opacity and the emergence of a knot around the time of the second $\gamma$-ray event indicate that this $\gamma$-ray outburst might be an 'orphan' flare powered by the 'ring of fire' mechanism.

## 2.1 Introduction

BL Lacertae (redshift $z = 0.069$, image scale 1.29 pc/mas), the prototypical BL Lac object, is characterized by strong flux variability from radio to $\gamma$-rays, high radio brightness (>1 Jy), superluminal motion of jet components, and linearly polarized emission. Villata et al. (2004) reported evidence for a (quasi-)periodic occurrence of major radio flares on a timescale of about eight years. BL Lac is known as a $\gamma$-ray bright AGN, beginning with the first detection of $\gamma$-ray emission by Catanese et al. (1997) in early 1995. Subsequent detections or reports occurred in 1997, 2005, 2011, 2012, and 2013 by Bloom et al. (1997), Albert et al. (2007), Arlen et al. (2013), Wehrle et al. (2016), and Gómez et al. (2016), respectively. BL Lac was highly active at $\gamma$-ray and radio in 2012, showing a very strong radio outburst that peaked at the end of 2012 (see also Gómez et al. 2016; Wehrle et al. 2016, for recent discussions). Gómez et al. (2016) detected two polarized stationary features in the jet at 0.1 mas and 0.25 mas from the core, which they interpreted as recollimation shocks. Arlen et al. (2013) found a $\gamma$-ray flare in 2011 with a radio counterpart following four months later. Subsequently, Wehrle et al. (2016) confirmed that a $\gamma$-ray flare in 2012 is associated with the historic 2012 radio outburst, showing a time-lag of 3–5 months (again with the $\gamma$-ray emission leading the radio emission).

The Korean VLBI Network (KVN) is a dedicated mm-radio VLBI array with the unique capability of observing at four frequencies simultaneously (Lee et al. 2014). The KVN covers 22, 43, 86, and 129 GHz in frequency, and consists of three antennas with a maximum baseline length of 476 km. Systematic monitoring of blazar jets with multi-frequency simultaneous

VLBI observations beyond 43 GHz is rare. Hence, the KVN will provide important information on variability, spectral properties, and evolution of blazar jets. We aim at exploring the connection between $\gamma$-ray and radio emission by monitoring the activity of the radio jet of BL Lac. In this study, we analyze the flux from and structure of BL Lac by employing dedicated KVN observations spanning three years in time, from January 2013 to March 2016; during this time, two $\gamma$-ray outbursts occured.

The reasons why we chose BL Lac, are (1) data quality and (2) source activity at $\gamma$-rays. The iMOGABA program (see Section 2.2) monitored about 30 $\gamma$-ray bright AGNs. However, the datasets of BL Lac were one of the best ones among all the target sources. In addition, we noticed that there was two notable $\gamma$-ray flares in BL Lac during the iMOGABA observations. In the following, we describe our data and observations in Section 2.2. In Section 2.3, we present the observational results, and we discuss the results in Section 2.4. Lastly, we summarize this paper in Section 2.5.

## 2.2 Observations and Data reduction

We primarily use KVN VLBI data obtained within the interferometric MOnitoring of GAmma-ray Bright AGN (iMOGABA) program[2]. iMOGABA monitors more than 30 $\gamma$-ray bright AGN via monthly (except during KVN maintenance times) KVN observations in single polarization (LCP) (Lee et al. 2016b). iMOGABA uses a snapshot mode, with several 5-minute observations spread over a few hours for each target, resulting in total integration times of few tens of minutes per source. The first observation (iMOGABA1) was performed in December 2012, with observations going on ever since. More details about iMOGABA can be found in Lee et al. (2013); Algaba et al. (2015); Hodgson et al. (2016); Lee et al. (2016b). As for the $\gamma$-ray activity of BL Lac, we follow the public database[3] (weekly light curve) of the *Fermi* Large Area Telescope (*Fermi*-LAT).

We collected data for BL Lac from 30 iMOGABA sessions (iMOGABA2 to iMOGABA32) from January 2013 (MJD 56308) to March 2016 (MJD 57448) for all four KVN frequencies.

---

[2] `https://mogaba.kasi.re.kr/`

[3] `http://fermi.gsfc.nasa.gov/ssc/data/access/lat/msl_lc/`

iMOGABA25 failed due to recording problems at Ulsan station. Due to technical or weather issues, we could not always obtain a full set (i.e., 22–129 GHz) of images in an iMOGABA session. Occasionally, the 129-GHz band had to be excluded due to instrumental problems. Some sessions suffered from an insufficient *uv* coverage at some frequencies or missing baselines after data reduction; hence, we discarded those images. In order to increase the number of measurements over time and to perform a cross-check, we included five KVN observations executed independently by the Plasma-physics of Active Galactic Nuclei (PAGaN) project (Kim et al. 2015; Oh et al. 2015). PAGaN employs full-track dual-polarization observations of selected targets, typically reaching a few hours of integration time per source and per session. Due to different on-source times, the dynamic ranges of the PAGaN data at 22, 43, and 86 GHz are about 1.5–2 times higher than the corresponding iMOGABA data on average. At 129 GHz, only one PAGaN data set of poor quality was available; thus a meaningful comparison is not possible. We summarize the iMOGABA and PAGaN observations in Table 2.1.

We reduced our data with the software packages `AIPS`[4] and `Difmap` (Shepherd et al. 1994). We followed the standard `AIPS` steps for calibration of amplitudes and phases, bandpass, and opacity correction. To compensate for known amplitude losses, we multiplied a factor 1.1 to `APARM(1)` within the `AIPS` task `APCAL` (see Lee et al. 2015). Detecting and imaging our target in data obtained at 86 and 129 GHz proved difficult because of high levels of visibility phase noise. Due to atmospheric and instrumental effects, such as tropospheric errors caused by the inhomogeneous distribution of water vapor, and high receiver temperatures (e.g., Rioja & Dodson 2011; Martí-Vidal et al. 2012; Algaba et al. 2015; Rioja et al. 2015), it is challenging to obtain good signal-to-noise (S/N) ratios, well-aligned phases, and sufficient coherence times at those high frequencies.

In order to increase coherence times, we applied the frequency phase transfer (FPT) technique (Rioja & Dodson 2011; Algaba et al. 2015; Zhao et al. 2015; Hodgson et al. 2016) to parts of our data. Based on the assumption that the tropospheric path delay is independent of the observing frequency, we transferred phase solutions obtained for 43 GHz, scaled up by the

---

[4] Astronomical Image Processing System, distributed and maintained by the National Radio Astronomy Observatory of the U.S.A. (`http://www.aips.nrao.edu/index.shtml`)

ratio of frequencies, to the higher frequencies (86 and 129 GHz) by using the option `XFER` in the `AIPS` task `SNCOR`. We obtained improved coherence times of about five minutes on average (according to Algaba et al. 2015 and Rioja et al. 2015, coherence times longer than five minutes can be reached even at 129 GHz) and thus improved S/N. Using FPT for iMOGABA data was suggested to us after we had started our analysis (Algaba et al. 2015). Therefore, for iMOGABA2 to iMOGABA23, we applied FPT only to sessions with poor data quality at 86 and/or 129 GHz, and to all data after iMOGABA23. The difference in measured flux between data with and without FPT is within 5% at 86 and 129 GHz, in agreement with the statistical errors – meaning the application (or not) of FPT does not bias our flux measurements.

We imaged our radio data manually with `Difmap`, using `CLEAN` (Högbom 1974) deconvolution and phase self-calibration. (We could not apply amplitude self-calibration because the KVN consists of three antennas.) We derived positions, flux densities, and sizes of radio components by fitting circular Gaussian profiles to them. We estimated and propagated parameter errors as suggested by Formalont (1999) and Lee et al. (2008). Before imaging the *uv* data, we flagged outlying visibilities (showing up as down-streaming features in visibility amplitude – *uv* radius diagrams) for a given antenna whenever they were clearly caused by bad antenna pointings. As far as possible, we compared our imaging results to those from the VLBA–Boston University Blazar Monitoring Program[5] as additional quality check. Our images showed the presence of a radio component (the 'knot') that corresponds to the jet. However, (re)detection of this component in the entire dataset proved difficult especially at the higher frequencies (cf. Figure 2.3). Each iMOGABA session observes simultaneously at 22, 43, 86, and 129 GHz for 24 hours, with 6 scans (corresponding to 30 minutes) on average for BL Lac, with only three antennas. The resulting sparse *uv* coverage leads to conspicuous side lobes and beam patterns that are (largely) identical in all four bands (when taking into account scaling with frequency), thus implying a risk of confusing artifacts with the actual radio jet. Therefore, we focus on analyzing the VLBI core in this study.

---

[5] `http://www.bu.edu/blazars/VLBAproject.html`

Table 2.1. Summary of observations

| Date | Session | Frequency[a] (GHz) | $t^{\mathrm{b}}_{obs}$ (min) |
|---|---|---|---|
| 2013-01-16 | iMOGABA2 | 22/43/86 | 25 |
| 2013-02-27 | iMOGABA3 | 22/43/86/129 | 25 |
| 2013-03-28 | iMOGABA4 | 22/43/86/129 | 20 |
| 2013-04-11 | iMOGABA5 | 22/43/86/129 | 30 |
| 2013-05-08 | iMOGABA6 | 22/43/86 | 25 |
| 2013-09-24 | iMOGABA7 | 22/43 | 25 |
| 2013-10-15 | iMOGABA8 | 22/43/86 | 20 |
| 2013-11-20 | iMOGABA9 | 22/43/86/129 | 30 |
| 2013-12-24 | iMOGABA10 | 22/43/86/129 | 35 |
| 2014-01-02 | PAGaN | 22/43 | 240 |
| 2014-01-27 | iMOGABA11 | 22/43 | 35 |
| 2014-02-28 | iMOGABA12 | 22/43/86/129 | 55 |
| 2014-03-05 | PAGaN | 86 | 109 |
| 2014-03-22 | iMOGABA13 | 22/43/86/129 | 35 |
| 2014-04-22 | iMOGABA14 | 22/43/86/129 | 35 |
| 2014-06-13 | iMOGABA15 | 22/43 | 45 |
| 2014-09-01 | iMOGABA16 | 22/43/86 | 30 |
| 2014-09-27 | iMOGABA17 | 22/86 | 30 |
| 2014-10-29 | iMOGABA18 | 22/43/86 | 30 |
| 2014-11-28 | iMOGABA19 | 22/43/86 | 25 |
| 2014-12-26 | iMOGABA20 | 22/43/86 | 40 |
| 2015-01-15 | iMOGABA21 | 22/43/86 | 35 |
| 2015-02-24 | iMOGABA22 | 22/43/86 | 35 |
| 2015-03-26 | iMOGABA23 | 22/43/86/129 | 35 |
| 2015-04-30 | iMOGABA24 | 22/43/86/129 | 35 |

Table 2.1 (continued.)

| Date | Session | Frequency[a] (GHz) | $t^{b}_{obs}$ (min) |
|---|---|---|---|
| 2015-05-27 | PAGaN | 43/129 | 251 |
| 2015-09-24 | iMOGABA26 | 22/43/86/129 | 30 |
| 2015-10-23 | iMOGABA27 | 22/43/86 | 35 |
| 2015-11-01 | PAGaN | 22/86 | 250 |
| 2015-11-04 | PAGaN | 43 | 250 |
| 2015-11-30 | iMOGABA28 | 22/43/86/129 | 35 |
| 2015-12-28 | iMOGABA29 | 22/43/86/129 | 35 |
| 2016-01-13 | iMOGABA30 | 22/43/86/129 | 40 |
| 2016-02-11 | iMOGABA31 | 22/43/86/129 | 30 |
| 2016-03-01 | iMOGABA32 | 22/43/86/129 | 30 |

Note. — [a] Frequencies with successful imaging; [b] Total on-source time per session.

## 2.3 Results

In this section, we present the multi-frequency behavior of BL Lac as obtained from our KVN data. During our observations, two $\gamma$-ray (0.1−300 GeV) outbursts occurred in November 2013 and March 2015. The first outburst, as well as its optical counterpart, was reported by Ramakrishnan et al. (2016) and Gómez et al. (2016). The second $\gamma$-ray outburst is visible in the data (their Figure 1) of Sandrinelli et al. (2017). Continuous data are provided by the weekly *Fermi*-LAT light curve[6] (which is preliminary and used as a trigger for follow-up multi-wavelength observations). One can easily recognize the two outbursts in the *Fermi*-LAT light curve, peaking at $5.3 \times 10^{-7}$ photons cm$^{-2}$ s$^{-1}$ at around MJD 56620 and at $7.2 \times 10^{-7}$ photons cm$^{-2}$ s$^{-1}$ at around MJD 57110, respectively. The $\gamma$-ray flux remained on a high level continuously after

---

[6] `http://fermi.gsfc.nasa.gov/ssc/data/access/lat/msl_lc/source/BL_Lac`

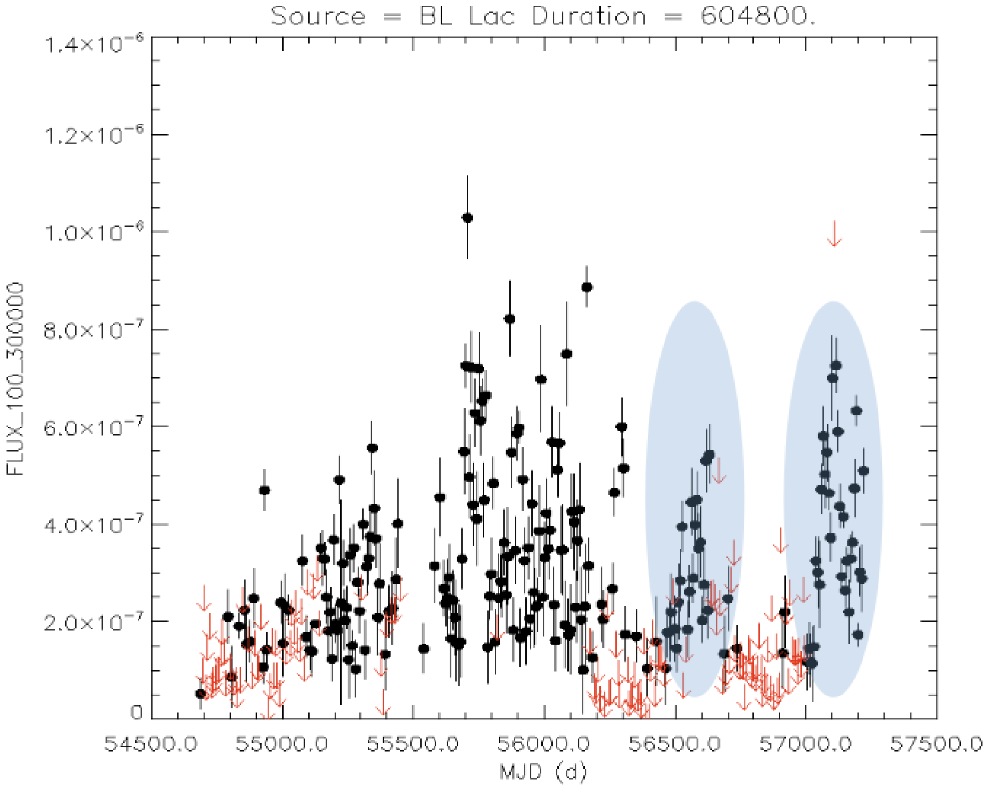

**Figure 2.1.** Public weekly $\gamma$-ray light curve of BL Lacertae produced by the LAT team. The blue shaded regions refer to the two $\gamma$-ray outbursts mentioned in Section 2.3. The red arrows indicate the upper limits. In this plot, the detection threshold is TS $\geq 25$ ($\sim 5\,\sigma$).

the second outburst; this is different from the first outburst which lasted ~6 months. The details can be found in Figure 2.1.

### 2.3.1 Radio morphology of BL Lac seen by the KVN

In a typical KVN map, our observations show two radio components, the VLBI ‘core’ and a single ‘knot’ (in the standard nomenclature used by, e.g., Kadler et al. 2008) south of the core that corresponds to the well-known jet of BL Lac (e.g., Stirling et al. 2003). Figure 2.2 shows a KVN map of BL Lac at 22, 43, 86, and 129 GHz (with contours offset in right ascension to avoid overlap); this map is typical for our iMOGABA data when regarding contours starting at three times the rms noise level. The KVN cores of BL Lac at different frequencies (always at

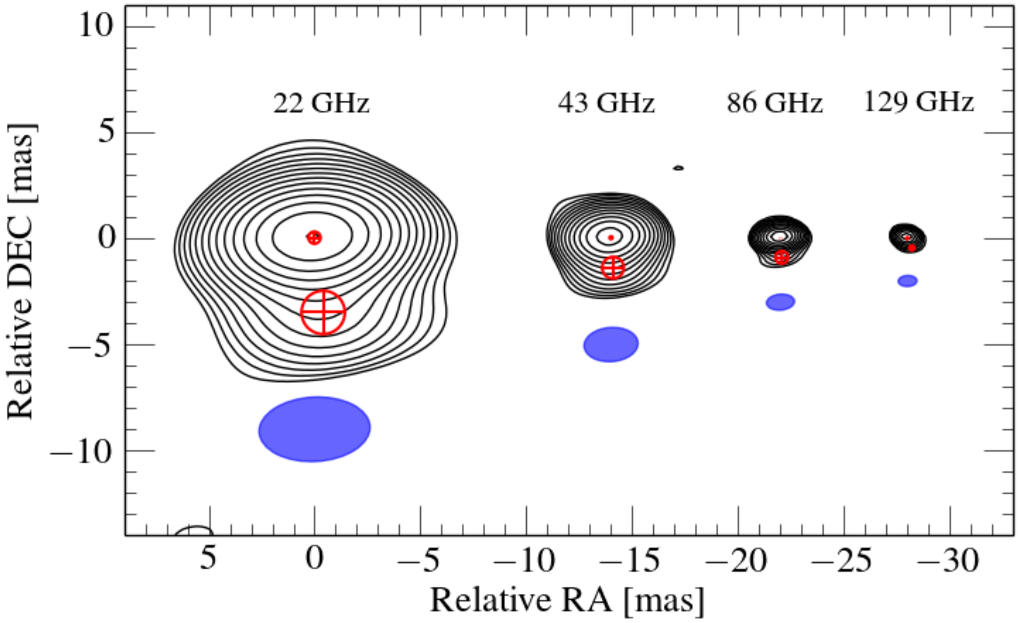

**Figure 2.2.** KVN total intensity maps of BL Lac at 22, 43, 86, and 129 GHz, from observation iMOGABA23 (cf. Table 2.1). To avoid overlap, contours are offset in RA. Identified radio components are marked with red ⊕ symbols representing size and position as derived from fitting Gaussian circular profiles. Blue ellipses indicate the corresponding clean beams. Contour levels start at 1.1%, 1.9%, 2.41%, and 6.9% of the peak intensity at 22, 43, 86, and 129 GHz, respectively, and increase by factors $\sqrt{2}$.

the map center) can be assumed to be identical; across our frequencies, core shift is less than about 0.2 mas (Dodson et al. 2017). The KVN core light curves (see Figure 2.3) are very similar in their structure, further supporting the conclusion that we observed the same structure at all frequencies. The location of radio knots is inversely proportional to the observing frequencies, with knots being located at roughly 3.4 mas, 1.8 mas, 0.9 mas, and 0.6 mas from the core at 22 GHz, 43 GHz, 86 GHz, and 129 GHz respectively. We expect the jet components of BL Lac at such distances to be optically thin (e.g., Denn et al. 2000). Hence, we concluded that our observations of the jet of BL Lac are heavily influenced by sensitivity and *uv* coverage of KVN, forcing us to refrain from quantitative conclusions.

Qualitatively, we note that the jet appears longer at lower frequencies (cf. Figure 2.2). The same trend can also be found in O'Sullivan & Gabuzda (2009a) and Abdo et al. (2011). This is a frequently observed feature of blazar jets which suggests that emission at lower frequencies originates from more extended regions in blazar jets (Valtaoja et al. 1992). In our case however, this observation is probably an artifact of the limited sensitivity of our KVN maps. The sensitivity decreases with increasing frequency, meaning that low-level flux contours are increasingly suppressed at higher frequencies.

### 2.3.2 Radio Light Curves

We monitored the flux densities of radio core and knot throughout our observing time as far as possible. Due to occasionally insufficient *uv*-coverage and/or high image noise, imaging of BL Lac or detection of the knot was not always possible at one or more frequencies. Especially, at 86 and 129 GHz we could detect a knot only in a few observations. Figure 2.3 shows the KVN multi-frequency light curves of BL Lac at 22, 43, 86, and 129 GHz. The light curves for all four frequencies follow very similar trends. The light curves of the core show relatively high flux levels, up to about 9 Jy, at the beginning and decay over time, reaching levels around 1 Jy at the end of our observations. We note that our observations cover the decay phase of the 2012 radio outburst (Wehrle et al. 2016). Flux densities of the knots are around 1 Jy at the beginning and decrease gradually by a factor of around two. We do not find obvious radio counterparts to the two $\gamma$-ray outbursts, even though any of the three local KVN core flux maxima located between the two $\gamma$-ray outbursts is a candidate for a counterpart to the first outburst.

To provide a quantitative description of the long-term flux evolution of the core, we fitted exponential functions

$$S_\nu = A_\nu \exp(-B_\nu t) + C_\nu \tag{2.1}$$

with $B_\nu \equiv 1/\tau_\nu$ and $\tau_\nu$ being the decay time scale at frequency $\nu$, to each core light curve. Given that the intrinsic scatter of the data points about the long-term trend – AGN light curves show red-noise like variability patterns with smaller variability amplitudes at shorter time scales (Press 1978; recently, e.g., Park & Trippe 2017) – is much larger than their statistical errors, we applied uniformly-weighted least-squares minimization. Figure 2.4 illustrates the fitting results for the four light curves (omitting the actual data for clarity). At the very beginning

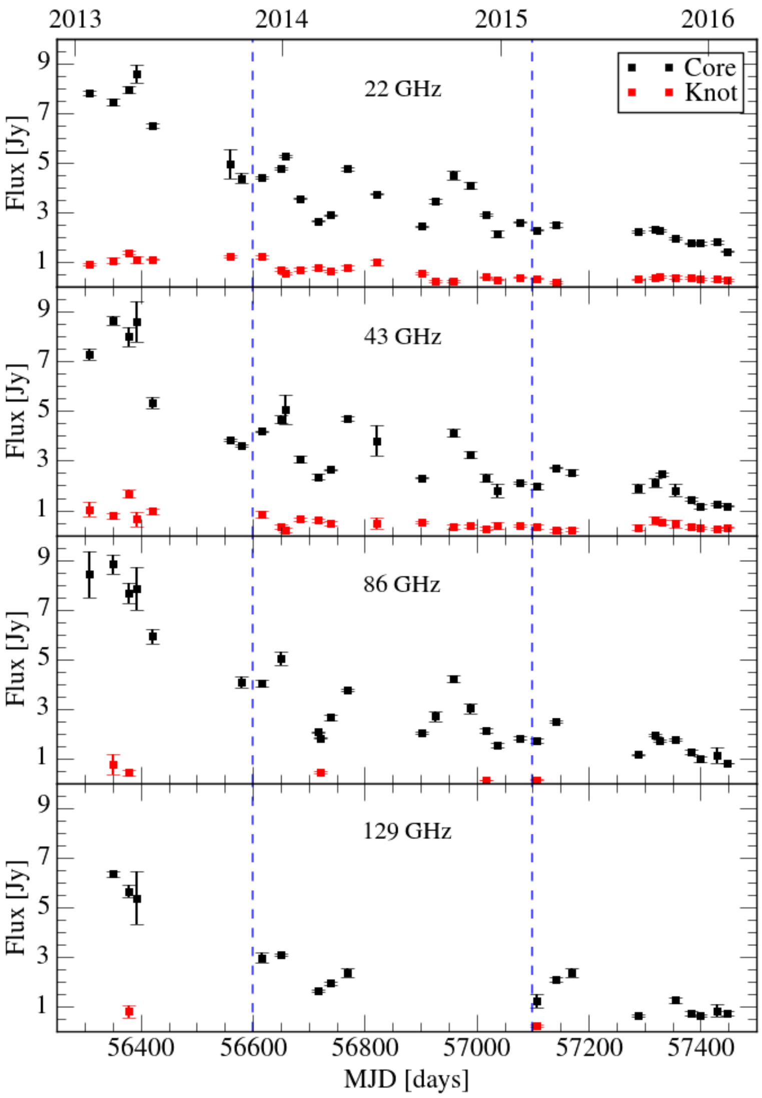

**Figure 2.3.** 22, 43, 86, and 129-GHz light curves of BL Lac obtained from KVN observations (both iMOGABA and PAGaN). The two blue dashed lines indicate $\gamma$-ray outbursts (see Figure 2.1). Core (black) and knot (red) are plotted separately.

of our observations, the fluxes at 22, 43, and 86 GHz are in good agreement; compared to these, the 129 GHz flux is lower by about 30%. Due to this, the flux density measurements at 129 GHz may not be robust and extra care should be taken when interpreting them and associated quantities. Later, fluxes are consistently higher at lower frequencies.

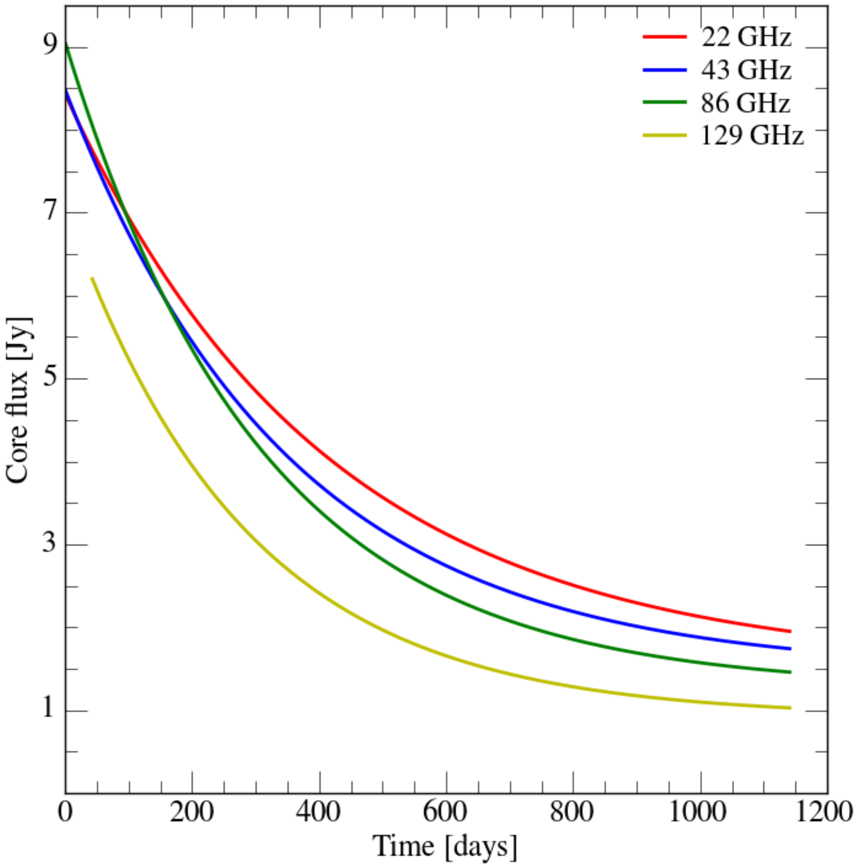

**Figure 2.4.** Exponential fits to the light curves of the core, quantifying the long-term flux evolution. Different colors indicate the four observing frequencies.

We obtain a decay timescale for each light curve from the exponential model. The timescales are 411 ± 85 days at 22 GHz, 352 ± 79 days at 43 GHz, 310 ± 57 days at 86 GHz, and 283 ± 55 days at 129 GHz. The formal errors provided by the fits reflect the intrinsic short-term variability of the source fluxes rather than the actual statistical uncertainties. Taking this into account, we note that the decay timescale depends on the observing frequency. We fit a power-law to the timescale − frequency data and re-scale the error bars such that $\chi^2/\mathrm{d.o.f.} = 1$. Figure 2.5 shows the resulting relation. The re-scaled errors on the timescales are ±3.9 days at 22 GHz, ±3.6 days at 43 GHz, ±2.6 days at 86 GHz, and ±2.5 days at 129 GHz. The best-fit line returns a power-law index of −0.208 ± 0.007. Using a linear approximation for the frequency range

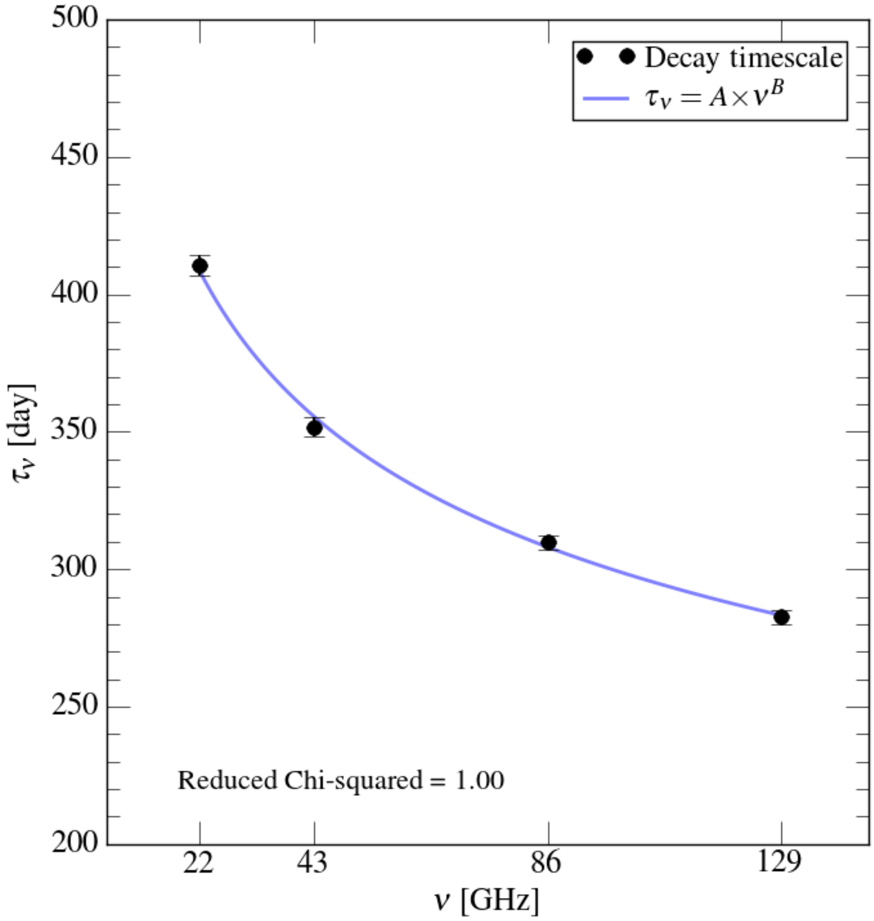

**Figure 2.5.** Decay timescale of the core flux as function of observing frequency. Both axes are linear. Errors have been re-scaled such that $\chi^2/\mathrm{d.o.f.} = 1$. The blue solid line represents the best power-law fit, with a power-law index of −0.208 ± 0.007.

covered by our data (and applying, again, error re-scaling), we find a slope of −1.05 ± 0.23 day/GHz – in other words, for each additional GHz in frequency, the decay timescale drops by about one day in the frequency range 22−129 GHz.

### 2.3.3 Spectral Indices and Spectrum of the Core

We analyzed the evolution of the spectrum of the core in view of a possible evolution of its opacity, beginning with spectral indices from pairs of adjacent frequencies (‘pairwise indices’).

As mentioned in Section 2.2, we could not always obtain measurements for all four frequencies, leading to different numbers of pairwise indices for the three frequency pairs. Due to the small time gap of three days between them, we treated the PAGaN observations of MJD 57327 and 57330 (2015 November 1 and 4) as a single measurement. We defined the spectral index $\alpha$ via $S_\nu \propto \nu^\alpha$, where $S_\nu$ is flux density of the core and $\nu$ is observing frequency. We adopt the conventional criterion that spectra with $\alpha < -0.5$ and $\alpha > -0.5$ are 'steep' and 'flat', respectively (e.g., Orienti et al. 2007; Netzer 2013). Figure 2.6 shows the pairwise spectral indices of the core as function of time. We obtained 31 spectral index values with an average value of −0.17 at 22−43 GHz, 27 indices with an average value of −0.14 at 43−86 GHz, and 16 indices with an average value of −0.89 at 86−129 GHz. Our observations show for the

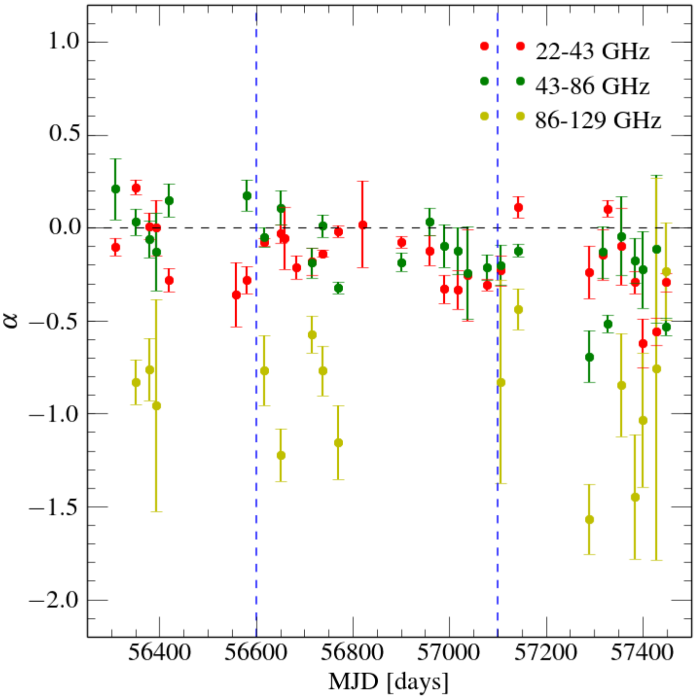

**Figure 2.6.** Pairwise spectral indices of the core as function of time, for the frequency pairs 22–43 GHz, 43–86 GHz, and 86–129 GHz. Different colors correspond to different frequency pairs. Vertical blue dashed lines mark the occurrence times of the two $\gamma$-ray outbursts.

first time explicitly that the VLBI core of BL Lac is optically thick at frequencies higher than 43 GHz over several years. This agrees with expectations that the core should be optically thick because of synchrotron self-absorption (SSA) (Denn et al. 2000; Wehrle et al. 2016). The spectral indices for the range from 22 to 86 GHz slightly decrease with time, in agreement with the trend illustrated by Figure 2.4. Figure 2.6 shows indication for a steady spectral hardening at 43−86 GHz from $\alpha \approx -0.3$ to $\alpha \approx -0.1$ for a few months around the time of the second $\gamma$-ray event, just after a rapid spectral softening. For the frequency pair 86−129 GHz, we see indication for the core becoming optically thin at these high frequencies; given the large errors, this conclusion has to be handled with care however.

Given that KVN provides multi-frequency data sets, we can obtain mm-wavelength spectra that are more sophisticated than the use of pairwise spectral indices. Whenever possible, we fit a power-law to spectra of the core consisting of the flux data that were obtained simultaneously at 22, 43, 86, and 129 GHz, thus making the standard assumption that BL Lac shows a synchrotron spectrum like all radio-loud AGN (e.g., Rani et al. 2011; Trippe et al. 2011). Figure 2.7 illustrates the estimation of a spectrum and shows the evolution of the spectral index $\alpha$ as function of time. We obtained 16 spectra in total. As expected from the pairwise spectral indices, BL Lac's core spectrum is flat (within errors) at the beginning and steepens slightly throughout our observations, down to $\alpha \approx -0.5$. We summarize all spectral indices in Table 2.2.

## 2.4 Discussion

The behavior of multi-waveband light curves provides important clues on the physical processes within blazar jets. Even though opacity and flux evolution depend on frequency, correlations between the flux variability at $\gamma$-rays and that at lower frequencies have been observed in blazar jets (as noted in Section 2.1). Unfortunately, there is no clear picture as yet: observed correlations (or the absence thereof) seem to change over time and from source to source (e.g., Marscher 2014). Simultaneous multi-frequency observations by KVN may shed light on the connection between $\gamma$-ray emission and emission at high radio frequencies (up to $\sim$130 GHz in our case). In this Section, we discuss the long-term decay of the 2012 radio outburst, the nature of the KVN core, and the connection between the two $\gamma$-ray outbursts and radio jet.

Table 2.2. Spectral indices of the core as function of time

| MJD[a] | $\alpha_{22-43}$ | $\alpha_{43-86}$ | $\alpha_{86-129}$ | $\alpha^{c}_{22-129}$ |
|---|---|---|---|---|
| 56308 | −0.11±0.05 | 0.21±0.17 | | |
| 56350 | 0.22±0.04 | 0.03±0.07 | −0.83±0.12 | −0.04±0.13 |
| 56379 | 0.01±0.07 | −0.06±0.10 | −0.76±0.17 | −0.14±0.09 |
| 56393 | 0.00±0.15 | −0.13±0.21 | −0.96±0.57 | −0.20±0.11 |
| 56420 | −0.28±0.06 | 0.15±0.09 | | |
| 56559 | −0.36±0.17 | | | |
| 56580 | −0.28±0.07 | 0.17±0.08 | | |
| 56616 | −0.08±0.02 | −0.05±0.05 | −0.77±0.19 | −0.17±0.08 |
| 56650 | −0.03±0.05 | 0.11±0.09 | −1.22±0.14 | −0.14±0.15 |
| 56659 | −0.06±0.17 | | | |
| 56684 | −0.21±0.06 | | | |
| 56716 | −0.18±0.08 | −0.19±0.08 | −0.57±0.10 | −0.24±0.04 |
| 56721 | | | | |
| 56738 | −0.14±0.02 | 0.01±0.06 | −0.77±0.13 | −0.17±0.08 |
| 56769 | −0.02±0.03 | −0.32±0.03 | −1.15±0.20 | −0.30±0.13 |
| 56821 | 0.02±0.23 | | | |
| 56901 | −0.08±0.03 | −0.19±0.05 | | |
| 56927 | | | | |
| 56959 | −0.12±0.08 | 0.03±0.07 | | |
| 56989 | −0.33±0.08 | −0.10±0.11 | | |
| 57017 | −0.33±0.10 | −0.12±0.12 | | |
| 57037 | −0.26±0.25 | −0.24±0.25 | | |
| 57077 | −0.31±0.03 | −0.21±0.07 | | |
| 57107 | −0.23±0.08 | −0.20±0.11 | −0.83±0.55 | −0.30±0.06 |
| 57142 | 0.11±0.06 | −0.12±0.03 | −0.44±0.11 | −0.09±0.07 |

Table 2.2 (continued.)

| MJD[a] | $\alpha_{22-43}$ | $\alpha_{43-86}$ | $\alpha_{86-129}$ | $\alpha^{c}_{22-129}$ |
|---|---|---|---|---|
| 57169 | | | | |
| 57289 | −0.24±0.14 | −0.69±0.14 | −1.57±0.19 | −0.56±0.15 |
| 57318 | −0.15±0.14 | −0.13±0.14 | | |
| 57327 | 0.10±0.05 | −0.52±0.05 | | |
| 57330[b] | 0.10±0.05 | −0.52±0.05 | | |
| 57356 | −0.10±0.21 | −0.04±0.21 | −0.85±0.28 | −0.19±0.09 |
| 57384 | −0.29±0.06 | −0.18±0.12 | −1.45±0.33 | −0.38±0.12 |
| 57400 | −0.62±0.13 | −0.23±0.21 | −1.04±0.36 | −0.51±0.08 |
| 57429 | −0.56±0.07 | −0.11±0.40 | −0.76±1.03 | −0.40±0.07 |
| 57448 | −0.29±0.05 | −0.53±0.05 | −0.24±0.26 | −0.39±0.04 |

Note. — [a] Same dates as in Table 2.1 in units of MJD; [b] Quasi-simultaneous with the data of MJD 57327; [c] Spectral index using 22, 43, 86, and 129-GHz data.

### 2.4.1 Variability and Cooling Time Scales

We find the highest fluxes for BL Lac right at the beginning of our observations. Wehrle et al. (2016) reported a strong outburst of BL Lac at 1.3 mm (225 GHz) at the end of 2012 preceded by strong $\gamma$-ray flaring. Accordingly, we may identify the 2012 radio outburst with the radio counterpart of the $\gamma$-ray flare(s) of the same year. Arguably, our observations cover the decay phase of the 2012 radio flare (see also Gaur et al. 2015). An exponential decay of radio luminosity is a common characteristic of blazar flares (Valtaoja et al. 1999; León-Tavares et al. 2011; Trippe et al. 2011; Chatterjee et al. 2012; Marscher 2014; Guo et al. 2016; Park & Trippe 2017). Unfortunately, our observations do not cover the rising stage of the radio outburst. Typically, the decay timescale of a flare in a radio AGN is about 1.3 times longer than its rise timescale (Valtaoja et al. 1999). This suggests rise timescales of ~316 days at 22 GHz, ~271 days at 43 GHz, ~238 days at 86 GHz, and ~218 days at 129 GHz.

The radio core of blazar jets is usually a compact, unresolved, and flat spectrum source that emits synchrotron radiation with high power. The radio core is known to be located a few parsecs downstream from the central engine (León-Tavares et al. 2011). As noted by Spada et al. (2001), synchrotron radiation is the main cooling mechanism for relativistic electrons in blazar jets at such distances from the central engine, while IC dominates inside the broad line region ($\sim 10^{15}$ m). Here, we assume synchrotron cooling to be the dominant cooling mechanism in the core region (Sokolov et al. 2004). (In general, inverse Compton losses are less important than synchrotron losses in a stationary synchrotron source; Pacholczyk 1970). A characteristic synchrotron cooling time can be defined via $\tau_{\rm cool} = E/\dot{E}$, with the electron energy $E = \gamma m c^2$ (with Lorentz factor $\gamma$, electron mass $m$, and speed of light $c$) and $\dot{E} = {\rm d}E/{\rm d}t$ (with time $t$) being the power radiated by a gyrating electron (e.g., Rybicki & Lightman 1997). In SI units and after transforming to the observer frame, the cooling time is

$$\tau_{\rm cool} = 7.74 \left[\frac{\delta}{1+z}\right]^{-1} B^{-2}\,\gamma^{-1} \text{ seconds} \tag{2.2}$$

where $B$ is the magnetic field strength, $\delta$ is the Doppler factor, and $z$ is the redshift. For BL Lac, $z = 0.069$ and $\delta \approx 7$ (Hovatta et al. 2009). Cooling times on the order of one year (assuming $\tau_{\rm cool} \approx \tau_\nu$; see Section 2.3.2) can be translated to $B \sim 2\,\mu$T and $\gamma \sim 10\,000$ which is consistent with the typical blazar magnetic field of $B \sim 1 - 10\,\mu$T (Lewis et al. 2016). Moreover, Agarwal et al. (2017) obtained the magnetic field of the BL Lac core at 4.8, 8, 14.5, and 22.2 GHz. They found $B$ to increase with frequency, with $B \sim 1\,\mu$T at 22 GHz on average. Electron Lorentz factors $\gamma \sim 10\,000$ are consistent with the fact that the peak frequencies of the synchrotron and IC humps in BL Lac's SED differ by about eight orders of magnitude (cf. Figure 27 of Wehrle et al. 2016).

The presence of longer decay time scales at lower frequencies, and the subsequent stratification of flux densities as function of frequency, might be an effect of longer synchrotron cooling times at lower electron energies (Marscher et al. 2008). In general, the synchrotron cooling time is longer at lower frequencies (Rybicki & Lightman 1997), which can be understood from the basic scaling relations of synchrotron radiation. An electron gyrating about

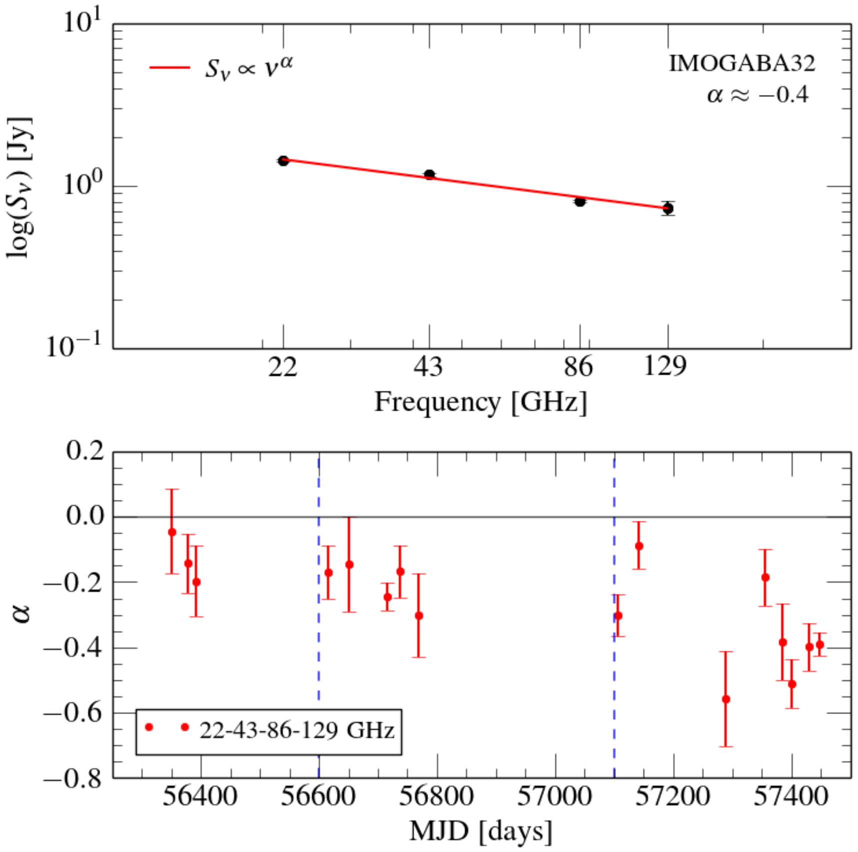

**Figure 2.7.** Radio spectra of the core from power-law fits to 22, 43, 86, and 129-GHz flux values. *Top:* An example spectrum, from data set iMOGABA32. *Bottom:* Spectral index $\alpha$ as function of time. Vertical blue dashed lines mark the occurrence times of the two $\gamma$-ray outbursts.

a magnetic field line with angular frequency $\omega_\mathrm{B}$ emits synchrotron radiation with a critical frequency $\nu_\mathrm{c} \propto \gamma^3 \omega_\mathrm{B}$ (e.g., Rybicki & Lightman 1997). With $\omega_\mathrm{B} \propto \gamma^{-1}$, $\nu_\mathrm{c} \propto \gamma^2$. Because $\tau_\mathrm{cool} \propto \gamma^{-1}$ (Equation 2.2), the cooling time follows $\tau_\mathrm{cool} \propto \nu_\mathrm{c}^{-1/2}$ for *optically thin* plasmas. In addition, one needs to consider that electron energies commonly follow power-law distributions of the form $N(\gamma) \propto \gamma^p$ (with $p < 0$); as the cooling time is a function of $\gamma$, high-energy electrons will cool down faster. Accordingly, single-power laws are widely used to describe synchrotron losses in blazar jets (see also Böttcher et al. 2003; Sokolov et al. 2004).

In our case however, the KVN core of BL Lac is *optically thick* (cf. Section 2.3.3), meaning that observations at different frequencies probe different regions with different magnetic field strengths. In general, $B \propto d^{-1}$, with $d$ being the distance from the central engine, in the VLBI core (Marscher 1995; Lobanov 1998a). Marscher (1995) suggested that the observed $\gamma$ becomes the maximum Lorentz factor for the given electron distribution, $\gamma_{\rm max}$, at the VLBI core. We assume $\gamma_{\rm max}$ to be constant in the core region (e.g., Kaiser 2006). Our data (Section 2.3.2) follow a relatively shallow scaling relation $\tau \propto \nu^{-0.2}$. For a conical Blandford & Königl (1979) jet, different observing frequencies probe different plasma surfaces. This results in the well-known 'core shift' relation $d \propto \nu^{-1}$ (Lobanov 1998a; but see also Agarwal et al. 2017). Such a scaling law is in tension with our observations: even for (approximately) constant values of $\gamma$, we would expect $B^2\gamma \propto d^{-2} \propto \nu^2$ and thus $\tau \propto \nu^{-2}$ – which is much steeper than our observed relation.

An alternative explanation for our result is provided by the assumption that the millimeter radio core of BL Lac is a standing recollimation shock (Gómez et al. 1997; Marscher et al. 2008). Such a shock forms where the gas pressure in the jet does not match the gas pressure of the ambient interstellar medium (e.g., Cawthorne et al. 2013). Numerical simulations by Dodson et al. (2017) suggest that the radio core of BL Lac follows the usual core shift relation at centimeter wavelengths and coincides with a recollimation shock (which is optically thin) at millimeter wavelengths (see also Marscher 2012a; Martí et al. 2016). In this picture, the recollimation shock is a physical structure at a fixed position; high frequency (mm to sub-mm) radiation may originate entirely from the shock. The core shift scaling starts to deviate from the relation $d \propto \nu^{-1}$ at wavelengths shorter than about one centimeter. At sufficiently high observing frequencies, the synchrotron radiation originates from the same plasma surface at all frequencies; the scaling of magnetic field strength with frequency breaks down, i.e., $B^2\gamma$ and $\tau$ become independent of frequency. We suspect that the KVN frequency bands cover the frequency range where this transition occurs in BL Lac, probably between 86 and 129 GHz. This interpretation is supported by the astrometric observations of Dodson et al. (2017), who find that the core shift relation beyond ~30 GHz is much shallower than $d \propto \nu^{-1}$ – in agreement with the signature of a recollimation shock (see also Wehrle et al. 2016; Gómez et al. 2016).

O'Sullivan & Gabuzda (2009a) find the millimeter radio core of BL Lac to be located $\lesssim$0.5 pc from the jet base.

### 2.4.2 Shock Evolution in The Core Region

The energy distribution of electrons in relativistic AGN jets is commonly assumed to follow a power law (Hughes et al. 1985; Ghisellini et al. 2002; Maselli et al. 2010; Rani et al. 2011; Trippe et al. 2011; Giommi et al. 2012; Karamanavis et al. 2016a), resulting in power law synchrotron spectra − in agreement with our KVN data. Throughout our observations, the long-term evolution of the core spectrum follows the overall long-term evolution of the core light curves (cf. Figures 2.4 and 2.7). At the beginning, the spectrum is approximately flat ($\alpha \approx 0$) while the core flux is at its highest levels; over time, the flux decreases and the spectrum becomes steeper. A hardening of the spectrum at higher fluxes is a signature of powerful shocks and is consistent with the known flux evolution of BL Lac since the 2012 radio outburst (Ghisellini et al. 2002; Gaur et al. 2015; Wehrle et al. 2016). The subsequent behavior of the spectrum (i.e., becoming steeper) over time indicates again that the source underwent radiative energy losses by synchrotron radiation and Compton scattering (Blumenthal & Gould 1970). A physical explanation is provided by the 'generalized shock model' of Valtaoja et al. (1992) which links the evolution of a shock to the observable evolution of its turnover peak frequency. As the shock evolves with time, the turnover peak frequency of the spectrum moves to lower frequencies − in good agreement with our observations (Figure 2.7).

The KVN core is consistent with being optically thick at least up to 86 GHz (cf. Figures 2.6 and 2.7) throughout our observations. This is in contrast to the observation that the core becomes optically thin at mm-wavelengths occasionally due to the emission from newly ejected jet components (Hodgson 2015). This apparent conflict can probably be resolved by taking into account that the KVN core is a blend of multiple components that would be spatially resolved by higher-resolution observatories (see also Rioja et al. 2014, 2015; Zhao et al. 2015). The long-term steepening of the spectrum which we observe (Figure 2.7) might be caused by the jet emission becoming brighter relative to the core emission over time. This implies that the core spectrum might continue its steepening until a jet component is ejected, and then return

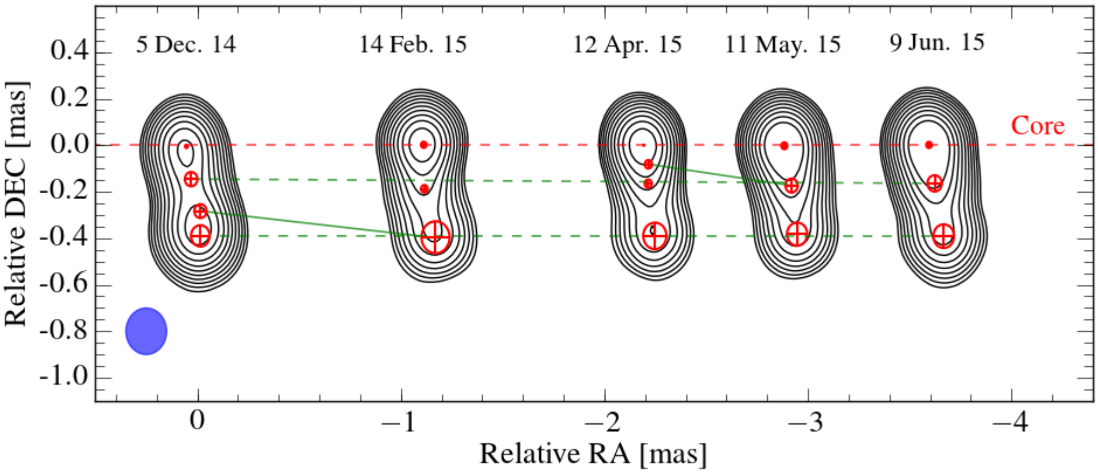

**Figure 2.8.** 43-GHz VLBA maps (from the BU data base) of BL Lac obtained around the time of the March 2015 $\gamma$-ray outburst. Contours represent total intensity levels ranging from 4% to 90.5% of the peak intensity. Red $\oplus$ denote circular Gaussian components, the blue ellipse indicates the clean beam. Maps are shifted along the abscissa for clarity; all maps are restored with the same $0.2 \times 0.2$ mas beam.

to $\alpha \approx 0$. At 129 GHz, the KVN core may be optically thin permanently – as expected at sufficiently high frequencies. However, we cannot ignore possible instrumental effects of the KVN that can result in unwanted amplitude drops and which are supposed to be more severe at higher frequencies (Algaba et al. 2015; Lee et al. 2016b).

### 2.4.3 The Radio–$\gamma$-Ray Connection

Radio and $\gamma$-ray light curves of blazars tend to be connected such that a $\gamma$-ray outburst precedes a radio outburst (Valtaoja & Teräsranta 1995; Jorstad et al. 2001b; Marscher et al. 2008, 2011; León-Tavares et al. 2011; Arlen et al. 2013; Raiteri et al. 2013; Max-Moerbeck et al. 2014a; Ramakrishnan et al. 2015; Karamanavis et al. 2016a; Wehrle et al. 2016). It has been suggested that a moving disturbance originating near the jet base produces flares both at radio and $\gamma$-rays as it propagates along the jet flow (Marscher et al. 2008; Max-Moerbeck et al. 2014a). In this scenario, the $\gamma$-ray outburst is assumed to occur in the inner jet region (upstream of the radio core) where the jet is opaque at radio wavelengths; the radio outburst becomes observable once the disturbance has passed through the radio core region. To add complexity to this issue, observations indicate that the production site of $\gamma$-ray outbursts is located parsecs downstream of the radio core at least occasionally (e.g., León-Tavares et al. 2011). In addition, recent studies (e.g., Wehrle et al. 2016, Hodgson et al. 2017) found recollimation shocks in blazar jets within 0.5 mas downstream from the core, and suggested the recollimation shocks as a candidate of the origin of $\gamma$-ray outbursts in blazar jets.

The typical rise time of radio outbursts is on the order of one year (e.g., Hovatta et al. 2008a). In blazars, the observed delays between $\gamma$-ray and radio outbursts range from hours to a few hundred days, with the $\gamma$-ray emission leading the radio emission (Arlen et al. 2013; Jorstad et al. 2013; Raiteri et al. 2013; Max-Moerbeck et al. 2014a; Ramakrishnan et al. 2015; Wehrle et al. 2016). Accordingly, the identification of the radio counterparts to a specific $\gamma$-ray outburst is not straightforward if significant variability such as the multiple outbursts (the three minor radio flux peaks) after the first $\gamma$-ray event in Figure 2.3 is present in the radio light curve. In our case, we do not find obvious radio counterparts to the two $\gamma$-ray outbursts.

The apparent absence of a radio – $\gamma$-ray correlation (like the absence of radio counterparts) in blazar jets or BL Lac objects has been noted before (Denn et al. 2000; León-Tavares et al. 2011; Orienti et al. 2013; Max-Moerbeck et al. 2014a; Ramakrishnan et al. 2016). The lack of radio counterparts can result from radio and $\gamma$ emission orignating from different regions (e.g., León-Tavares et al. 2011); in this scenario, $\gamma$ emission results from IC scattering near the core with seed photons from the accretion disk, the outflowing broad-line region (BLR), or the dusty torus. A complex variability pattern could cause a weak radio counterpart to be 'buried' under radio outbursts that are unrelated to the $\gamma$-ray emission. Indeed, already Valtaoja et al. (1999) noted that light curves of BL Lac are difficult to decompose into individual outbursts. Gaur et al. (2015) suggested geometry effects to be important, specifically variable Doppler boosting of the jet emission due to viewing angle changes. This might cause radio counterparts to be missed or underestimated.

Last but not least, the $\gamma$-ray outbursts of 2013 and 2015 might be 'orphan' events that show no correlation with the luminosity at longer wavelengths. An orphan $\gamma$-ray outburst was observed in the blazar PKS 1510-089 by Marscher et al. (2010); MacDonald et al. (2015)

explained this outburst as the result of a disturbance passing through the inner jet region. To further complicate matters, BL Lac shows (apparent) radio counterparts to $\gamma$-ray outbursts at least in some cases (Arlen et al. 2013; Wehrle et al. 2016). Not only the light curves but also the evolution of the radio spectrum can be related to the $\gamma$-ray activity of blazars. For the quasar 3C 454.3, Jorstad et al. (2013) found that $\gamma$-ray outbursts coincide with increases in – spectroscopically determined – core opacity. As shown in Figure 2.6, the spectral index of BL Lac's core at 43–86 GHz reaches a local minimum, with $\alpha \approx -0.3$, roughly two months before the second $\gamma$-ray outburst. From then on, the spectral index, and thus the core opacity, increases up to $\alpha \approx -0.1$ a few weeks after the $\gamma$-ray outburst. This can be explained by the passage of a newly ejected jet component through the core: while in the core region, the new component is obscured and temporarily increases (or dampens the long-term decrease of) the flux from the optically thick core, resulting in increased values of $\alpha$. This interpretation is strengthened by the results of Arlen et al. (2013) who found a $\gamma$-ray outburst in June 2011 (at MJD 55711) to coincide with the ejection of a new jet component.

The connection between $\gamma$-ray outbursts and ejections of new components is a known feature of blazars (Marscher et al. 2010, 2011; Arlen et al. 2013; Jorstad et al. 2013; Gómez et al. 2016; Wehrle et al. 2016) which is, however, not a universally valid relation (Denn et al. 2000; Jorstad et al. 2001b). We used archival VLBA data from the BU data base to search for a new jet component in spring 2015; the maps are shown in Figure 2.8. Indeed, a new jet component might have appeared about 0.1 mas south of the VLBA core in April 2015 which, however, only shows up in the April 2015 map – meaning we cannot claim the occurence of a new jet component with sufficient certainty. If, indeed, a new jet component appeared in April 2015, this could explain the occurrence of an orphan $\gamma$-ray outburst in March 2015 via the 'ring of fire' mechanism (MacDonald et al. 2015). In this picture, an orphan $\gamma$-ray outburst arises from a relativistic plasma cloud moving through the inner jet region and precedes the emergence of a new radio jet component – by ~20 days in the case of PKS 1510-089, and possibly by a similar amount of time in case of BL Lac in 2015 (~25 days).

## 2.5 Summary

We analyzed multi-frequency KVN radio data of BL Lac spanning three years, from January 2013 to March 2016 to study the connection between radio and $\gamma$-ray emission in blazar jets. We obtained light curves and spectra of the radio core at mm-wavelengths during a period when BL Lac showed two $\gamma$-ray outbursts that occurred in November 2013 and March 2015. We summarize our main results in the following.

1. Our observations cover the aftermath of the major radio flare that occurred in 2012. During the entire time of our observations, the radio flux from the KVN radio core decayed exponentially, and two $\gamma$-ray outbursts occured in BL Lac. We found decay time scales $\tau$ of 411±85 days (22 GHz), 352±79 days (43 GHz), 310±57 days (86 GHz), and 283±55 days (129 GHz), with formal errors including intrinsic short-term variability. Assuming synchrotron cooling, such decay times are consistent with magnetic fields $B \sim 2\,\mu$T and electron Lorentz factors $\gamma \sim 10\,000$.

2. We find that the flux decay time scales with observing frequency like $\tau \propto \nu^{-0.2}$. This scaling law is much shallower than the synchrotron energy loss expected from optical depth effects in a Blandford & Königl (1979) jet. Therefore, we suspect the KVN radio core to be a standing recollimation shock (e.g., Marscher et al. 2008) – in agreement with independent recent astrometric observations (Dodson et al. 2017) of the core shift.

3. The radio core spectrum is initially flat ($\alpha \approx 0$) and steepens with decreasing flux, reaching $\alpha \approx -0.5$ at the end of our observations. This is in agreement with the 'generalized shock model' of Valtaoja et al. (1992) wherein the turnover peak moves to lower frequencies when the shock decays, with the shock corresponding to the 2012 radio flare.

4. There is no obvious radio counterpart to any of the two $\gamma$-ray outbursts covered by our study. Possible explanations are: (i) the $\gamma$-ray emission originates downstream of the core; (ii) the radio counterparts are masked by the complex intrinsic red-noise type variability; (iii) geometry effects like variations in Doppler boosting; (iv) there is actually no radio counterpart – i.e., the $\gamma$-ray outbursts are 'orphans'.

5. The temporary increase in the core opacity two months before the second $\gamma$-ray outburst, as well as the outburst itself, might both be due to the emergence of a new jet component. The detection of a new VLBA radio knot in April 2015 tentatively suggests that the second $\gamma$-ray event might be an orphan $\gamma$-ray event powered by the 'ring of fire' mechanism.

Overall, our results strengthen the case for a causal connection between the radio and $\gamma$-ray activity in BL Lac, and potentially in blazars in general. Even though, we are still missing many important details. Future studies will need to explore if recollimation shocks are a general features of blazar jets; under which circumstances one may expect radio-flux counterparts to $\gamma$-ray outbursts; and which physical mechanism causes orphan $\gamma$-ray flares.

# Chapter 3

# Exploring The Nature of The 2016 $\gamma$-Ray Emission in The Blazar 1749+096[1]

## Abstract

Recent *Fermi*-Large Area Telescope (LAT) light curves indicate an active $\gamma$-ray state spanning about five months from 2016 June to 2016 October in the BL Lac object 1749+096 (OT 081). During this period, we find two notable $\gamma$-ray events: an exceptionally strong outburst followed by a significant enhancement (local peak). In this study, we analyze multi-waveband light curves (radio, optical, X-ray, and $\gamma$-ray) plus very-long baseline interferometry (VLBI) data to investigate the nature of the $\gamma$-ray events. The $\gamma$-ray outburst coincides with flux maxima at longer wavelengths. We find a spectral hardening of the $\gamma$-ray photon index during the $\gamma$-ray outburst. The photon index shows a transition from a softer-when-brighter to a harder-when-brighter trend at around $1.8 \times 10^{-7}$ ph cm$^{-2}$ s$^{-1}$. We see indication that both the $\gamma$-ray outburst and the subsequent enhancement precede the propagation of a polarized knot in a region near the VLBI core. The highest polarized intensity, 230 mJy, and an electric vector position angle rotation, by $\sim 32°$, are detected about 12 days after the $\gamma$-ray outburst. We conclude

---

[1] Published in the *Monthly Notices of the Royal Astronomical Society*: Kim et al. 2018, MNRAS, 480, 2324

that both $\gamma$-ray events are caused by the propagation of a disturbance in the mm-wave core.

## 3.1 Introduction

The BL Lac object 1749+096 (OT 081, redshift 0.32, image scale 4.64 pc/mas, assuming $H_0$ = 71 km Mpc s$^{-1}$, $\Omega_\Lambda = 0.73$, and $\Omega_m = 0.27$) is a flat spectrum radio source emitting variable radio radiation in total intensity and linear polarization (Stickel et al. 1988; Gabuzda et al. 1996). 1749+096 has been classified as a low-synchrotron peaked (LSP) blazar,[2] has been observed at X-rays, but was not detected at $\gamma$-rays before the advent of *Fermi* (Sambruna et al. 1999). A review of the physical characteristics of this highly compact radio source can be found in Lu et al. (2012), covering features such as multi-frequency variability from radio to X-ray, a quiescent flux level of below 1 Jy at high radio frequencies (above 37 GHz), a curved extended jet, and superluminal motion of jet components, with apparent speeds from $5c$ to $21c$. Jorstad et al. (2017) presented a recent estimate of Doppler factor of $\sim$17.7 and viewing angle of $\sim$2.4° in the jet of 1749+096. The first $\gamma$-ray detection of 1749+096 was reported by Abdo et al. (2009). Interestingly, there were no $\gamma$-ray flares until 2015, which is why the $\gamma$-ray outburst in 2016 is notable. O'Sullivan & Gabuzda (2009b) revealed the linear polarization of the 1749+096 jet at 4.6 – 43 GHz by using very long baseline array (VLBA) observations. They found that the radio core shows a degree of linear polarization of about 3% across the range of their frequencies, with the polarization angle being about $-50^\circ$ at 43 GHz. Additionally, 1749+096 is known to show a Faraday rotation measure (RM) significantly different from zero at cm-wave bands (Pushkarev 2001). Contrary to this, however, O'Sullivan & Gabuzda (2009b) found no significantly non-zero RM at frequencies up to 43 GHz in the radio core during a flare, thus indicating that the underlying magnetic field is most likely responsible for EVPA changes in some specific circumstances (Homan et al. 2002). Recently, it was also found that 1749+096 shows variability in optical polarization on time scales of a few days (Uemura et al. 2017).

As I mentioned above, the 2016 $\gamma$-ray flare is unique because it is the strongest one in this source and there was no significant $\gamma$-ray flaring event since the *Fermi*-LAT was launched (i.e., 2008). This suggests changes in the source properties and/or physical conditions, which

---

[2] `http://www.physics.purdue.edu/MOJAVE/sourcepages/1749+096.shtml`

makes this $\gamma$-ray flare worthwhile to be explored. In this study, we explore the powerful $\gamma$-ray outburst in 1749+096 that occurred in the middle of 2016 by using multi-waveband observations including, especially, VLBI data. Overall, the multi-waveband data span about two years (2015 and 2016) across a frequency range from radio to $\gamma$-rays obtained from the Korean VLBI Network (KVN) at 22, 43, 86, and 129 GHz; the Owens Valley Radio Observatory (OVRO) at 15 GHz; the VLBA at 43 GHz; the All-Sky Automated Survey for Supernovae (ASAS-SN) in the optical V-band; *Swift*-XRT at X-rays; and *fermi*-LAT at $\gamma$-rays. Due to a rather spotty $\gamma$-ray light curve, we focus on a specified $\gamma$-ray active period spanning ~5 months (see Figure 3.1) which includes both the $\gamma$-ray outburst and a notable local peak (temporary flux enhancement). We address multi-waveband correlations, the evolution of the $\gamma$-ray spectrum, and the linear polarization at 43 GHz as observed by the VLBA. We discuss the connection between the $\gamma$-ray events and radio core activity, assuming that the primary candidate of the $\gamma$-ray production site is the radio core.

## 3.2 Observations and Data

### 3.2.1 KVN 22/43/86/129 GHz & VLBA 43 GHz

We obtained multi-frequency VLBI data from the Interferometric Monitoring of Gamma-ray Bright AGNs (iMOGABA) project.[3] iMOGABA employs the KVN for multi-frequency simultaneous observations at 22, 43, 86, and 129 GHz in single polarization (LCP). The KVN consists of three identical (diameter of 21 m) antennas with baseline lengths up to ~470 km; accordingly, angular resolutions are on the order of a few milliseconds of arc. iMOGABA has been monitoring ~30 $\gamma$-ray bright AGNs monthly since late 2012 (see, e.g., Lee et al. 2013; Algaba et al. 2015). Data reduction was conducted with the KVN pipeline (Hodgson et al. 2016) which applies all standard procedures required for reduction of VLBI data. We used the frequency phase transfer (FPT) technique (Zhao et al. 2018) to improve the quality of the data from the higher frequency bands. We followed the procedure used in Lee et al. (2016b) for imaging our data with the software package `Difmap` (Shepherd 1997). We conservatively es-

---

[3] `http://radio.kasi.re.kr/sslee`

timated an error of 10% on the flux density of each image component; for our 129 GHz data, we applied a 30% error due to possible systematic amplitude losses (Kim et al. 2017). Usually, we detected only one component (i.e., the KVN core) at the map center over the four frequencies owing to the relatively large beam size of the KVN and its limited sensitivity. In a few cases, closure phase analysis at 43 and 86 GHz made it possible to detect a jet pointing toward the northeast – which is consistent with the known morphology of the radio jet of 1749+096 (e.g., Lu et al. 2012). Given the performance and limitations of the KVN, we consider those detections marginal and use only the KVN core in this study.

We selected seven VLBA observations (2016 June to 2016 November) around the time of the two $\gamma$-ray events (see Figure 3.1) from the Boston University blazar group (BU) archival dataset[4] to look into the source more deeply, including the linear polarization at 43 GHz. The BU group has been monitoring several tens of $\gamma$-ray bright blazars monthly via the VLBA in close association with the *Fermi*-LAT (Jorstad & Marscher 2016). The public BU data were already fully calibrated as described in Jorstad et al. (2017). Hence, we simply used the calibrated visibility data to produce Stokes $I$, $Q$, and $U$ maps. We imaged the data with `Difmap` and produced linear polarization maps using the Astronomical Image Processing System (AIPS) task `COMB` (van Moorsel et al. 1996). We note that the BU observations missed the SC and KP stations on 2016 September 5 and the HN and MK stations on 2016 October 6. Hence, results from those epochs need to be interpreted with care. We fit circular Gaussian profiles to the image components in the total intensity maps to investigate the evolution of their flux densities, assuming again a conservative error of 10%.

### 3.2.2 OVRO 15 GHz

We collected 15 GHz data of 1749+096 from the OVRO 40 m telescope monitoring program (Richards et al. 2011). In close association with the *Fermi*-LAT program, the OVRO has been monitoring more than 1800 blazars about twice per week since 2008. The large sample size and the high cadence allow for a detailed exploration of blazar variability at cm-wavelengths. Details of the data reduction process can be found in Richards et al. (2011). The calibrated

---

[4] `http://www.bu.edu/blazars/VLBA_GLAST/1749.html`

OVRO data is available via the OVRO Internet database.[5] In this study, we use OVRO flux data spanning from the beginning of 2015 to early 2017.

### 3.2.3 ASAS-SN

We obtained optical V-band data from the All-Sky Automated Survey for Supernovae (ASAS-SN) project[6] (Shappee et al. 2014; Kochanek et al. 2017). The survey is ongoing every night with 20 telescopes located around the globe including Hawaii, Chile, and South Africa. The ASAS-SN aims to survey and discover bright transients down to a V-band magnitude of about 17 across the entire sky. The project provides an online tool that produces an aperture photometry light curve for an arbitrary point on the celestial sphere, thus making it possible to study sources other than supernovae. We extract optical light curve of 1749+096 by using this online tool.

### 3.2.4 Swift-XRT

We collected X-ray data (0.3–10 keV) from *Swift*-XRT observations (Gehrels et al. 2004). The *Swift*-XRT is a mission launched in 2004 to investigate X-ray afterglows of $\gamma$-ray bursts (GRB). The UK Swift Science Data Centre[7] provides an automatic online pipeline that produces high level XRT products for non-GRBs with the software package HEASOFT v6.22. We employ the online pipeline to generate an X-ray light curve of 1749+096 with a $3\sigma$ cutoff. Details of the pipeline and the data reduction process are provided by Evans et al. (2007).

### 3.2.5 Fermi-LAT

The *Fermi*-LAT $\gamma$-ray space mission was launched in 2008 June to explore the high energy sky (Atwood et al. 2009). The LAT is designed to cover the energy range of 20 MeV–300 GeV, and performs an all-sky survey with its large field of view (2.4 sr). We use the *Fermi* software `ScienceTools v10r0p5` and the instrument response function (IRF) `P8R2_SOURCE_V6`

---

[5] `http://www.astro.caltech.edu/ovroblazars/index.php?page=home`

[6] `http://www.astronomy.ohio-state.edu/asassn/index.shtml`

[7] `http://www.swift.ac.uk/index.php`

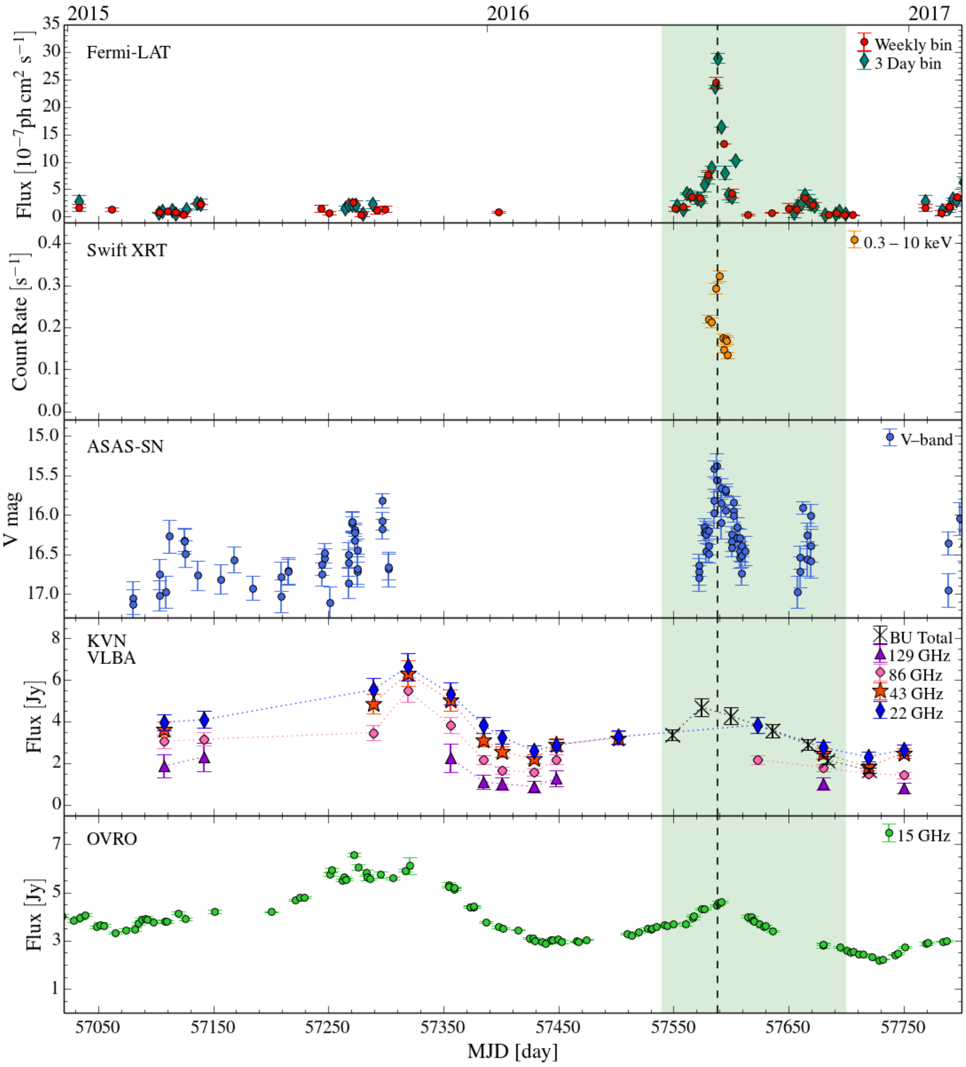

**Figure 3.1.** Multi-waveband light curves of 1749+096. From top to bottom: *Fermi*-LAT at 0.1–300 GeV, *Swift*-XRT at 0.3–10 keV, ASAS-SN at optical V-band, KVN (iMOGABA) at 22/43/86/129 GHz plus VLBA (BU) at 43 GHz, and OVRO at 15 GHz. The data spans the period from 2014 December 29 to 2017 February 16. The light green shaded region indicates the $\gamma$-ray active period (MJD 57540–57700). The black dashed vertical line indicates the 2016 July 19 (MJD 57588) $\gamma$-ray outburst.

to extract light curves of 1749+096 from the raw LAT data. We essentially follow the data reduction steps employed by Prince et al. (2017). The initial search radius was set to 20° around

1749+096. We selected events in the SOURCE class (Pass 8) with an energy range of 0.1–300 GeV. To exclude atmospheric background events (i.e., contamination from the Earth limb $\gamma$-radiation) and select good time invervals (GTIs), we applied the `zmax` option in `gtltcube` (`zmax=90`°) plus the filter `DATA_QUAL==1 && LAT_CONFIG==1` which is the currently recommended procedure. We extracted source models within the search window from the third *Fermi*-LAT catalog (3FGL). We set the spectral parameters for sources within and outside the Region of Interest (ROI) of 10° to be free and fixed to the catalog values, respectively. A power-law (PL) function was applied to the photon spectra of 1749+096. We performed an unbinned likelihood analysis where the significance of the $\gamma$-ray flux is evaluated by maximum likelihood (ML) test statistics (e.g., Paliya et al. 2015). We modelled the contribution by diffuse background sources with the recent isotropic background model `iso_P8R2_SOURCE_V6_v06` and the galactic diffuse emission model `gll_iem_v06`. We use the Perl script `like_lc.pl`[8] written by R. Corbet to produce $\gamma$-ray light curves. A weekly $\gamma$-ray light curve of 1749+096 is generated using the criterion `TS=9` (corresponding to a $3\sigma$ cutoff), flux values below this threshold are rejected. We also provide 3-day binned $\gamma$-ray light curve for further analysis. During the photon index analysis, we noted and rejected a few outliers (three and two data points in the weekly and 3-day binned data, respectively) deviating by more than $2\sigma$ from the weekly photon index trend. All relevant files and data are provided by the *Fermi* data web site.[9]

## 3.3 Results and Analysis

### 3.3.1 Multi-waveband light curves

Figure 3.1 shows the multi-waveband light curves spanning from 2014 December 29 to 2017 February 16 (MJD 57020–57800). Until mid-2016, 1749+096 is $\gamma$-ray quiet with fluxes $\lesssim 2 \times 10^{-7}$ ph cm$^{-2}$ s$^{-1}$ and detected only occasionally, whereas radio observations find enhanced activity peaking around mid-2015. In 2016 July, a powerful $\gamma$-ray outburst occurs, rising to about ~15 times the quiescent level within 36 days (in the 3-day binned data). The $\gamma$-ray flux peaked at $2.9 \times 10^{-6}$ ph cm$^{-2}$ s$^{-1}$ on 2016 July 19 (MJD 57588±1.5 d; 3-day binned

---

[8] `https://fermi.gsfc.nasa.gov/ssc/data/analysis/user/`

[9] `https://fermi.gsfc.nasa.gov/ssc/data/access/`

data). Counterparts to this $\gamma$-ray event can be found at all wavebands (radio, optical, and X-ray). The X-ray, optical, and cm-wave (OVRO 15 GHz) counterparts peaked on 2016 July 20 (MJD 57589), 2016 July 18 (MJD 57587), and 2016 July 22 (MJD 57591) respectively, meaning that the X-ray and optical counterparts were simultaneous with the $\gamma$-ray outburst within the error of $\pm1.5$ day given by the time resolution of the $\gamma$-ray light curve. The 15-GHz peak occurs $\sim$3 days after the $\gamma$-ray peak; the difference might actually be larger because the OVRO light curce shows a gap right after its apparent maximum on MJD 57591. In addition to the 2016 July the $\gamma$-ray outburst, a smaller temporary $\gamma$-ray flux enhancement occurred on 2016 October 2 (MJD 57663$\pm$1.5 d), reaching up to about $3.9\times10^{-7}$ ph cm$^{-2}$ s$^{-1}$. This event appears to have no counterparts at radio wavelengths.

Unfortunately, the available information at mm-wavelengths is poor during the period we specify as '$\gamma$-ray active' from 2016 June 1 to 2016 November 8 (the period indicated in Figure 3.1). However, we do see a radio counterpart to the $\gamma$-ray outburst at mm-wavelengths from the BU data; due to the rather large sampling intervals of the BU data, $\sim$1 month, it is unclear where the mm-wave light curve peaks exactly. From the iMOGABA and OVRO light curves, we find a period of enhanced mm-radio flux in mid-2015. Contrary to the subsequent radio flare in the middle of 2016, we do not find a corresponding increase in $\gamma$-ray activity. Overall, 1749+096 shows rather quiescent, and frequently undetectable, $\gamma$-ray emission during most of our observations except the $\gamma$-ray active period in 2016. Thus, we focus on this period in the further analysis.

### 3.3.2 Multi-wavelength flux correlations

A physical connection between the emission at various wavelengths is apparent already from the morphology of the light curves (cf. Figure 3.1). For a more quantitative analysis, we computed Pearson ($r_p$) and Spearman rank ($r_s$) correlation coefficients to probe the degrees of correlation between the $\gamma$-ray light curve and the emission at lower energy bands. We included all data from the period of enhanced $\gamma$-ray activity in mid-to-end 2016 that are simultaneous with the $\gamma$-ray data within the bin size of three days. For the optical data, we used flux estimates in linear units, in mJy, provided by the ASAS-SN online database along with the V band mag-

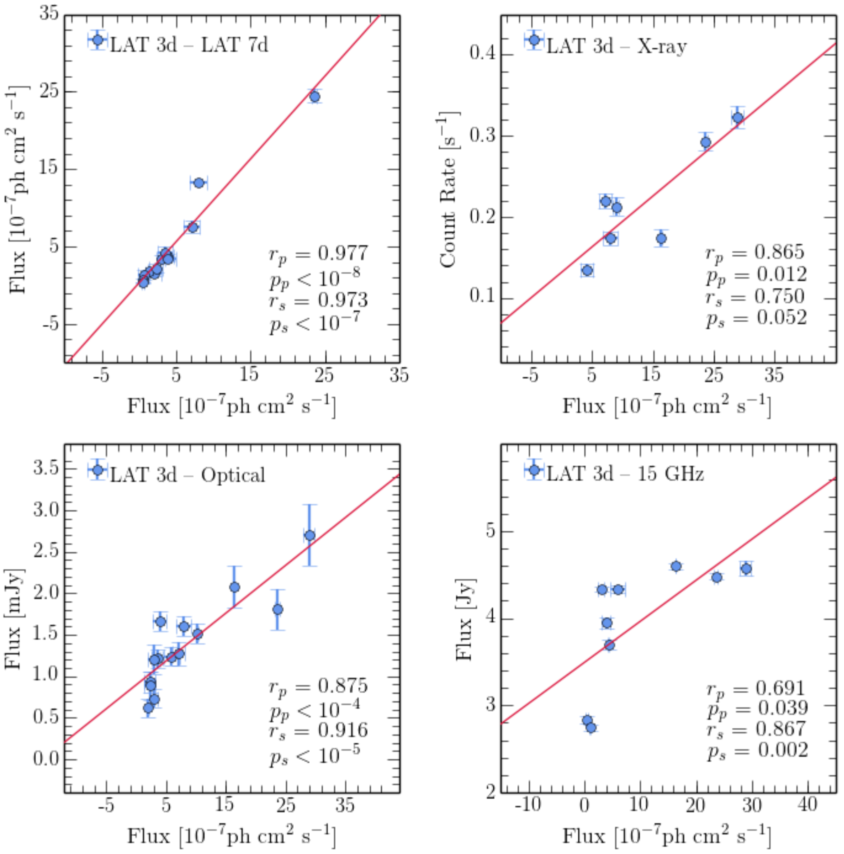

**Figure 3.2.** Correlations between $\gamma$-ray flux (3-day binning) and three other wavebands (X-ray, optical, and 15-GHz radio) for the time of high $\gamma$-ray activity in mid-to-end 2016. The top left panel shows the correlation between 3-day and 7-day $\gamma$-ray light curves as a consistency check. Correlations are tested with data points that are simultaneous within the bin size (i.e., ±1.5 days) of the $\gamma$-ray data. Each panel gives Pearson ($r_p$) and Spearman rank ($r_s$) correlation coefficients values together with the corresponding false alarm probabilities ($p$ values). Red lines indicate the best-fit linear relationships.

nitudes. The OVRO 15 GHz data represent the radio band in the correlation analyis; the other radio light curves did not provide enough simultaneous data points. We assume false alarm probabilities $p \leq 0.05$ to indicate statistically significant correlations (e.g., Leung et al. 2014). Figure 3.2 shows the results of the correlation analysis. All correlation coefficients, with values $r_p \geq 0.69$ and $r_s \geq 0.75$, point toward strong positive correlations between emission at $\gamma$-rays

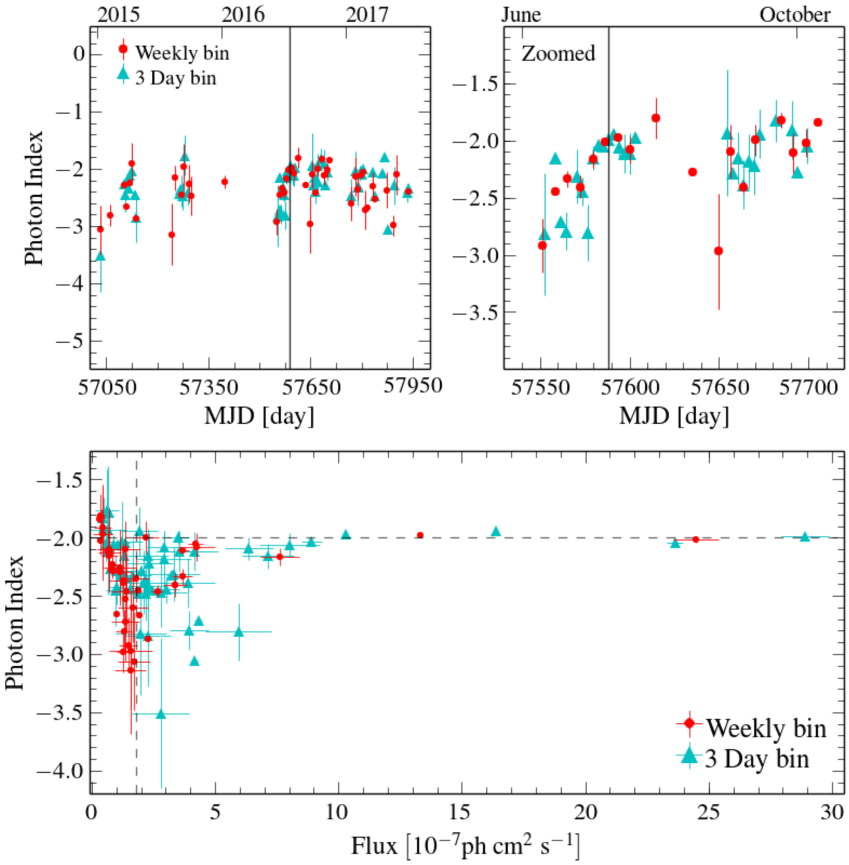

**Figure 3.3.** Evolution and distribution of the $\gamma$-ray photon index $\Gamma$ from the LAT data; red points mark the values for the weekly light curve, cyan points the values for the 3-day light curve. *Top panels:* $\Gamma$ as function of time. Vertical solid lines indicate the $\gamma$-ray outburst on MJD 57588. The top left panel spans the entire time of our observations, the top right panels focuses on the period of high $\gamma$-ray activity in 2016; note the different axis scales. *Bottom panel:* $\Gamma$ as funcion of $\gamma$-ray flux. The dashed horizontal and vertical lines represent a photon index of $\Gamma = -2$ and a flux of $1.8 \times 10^{-7}$ ph cm$^{-2}$ s$^{-1}$, respectively.

and at lower frequencies. False alarm probabilities are lower than 0.05 with the (marginal) exception of $p_s = 0.052$ for the X-ray–$\gamma$-ray pair.

Table 3.1. Properties of the polarized VLBA component

| Date | $m_{\text{total}}$ (%) | $\text{PI}_{\text{peak}}$ (mJy/beam) | $\text{EVPA}_{\text{peak}}$ (°) | rms[a] (mJy/beam) |
|---|---|---|---|---|
| 2016 June 11 | 5.9 | 189 | −14 | 0.69 |
| 2016 July 5 | 4.5 | 208 | −19 | 0.54 |
| 2016 July 31 | 4.9 | 232 | −51 | 2.73 |
| 2016 September 5 | 2.4 | 84 | −3 | 0.97 |
| 2016 October 6 | 1.3 | 30 | −39 | 1.01 |
| 2016 October 23 | 5.0 | 102 | −32 | 0.59 |
| 2016 November 28 | 3.6 | 51 | −10 | 0.42 |

Note. — [a] rms noise of residual polarization map.

### 3.3.3 LAT $\gamma$-ray photon indices

We quantify the $\gamma$-ray spectrum of 1749+096 using the photon index $\Gamma$, which is defined as $dN/dE \propto E^{+\Gamma}$ with $N$ being the number of photons and $E$ being the photon energy. Figure 3.3 shows the photon indices obtained from the 3-day binned and weekly binned LAT light curves at 0.1–300 GeV as function of time and as fuction of $\gamma$-ray flux, respectively. The photon index varies from $-3.5$ to $-1.7$ during the time of our observations; the two-year average value is $\Gamma = -2.3$. The photon index time series indicates a spectral hardening (i.e., an increase of $\Gamma$) around the time of the 2016 July $\gamma$-ray outburst. More specifically, the photon indices increase from about $-3$ to about $-2$ during the $\sim$40 days before the $\gamma$-ray outburst. The photon index appears to decrease (from $-1.7$ to $-3.5$) with increasing flux until the $\gamma$-ray flux reaches about $\sim 1.8 \times 10^{-7}$ ph cm$^{-2}$ s$^{-1}$. With further increasing flux the photon index increases again and approaches a plateau at $\Gamma \approx 2$ for fluxes $\gtrsim 6 \times 10^{-7}$ ph cm$^{-2}$ s$^{-1}$.

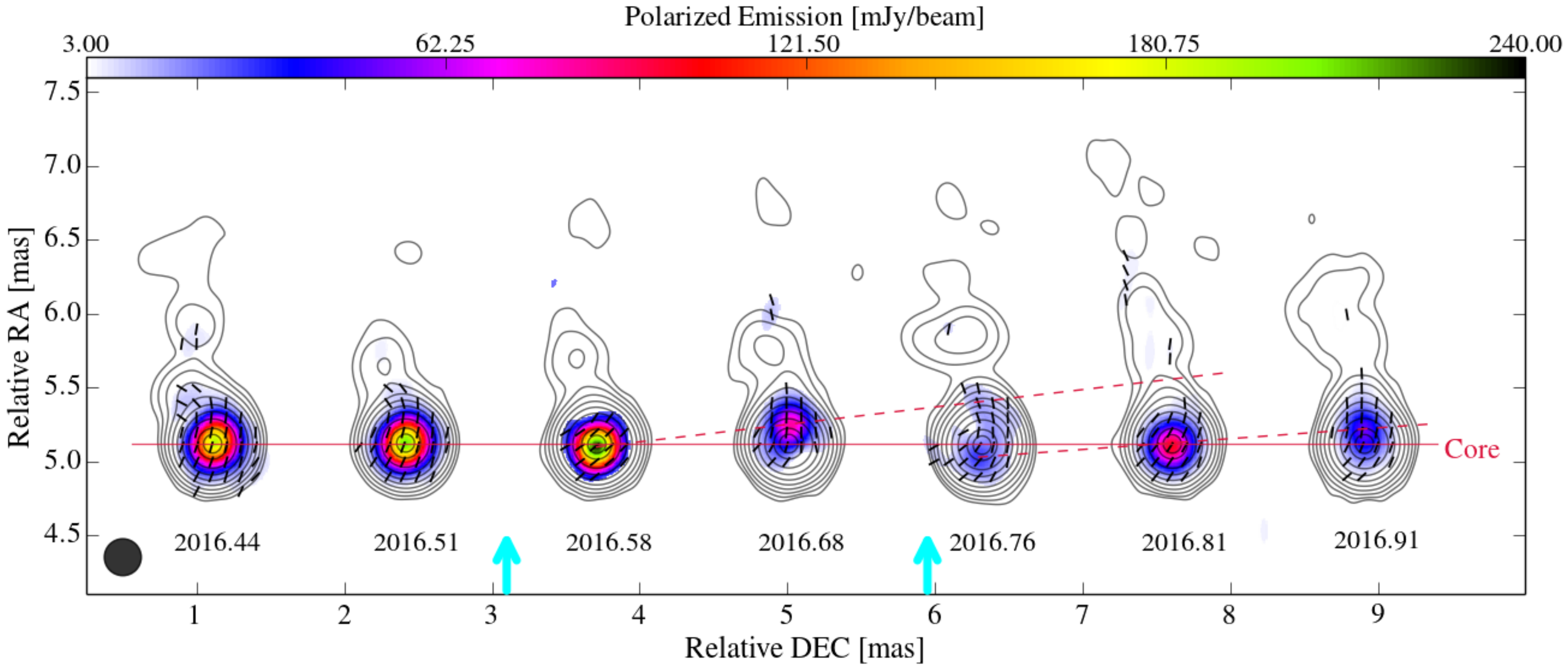

**Figure 3.4.** Linearly polarized flux density (*color scale*), EVPA (*black line segments*), and total intensity structure (*background contours*) of 1749+096 at 43 GHz as observed with the VLBA; from left to right: 2016 June 11, 2016 July 5, 2016 July 31, 2016 September 5, 2016 October 6, 2016 October 23, and 2016 November 28. The cyan arrows at the declination axis indicate the times of the two major $\gamma$-ray events: the 2016 July 19 outburst and the 2016 October 2 maximum. All maps are restored with a circular beam with a size of $0.25 \times 0.25$ mas (displayed at the bottom left). Contour levels increase by factors of two from 0.25% to 64%, plus one additional countour corresponding to 85% of the maximum total intensity. The two tilted red dashed lines indicate the apparent motion of the peak of the *polarized* emission. The horizontal red solid line indicates the location of the 7-mm core.

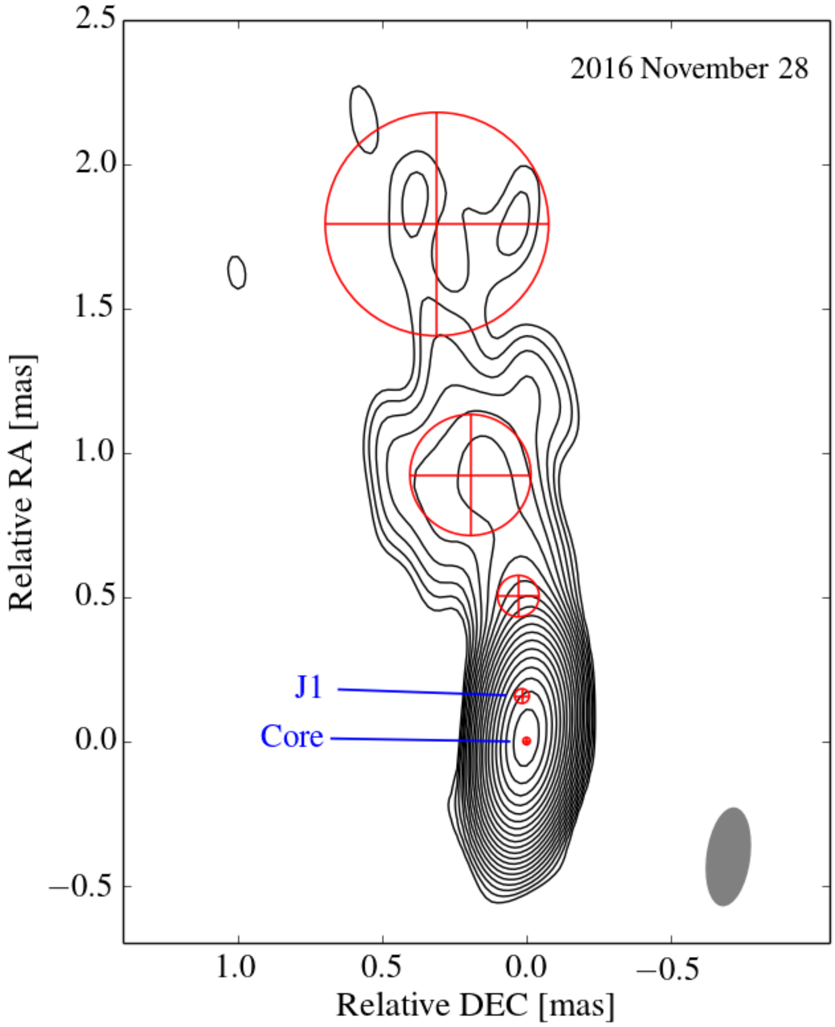

**Figure 3.5.** VLBA map of 1749+096 observed on 2016 November 28, from model component fitting. Individual circular Gaussian components are marked with red ⊕. The beam size (illustrated at the bottom right) is 0.34 × 0.15 mas at −7.6°. Contour levels increase by factors of $\sqrt{2}$ from 0.11% to 79.32% of the total intensity peak. Blue solid lines point to the VLBA 43-GHz core and the jet component J1, respectively.

### 3.3.4 Linear polarization at 43 GHz

Figure 3.4 shows the 7-mm (43 GHz) linear polarization in the innermost few parsecs of the radio jet of 1749+096. Polarized intensity scale and EVPA markers are plotted over the total

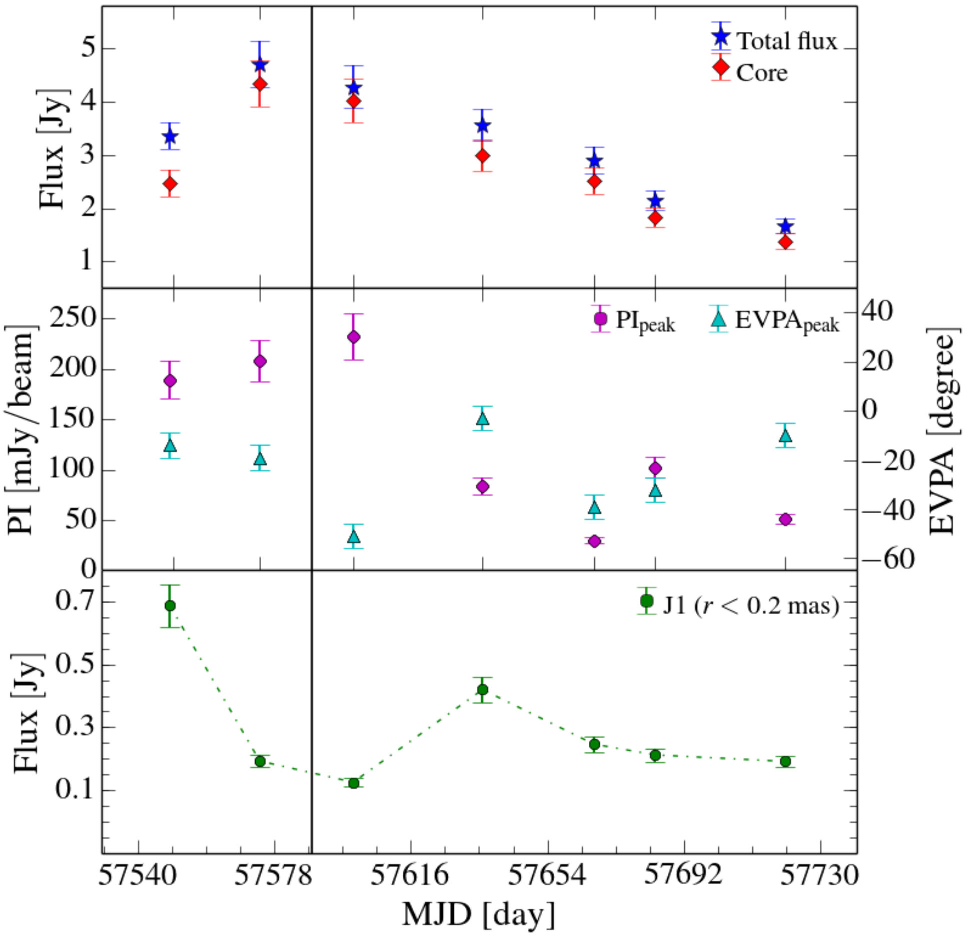

**Figure 3.6.** Evolution of flux density and the polarized component of 1749+096 obtained from the BU data; 2016 June 11 – 2016 November 28. *Top panel:* Core flux and total source flux. *Middle panel:* PI and EVPA listed in Table 3.1 with error of 10% and 5°, respectively. *Bottom panel:* Evolution of the jet component J1, located at ∼ 0.2 mas from the core. The vertical solid line marks the time of the 2016 July γ-ray outburst.

intensity contour. We applied an $8\sigma$ cutoff to the polarized intensity. We calculate fractional linear polarizations (defined as $m = \sqrt{Q^2 + U^2}/I$, where $I$, $Q$, and $U$ are Stokes parameters) by using CLEANed fluxes. We estimate a typical thermal noise of ∼1 mJy/beam in the polarized emission. Jorstad et al. (2005) suggests typical systematic errors of the BU data of ∼1% in fractional polarization and ∼5° in polarization angle for bright components, up to around 10°

in the worst case (see also Roberts et al. 1994 for discussion of uncertainties in the measured polarization). On average, we found a fractional linear polarization of ~3.9% throughout the BU dataset. Our further analysis focused on monitoring the properties of the polarized source component, corresponding to the peak of the polarized emission, which usually overlaps with the VLBA core. We summarize the polarization properties of 1749+096 in Table 3.1. Through 2016 June and 2016 July, the polarized flux increases notably. After the $\gamma$-ray outburst on 2016 July 19, the polarized intensity reaches its highest value, ~230 mJy, and displays a rotation of the EVPA by about 32° with respect to the previous epoch. In 2016 September, the polarized component had moved down the jet, with the EVPA being aligned closely to the jet axis which is located at a position angle of ~7.5° (the average position angle of all the jet components in Table 3.2). A new polarized component emerged *upstream* of the VLBA core just four days after the 2016 October 2 $\gamma$-ray flux maximum.

### 3.3.5 Flux evolution near the core

In addition to the polarized flux, the BU data provide important information on the (total intensity) structure of the innermost region of 1749+096. In order to trace the flux evolution of the various source components, we fit circular Gaussian profiles to them. The fitted parameters of all components are displayed in Table 3.2. Despite the clear evolution of the location of the polarized flux near the core (Section 3.3.4), we do not find indication for the ejection of a new jet component. As we might have missed a new component due to insufficient angular resolution or a smaller Doppler factor (i.e., a change of orientation in the curved jet), we took a closer look at the behaviour of the jet component J1. This component is located within 0.2 mas from the core in all 43-GHz VLBA maps (see Figure 3.5 and Table 3.2). Figure 3.6 shows the flux evolution of the core, J1, the polarized component, and total integrated source flux. The total flux is dominated by the core which contributes about 86% of the total observed flux on average. The core flux peaks at the time of the 2016 July $\gamma$-ray outburst, thus suggesting the core as the origin of the radio flux counterpart to the $\gamma$-ray flare. In 2016 September, the flux of the component J1 increases by a factor of about 3 compared to 2016 July, a bit more than one month after the 2016 July $\gamma$-ray outburst.

Parameters of the model fitted jet components in the 43 GHz total intensity images.

| Date | MJD | ID[a] | Flux (Jy) | Distance[b] (mas) | Angle[c] (°) | Diameter (mas) | $B^d_{\rm maj}$ (mas) | $B^d_{\rm min}$ (mas) | $B^d_{\rm PA}$ (°) | rms[e] (mJy/beam) |
|---|---|---|---|---|---|---|---|---|---|---|
| 2016 June 11 | 57550 | C | 2.47 | 0.00 | – | 0.02 | 0.35 | 0.15 | −6.33 | 1.02 |
| | | J1 | 0.69 | 0.09 | −12.69 | 0.04 | | | | |
| | | J2 | 0.09 | 0.39 | 22.58 | 0.16 | | | | |
| | | J3 | 0.03 | 0.81 | 7.94 | 0.14 | | | | |
| | | J4 | 0.08 | 1.43 | 9.16 | 0.67 | | | | |
| 2016 July 5 | 57574 | C | 4.35 | 0.00 | – | 0.03 | 0.40 | 0.16 | −12.60 | 1.09 |
| | | J1 | 0.19 | 0.14 | −0.11 | 0.05 | | | | |
| | | J2 | 0.09 | 0.55 | 15.48 | 0.21 | | | | |
| | | J3 | 0.07 | 1.39 | 7.81 | 0.64 | | | | |
| 2016 July 31 | 57600 | C | 4.02 | 0.00 | – | 0.03 | 0.35 | 0.17 | −7.63 | 1.41 |
| | | J1 | 0.12 | 0.17 | 0.30 | 0.04 | | | | |
| | | J2 | 0.06 | 0.53 | 15.15 | 0.17 | | | | |
| | | J3 | 0.03 | 0.79 | 13.23 | 0.10 | | | | |
| | | J4 | 0.05 | 1.46 | 2.73 | 0.43 | | | | |
| 2016 September 5 | 57636 | C | 2.99 | 0.00 | – | 0.02 | 0.49 | 0.17 | −20.40 | 1.44 |
| | | J1 | 0.42 | 0.10 | 11.65 | 0.03 | | | | |
| | | J2 | 0.05 | 0.43 | −0.53 | 0.08 | | | | |

**Table 3.2.** [a] Higher ID numbers Jx correspond to larger downstream distances from the core; [b] Distance from the core; [c] Position angle relative to core component; [d] Parameters of the elliptical beam: major axis, minor axis, position angle; [e] rms noise of residual map.

Parameters of the model fitted jet components in the 43 GHz total intensity images.

| Date | MJD | ID[a] | Flux<br>(Jy) | Distance[b]<br>(mas) | Angle[c]<br>(°) | Diameter<br>(mas) | $B^d_{\mathrm{maj}}$<br>(mas) | $B^d_{\mathrm{min}}$<br>(mas) | $B^d_{\mathrm{PA}}$<br>(°) | rms[e]<br>(mJy/beam) |
|---|---|---|---|---|---|---|---|---|---|---|
| | | J3 | 0.07 | 0.69 | 15.21 | 0.22 | | | | |
| | | J4 | 0.04 | 1.54 | 2.12 | 0.41 | | | | |
| 2016 October 6 | 57667 | C | 2.51 | 0.00 | – | 0.05 | 0.63 | 0.20 | −28.00 | 1.48 |
| | | J1 | 0.25 | 0.15 | −2.75 | 0.08 | | | | |
| | | J2 | 0.10 | 0.73 | 10.75 | 0.32 | | | | |
| | | J3 | 0.04 | 1.78 | 9.65 | 0.76 | | | | |
| 2016 October 23 | 57684 | C | 1.83 | 0.00 | – | 0.02 | 0.35 | 0.15 | −3.96 | 0.99 |
| | | J1 | 0.21 | 0.13 | 5.94 | 0.04 | | | | |
| | | J2 | 0.03 | 0.45 | 10.39 | 0.14 | | | | |
| | | J3 | 0.04 | 0.87 | 11.40 | 0.21 | | | | |
| | | J4 | 0.04 | 1.69 | 8.76 | 0.55 | | | | |
| 2016 November 28 | 57720 | C | 1.38 | 0.00 | – | 0.03 | 0.34 | 0.15 | −7.63 | 0.53 |
| | | J1 | 0.19 | 0.16 | 5.57 | 0.05 | | | | |
| | | J2 | 0.02 | 0.50 | 3.15 | 0.14 | | | | |
| | | J3 | 0.05 | 0.94 | 11.85 | 0.42 | | | | |
| | | J4 | 0.03 | 1.82 | 9.81 | 0.77 | | | | |

**Table 3.2.** Continued.

## 3.4 Discussion

### 3.4.1 $\gamma$-ray activity

The 2016 July $\gamma$-ray outburst is an exceptional event with no precedent since the beginning of $\gamma$-ray observations in 2009. During phases of low as well as very high $\gamma$-ray fluxes, we observe photon indices close to the value $\Gamma \approx -2.2$ expected for LSP blazars, suggesting a spectral break located at around 100 MeV or less (Lico et al. 2017). Else than intermediate-synchrotron peaked (ISP) and high-synchrotron peaked (HSP) blazars, LSP blazars are known to experience severe cooling in the energy range 0.1–300 GeV (i.e, our LAT band), thus producing the IC component of the SED (Lico et al. 2017). During the 2016 July $\gamma$-ray outburst we observe an increase in photon index (see Figure 3.3), meaning a spectral hardening with increasing flux (e.g., Nandikotkur et al. 2007). Such behavior is rare in BL Lac objects (Lico et al. 2014). Kushwaha et al. (2014) suggested shock acceleration as explanation for the hardening of $\gamma$-ray spectra. In our case, the temporal agreement of the apex of the spectral hardening with the $\gamma$-ray flux peak points toward shock acceleration inducing a surge of $\gamma$-ray photons at higher energies efficiently (Kusunose et al. 2000).

Abdo et al. (2010b) found a transition between a harder-when-brighter trend and a softer-when-brighter trend in PKS 1510−089 for energies above 0.2 GeV. In their observation, photon indices softened with fluxes increasing up to $\sim 2.4 \times 10^{-7}$ ph cm$^{-2}$ s$^{-1}$, then hardened again with fluxes increasing further. This matches our observation of decreasing photon index with the flux increasing up to about $1.8 \times 10^{-7}$ ph cm$^{-2}$ s$^{-1}$ (weekly light curve, see Figure 3.3). Assuming a threshold value of $1.7 \times 10^{-7}$ ph cm$^{-2}$ s$^{-1}$, we find a strong negative correlation ($r_p = -0.86$) between $\gamma$-ray flux and $\Gamma$, corresponding to a softer-when-brighter scaling. The physical mechanisms behind this softer-when-brighter trend as well as the inversion of this trend at a certain threshold flux are unclear (Abdo et al. 2010b). Candidate mechanisms are a change in emission mechanism (e.g., Asano et al. 2014), the cooling time scale (e.g., Dotson et al. 2012), or the magnetic field strength (e.g., Kusunose et al. 2000).

### 3.4.2 Multi-wavelength correlations

The $\gamma$-ray outburst in 2016 July was accompanied by simultaneous flux enhancements from radio to X-rays, indicating a physical connection across all wavelengths (Jorstad et al. 2001a; León-Tavares et al. 2011; Lico et al. 2017). The fact the source flux from radio to $\gamma$ peaks simultaneously within few days strongly suggests that the emission at all wavelengths (largely) originates from the same location within the source (León-Tavares et al. 2011; Wehrle et al. 2012; Jorstad et al. 2013; Casadio et al. 2015a). A possible exception is the 15-GHz radio peak which we cannot locate exactly and which might be delayed by up to a few more days relative to the events at higher energy bands. If it were indeed delayed, we would have to assume a displacement of the radio emitting region relative to the regions emitting higher energy radiation. This is supposed to occur when the emission at higher energies is produced in a region that is optically thick at 15 GHz; radio light is emitted only once the disturbance in the jet has entered a region transparent at 15 GHz (Wehrle et al. 2012; see also Agudo et al. 2011b, for discussion of a physically extended disturbance).

Figure 3.6 shows that the BU VLBA core is the origin of the 7-mm outburst, thus implying a connection between the mm-wave core and the simultaneous events at higher energy bands (e.g., Agudo et al. 2011b; Wehrle et al. 2012; Jorstad et al. 2013). The peak of the $\gamma$-ray outburst seems to coincide with the peak of the 7-mm emission. This is unexpected as the conventional picture of the radio–$\gamma$-ray connection expects a $\gamma$-ray outburst at the onset (during the rise) of a radio flare (Marscher 2016; but see also Valtaoja & Teräsranta 1995; Max-Moerbeck et al. 2014a, for various timings of $\gamma$-ray events relative to radio flares). However, we note that a considerable number of studies observed $\gamma$-ray outbursts being (quasi-)simultaneous with radio flares (e.g., León-Tavares et al. 2011; Wehrle et al. 2012; Lico et al. 2014; Casadio et al. 2015a).

### 3.4.3 Origin of the $\gamma$-ray outburst

The relative timing of the $\gamma$-ray outburst and the 7-mm outburst of the VLBA core suggests the mm-wave core to be the production site of the $\gamma$-radiation (Wehrle et al. 2012; Jorstad et al. 2013; Casadio et al. 2015a). The behaviour of the polarized VLBA component after the 2016 July $\gamma$-ray outburst supports this idea (see Figure 3.4). The linear polarization image of

2016 September 5 shows clearly that the region of polarized emission, which was located at the VLBI core before, moved down the jet. This can be interpreted as the signature of a shock emerging within, and moving away from, the core (e.g., Ros et al. 2000; Marscher et al. 2008; Pushkarev et al. 2008; Marscher et al. 2010; Agudo et al. 2011b; Wehrle et al. 2012; Marscher et al. 2012b; Jorstad et al. 2013). This picture connects the $\gamma$-ray outburst with the passage of a propagating disturbance, like a new jet component, through the core. The flux evolution of component J1, that was detected within 0.2 mas from the core consistently over six months, supports this idea (see Figure 3.6). The enhancement of the flux from J1 as observed on 2016 September 5 is consistent with the disturbance propagating through a region downstream of the core (Casadio et al. 2015a; Hodgson et al. 2017). However, we do not find a newly emerging feature in the (total intensity) VLBA maps that could be associated with displacement of the polarized component. Interestingly, Lico et al. (2014) and Ros et al. (2000) encountered similar situations in Mrk 421 and 3C 345. The absence of a directly observed new jet component may be attributed to a complex structure of the jet around the core or spatial blending of multiple emission regions in the jet (Ros et al. 2000; Jorstad et al. 2013; Hodgson et al. 2017).

As noted in Section 3.4.1, the evolution of the $\gamma$-ray spectrum of 1749+096 around the time of the 2016 July $\gamma$-ray flare is consistent with the acceleration of a relativistic shock. Further evidence in favor of this interpretation is provided by the evolution of the BU VLBA core flux both in total intensity and linear polarization during 2016 June and 2016 July. The polarized flux reached its maximum on 2016 July 31, when the BU core flux was in decline already (see Figure 3.6). This is the signature expected from a disturbance propagating through the core (e.g., Lico et al. 2014) but may also be connected to the evolution of a relativistic shock (Ros et al. 2000; see also León-Tavares et al. 2012 for discussions of strong core polarization). The maximum of the polarized intensity, about 230 mJy/beam, coincides with an EVPA swing by $\sim 32°$ in the core region on 2016 July 31. Hughes et al. (2011) suggested that initially random and turbulent magnetic fields in a blazar jet can be compressed by a propagating oblique shock, thus leading to both an enhancement of polarized intensity and a swing of the EVPA (Laing 1980; Hughes et al. 1985, 1991). Accordingly, we suggest that the passage of a propagating disturbance through the mm-wave core is responsible for the $\gamma$-ray outburst. (Marscher et al.

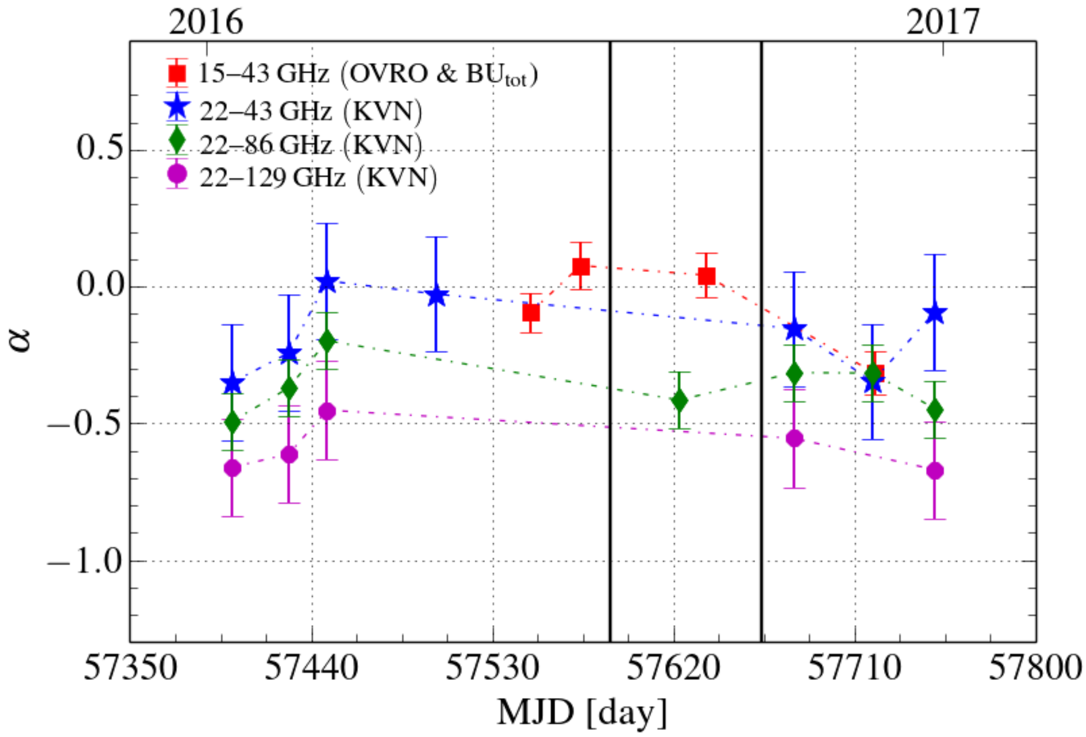

**Figure 3.7.** Pairwise spectral indices ($S_\nu \propto \nu^\alpha$) of 1749+096 at radio wavelengths observed in 2016. Different colors and symbols indicate different frequency pairs. The epochs of the $\gamma$-ray events are indicated by two black vertical solid lines.

2008; Agudo et al. 2011b; Wehrle et al. 2012; Jorstad et al. 2013). Further clues for constraining the production site of the optical-to-$\gamma$-ray outbursts could be provided by the opacity of the core at 7 mm (see Section 3.4.4) during the event. It seems that the $\gamma$-ray outburst is contemporaneous with its 7-mm counterpart, whereas the cm-wave counterpart in the OVRO light curve is slightly delayed relative to the peak of the $\gamma$-ray outburst. This leads us to consider a region downstream of the mm-wave core to be the origin of the $\gamma$-ray outburst. This is in agreement with the disturbance being spatially extended (e.g., Agudo et al. 2011b). The duration of the $\gamma$-ray outburst, roughly 50 days, can be considered as the time needed for the disturbance to pass through the mm-wave core (Jorstad et al. 2013). Then, the strongest $\gamma$-ray emission might be produced by the back region of the propagating disturbance ~10 days before the disturbance fully escapes the mm-wave core.

### 3.4.4 The enhanced $\gamma$-ray emission in 2016 October

We find a notable $\gamma$-rays flux enhancement around 2016 October 2. Contrary to the prior (2016 July) $\gamma$-ray outburst, this local peak was, if at all, accompanied only by an optical counterpart without corresponding flux enhancements at radio and X-rays. The 43-GHz linear polarization maps obtained after the time of the $\gamma$-ray enhancement show a polarized component propagating down the jet from the BU core. This suggests the presence of a propagating disturbance similar to the situation discussed in Section 3.4.2. Notably, we observe an upstream displacement of the polarized component relative to the peak of the total intensity on 2016 October 6. However, the data from this epoch need to be interpreted with care owing to reduced sensitivity and resolution caused by antennas missing from the array (see Section 3.2.1). We calculated spectral indices of 1749+096 from the radio data as follows. For the pair of 15–43 GHz, we employed OVRO and the BU total fluxes observed within 1 day, assuming that the VLBI-scale structure of the source dominates the OVRO fluxes (the ratio of the OVRO and BU fluxes is 1.1 on average). Although the data points are sparse, it seems that the source was opaque ($\alpha \sim 0$) at 43 GHz during the $\gamma$-ray flaring period. This is consistent with what O'Sullivan & Gabuzda (2009b) reported (i.e., a spectral index of the core region of 1749+096 $\sim -0.1$ between 12.9 and 43 GHz). We consider that the second $\gamma$-ray event might have been caused by a propagating disturbance at (nearly) the same location in the jet as the first $\gamma$-ray event, but with smaller Doppler factor and energization. This explains the relatively lower $\gamma$-ray flux density and the absence of a radio counterpart compared to the major $\gamma$-ray outburst.

## 3.5 Summary

In this study, we explored the nature of two $\gamma$-ray events, the 2016 July outburst and the 2016 October flux enhancement, in the blazar 1749+096. From the combined evidence provided by multi-waveband flux observations plus 43-GHz VLBA maps, we conclude that both $\gamma$-ray events are connected to the propagation of a disturbance in the jet (Jorstad et al. 2001b; Marscher et al. 2008; Jorstad & Marscher 2016). Regarding the origin of the two $\gamma$-ray events, we suggest the 'parsec-scale scenario' (e.g., Agudo et al. 2011b; Wehrle et al. 2012; Jorstad et al. 2013) where a relativistic shock moving down the jet causes an enhancement of $\gamma$-ray flux in the radio core by providing highly accelerated electrons. As the disturbance passes through the mm-wave core, the VLBA core flares simultaneously with the fluxes at the higher energy bands. Eventually, a moving feature can be seen in the linear polarization images. Given that the cm-wave flux peak is slightly delayed (around 5 days) relative to the $\gamma$-ray outburst, we tentatively conclude that a region downstream of the mm-wave core is the origin of the $\gamma$-ray outburst. The $\gamma$-ray outburst matches the growth of a strong shock. We find a hardening of the $\gamma$-ray spectrum with increasing flux during the rising stage of the $\gamma$-ray outburst. The subsequent presence of abundant polarized emission in the core region further supports the presence of growing shock (León-Tavares et al. 2012).

In the case of the $\gamma$-ray enhancement on 2016 October 2, we find an upstream displacement of the polarized peak relative to the total intensity in the linear polarization image on 2016 October 6. Given the opacity of 1749+096 at 43 GHz, however, the polarized component cannot be detected upstream of the BU core due to synchrotron self-absorption. For this $\gamma$-ray event, we expect that the event was less energized with relatively smaller Doppler factor, thus resulting in some differences in the observed evolution between the two $\gamma$-ray events.

The origin of the bulk of the seed photons remains unclear for both $\gamma$-ray events. In general, both the internal IC process with seed photons from the jet itself (Marscher et al. 2010), and external Compton (EC) scattering with seed photons from the dusty torus at parsec-scales or the BLR at subparsec-scales (see also León-Tavares et al. 2011, for discussion of outflowing BLR at parsec-scales) can be considered. Given the observed hardening of the $\gamma$-ray spectrum however, the EC process with infrared seed photons from the dusty torus might be the dominant emission mechanism for the 2016 July $\gamma$-ray outburst (Agudo et al. 2011b). A better understanding of $\gamma$-ray flares in blazar jets not only requires monitoring the properties of the linear polarization (which reflects the underlying magnetic field configuration; e.g., Homan et al. 2002; Marscher et al. 2012b), but also changes in jet component Doppler factors caused by viewing angle variations that could substantially affect the observed $\gamma$-rays (Jorstad et al. 2001b; Casadio et al. 2015a; Raiteri et al. 2017).

# Chapter 4

# Investigating The Connection between $\gamma$-Ray Activity and The Relativistic Jet in 3C 273 during 2015–2019[1]

## Abstract

The powerful radiation over the entire electromagnetic spectrum and its radio jet activity of the blazar 3C 273 offer the opportunity of studying the physics of $\gamma$-ray emission from active galactic nuclei. Since the historically strong outburst in 2009, 3C 273 showed relatively weak emission in the $\gamma$-ray band over several years. However, recent *Fermi*-Large Area Telescope observations indicate higher activity during 2015–2019. We constrain the origin of the $\gamma$-ray outbursts toward 3C 273 and investigate their connection to the parsec-scale jet. We generated *Fermi*-LAT $\gamma$-ray light curves with multiple binning intervals and studied the spectral properties of the $\gamma$-ray emission. Using a 3 mm ALMA light curve, we studied the correlation between radio and $\gamma$-ray emission. The relevant activity in the parsec-scale jet of 3C 273 was investigated with 7 mm VLBA observations that were obtained close in time to notable $\gamma$-ray outbursts. We find two prominent $\gamma$-ray outbursts in 2016 (MJD 57382) and 2017 (MJD 57883) accompanied by millimeter-wavelength flaring activity. The $\gamma$-ray photon index time series show a weak

---

[1] Published in the *Astronomy & Astrophysics*: Kim et al. 2020, A&A, 636, A62

hump-like feature around the $\gamma$-ray outbursts. The monthly $\gamma$-ray flux–index plot indicates a transition from softer-when-brighter to harder-when-brighter states at $1.03 \times 10^{-7}$ ph cm$^{-2}$ s$^{-1}$. A significant correlation between the $\gamma$-ray and millimeter-wavelength emission is found, and the radio lags the $\gamma$-rays by about 105–112 days. The 43 GHz jet images reveal the known stationary features (i.e., the core, $S1$, and $S2$) in a region upstream of the jet. We find an indication for a propagating disturbance and a polarized knot between the stationary components at about the times of the two $\gamma$-ray outbursts. Our results support a parsec-scale origin for the observed higher $\gamma$-ray activity, which suggests that this is associated with standing shocks in the jet.

## 4.1 Introduction

The flat-spectrum radio quasar 3C 273 is one of the most extreme blazars, showing strong and flaring radiation throughout the electromagnetic spectrum. 3C 273 displays a bright extended relativistic jet in centimeter to millimeter VLBI images and is known to be a powerful high-energy emitter (Bruni et al. 2017), making it one of the best sources for studying the nature of the $\gamma$-ray emission from blazars. Several recent studies (Rani et al. 2013b; Chidiac et al. 2016; Lisakov et al. 2017) have indicated that a region close to the jet apex and not the 7 mm core is the place of origin of bright $\gamma$-ray outbursts. Using the energy dependence of electron cooling times, we can determine the site of the inverse Compton (IC) scattering that generates the $\gamma$-ray emission (Dotson et al. 2012). This provides information on the place of origin of the IC seed photons (the BLR or a dusty torus) and thus provides a distance scale (subparsec or parsec) for the $\gamma$-ray production in the jet (Dotson et al. 2015; Coogan et al. 2016). A common assumption in many scenarios that were envoked to explain the blazar $\gamma$-ray flaring activity is that a plasma blob moves downstream from the jet; these structures that travel along the jet are frequently observed. As it propagates along the jet, the blob can pass and interact with standing shocks (e.g., Wehrle et al. 2016; Hodgson et al. 2017; see also Böttcher 2019, for a discussion of $\gamma$-ray flares with different origins). The latter may appear as stationary features (e.g., Gómez et al. 1997; Hervet et al. 2016) in the VLBI jets.

Costamante et al. (2018) reported that in the jets of FSRQs, $\gamma$-ray emission originates ‘almost always’ (both high/low states) from a region outside the BLR. The idea inspired me to design this study. The FSRQ 3C 273 was selected to investigate two intermediate-level $\gamma$-ray flares recently occurred in the source. Moreover, the jet of 3C 273 is known to have multiple stationary features (i.e., the RCSs) near the radio core (Lisakov et al. 2017), which makes this powerful jet suitable to explore phenomenology of the compact, stationary components. In this study, we investigate the 2015–2019 $\gamma$-ray emission of 3C 273 that is associated with its relativistic jet to explore the origin of $\gamma$-ray outbursts. The observations and data are described in Section 2. In Section 3 we present our results and analysis. Finally, we discuss and conclude on the observed phenomena in Sections 4 and 5, respectively. We use the following cosmological parameters: $H_0 = 71\,\mathrm{km\,Mpc\,s^{-1}}$, $\Omega_\Lambda = 0.73$, and $\Omega_m = 0.27$, corresponding to an angular scale of 2.71 pc/mas at the redshift of 3C 273, $z = 0.158$ (Strauss et al. 1992).

## 4.2 Observations

### 4.2.1 Fermi-LAT

We analyzed Pass 8 $\gamma$-ray data obtained by the *Fermi*-LAT (Atwood et al. 2009). The data were calibrated following the standard unbinned likelihood procedure[2]. We selected SOURCE class events at 0.1–300 GeV measured between 2015 January 1 and 2018 December 10 (MJD: 57023–58462). Filter parameters `DATA_QUAL>0 && LAT_CONFIG==1` and `zmax=90`° were selected for the good-time intervals and to minimize the Earth limb $\gamma$-ray contamination. We defined a region of interest (ROI) of 15° × 15° centered at 3C 273, and included all sources in the 4FGL catalog (i.e., The Fermi-LAT Collaboration et al. 2019) within the ROI. To take diffuse background sources into account, Galactic diffuse emission `gll_iem_v07` and isotropic background emission `iso_P8R3_SOURCE_V2_v1` templates were applied. The significance of $\gamma$-ray signals was evaluated with the maximum likelihood test statistic (TS). First, we optimized the background model using the ScienceTools (`v11r5p3`). We performed a maximum likelihood fit to the data covering half of the whole period and left the spectral parameters of all sources free. For the two diffuse backgrounds, the normalizations, including the index of the Galactic diffuse emission, were left free. The sources with TS $<$ 10 in the background model obtained

---

[2] `https://fermi.gsfc.nasa.gov/ssc/data/analysis/documentation/`

from the first optimization were removed, then a second optimization was performd with the updated model. To produce the final $\gamma$-ray light curves, we left the spectral parameters free for sources within 3° from the ROI center, plus the normalizations for the diffuse backgrounds. All the other parameters were fixed to the results of the second optimization. The spectral model of 3C 273 was assumed to be a power-law model[3] defined as $dN/dE \propto E^{+\Gamma}$ , with $N$ being the number of photons, $E$ the photon energy, and $\Gamma$ the photon index. We computed $2\sigma$ upper limits for $\gamma$-ray signals detected with TS $< 9$ or $\Delta F_\gamma / F_\gamma > 0.5$, where $F_\gamma$ and $\Delta F_\gamma$ indicate the flux and its error, respectively. As binning intervals for the $\gamma$-ray light curves, we selected 30 and 7 days for the full time range (i.e., 2015–2019), and one day for flaring periods to provide a zoom-in view. Based on the average flare duration of 12 days reported in Abdo et al. (2010c), weekly and monthly time bins are appropriate to describe the global $\gamma$-ray activity of blazars, as also noted in previous studies (Rani et al. 2013b; Chidiac et al. 2016; Meyer et al. 2019). 3C 273 was not very bright during 2015–2019. Thus, we preferred an interval of at least 7 days to achieve a high signal-to-noise ratio. Weekly binning also coincides with the average sampling interval of the ALMA data used in this study (see Section 4.3.3).

### 4.2.2 ALMA band 3

We make use of a radio light curve of 3C 273 provided by the Atacama Large Millimeter / submillimeter Array (ALMA)[4] spanning from 2015 January to 2018 December. The flux data were obtained at ALMA band 3 (84–116 GHz), and most them have been taken at 91 and 103 GHz. When several flux measurements were made on a single day, the data point with the smallest error was considered here. Further details of the observations can be found in Bonato et al. (2018).

### 4.2.3 VLBA 43 GHz

The VLBA-BU-BLAZAR program (i.e., Jorstad & Marscher 2016) monitors bright $\gamma$-ray blazars (34 blazars and 3 radio galaxies) every month with the Very Long Baseline Array

---

[3] `https://fermi.gsfc.nasa.gov/ssc/data/analysis/scitools/source_models.html`

[4] `https://almascience.eso.org/alma-data/calibrator-catalogue`

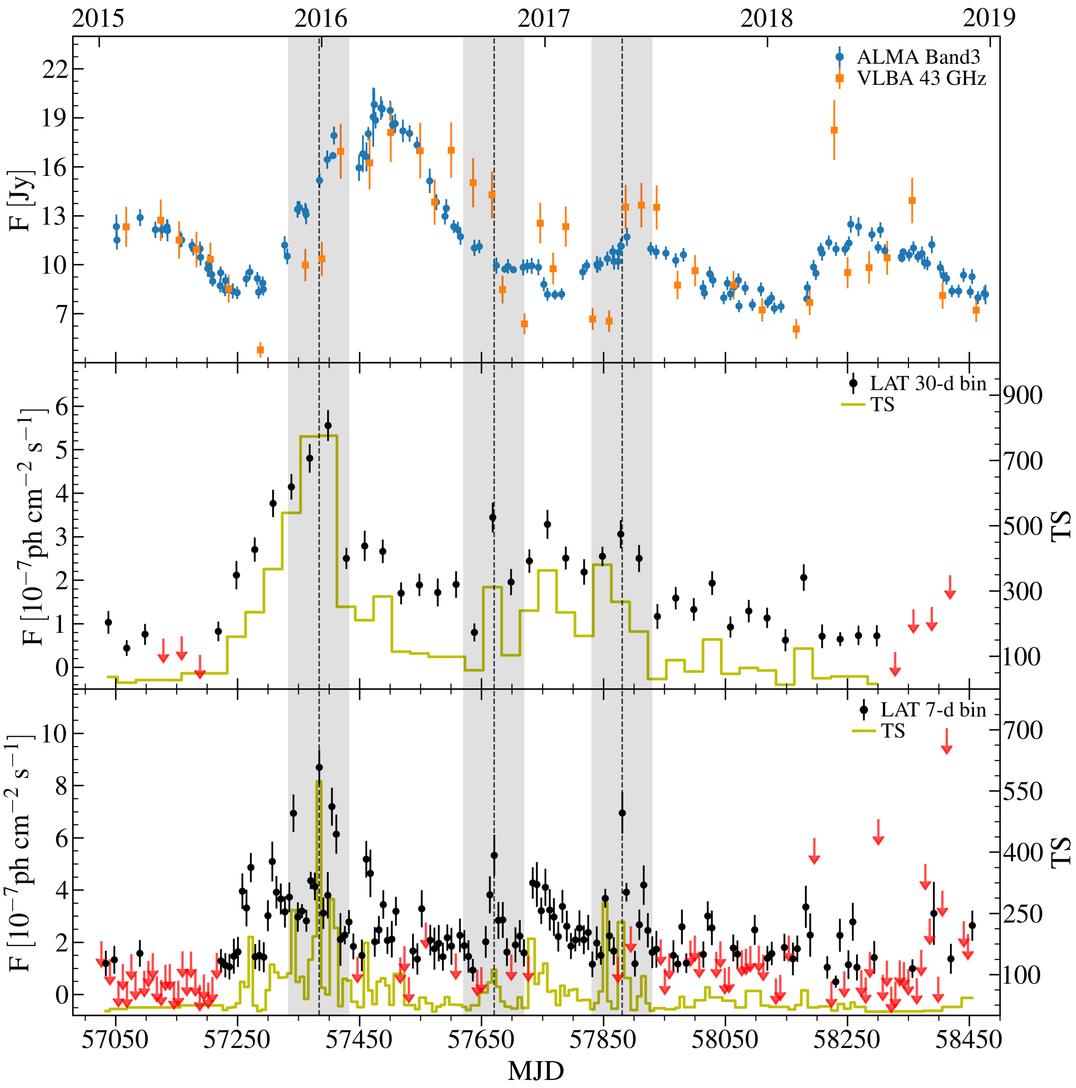

**Figure 4.1.** $\gamma$-ray and radio light curves of 3C 273 in 2015–2019. From top to bottom: ALMA band 3 (~100 GHz) overlaid on the VLBA 43 GHz total flux, *Fermi*-LAT fluxes using monthly binning, and *Fermi*-LAT fluxes using weekly binning. For the $\gamma$-ray light curves, the $2\,\sigma$ upper limits are indicated by red downward arrows. The vertical dashed lines show three $\gamma$-ray outbursts that are identified in the weekly light curve. Each of the shaded areas spans 100 days centered at the peak of a $\gamma$-ray outburst.

(VLBA) at 43 GHz. We used fully calibrated data for 3C 273, which are publicly available[5].

---

[5] `https://www.bu.edu/blazars/VLBAproject.html`

The data were imaged with the software package `Difmap` (Shepherd 1997). The image analysis was performed with several datasets observed close to the time of two $\gamma$-ray outbursts: 2015 December to 2016 April and 2017 April to 2017 August (ten epochs in total). We considered a conservative flux density accuracy of 10%. For the positions of the brightest and compact knots, about one in ten of the synthesized beam dimensions were used (e.g., Lister et al. 2009). A full description of the VLBA-BU-BLAZAR data can be found in Jorstad et al. (2017). We further produced linear polarization maps similar to those of Kim et al. (2018b) for all epochs. We also used the CLEANed model components provided by the BU group on their website[6] to investigate the 43 GHz fluxes during 2015–2019. We followed Lee et al. (2016a) in our calculations of brightness temperatures and resolution limits for observed jet components. The rms noise of a jet component was estimated from an area spanning $3 \times 3$ beam sizes centered at the position of the component.

## 4.3 Results

### 4.3.1 Light curves

Figure 4.1 shows the $\gamma$-ray and radio light curves of 3C 273 from 2015 January 11 to 2018 December 24 (MJD: 57033–58476). The 3 mm ALMA light curve comprises one major flare and three minor flares during this time, with an average radio flux of 11±3 Jy and a minimum of about 7 Jy. The major flare spans from mid-2015 to late-2016, and the peak reaches ~20 Jy on 2016 March 27 (MJD 57474). This implies an increase in the flux density by a factor of about 2.5. We also note the presence of a substructure in this flare: an additional peak of ~18 Jy on 2016 January 21 (MJD 57408). Interestingly, it seems that each ALMA flare has some substructure ("subflares"). The other minor flares lasted for less than a year, with relatively weak peaks below 13 Jy. The 43 GHz VLBA fluxes essentially follow the ALMA light curve, but the relatively long cadence (~30 days) prevents a more exact comparison. We note that the 43 GHz fluxes are both higher and lower than the ALMA fluxes at different times. This implies a variable radio spectrum at millimeter-wavelengths. It is worth noting that a significant fraction

---

[6] `https://www.bu.edu/blazars/VLBA_GLAST/3c273.html`

of the total VLBI flux, about 1–6 Jy depending on the time, is contributed by the extended jet structure beyond 0.3–0.4 mas from the core (see Figure 4.7).

The monthly and weekly binned $\gamma$-ray light curves yield average fluxes of $(2.0 \pm 1.2) \times 10^{-7}\,\mathrm{ph\,cm^{-2}\,s^{-1}}$ and $(2.6 \pm 1.4) \times 10^{-7}\,\mathrm{ph\,cm^{-2}\,s^{-1}}$, respectively. It is worth noting that 3C 273 has been in a relatively low-$\gamma$-ray flux state since the historical powerful outburst around 2009 September (see Lisakov et al. 2017; Meyer et al. 2019). However, we find three notable and distinguishable $\gamma$-ray events in our light curves. The first event (2016A) can be found in the monthly light curve, and the peak reaches $5.6 \times 10^{-7}\,\mathrm{ph\,cm^{-2}\,s^{-1}}$ on 2016 January 11 (MJD 57398). This $\gamma$-ray outburst overlaps in time with the major ALMA flare. The other events can be identified more clearly in the weekly light curve. We find the second event (2016B) on 2016 October 9 (MJD 57670) with a peak of $5.3 \times 10^{-7}\,\mathrm{ph\,cm^{-2}\,s^{-1}}$. The third event (2017A) appeared on 2017 May 7 (MJD 57880) with a peak of $7.0 \times 10^{-7}\,\mathrm{ph\,cm^{-2}\,s^{-1}}$. These outbursts seems to have 3 mm radio counterparts that are weaker than the counterpart to the first $\gamma$-ray event. In particular, the third event is evident only in the light curve with weekly binning. Similarly, the peak of the first $\gamma$-ray outburst can be localized more precisely in the weekly light curve, with a flux of $8.7 \times 10^{-7}\,\mathrm{ph\,cm^{-2}\,s^{-1}}$ on 2015 December 27 (MJD 57383).

To analyze the $\gamma$-ray flares in more detail and to minimize the binning effect, we produced $\gamma$-ray light curves with one-day time binning for each outburst (e.g., Marscher et al. 2010; Wehrle et al. 2016). Figure 4.2 shows the daily $\gamma$-ray light curves, which cover the time ranges indicated by the shaded areas in Figure 4.1. The first outburst peaks on 2015 December 26 (MJD 57382) with a flux of $1.4 \times 10^{-6}\,\mathrm{ph\,cm^{-2}\,s^{-1}}$. For the second and third outbursts, the peaks occur on 2016 October 8 (MJD 57669) with a flux of $9.4 \times 10^{-7}\,\mathrm{ph\,cm^{-2}\,s^{-1}}$ and on 2017 May 10 (MJD 57883) with a flux of $2.5 \times 10^{-6}\,\mathrm{ph\,cm^{-2}\,s^{-1}}$, respectively. The 2016A event is by far the most prominent, showing variable enhanced activity around its peak, whereas the $\gamma$-ray activity around the peaks of the 2016B and 2017A events appears to be substantially weaker. We do not see any notable temporal variation in the photon indices derived from the three daily light curves; the average photon index values are $-2.80$, $-3.58$, and $-2.85$. The first and third outbursts are easily identified in their daily light curves because of their brightness and high statistical significance, whereas the 2016B outburst is weak and shows relatively low

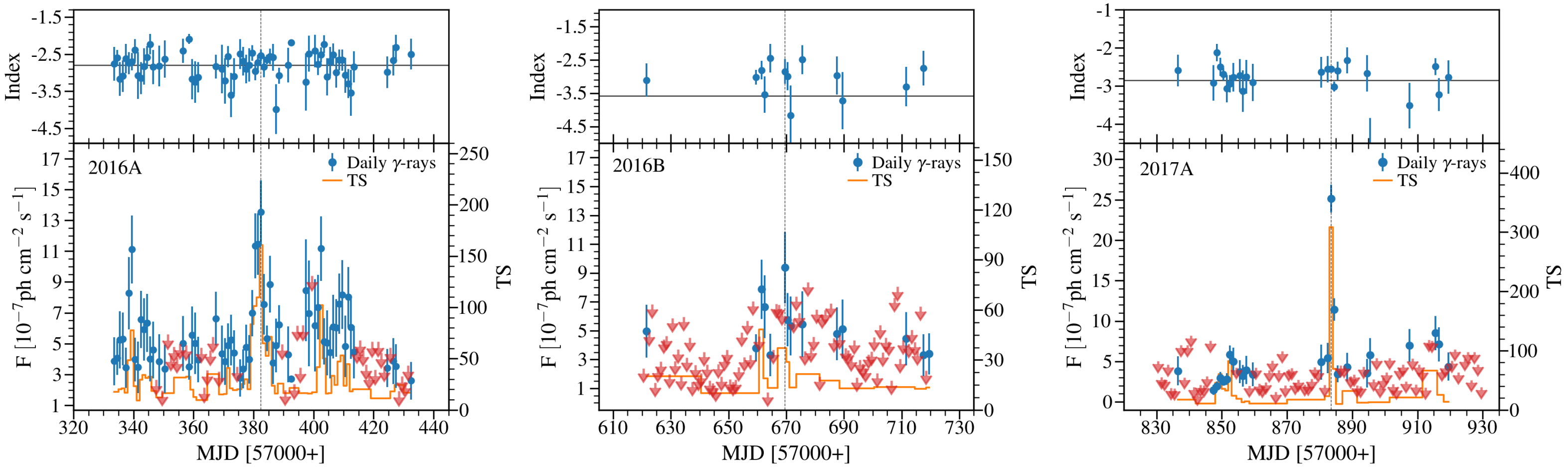

**Figure 4.2.** Zoomed-in $\gamma$-ray light curves of 3C 273, binned into one-day time bins, for the three $\gamma$-ray flaring periods indicated by the shaded areas in Figure 4.1. The upper panels in each diagram show the photon indices at the same time resolution. Average photon index values are marked by horizontal solid lines. The vertical dashed lines mark the peak times of the $\gamma$-ray outbursts in the daily light curves.

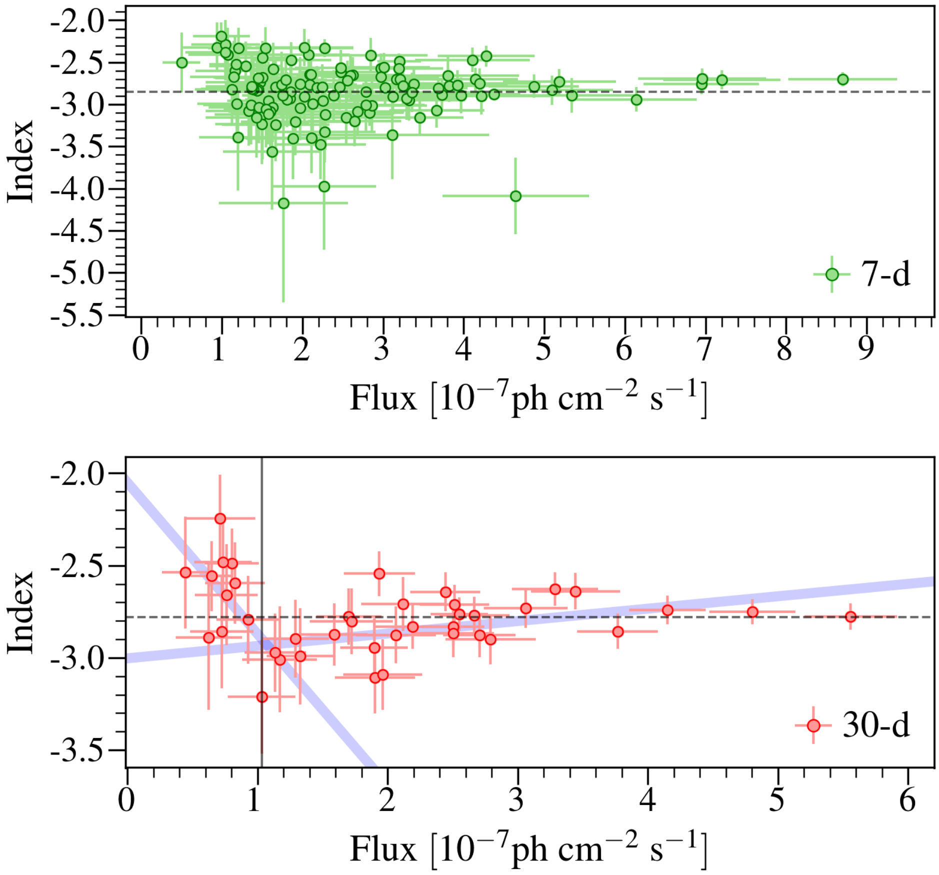

**Figure 4.3.** Photon index vs. flux for the weekly binned (*top*) and monthly binned (*bottom*) $\gamma$-ray light curves. The dashed lines indicate the average photon index values. The vertical solid line in the bottom panel marks a break flux value of $1.03 \times 10^{-7}$ ph cm$^{-2}$ s$^{-1}$. The light blue lines show the linear regression lines for photon indices above and below the break flux.

TS. Furthermore, the quality of the BU data obtained on 2016 October 6 is rather poor because two VLBA antennas were not available. We therefore focus on the 2016A and 2017A $\gamma$-ray outbursts in our further analysis.

### 4.3.2 Photon indices from weekly and monthly $\gamma$-ray light curves

In Figure 4.3 we present the photon indices derived from the LAT light curves (see Section 4.2.1 for details) as a function of $\gamma$-ray flux. The indices range from $-4.5$ to $-2.0$ for weekly binning, and from −3.5 to −2.0 for monthly binning. Their averages are −2.85 and −2.78, respectively. We do not see any correlations (i.e., softer-when-brighter or harder-when-brighter trends) for the weekly $\gamma$-ray fluxes. However, simple visual inspection of the monthly data suggests different trends above and below a flux of about $1.03 \times 10^{-7}$ ph cm$^{-2}$ s$^{-1}$. For fluxes below the threshold, flux and photon index show a negative correlation with a Pearson coefficient of −0.49 at a confidence level of 87%; above the threshold, the correlation is positive, with a Pearson coefficient of 0.48 at a confidence level of 99%. Accordingly, the source appears to have been in a harder-when-brighter spectral state at $\gamma$-ray fluxes above $1.03 \times 10^{-7}$ ph cm$^{-2}$ s$^{-1}$. There is also an indication of a softer-when-brighter trend at lower fluxes, but the confidence level is too low for us to conclude about this.

The evolution of the photon index with time during 2015–2019 is shown in Figure 4.4 using weekly and monthly binning. Overall, the uncertainties of the photon indices are too large for a meaningful quantitative analysis. We therefore limit ourselves to a qualitative discussion of potential patterns or trends in the data. There is an indication for gradual temporary increases of the monthly photon indices during the two $\gamma$-ray outbursts. The first hump spans ∼180 days (MJD: 57278–57458) with a peak value of −2.74 on MJD 57338, while the second hump spans ∼120 days (MJD: 57818–57938) with a peak value of −2.73 on MJD 57878. Interestingly, the 2016 $\gamma$-ray outburst lags the local peak of the first bump by about 44 days, whereas the 2017 outburst coincides with the local peak of the second hump. This might indicate that many regions emit in $\gamma$-rays in the jet, which would suggest that a first dissipation zone is responsible for these local peaks.

The weekly indices seem to be fluctuating randomly without showing any noteworthy trends throughout our observations. We attribute this to the combination of typically modest variations in the spectral index (e.g., Abdo et al. 2010a; Lisakov et al. 2017) and low-photon-number statistics, which causes a substantial scattering of the photon index values (Nandikotkur et al. 2007; Rani et al. 2013b). The photon statistics improves with stronger source activity (e.g., Paliya 2015). However, 3C 273 was relatively weak during 2015–2019 (cf. Section 4.3.1). Nandikotkur et al. (2007) found that binning data into longer time intervals can reduce the large error bars of the spectral index values. Thus, the monthly indices arguably describes the $\gamma$-ray

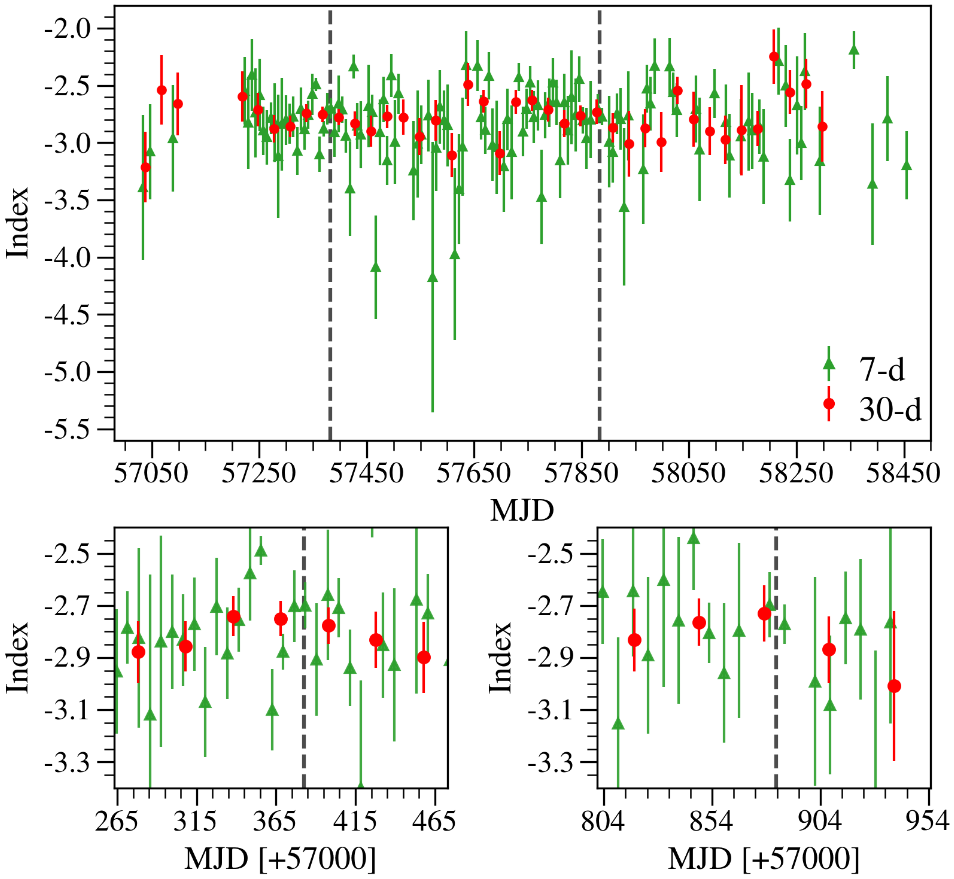

**Figure 4.4.** Photon index vs. time of the weekly and monthly $\gamma$-rays. The *top* panel shows the entire time range of our observations. The *bottom* panels provide zoomed-in views on the data around the times of the 2016A and 2017A $\gamma$-ray outbursts defined in Figure 4.2 (marked by vertical dashed lines). Error bars correspond to 1 $\sigma$ uncertainties.

spectral variations in our data better than the weekly indices.

### 4.3.3 Correlation between the radio and $\gamma$-ray light curves

We employed the discrete correlation function (DCF; Edelson & Krolik 1988) to investigate the relationship between $\gamma$-ray and radio emission. The average sampling interval for the ALMA light curve is ~9.8 days. When we disregard the upper limits, the average sampling intervals of the weekly and monthly $\gamma$-ray light curves are ~11.7 and ~32.3 days, respectively. We there-

Table 4.1. Results of our correlation analysis for the 2015–2019 data.

| Parameter | LAT 7d vs. ALMA | LAT 30d vs. ALMA |
|---|---|---|
| $a^1$ | $0.57 \pm 0.03$ | $0.79 \pm 0.08$ |
| $c$ (days) | $-105 \pm 4$ | $-112 \pm 6$ |
| \|w\| (days) | $70 \pm 4$ | $70 \pm 6$ |
| $r_p$ | 0.48 | 0.67 |
| $p_p$ (%) | $> 99.99$ | $> 99.99$ |

Note. — [1] Amplitude of the DCF curve.

fore used time steps of 12 and 33 days for the DCF analysis for the weekly and monthly binned $\gamma$-ray fluxes, respectively. To determine the height and location of a DCF peak, we fit a Gaussian function defined as $DCF(t) = a \times \exp\left[-(t-c)^2/2w^2\right]$ to the DCF curve, with $a$ being the amplitude, $c$ the time lag, and $w$ the width of the Gaussian profile. The statistical significance of the correlation was calculated following Rani et al. (2013a) by calculating the Pearson correlation coefficient for the ALMA data and LAT data and its uncertainty after applying the time shift derived from the Gaussian fit to the DCF curve.

The results of the correlation analysis are shown in Figure 4.5 and summarized in Table 4.1. The Gaussian fits to the DCF curves find time delays of $-105 \pm 4$ and $-112 \pm 6$ days ($\gamma$-ray leading) for the weekly and monthly binned $\gamma$-ray light curves, respectively. These estimates are consistent with each other within the errors. We note that the location of the DCF peak varies considerably (with a standard deviation of $\sim$12.5 days) when different time-delay bins are used to calculate the DCF for the weekly and monthly $\gamma$-ray fluxes. However, the time delays found from the Gaussian fits are only weakly affected by the binning of the DCF (with a standard deviation of $\sim$0.9 days). When we apply the best-fit delays, the Pearson correlation analysis resulted in coefficient values of 0.67 for the pair with the monthly $\gamma$-ray fluxes and 0.48 for the pair with the weekly $\gamma$-ray fluxes at significance levels of $> 99\%$ for both (see

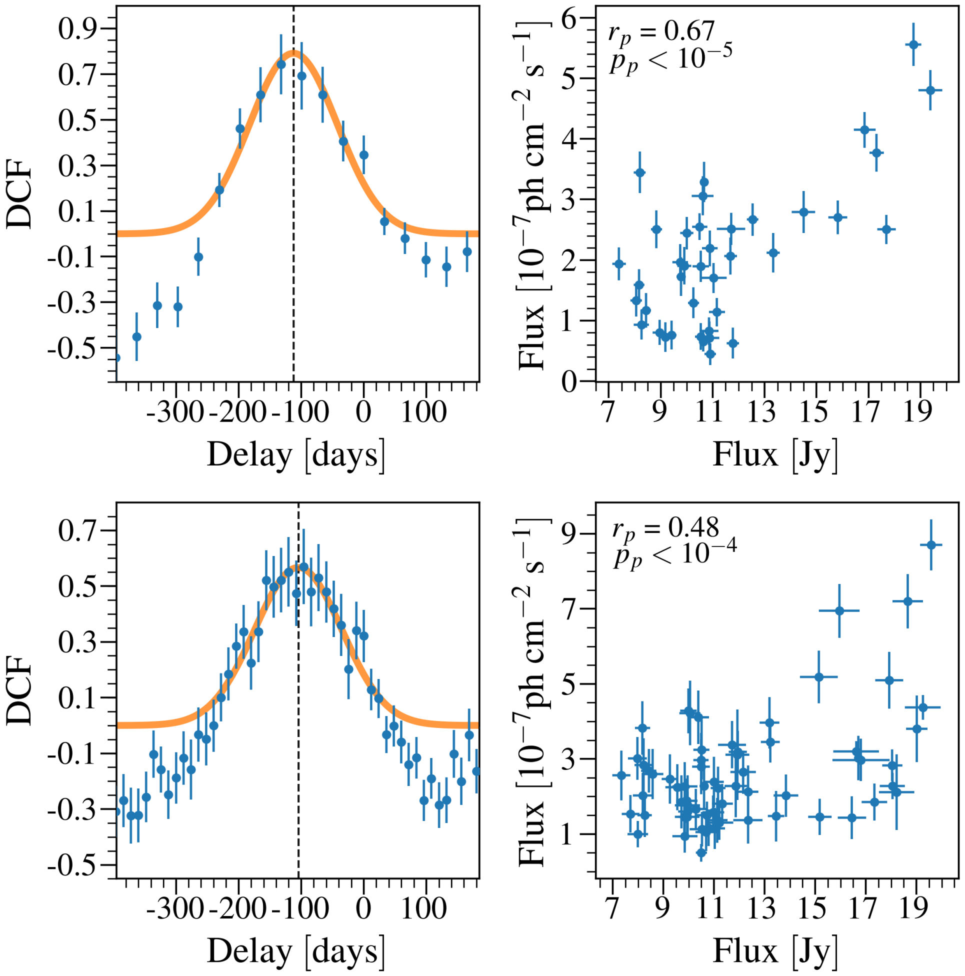

**Figure 4.5.** DCF curves and flux–flux plots comparing the 3 mm radio and $\gamma$-ray light curves in 2015–2019 for the monthly $\gamma$-ray fluxes (*top panels*) and the weekly $\gamma$-ray fluxes (*bottom panels*). Orange curves in the left panels indicate the best Gaussian fits to the DCF curves. For the flux-flux plots (right panels), the ALMA light curve has been shifted in time by the delays found from the Gaussian fits. The Pearson correlation coefficients ($r_p$) and corresponding $p$-values ($p_p$) are shown in the flux-flux plots.

Figure 4.5).

Simple visual inspection of Figure 4.1 caused us to suspect that the DCF is dominated by data from the time range 2015–2017. We therefore repeated our correlation analysis using the parts of the light curves in that time range (see Figure 4.6). We used the weekly $\gamma$-ray light

Table 4.2. Results of our correlation analysis for the 2015–2017 data.

| Parameter | LAT 7d vs. ALMA |
|---|---|
| $a$ | $0.66 \pm 0.05$ |
| $c$ (days) | $-107 \pm 5$ |
| \|w\| (days) | $57 \pm 5$ |
| $r_p$ | 0.57 |
| $p_p$ (%) | 99.98 |

curve, which includes the fine structure of the flares and is sampled about as densely as the ALMA fluxes. We find a clear correlation comparable to the results in Table 4.1, which confirms the initial impression that the major $\gamma$-ray and radio flares in 2015–2017 dominate the correlation between the full (2015–2019) light curves. The results of the analysis are summarized in Table 4.2. We also checked the 2017–2019 data, but found the DCF to be consistent with random fluctuations.

### 4.3.4 Parsec-scale jet near the 43 GHz core

We investigated the parsec-scale jet of 3C 273 during times of elevated $\gamma$-ray and radio band activity using VLBA maps. Considering the time-lags between $\gamma$-ray and radio fluxes, we chose two sets of VLBA-BU-BLAZAR observations that span about four months after each $\gamma$-ray outburst, shown in Figure 4.7 and 4.8. All maps are aligned at the position of the core, which is taken to be the upstream end of the jet. In each data set, the structure of the jet was represented by a number of two-dimensional circular Gaussians fitted to the visibility domain. The resultant models consist of 7–10 components whose parameters are summarized in Appendix A.1. We found three stationary features: the core, and two additional components labeled $S1$ and $S2$, which have been identified in a previous study (i.e., Lisakov et al. 2017), with $S1$ and $S2$ located at about 0.16 and 0.33 mas from the core, respectively.

Figure 4.7 and 4.8 shows a spatial displacement of the 7 mm emission during the two $\gamma$-ray

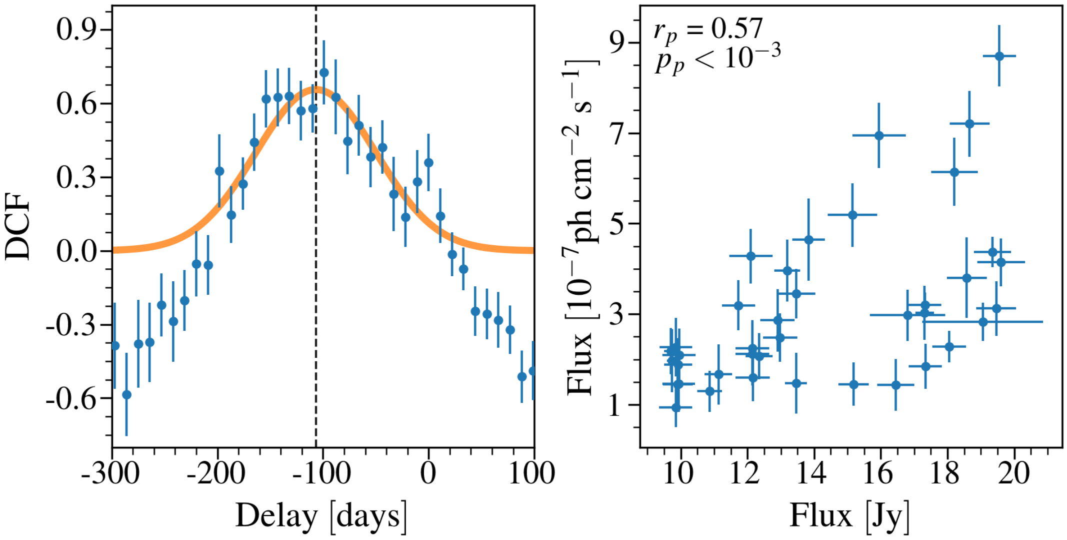

**Figure 4.6.** Same as Figure 4.5, but using only the weekly $\gamma$-ray fluxes in the time range 2015–2017.

outbursts. The sequence of maps in Figure 4.7 begins on MJD 57361. The second epoch is just 6 days after the 2016 $\gamma$-ray outburst. In this epoch, the total intensity peak is located at the $S1$ position. Then, the peak moves down to the $S2$ position on MJD 57501 and increases its intensity to ∼9 Jy/beam. The proper motion of this displacement is about 0.59 mas/year, which corresponds to an apparent speed of ∼6.0 $c$ (with $c$ being the speed of light). Interestingly, a displacement of the emission peak like this is also observed for the 2017 $\gamma$-ray outburst, but it is weaker. In Figure 4.8, the initial position on MJD 57859 of the peak intensity coincides with the core. Then, until MJD 57886, which is 3 days after the 2017 $\gamma$-ray outburst, it moves downstream to a location between the core and $S1$. The further motion of the emission peak cannot be clearly recognized until MJD 57937, when the flux increases to ∼4.8 Jy/beam. At this time, both the core and $S1$ have became simultaneously brighter. On MJD 57971, the flux peak is localized at the position of $S1$ and shows a decrease in total intensity. This corresponds to a proper motion of about 0.37 mas/year, translating into an apparent speed of ∼3.8 $c$. The proper motions are consistent with the radial speeds of the newborn components reported in Lisakov et al. (2017).

Figure 4.9 shows the fluxes and distances from the core as function of time for the core, $S1$,

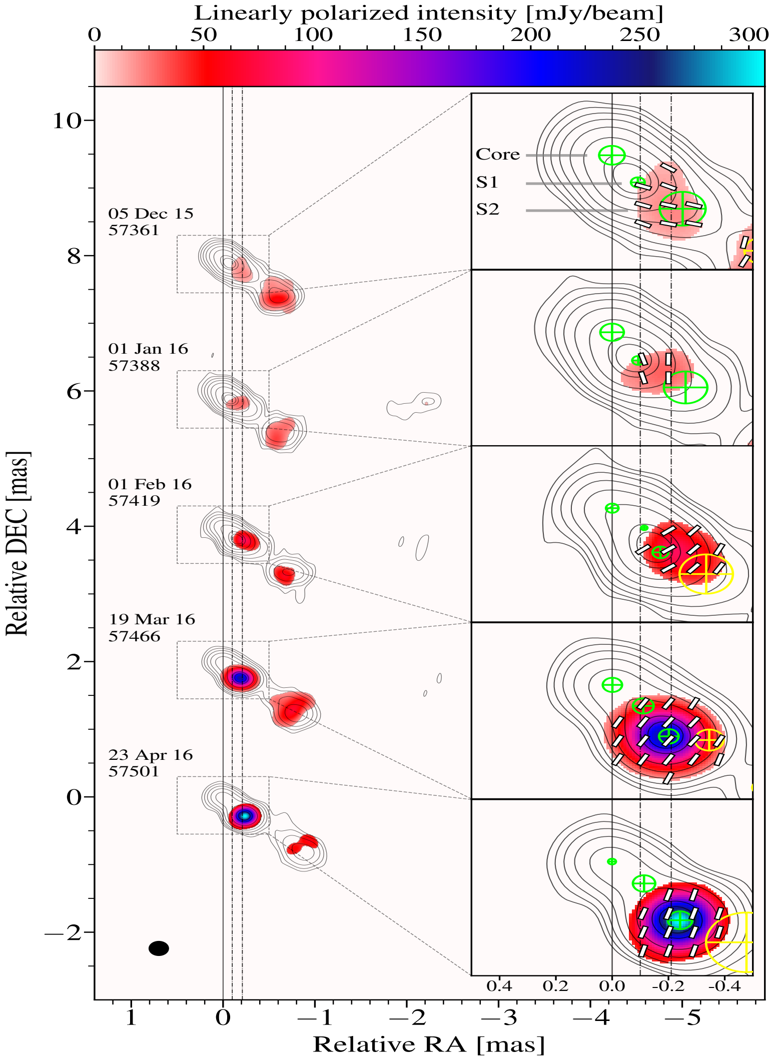

**Figure 4.7.** 7 mm VLBA images of 3C 273 during the 2016 $\gamma$-ray outburst. The contours and color scale represent the total intensity and linearly polarized intensity, respectively. Contour levels are 1%, 2%, 4%, 8%, etc., 64%, 80% of the peak intensity. A zoomed-in view on the core region is provided in the subplots. White line segments indicate the EVPA directions uncorrected for Faraday rotation. Circular Gaussian jet components are indicated by green (for the three stationary components) and yellow (for the others) cirles with a cross. The vertical dot-dashed lines show the average positions of the $S1$ (=0.1 mas) and $S2$ (=0.21 mas) components projected onto the $x$-axis. The vertical solid line indicates the core position. All maps are restored with a 0.2×0.2 mas beam (indicated at the bottom left).

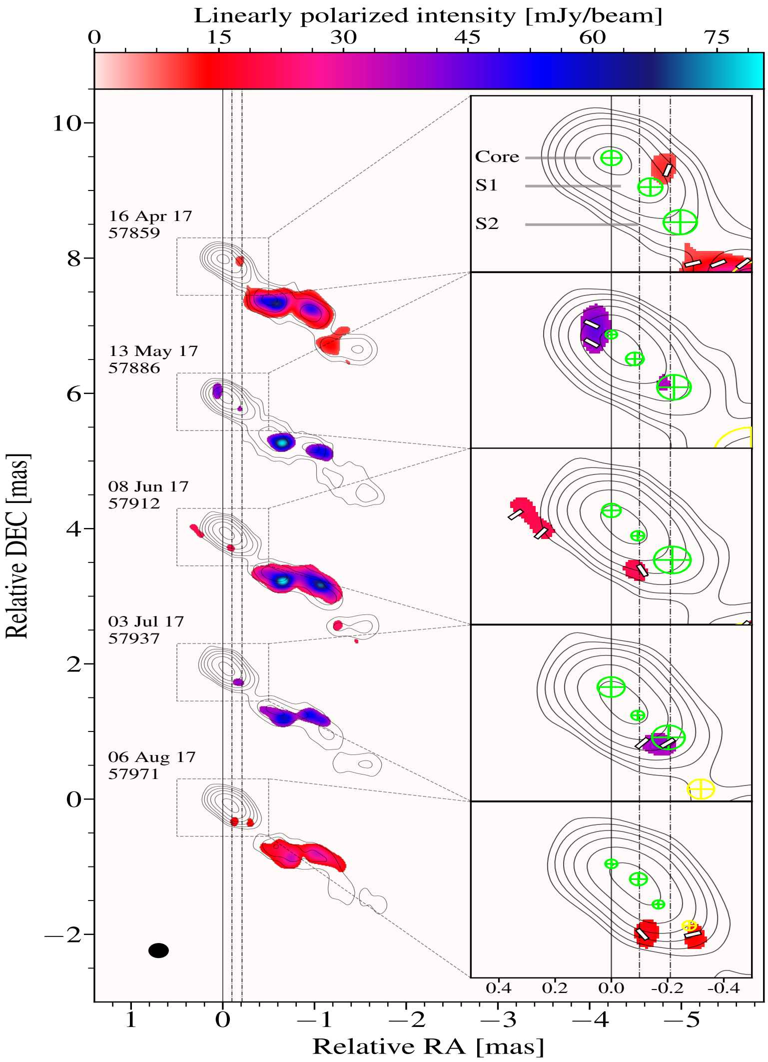

**Figure 4.8.** Same as in Figure 4.7, but for the 2017 $\gamma$-ray outburst. Contour levels are 2.5%, 5%, 10%, etc., 40%, 80% of the peak intensity.

and $S2$ as determined from the VLBA data. The $S1$ flux peaks almost simultaneously with the 2016 $\gamma$-ray outburst. The flux of $S2$ increases rapidly, by a factor of 10, just after the 2016 $\gamma$-ray outburst. The core remains quiescent. The 2017 $\gamma$-ray outburst coincides with the rise of a flare of $S1$. In addition, the core fluxes during the first two epochs (i.e., MJD 57859 and 57886) are consistent with each other within the errors, but increase rapidly thereafter. This suggests that the 2017 $\gamma$-ray outburst also coincides with the onset of the core flare. This connection can also be made for $\gamma$-ray outburst and the $S2$ flare in 2016. Notably, $S2$ doubles its flux in a month until MJD 57971. As evident in Figures 4.7 and 4.8, the positions of the presumably stationary components show some variation in both epochs we studied. $S2$ moved toward the core from MJD 57388 to 57419 by about ~0.1 mas, accompanied by a rapid increase in its flux. $S2$ then slowly returned to its initial core distance. In the 2017 observations, we note a tendency for both $S1$ and $S2$ to move toward the core. In general, $S1$ moves less than $S2$.

Because the combined total flux density of the core, $S1$, and $S2$ components dominate the millimeter-wavelength emission of 3C 273, we can conclude that the two radio flares and the $\gamma$-ray production occur in this region of the jet. We note that $S2$ is responsible for the major ALMA flare (peaking on MJD 57474). We suggest that the subflare (peaking on MJD 57408) within the major ALMA flare might be associated with the activity in $S1$. For the second ALMA flare (around MJD 57888), associated with the 2017 $\gamma$-ray outburst, both the core and $S1$ contribute equally.

### 4.3.5 Polarization

Figures 4.7 and 4.8 present distributions of the linearly polarized intensity overlaid on the total intensity contours. We only mapped out polarized emission that exceeded a conservative significance threshold of $9\,\sigma$. In the core region, the polarized emission is weak and only observed in a single epoch (MJD 57886), which is consistent with other studies (i.e., Attridge et al. 2005; Jorstad et al. 2005). In the 2016 observations, we find a polarized knot that is spatially connected to $S1$ and $S2$ and shows systematic variations in position and intensity. Just after the 2016 $\gamma$-ray outburst (MJD 57388), the polarized knot appears to encounter $S2$ while still covering the $S1$ region. It then appears to pass through the $S2$ region (MJD 57419) while showing an increase in polarized intensity. This suggests that the emergence of the polarized knot precedes the total intensity peak, which leads us to the conclusion that we observe the downstream propagation of a disturbance in both total and polarized intensity. The polarized intensity peaks in the time from MJD 57466 to 57501 at ~300 mJy in the $S2$ region.

In 2017, the polarized emission is weaker and shows a more complicated structure. We detect a polarized knot upstream of the core on MJD 57886, immediately after the 2017 $\gamma$-

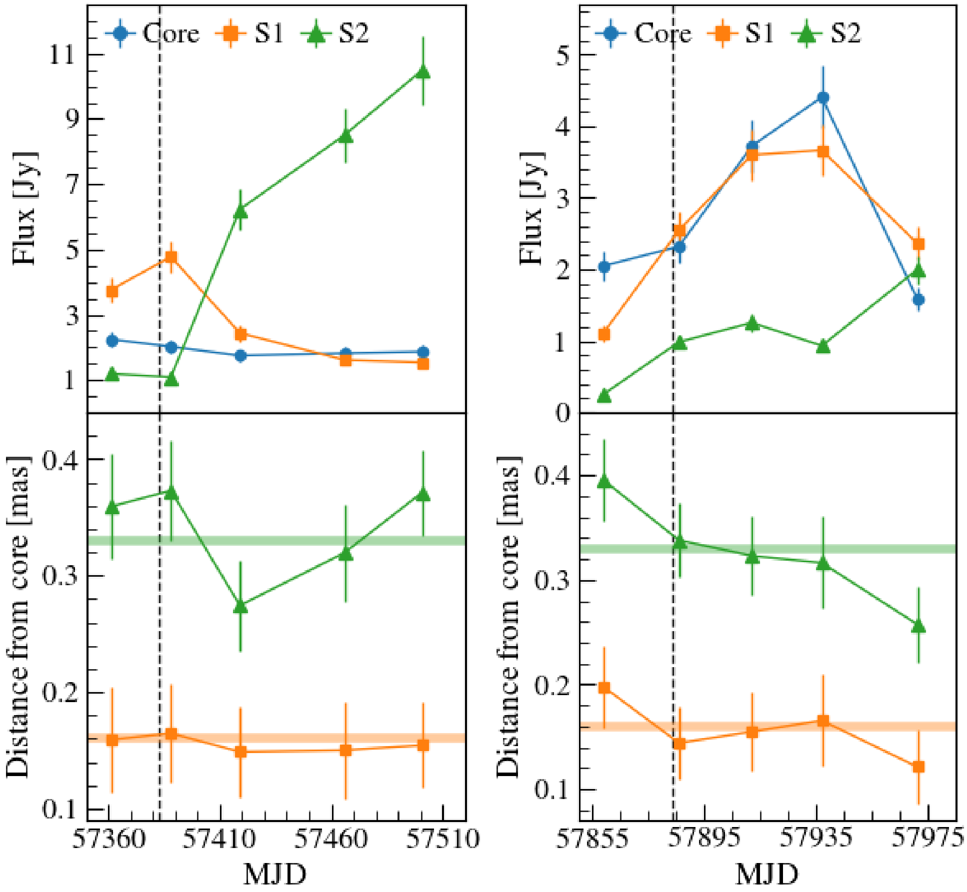

**Figure 4.9.** *Left:* Flux density (*top*) and distance from the core (*bottom*) of the core, $S1$, and $S2$ derived from Gaussian modeling of the jet components as shown in Figure 4.7. *Right:* Same as the left panels, but for the observations in Figure 4.8. The vertical dashed lines correspond to the times of the 2016 and 2017 $\gamma$-ray outbursts. The average distances of $S1$ and $S2$ (i.e., 0.16 and 0.33 mas from the core) are indicated by the horizontal solid lines.

ray outburst. It disappears before the following observations. This behavior might indicate an energetic physical process (e.g., acceleration) that occurs upstream of the core, thus suggesting an association between the millimeter-wavelength core and the high-energy emission. Weak polarization is detected around $S2$ at two epochs (MJD 57886 and 57937), probably implying physical or geometrical changes in that region.

## 4.4 Discussion

### 4.4.1 Positional variations of the stationary components

The 7 mm VLBA observations reveal two stationary components in the jet of 3C 273, $S1$ and $S2$, which have been reported before by Lisakov et al. (2017). These features are thought to be multiple recollimation shocks (RCS) that have been predicted by relativistic magnetohydrodynamics (MHD) simulations (e.g., Gómez et al. 1995; Mizuno et al. 2015). We found a wiggling (up- and downstream) motion of $S2$ (see also Figure 2 of Lisakov et al. 2017, for a similar pattern). $S2$ moved toward the core (inward motion) by about ~0.1 mas from MJD 57388 to 57419 while increasing its flux. It then shifted downstream back to its original position (see Figure 4.9). Because a new moving knot ($J1$, which appeared on MJD 57419) was passing through the $S2$ region in MJD 57388, both components can appear blended into a single feature, leading to a shift of the centroid downstream of the initial position of $S2$. After the passage, the two components appear to split, resulting in an apparent inward motion of $S2$. The apparent displacement of a stationary jet component matches the signature expected for an RCS zone breakout (e.g., Abeysekara et al. 2018). When a moving blob with high kinetic energy starts interacting with the standing RCS localized in the region where the magnetic field becomes unstable, there could be (1) an enhancement of nonthermal emission, (2) a strong instability of the magnetic field configuration (e.g., tearing instability; Del Zanna et al. 2016), and (3) a positional displacement by the underlying flow with increasing kinetic power of the jet (Hervet et al. 2016). This scenario also predicts some fast $\gamma$-ray emission induced by magnetic reconnection, but the observed photon indices around MJD 57405 in Figure 4.2 appear too soft (Ding et al. 2019). A more conventional interpretation for the $S2$ motions would be an opacity effect (e.g., Lobanov 1998b). Variations in opacity can occur when flaring components pass through these regions (e.g., Plavin et al. 2019), resulting in an apparent spatial drift.

Yet another possible explanation for the apparent motion of $S2$ in 2016 is the so-called core shuttle effect. Changes in the physical state, and thus in the opacity of the core, that are due to a propagating disturbance may cause a wiggling of the core position. However, the core was in a quiescent state during the time of the $S2$ motion, implying the absence of newly formed jet components. Moreover, a core shuttle should also affect the separation of $S1$ from the core, which is not observed. In 2017, however, a core shuttle might have affected the separations of both $S1$ and $S2$ from the core, which changed simultaneously (see Figure 4.9) and coincided with an increase in the flux density of the core.

### 4.4.2 2016 $\gamma$-ray outburst

Our VLBA analysis in Sections 4.3.4 and 4.3.5 found that the millimeter-wavelength activity in 3C 273 is confined to the most upstream few parsecs of the jet. For the 2016 $\gamma$-ray outburst, the flaring of the stationary components $S1$ and $S2$ strongly suggests that the $\gamma$-ray outburst has a physical connection with these regions. This is further supported by the clear $\gamma$-ray and radio correlation, which can be attributed to the major ALMA flare close to the 2016 $\gamma$-ray outburst (see also Meyer et al. 2019, for their LCCF result on 3C 273). Moreover, the contemporaneous displacements of the total intensity peak and the polarized knot indicate that a moving disturbance played an important role in producing the high-energy emission.

Many studies have reported the connection between parsec-scale radio jets and $\gamma$-ray outbursts: $\gamma$-ray outbursts tend to be accompanied by radio flares and strongly polarized jet features (Agudo et al. 2011a; Jorstad et al. 2013; Wehrle et al. 2016; Kim et al. 2018b; Park et al. 2019b). In our case, an obvious connection is provided by the contemporaneous flares in $\gamma$-ray and radio bands. Based on the timing of its radio variability, we can regard $S1$ as the place of origin of the 2016 $\gamma$-ray outburst. When we consider the sampling interval of the VLBA observations (i.e., ~30 days), the $S1$ flare clearly coincides with the $\gamma$-ray outburst, implying a cospatial emission region. Such an event can be caused by the passage of a powerful disturbance through a standing feature, which is visually confirmed in Figure 4.7. We provide the source-frame brightness temperatures for each stationary component in Figure 4.10. Clearly, $S1$ reaches $2.3 \times 10^{12}$ K, which implies that particle energy dominated during the $\gamma$-ray outburst. This strengthens the argument that $S1$ is responsible for the $\gamma$-ray outburst. The plasma in the region of the standing shock is likely to be turbulent (Marscher 2016). In this case, particles in $S1$ can be accelerated by second-order Fermi acceleration (e.g., Asano et al. 2014) and/or magnetic reconnections (e.g., Sironi & Spitkovsky 2014) in disordered magnetic fields.

A moving shock is able to further compress and energize the already excited particles, thus producing strong $\gamma$-ray emission.

However, we cannot rule out the possibility that $S2$ is responsible for the 2016 $\gamma$-ray outburst. A polarized knot that enters the $S2$ region is detected just after the $\gamma$-ray outburst. This might be attributed to a shock interaction between $S2$ and a disturbance, which would cause a $\gamma$-ray flare in $S2$ (e.g., Agudo et al. 2011a; see also Hughes 2005, for a discussion of plasma compression resulting in magnetic field enhancement). Such a scenario is natural as the disturbance continues to travel along the jet. However, we noted several interesting phenomena accompanying this particular disturbance. From MJD 57388 to 57419, the total intensity peak and the polarized knot propagated downstream simultaneously but were located at different positions. Subsequently, the strong radio flare occurred in $S2$, which dominates the estimate for the $\gamma$-ray to radio time delay of $\sim$100 days. Taken together, the observations suggest a large size of the emitting blob (e.g., Lisakov et al. 2017). It has been suggested that the high-energy electrons can be confined to a narrow and thin region of a shock front (Wehrle et al. 2012; Marscher 2014). As the moving blob begins to interact with $S2$, a strong $\gamma$-ray emission could have occurred in the shock front, which is the injection site (e.g., Agudo et al. 2011b). The strong $S2$ flare reaching up to $\approx$10.5 Jy is remarkable. During the passage of a disturbance in the $S2$ region, the increase in particle density and/or magnetic field strength appears to be huge and might have caused a temporary change of the opacity in the shocked region (e.g., Kravchenko et al. 2016). Lisakov et al. (2017) found that one of the flares in the 43 GHz core (event $B_7$ in their nomenclature) peaked when it reached its most downstream position. We find such a pattern for $S2$ in Figure 4.7 (i.e., from MJD 57419 to 57501). This is indicates that $S2$, like the core, is indeed a recollimation shock.

The association of the $\gamma$-ray emission with the $S1$ or $S2$ regions in the jet ($\geq 10^4\ R_s$) disfavors the BLR as the source of seed photons. At the distances of $S1$ and $S2$, the BLR is not thought to be an effective source of seed photons for IC scattering unless the BLR is more extended than expected (León-Tavares et al. 2013). Recent studies found indications that the majority of $\gamma$-ray bright Flat-Spectrum Radio Quasars (FSRQs) radiate $\gamma$-rays beyond the BLR region. This supports the parsec-scale scenario (Costamante et al. 2018; Meyer et al. 2019).

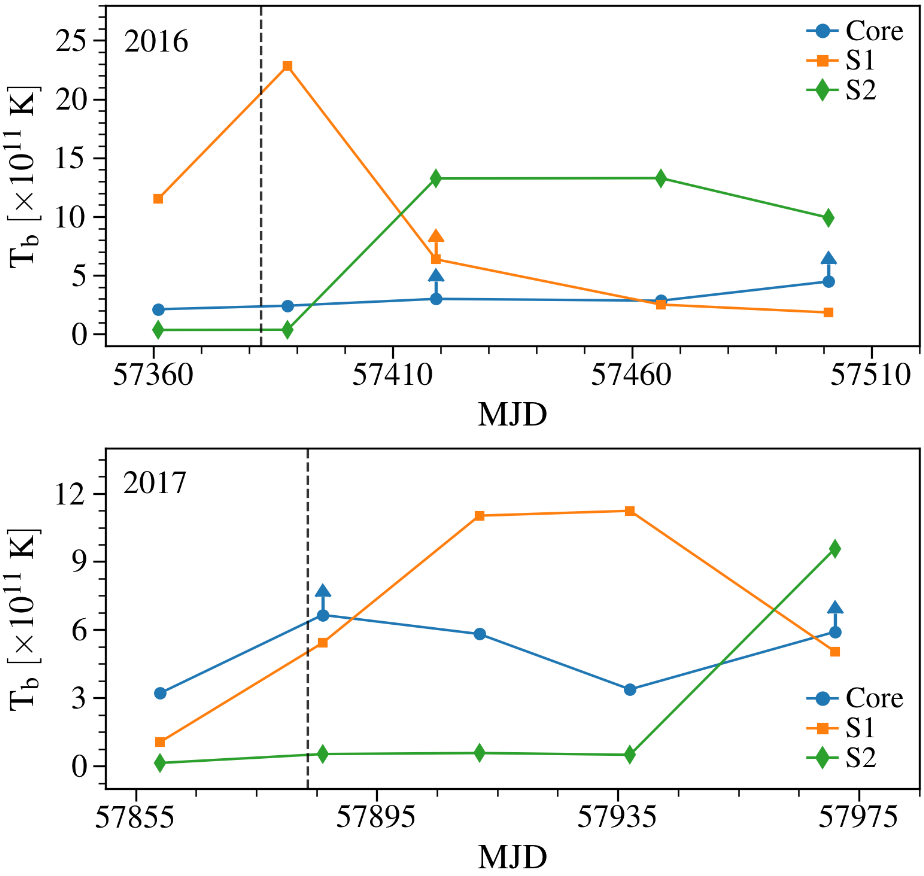

**Figure 4.10.** Source-frame brightness temperatures ($T_b$) of the core, $S1$, and $S2$. Vertical dashed lines indicate the times of the $\gamma$-ray outbursts. Upward arrows mark limits on $T_b$, calculated using the spatial resolution limit for each component whenever the observed size is smaller than this limit.

Dotson et al. (2012) suggested energy-dependent cooling times for $\gamma$-ray emission produced through infrared (IR) seed photons from the dusty torus. Inverse Compton scattering of IR seed photons occurs in the Thomson regime, whereas the Klein−Nishina regime is relevant for higher-energy seed photons (e.g., UV photons from the BLR region), resulting in energy-independent cooling times (see Blumenthal & Gould 1970). We tried to test this theory by using $\gamma$-ray data binned into very short intervals (e.g., 3 hours). However, insufficient photon statistics prevented the creation of meaningful $\gamma$-ray light curves. More powerful flares or brighter blazars might be suitable for such an analysis. Lower-energy seed photons could originate from the dusty torus or the jet itself (e.g., Marscher et al. 2010; Wehrle et al. 2016; see also Banasiński & Bednarek 2018, for discussion of another emitting blob in the jet that provides seed photons).

### 4.4.3 2017 $\gamma$-ray outburst

We found a fast and short $\gamma$-ray outburst on MJD 57883 (see Figure 4.2). The contemporaneous radio flaring activity in both the core and $S1$ makes it difficult to interpret the $\gamma$-ray outburst, however. The total intensity radio maps obtained just after the $\gamma$-ray outburst suggest a strong disturbance that is localized between the core and $S1$. As discussed before, we assumed that the core was in the onset of its flare while $S1$ was already in the middle of its flare at the time of the $\gamma$-ray outburst. This can be explained by several moving disturbances. The polarization image of the jet observed in MJD 57886 shows a weak polarized knot near the core, which indicates the emergence of a new disturbance. We therefore considered two propagating disturbances around the time of the $\gamma$-ray outburst: one interacting with the core ($K1$), and one interacting with $S1$ ($K2$). This picture is consistent with the jet features observed on MJD 57971: (1) for $K1$, the total intensity peak located at $S1$, and (2) for $K2$, the enhanced flux of $S2$. An increasing trend in the core size from MJD 57886 to 57937 might further support the presence of $K1$.

Figure 4.2 shows that the 2017 $\gamma$-ray outburst lasted for a short time (probably less than a day), very different from the 2016 outburst. The short timescale suggests a small emitting region (e.g., Petropoulou & Dimitrakoudis 2015), implying a region in the jet located closer to the central engine (Tavecchio et al. 2010). The relatively low apparent component speeds around the $\gamma$-ray outburst further support this idea (Rani et al. 2018). We also note that the $\gamma$-ray outburst triggered a millimeter-wavelength flare in the core that might have been accompanied by the emergence of a polarized knot nearby. The core is therefore likely to be responsible for the $\gamma$-ray outburst. A timing of events like this ($\gamma$-ray outbursts occurring at the very beginning of a radio flare) is common in blazars (e.g., Marscher 2016; Lisakov et al. 2017). The $\gamma$-ray outburst could have been caused by the interaction of the standing shock and a strong disturbance (i.e.,

$K1$) propagating down the jet, in the same manner as explained in Section 4.4.2. In addition, the brightness temperature of the core peaks at the time of the $\gamma$-ray outburst, which further supports this scenario.

It is worth noting that there seems to be a discrepancy in position between the polarized knot and the core component. This might be due to variable opacity in the core region (e.g., Lisakov et al. 2017), when the core region temporarily becomes partially optically thin. The 3 mm to 7 mm spectral index indeed varied rapidly around the time of the $\gamma$-ray outburst (see Figure 4.1). When we modeled the minor ALMA flare that is associated with the $\gamma$-ray outburst as a combination of an exponentially rising and an exponentially declining part, we found a 3 mm peak at MJD 57897±7 (see Figure 4.11). This corresponds to a time delay of

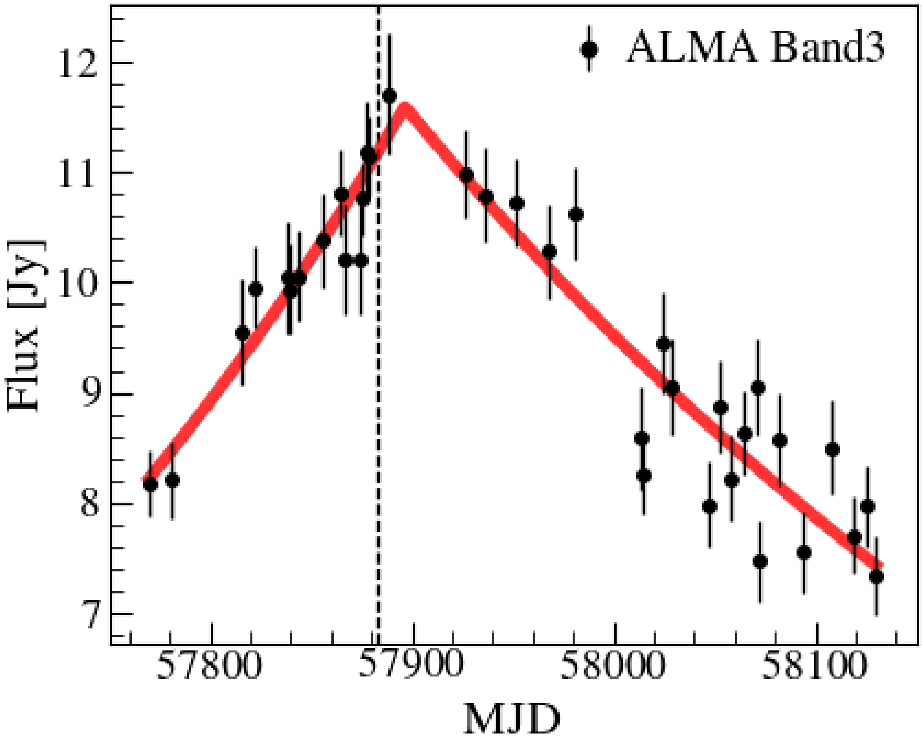

**Figure 4.11.** 3 mm ALMA light curve around the time of the 2017 $\gamma$-ray outburst (vertical dashed line). The model that combines an exponential rise with a subsequent exponential decay (as introduced by Valtaoja et al. 1999, but without fixing the decay timescale) is indicated by the red curve.

about 40 days relative to the 7 mm core flare observed on MJD 57937. The nonzero time lag implies optically thick emission, but the source of the ALMA flare is unknown (i.e., between the core, $S1$, and $S2$). Nevertheless, this is relevant with respect to the result of Chidiac et al. (2016), who found a time delay of ∼50 days between the 43 and 230 GHz light curves of 3C 273. In short, we are not able to determine the opacity condition in the core during the $\gamma$-ray outburst.

In the conventional view, the core shift might play a role, although it is expected to occur at very small submilliarcsec scales at wavelengths below 7 mm (Vol'vach et al. 2013; Lisakov et al. 2017). Interestingly, the 2017 $\gamma$-ray outburst coincides with not only the onset of the 7 mm flare in the core, but also with the peak of the 3 mm flare at the same time. Thus, we suggest that a moving blob (i.e., $K1$) started to interact with the 7 mm core, while the blob (probably its tail part) still passed through the 3 mm core. This scenario could explain the polarized feature that appeared on MJD 57886 upstream from the 7 mm core. Furthermore, a passage of $K1$ through the 3 mm core can explain the contemporaneous $\gamma$-ray and 3 mm flares (e.g., Jorstad et al. 2013; Wehrle et al. 2016). Based on our observations of the $\gamma$-ray outburst, however, we cannot definitively locate the origin of the $\gamma$-ray outburst between the 3 and 7 mm core. When the millimeter-wavelength core is considered the $\gamma$-ray production site, IR emission from the dusty torus (e.g., Marscher 2014), stationary knots (e.g., Wehrle et al. 2016), or from the jet sheath are candidate sources of seed photons, as discussed in the previous section.

### 4.4.4 $\gamma$-ray spectra

Overall, spectral index values around −2.8 (Figure 4.3) are close to the value reported in Harris et al. (2012). The typical photon indices of $\gamma$-ray bright FSRQs, which are around −2.4, mean that 3C 273 shows a softer photon index, however (see Harris et al. 2012; Linford et al. 2012). Although 3C 273 was less $\gamma$-ray bright than these extreme FSRQs (e.g., 3C 279 and 3C 454.3), it seems that the difference in photon index values is a sign of different source physics, like a spectral break or additional emitting components (Harris et al. 2012; H.E.S.S Collaboration et al. 2018; see also Costamante et al. 2018, for the exception of 3C 273 at constraining high/low states). We also note that our parsec-scale scenario supports what Harris et al. (2012) reported:

$\gamma$-ray absorption by BLR photons is disfavored in $\gamma$-ray bright FSRQs.

$\gamma$-ray outbursts, accompanied by variability of the $\gamma$-ray spectral index, have been reported in many previous studies (Rani et al. 2013b, 2018; Kim et al. 2018b; Ding et al. 2019). The usual combination is an increase in $\gamma$-ray flux density and hardening of photon indices. Unfortunately, we are not able to draw a clear quantitative conclusion from our data becuase the photon statistics are insufficient. However, a simple visual inspection of the monthly binned photon indices in Figure 4.4 suggests such an evolution for both the 2016 and 2017 $\gamma$-ray outbursts. The peak of the 2016 $\gamma$-ray outburst lags a local maximum in the spectral index time series on MJD 57338 by about 40 days, whereas the $\gamma$-ray peak of the 2017 outburst coincides with a local photon index peak on MJD 57878. If we identify each of the local photon index peaks with the first shock interaction between a strong disturbance propagating down the jet and the millimeter-wave core, we can make a smooth connection to our parsec-scale scenario for both $\gamma$-ray outbursts.

The overall spectral behavior of the monthly binned $\gamma$-rays shown in Figure 4.3 indicates a transition from a softer-when-brighter state to a harder-when-brighter state at a critical $\gamma$-ray flux of around $1.03 \times 10^{-7}\,\mathrm{ph\,cm^{-2}\,s^{-1}}$, but the softer-when-brighter trend is only marginally significant (see also Abdo et al. 2010b; Paliya 2015; Kim et al. 2018b, for similar trends in other sources). This transition can be explained by a balance between acceleration and cooling of relativistic particles, which in turn implies that cooling is dominant for the softer-when-brighter trend. This transition might also be related to a shift of the IC peak in the SED (Shah et al. 2019). As the source power increases during strong flares, the IC peak can be shifted to higher energies, which results in a harder-when-brighter trend.

## 4.5 Summary

The detailed analysis of the $\gamma$-ray and radio activity of the blazar 3C 273 during 2015–2019 enables us to address the nature of flaring activity and its connection to the parsec-scale jet. During our observations, 3C 273 experienced two significant $\gamma$-ray outbursts, accompanied by strong flaring activity at millimeter-wavelengths. We identified three quasi-stationary components in the compact inner region of the jet: the core, $S1$, and $S2$. These features are confirmed to be the main sources of the observed millimeter-wavelength emission, exhibiting powerful flaring variability. The joint analysis of the $\gamma$-ray and radio data revealed a strong correlation between the two energy regimes and provided strong evidence that the inner jet region is the production site of $\gamma$-ray emission. Overall, the observed behavior can be explained by a scenario in which the radio and $\gamma$-ray flares are produced in the core–$S\,1$–$S\,2$ region by moving disturbances and their interaction with the standing shocks. The emergence of notable polarized knots and high brightness temperatures (up to $\sim\ 10^{12}\,K$) around the times of the $\gamma$-ray outbursts further support this scenario. As the blob propagates down the jet, it causes changes in the physical conditions in the ambient flow, resulting in the observed spatial displacements of stationary components (the core and $S\,2$) and variations in spectral properties.

# Chapter 5

# Radio and $\gamma$-Ray Activity in The Jet of The Blazar S5 0716+714[1]

## Abstract

We explore the connection between the $\gamma$-ray and radio emission in the jet of the blazar 0716+714 by using 15, 37, and 230 GHz radio and 0.1-200 GeV $\gamma$-ray light curves spanning 10.5 years (2008–2019). We find significant positive and negative correlations of radio frequencies with those at $\gamma$-rays in different time ranges. The time delays of the correlations suggest that the observed $\gamma$-ray flares originated from multiple regions upstream of the radio core: from subparsec scales to a few parsecs from the central engine. From the kinematic analysis performed using the VLBA at 43 GHz, we identified 14 jet components moving downstream the jet. Their apparent speeds range from 6 to 26 $c$, showing notable variations in the position angle upstream the stationary component (~0.53 mas from the core). Variation in the brightness temperature along the jet follows a power-law, with changes in the exponent at the location of a stationary component. We also find that the periods of the significant correlations overlap with the time when the jet was oriented to the north. Our results indicate that the passage of the propagating disturbances (or shock) through the radio core and directionality of the jet might be responsible for the observed correlated behaviors between the radio and $\gamma$-ray variability.

---

[1] Under review by the *Astrophysical Journal*: Kim et al. 2021, ApJ, submitted

We suggest that the positive correlation and the unusual anti-correlation are connected to each other in a physical scenario describing the production of $\gamma$-ray flare and dip by a moving shock at different distance scales from the jet apex.

## 5.1 Introduction

S5 0716+714 (hereafter 0716+714) is one of the most active BL Lacertae objects that also shows intra-day variability (e.g. Liao et al. 2014). The early high angular resolution study performed with the Very Long Baseline Interferometry Space Observatory Program in 2000 (VSOP, Bach et al. 2006) located the short term variability of the blazar within the innermost 100 $\mu$as region near the radio core (surface of the optical depth $\tau_{\nu} \sim 1$). Later, on 2015 January 3-4, 0716+714 has been observed by the *RadioAstron* space VLBI mission (Kardashev et al. 2013). These observations, conducted at 22 GHz (Kravchenko et al. 2020), revealed complex structure within the inner 100 $\mu$as of the jet: the unresolved core with a size of $< 12 \times 5\,\mu$as extended toward the southeast, and then a change of the jet position angle by about 95° toward the northeast. A compact linearly polarized component is detected at a position of 58 $\mu$as downstream from the core, that might be associated with the stationary feature (Rani et al. 2015; Jorstad et al. 2017) which is considered to be a recollimation shock.

The observations provide an estimate of the 0716+714 jet viewing angle of $\leq 5^{\circ}$ (Bach et al. 2005; Hovatta et al. 2009; Jorstad et al. 2017), while a stacked-epoch analysis shows that the intrinsic opening angle of its outflow is about 2° (Pushkarev et al. 2017). Alongside the significant curvature in the innermost 100 $\mu$as (Kravchenko et al. 2020), this suggests that the blazar jet has been viewed at an angle smaller than the opening angle itself, i.e. directly inside the outflow.

Analysis of the correlation between multi-waveband emissions is crucial to explore the physics of the long-term flux variations such as the radiative processes and the location of the emission region (e.g., Liodakis et al. 2018b). Previous studies on 0716+714 revealed a tight correlation between optical and $\gamma$-ray bands (Larionov et al. 2013; Rani et al. 2013a; Ramakrishnan et al. 2016). Variability of the emission in 0716+714 at these frequencies usually occurs contemporaneously without significant time delays. Such tight correlation with the emission at lower frequencies supports the leptonic models for the observed flux variations (Mastichiadis & Kirk 1997; Li & Kusunose 2000; Böttcher & Chiang 2002). The connection becomes much more complicated with radio emission. It has been reported that the $\gamma$-rays show no significant correlation with the radio emission in the source (Max-Moerbeck et al. 2014a; Ramakrishnan et al. 2015). On the other hand, Rani et al. (2013a, 2014) reported not only significant correlations, but also anti-correlated behavior. Butuzova (2018) explains these changes from positive to negative correlations by a helical jet model of 0716+714, where quantities observed at different wavelengths form in spatially separated regions and at different fixed distances from the jet base. Moreover, different mechanisms might be responsible for the generation of high-energy emission in different locations along the jet. Alongside, as Ramakrishnan et al. (2015) noted, the rapid variability of 0716+714 complicates the study of the correlated behavior between different frequency bands. In this paper, we aim to further investigate the blazar's behavior at radio and gamma-ray bands and to pinpoint the site of their production in the jet.

This study was motivated by our preliminary results of a correlation analysis between 37 GHz radio and $\gamma$-ray light curves in 0716+714. The blazar 0716+714 is obviously an interesting target source with its extreme variability at both radio and $\gamma$-rays. The preliminary test indicated the presence of significant anti-correlations in this source, which is rare. Hence, we began a detailed study to explore this unusual phenomenon. 0716+714 has no spectroscopic redshift identification because of its featureless optical continuum and bright nucleus in the optical. Here we adopt the value of $z = 0.31 \pm 0.08$, derived from the photometric detection of the blazar's host galaxy (Nilsson et al. 2008), which is compatible with other estimates (Danforth et al. 2013; MAGIC Collaboration et al. 2018). Throughout the paper, we assume a flat $\Lambda$CDM cosmology with a matter density $\Omega_{\mathrm{m}} = 0.3$, cosmological constant $\Omega_{\Lambda} = 0.7$ and Hubble constant $H_0 = 70 \mathrm{km\ s^{-1} Mpc^{-1}}$, (Bennett et al. 2014; Planck Collaboration et al. 2016). This corresponds to a luminosity distance $D_{\mathrm{L}}$ of 1.6 Gpc and a scale of 4.56 pc per mas at the redshift of 0.31.

## 5.2 Observations

### 5.2.1 cm-wavelength data

We have used 15 GHz and 37 GHz continuum single-dish monitoring data from the Owens Valley Radio Observatory (Richards et al. 2011) and Metsähovi Radio Observatory operated by the Aalto University in Finland (Teraesranta et al. 1998), respectively. Interferometric multi-epoch observations were obtained through the VLBA-BU-BLAZAR monitoring program at 43 GHz (Jorstad et al. 2017).

### 5.2.2 SMA 230 GHz (1.3 mm)

The 230 GHz (1.3 mm) flux density data was obtained at the Submillimeter Array (SMA) near the summit of Mauna Kea (Hawaii). 0716+714 is included in an ongoing monitoring program at the SMA to determine the fluxes of compact extragalactic radio sources that can be used as calibrators at mm wavelengths (Gurwell et al. 2007). Available potential calibrators are from time to time observed for 3 to 5 minutes, and the measured source signal strength calibrated against known standards, typically solar system objects (Titan, Uranus, Neptune, or Callisto). Data from this program are updated regularly and are available at the SMA website[2].

### 5.2.3 $\gamma$-ray flux

Gamma-ray fluxes in the range of 0.1-200 GeV were obtained with the *Fermi*-LAT, compiling data from 2008 through the beginning of 2019. The analysis was done using the *Fermi* `Science Tools` software package[3] version v10r0p5 and Pass 8 data, including the instrument response functions gll_iem_v07 and the iso_P8R3_SOURCE_V2_v1 diffuse source models. LAT photon data were selected within a 15 degree radius centered on the source, using the `gtselect` tool with evclass of 128, evtype of 3 and maximum zenith angle of 90 degrees. Sources from the 4FGL catalog (Acero et al. 2015) with high test statistics (TS $\geq$ 25, Mattox et al. 1996) were used to generate the background source model. 0716+714 was modelled using a log-parabolic

---

[2] `http://sma1.sma.hawaii.edu/callist/callist.html`

[3] `http://fermi.gsfc.nasa.gov/ssc/`

photon spectrum ($dN/dE = N_0(E/E_\mathrm{b})^{-(\alpha+\beta\log(E/E_\mathrm{b}))}$, where $E_\mathrm{b} = 428.655\,\mathrm{MeV}$, $\alpha$=2.01 and $\beta$=0.0375). We produce a weekly binned light curve. For each time bin, the integrated flux values were computed using the maximum-likelihood algorithm implemented in the science tool `gtlike` to estimate the significance of a detection. We used a detection criterion which corresponds to a maximum-likelihood test statistic TS > 10 (Abdo et al. 2011). Otherwise a $3\sigma$ upper limit of the flux was computed. More details on gamma-ray data reduction can be found in Williamson et al. (2014).

## 5.3 Results

### 5.3.1 Radio and $\gamma$-ray light curves

Figure 5.1 shows the OVRO (15 GHz), Metsähovi (37 GHz), SMA (230 GHz), and LAT (0.1–200 GeV) light curves of 0716+714 from MJD 54687 to MJD 58490 (August 2008 to January 2019). 0716+716 is highly variable at all bands, while the average flux density and variability become stronger and faster at shorter wavelengths. At the radio frequencies, the fluxes were sampled irregularly and the average sampling intervals are of ~6, 5, and 12 days at 15, 37, and 230 GHz, respectively. From the weekly $\gamma$-ray light curve, two distinct groups of flaring states can be distinguished. First, there are three minor, short-term (month scales) flares in a quiescent period until 2011. Afterwards, three major, long-term (year scales) flares can be seen over 2011–2013, 2014–2016, and 2017–2019, respectively. In the radio light curves, one can also notice that 0716+714 flared quite frequently: there are roughly 20–30 events throughout our observations, which yields an average timescale of a radio flare of a month. This is untypical for blazars, which usually show characteristic radio variability time scales of years (e.g., Hovatta et al. 2007; Trippe et al. 2011).

### 5.3.2 Correlation analysis

#### 5.3.2.1 Long-term correlation with the 37 GHz data

We investigate a correlation between the observed radio and gamma-ray light curves for the entire time range. We employed the discrete cross-correlation function (DCF; Edelson & Krolik

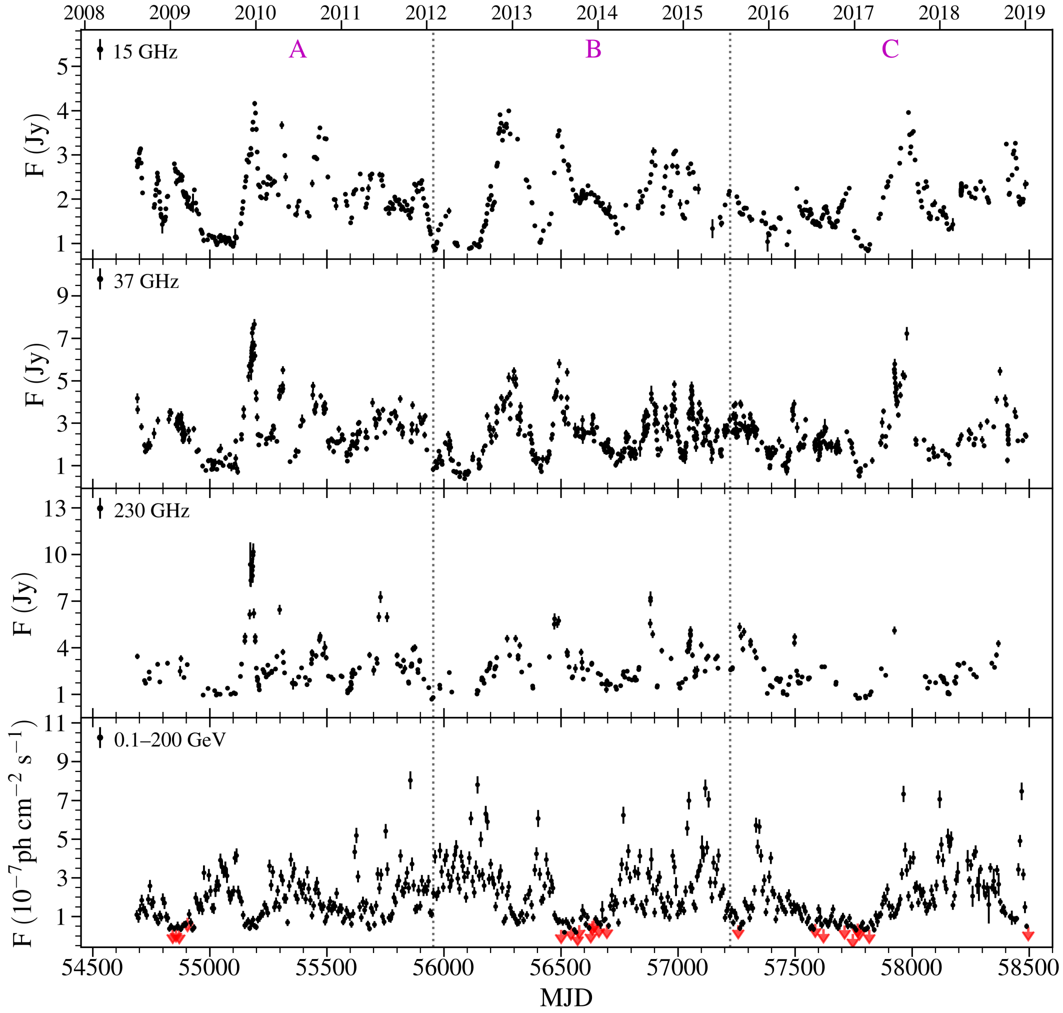

**Figure 5.1.** From top to bottom: light curves of the blazar 0716+714 at radio (15, 37 and 230 GHz) and $\gamma$-ray (0.1–200 GeV) bands. The $\gamma$-ray light curve was binned weekly, and the red arrows indicate $3\sigma$ upper limits. The vertical dashed lines distinguish three 3.5 year regions (*A*, *B*, and *C*), which divide the whole time range into three equal segments (see Section 5.3.2.1).

1988). The confidence levels of the DCF curves were evaluated by simulating $\gamma$-ray light curves in the manner of Emmanoulopoulos et al. (2013). In order to obtain input parameters for the simulation, the spectral slope (defined by a simple power-law spectral density as PSD $\propto 1/\nu^{\beta}$) was estimated by using the periodogram. We also found the probability density function (PDF) of the $\gamma$-rays, using Log-normal and gamma ($\Gamma$) functions. To measure the periodogram of the $\gamma$-rays, we made the weekly-binned $\gamma$-ray light curve distributed evenly by filling out a small number of missing flux points (i.e., upper limits) with linear interpolation; the difference between the upper limits and the resultant fluxes is on average $\pm 0.1 \times 10^{-7}\,\mathrm{ph\,cm^{-2}\,s^{-1}}$. For consistency, this interpolated $\gamma$-ray light curve was used in the simulation and DCF analysis throughout this study and the bin size of the DCF was determined by the larger sampling interval between two time series.

We generated 10000 artificial $\gamma$-ray light curves 10 times longer than the length of input light curve to minimize the red-noise leakage effect (Uttley et al. 2002). Then, a sub-sample that has the same length as the input light curve, was randomly selected from the artificial long light curve, and re-scaled by the mean and standard deviation of the input data. In the simulation, we sampled the artificial light curves exactly the same as the input weekly $\gamma$-ray data, since the $\gamma$-ray fluxes are averaged measurements over a certain time interval (i.e., 7 days). In this case, we expect that the aliasing effect is insignificant (Emmanoulopoulos et al. 2013). Since the DCF coefficient values do not always follow a Gaussian distribution, we draw a cumulative distribution function (CDF) of the DCF coefficients to find the 95, 99, and 99.9% confidence levels (Robertson et al. 2015).

First, we investigated the overall radio-to-$\gamma$-ray correlation with the 37 GHz radio data owing to its denser sampling and because of non-zero contribution of interstellar scintillation up to 15 GHz (Koay et al. 2019). Figure 5.2 shows the resultant DCF over the whole observed time range adopting a seven-day binning. Analysis gives a significant negative correlation exceeding the 99% confidence level. The DCF peak of −0.25 is located at the delay of around 15 days, with the radio leading the $\gamma$-rays.

To explore the origin of this unusual correlation more deeply, we split the whole time range into three 3.5 year regions regularly: *A* (MJD 54687–55954.7), *B* (MJD 55954.7–57222.3), and *C* (MJD 57222.3–58490). The correlation analysis was performed again within these time ranges in the same manner. The results are shown in Figure 5.3, 5.4, and 5.5. In *A*, we found two DCF peaks exceeding the 95% confidence levels. A negative correlation was again found at 21 days with the coefficient of −0.39. In addition, there is a positive correlation at about

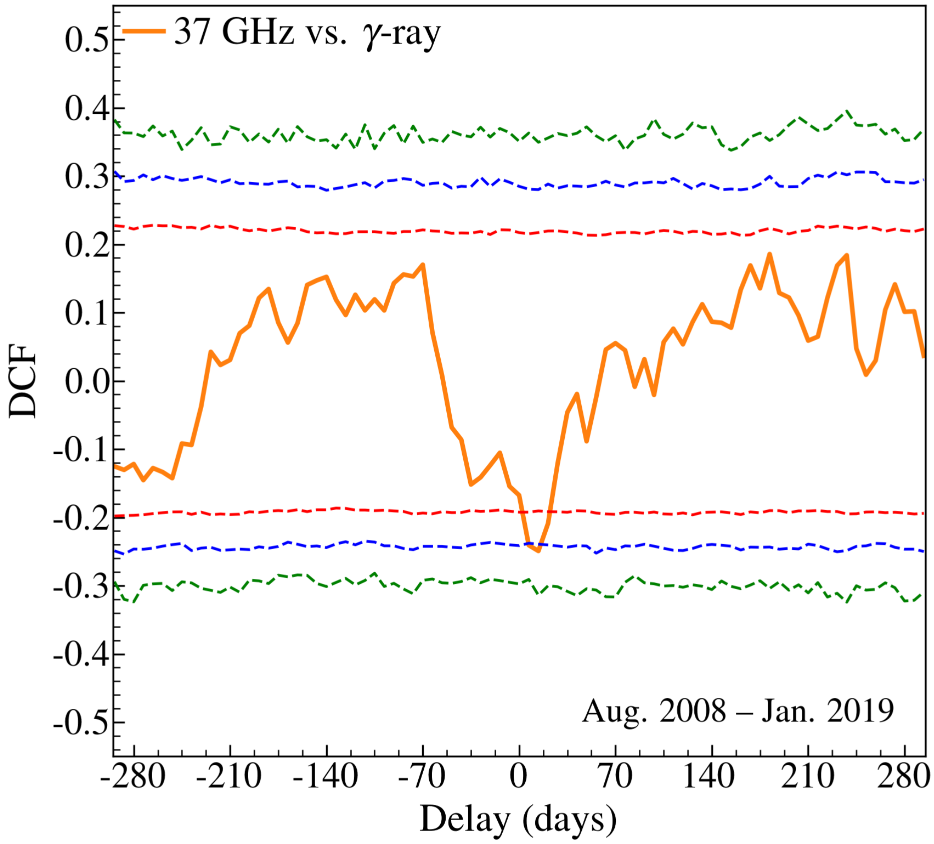

**Figure 5.2.** DCF curve between the 37 GHz and $\gamma$-ray light curves over the full time range. The red, blue, and green dashed lines denote the 95, 99, 99.9 % confidence levels, respectively.

$-125$ days with the coefficient of ~0.48. A similar trend can be seen in *B*. The negative correlation now became more significant than the one in *A*, by exceeding the 99% confidence level. Its location is 14 days with the coefficient of $-0.43$. Also, there are two positive correlations exceeding the 95% confidence level. Given their strength and delay, the one located at $-112$ days with the coefficient of 0.3 seems more probable. In the case of *C*, there are multiple positive correlations exceeding the 95% confidence level. Given their delays (i.e., radio-leading) and the relatively sparse sampling of the radio data in this period, these multiple DCF correlations seem to be artifacts (see Section 5.3.2.2).

The results above suggest that there are significant correlations between the radio and $\gamma$-

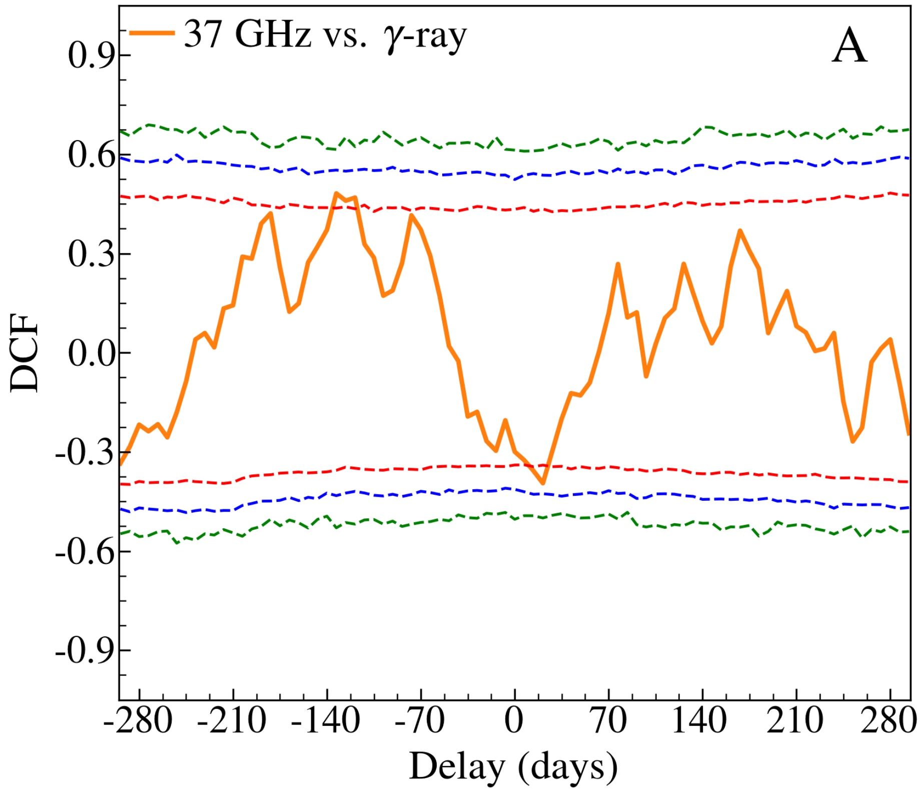

**Figure 5.3.** DCF curves between the 37 GHz and $\gamma$-ray light curves in the *A* (MJD 54687–55954.7) period. The red, blue, and green dashed lines denote the 95, 99, 99.9 % confidence levels, respectively.

ray light curves in each of the *A* (2008–2012) and *B* (2012–2016) periods, plus a potential positive correlation in *C*. We also noticed the presence of anti-correlated radio/$\gamma$-ray variability in these periods. As we have seen, the coefficient values became larger adopting the shorter time range. This suggests that the rapid variability with many flaring events may weaken any real correlations.

#### 5.3.2.2 Optimization of the probable time ranges

We further explored the main source of the significant radio-to-$\gamma$-ray correlations by narrowing down the time range. During the correlation analysis between the $\gamma$-ray and the observed unevenly sampled radio light curves, we noticed that some of the huge empty bins (i.e., time

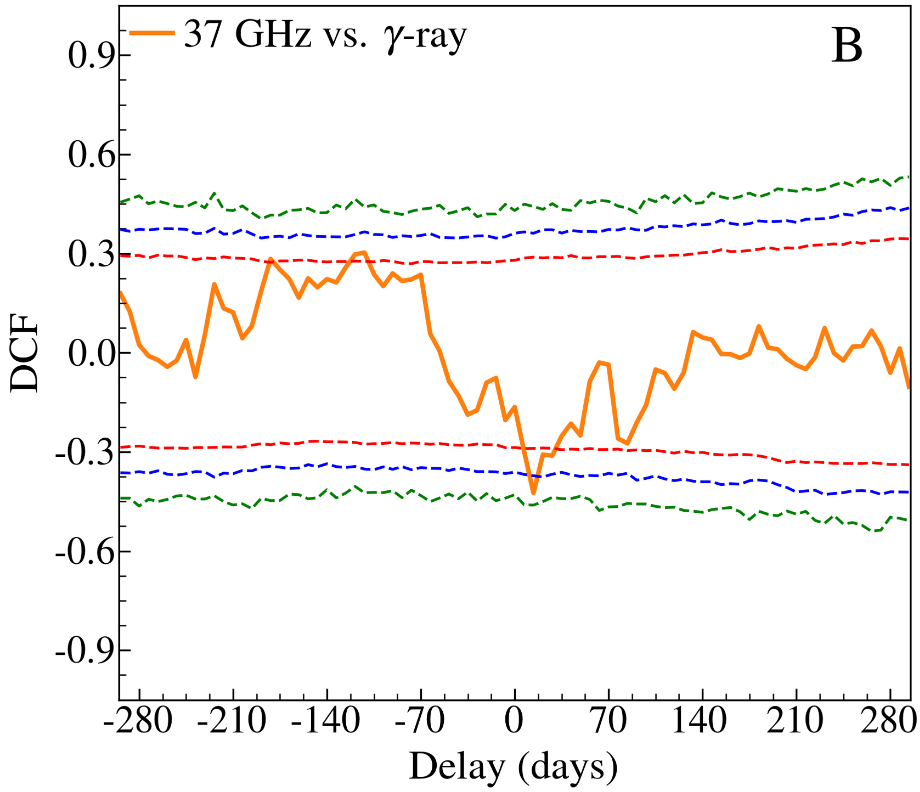

**Figure 5.4.** DCF curves between the 37 GHz and $\gamma$-ray light curves in the $B$ (MJD 55954.7–57222.3) period. The red, blue, and green dashed lines denote the 95, 99, 99.9 % confidence levels, respectively.

gaps between the data points) in the radio light curves result in spurious DCF peaks. Particularly, this was severe in the $C$ period of the 37 and 230 GHz data. To reduce this effect, we approximated the observed radio light curves using interpolation and the method of the Hanning window (e.g., Max-Moerbeck et al. 2014b; Ramakrishnan et al. 2016). The modelled radio light curves were then sampled by their observed average sampling intervals regularly. Since the radio and $\gamma$-ray light curves were sampled differently, we employed the DCF to measure the cross-correlation.

The time range was searched in each of the $A$, $B$, and $C$ periods. For this test, the 37 GHz light curve was used again. First, we made a window shifting from left to right in the time domain of each 3.5 year period. Due to the frequent and short radio flares, every DCF peak

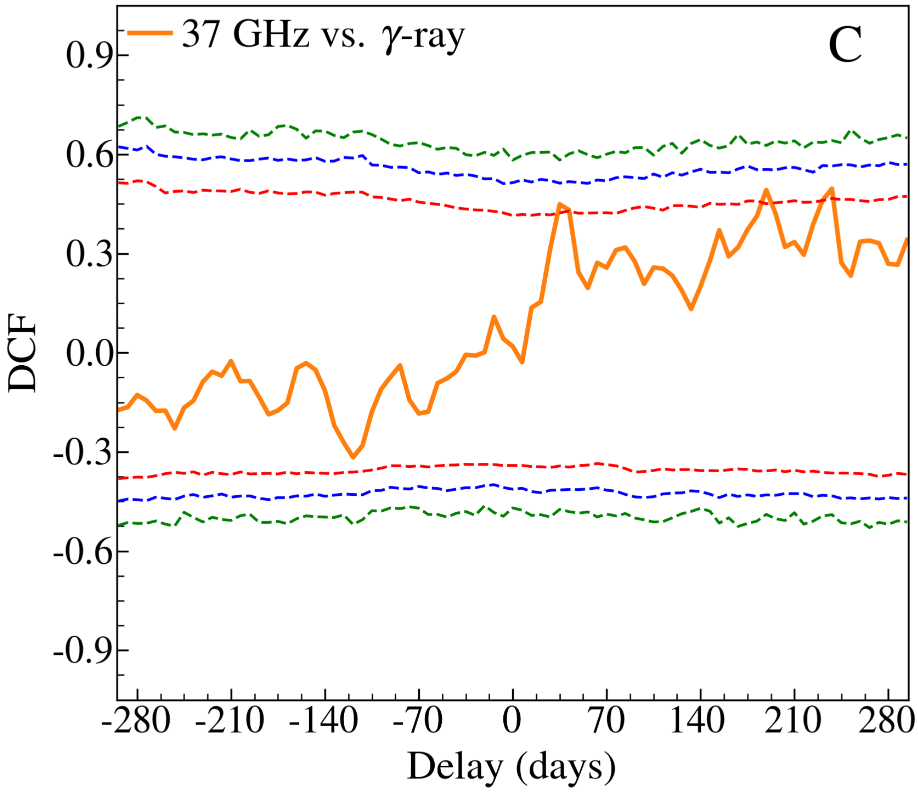

**Figure 5.5.** DCF curves between the 37 GHz and $\gamma$-ray light curves in the *C* (MJD 57222.3–58490) period. The red, blue, and green dashed lines denote the 95, 99, 99.9 % confidence levels, respectively.

decreases considerably with increasing the size of the window (see also Ramakrishnan et al. 2015, for the effects of the rapid variability on the correlation). Hovatta et al. (2008b) reported an average AGN flare timescale of one year at 37 GHz. Considering the 27 individual 37 GHz flares identified by Kravchenko et al. (2020), however, the typical flare duration (e.g., Abdo et al. 2010c) of 0716+714 can be approximated to be about 4 months (see also Lee et al. 2017, for similar estimates in the source). Furthermore, the jet of 0716+714 is known to have frequent ejections of new radio jet components (e.g., every half year; Jorstad et al. 2017), which coincide with the numerous radio flares shown in Figure 5.1. Hence, we considered 1.5 years as a reasonable size of the window.

At every time step, we generated and collected DCF curves (~720 DCF curves in to-

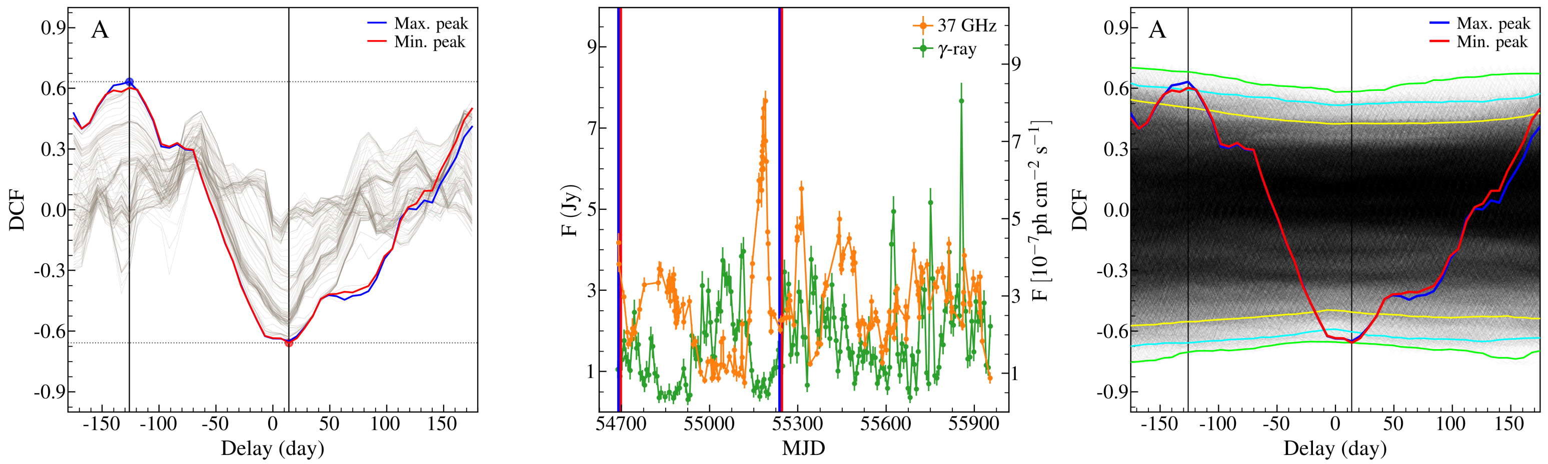

**Figure 5.6.** From left to right: DCF curves searched with the 1.5 year window, the observed 37 GHz and $\gamma$-ray light curves, and the probable DCF curves with ~15000 DCF curves obtained from random selection. From top to bottom, each row indicates the *A*, *B*, and *C* periods, respectively. The corresponding 1.5 year time ranges of the maximum (Max.) and minimum (Min.) DCF curves are shown in the 3.5 year light curves with the blue and red vertical lines, respectively. In the third column, the yellow, cyan, and green curves denote the 95, 99, 99.9% confidence levels, respectively. The strongest positive and negative coefficients are denoted by the vertical black lines.

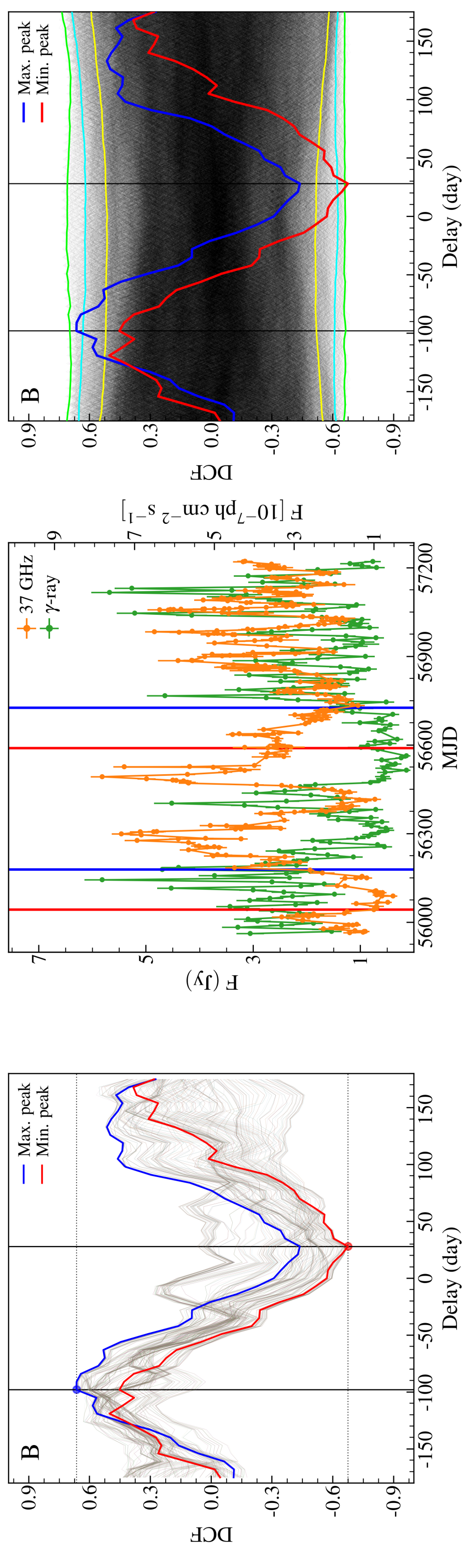

**Figure 5.6.** Continued.

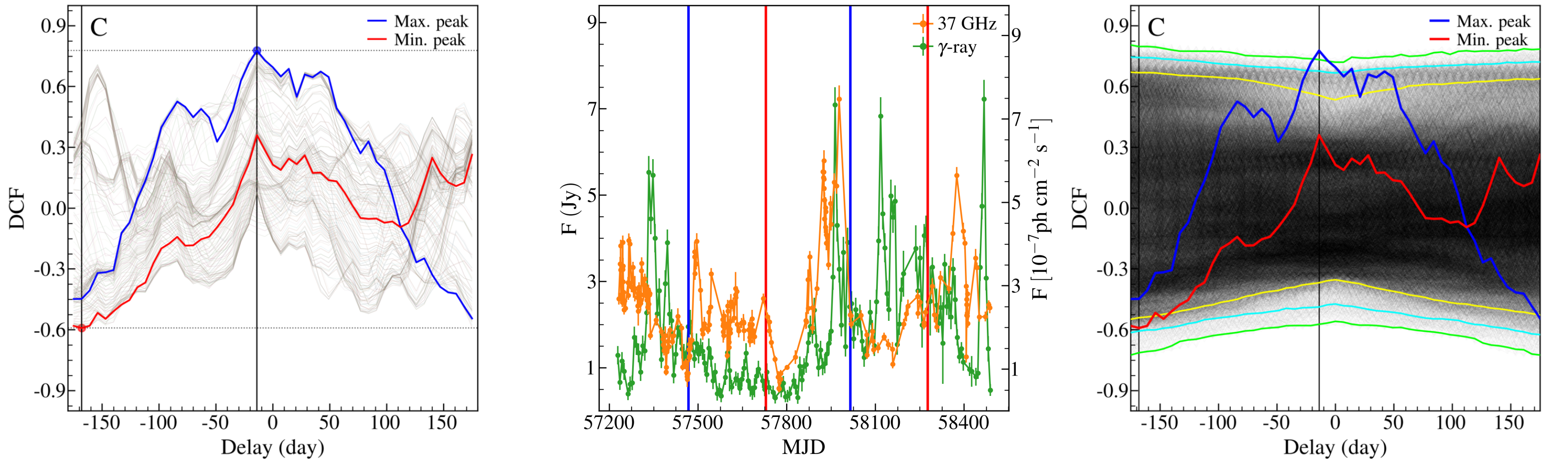

**Figure 5.6.** Continued.

Table 5.1. The optimum 1.5 year regions found with the 37 GHz data.

| Time<br>(MJD) | Delay[1]<br>(days) | DCF[2] |
|---|---|---|
| $T1$: 54697.5 – 55245.0 | 14 | −0.66 |
| $T2$: 56042.0 – 56589.5 | 28 | −0.67 |
| $T3$: 57467.0 – 58014.5 | −14 | 0.78 |

Note. — [1] +: radio leading, −: $\gamma$-ray leading; [2] DCF coefficient values.

tal), while the window passes through the 37 GHz and $\gamma$-ray light curves in parallel. We then found two DCF curves which produce either the strongest positive or negative DCF peaks. If a strongest (Max. or Min.) coefficient appears from a number of consecutive steps, the middle one among them was selected and considered as the probable time range of the strongest correlation. The panels in the first column of Figure 5.6, show the results of this search. The 1.5 year time ranges of the selected DCF curves are displayed in the second column of Figure 5.6. To check if the DCF curves we found are unique, we generated DCF curves of all possible 1.5 year pairs in each 3.5 year period (~15000 DCF curves for each of the $A$, $B$, and $C$ periods) by random selection (any duplications were rejected). The third column of Figure 5.6 shows the result of this random pair test. Interestingly, we found that the negative peaks only exceeded the 99.9% confidence level in $A$ and $B$, while it was the positive peak in $C$. Thus, we considered that the three 1.5-year time ranges ($T1$, $T2$, and $T3$ hereafter) yielding these significant peaks, are the most probable sources of the significant correlations/anti-correlations between the radio and $\gamma$-ray light curves, for the $A$, $B$, and $C$ periods, respectively. We summarize the results of this test in Table 5.1.

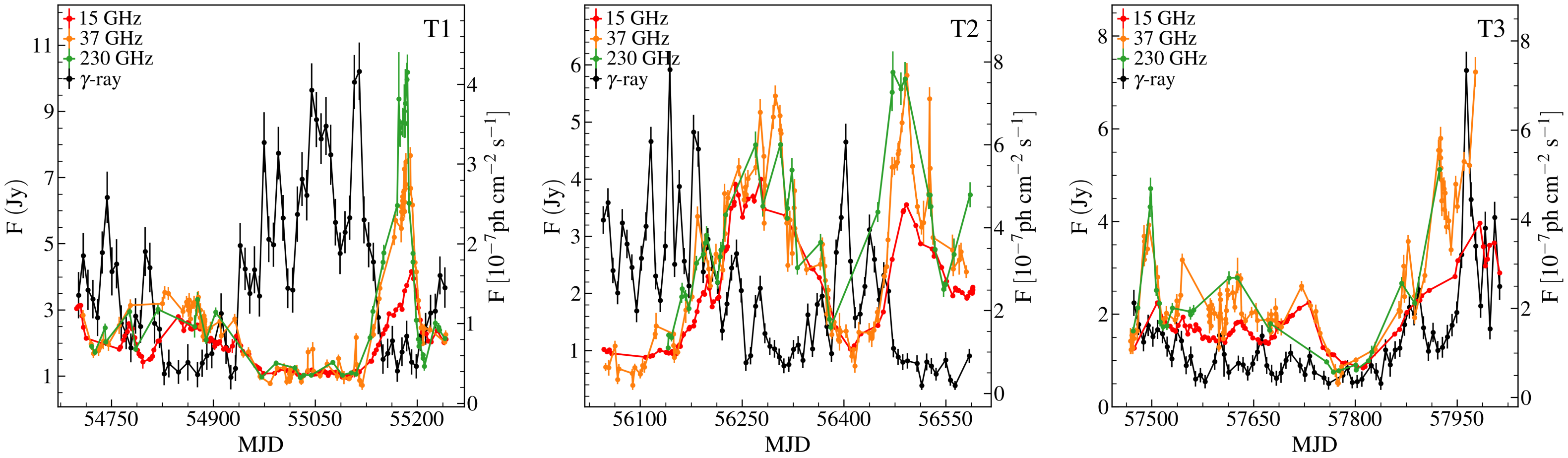

**Figure 5.7.** From top to bottom: the observed radio and $\gamma$-ray light curves, the calculated DCF curves with the 15, 37, and 230 GHz data, respectively. Each column represents the different periods ($T1$, $T2$, and $T3$). In the DCF plots, the orange curve indicates the DCF curve. The red, blue, and green solid lines denote the 95, 99, 99.9 % confidence levels, respectively.

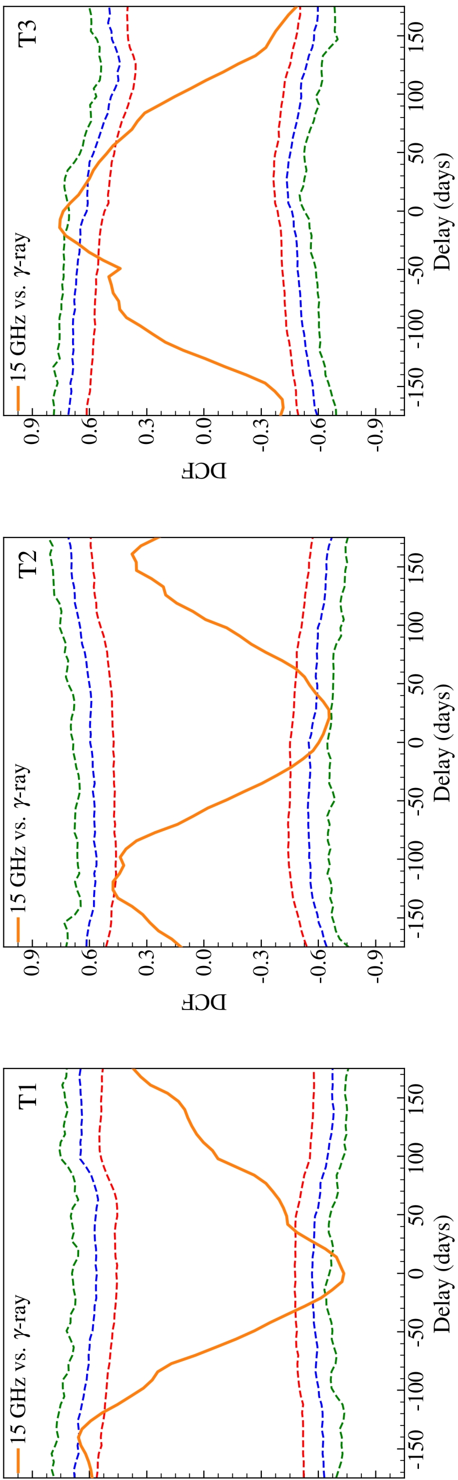

**Figure 5.7.** Continued.

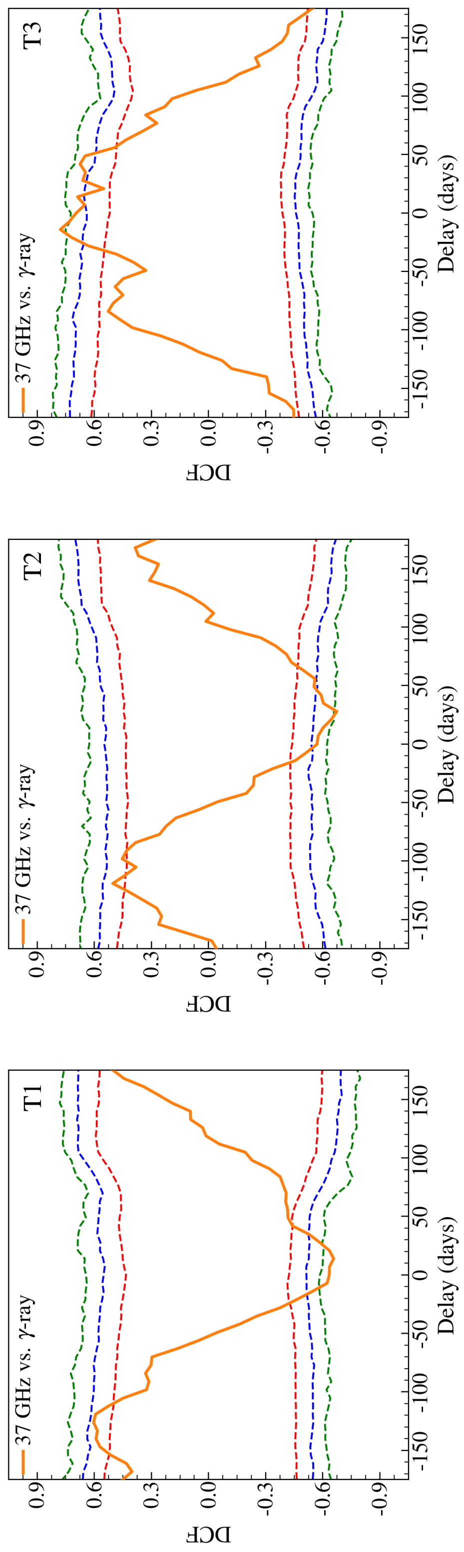

**Figure 5.7.** Continued.

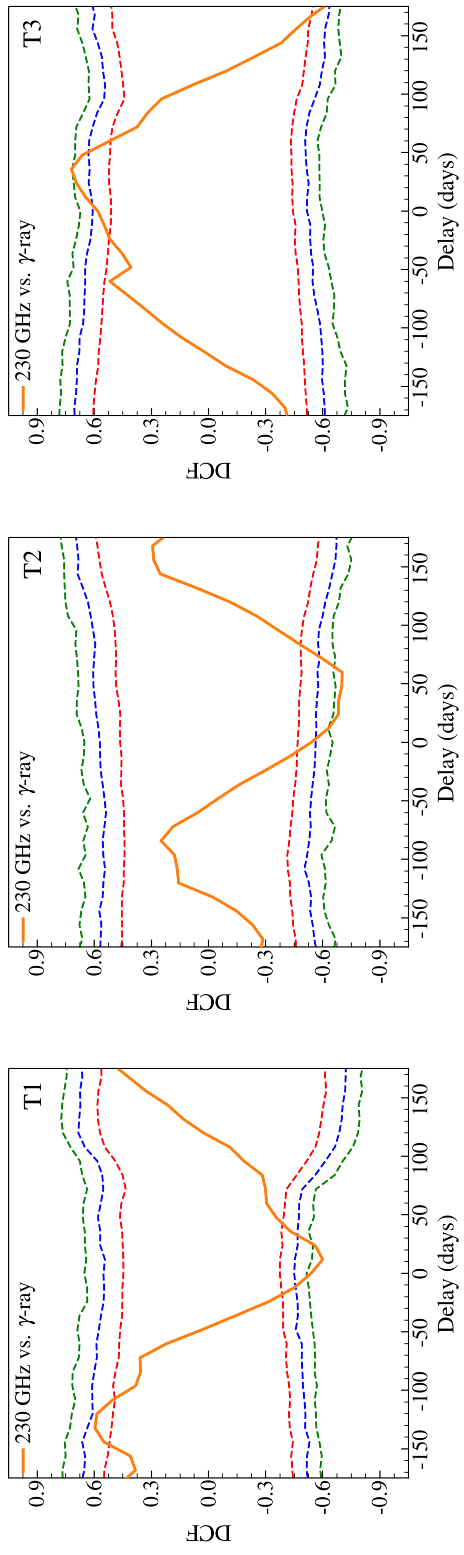

**Figure 5.7.** Continued.

#### 5.3.2.3 DCF curves over the $T1$, $T2$, and $T3$ periods

For the $T1$, $T2$, and $T3$ periods, we performed the statistical test in the same manner as in Section 5.3.2.1, but using all radio bands. Figure 5.7 shows the results of the DCF analysis between the radio (15, 37, and 230 GHz) and $\gamma$-ray light curves. As expected, we find significant anti-correlations in both the $T1$ and $T2$ periods at all the radio frequencies. In addition to this, there are positive correlations located overall at the delays between $-150$ and $-100$ days, though these are less significant than the anti-correlations. Thus, our DCF results are consistent with the indication hinted by the long-term correlations presented in Section 5.3.2.1. We also find that there is a significant positive correlation in the $T3$ period.

The location of the negative DCF peaks indicates that the radio variations lead the $\gamma$-rays. This seems to be caused by the fact that the negative correlation occurs from a ‘peak-to-valley’ feature in the light curves. Thus, one should be careful about the order of the flares in the case of a negative correlation in the time domain. Meanwhile, we noticed that the delays of the positive correlations in $T1$ and $T2$ indicate a ‘$\gamma$-ray leading’ feature which is typical for blazars (e.g. Pushkarev et al. 2010). However, the positive correlation between the $\gamma$-rays and the 230 GHz data in $T3$ shows the opposite trend. The relatively poor sampling of the 230 GHz data during this period missed the major radio flare that was observed in the other two radio frequencies around MJD 57980 completely. In view of this, we were unable to estimate an accurate DCF curve for the 230 GHz data in the $T3$ period and do not consider it in further analysis.

To estimate the location and time lag of each DCF peak, we fit one or two Gaussian functions of a form $\mathrm{DCF}(t) = a \times \exp\left[-(t-c)^2/2w^2\right]$, with $a$, $c$, and $w$ being the amplitude, delay, and width of the Gaussian profile, respectively (e.g., Rani et al. 2013a; Berton et al. 2018). Figure 5.8 and Table 5.2 show the fits and resultant parameters of the fitted Gaussian profiles, respectively. For all the $T1$, $T2$, and $T3$ periods, the centimeter to millimeter radio light curves are highly correlated/anti-correlated with the $\gamma$-rays with similar coefficient values, thus suggesting the same physical processes behind the 15, 37, and 230 GHz fluxes (e.g., Rani et al. 2013a; Angelakis et al. 2019). We also noticed that there is a frequency-dependent delay in the DCF peaks. For both the positive and negative correlations, the peak position becomes more distant from the zero-lag with higher radio frequencies.

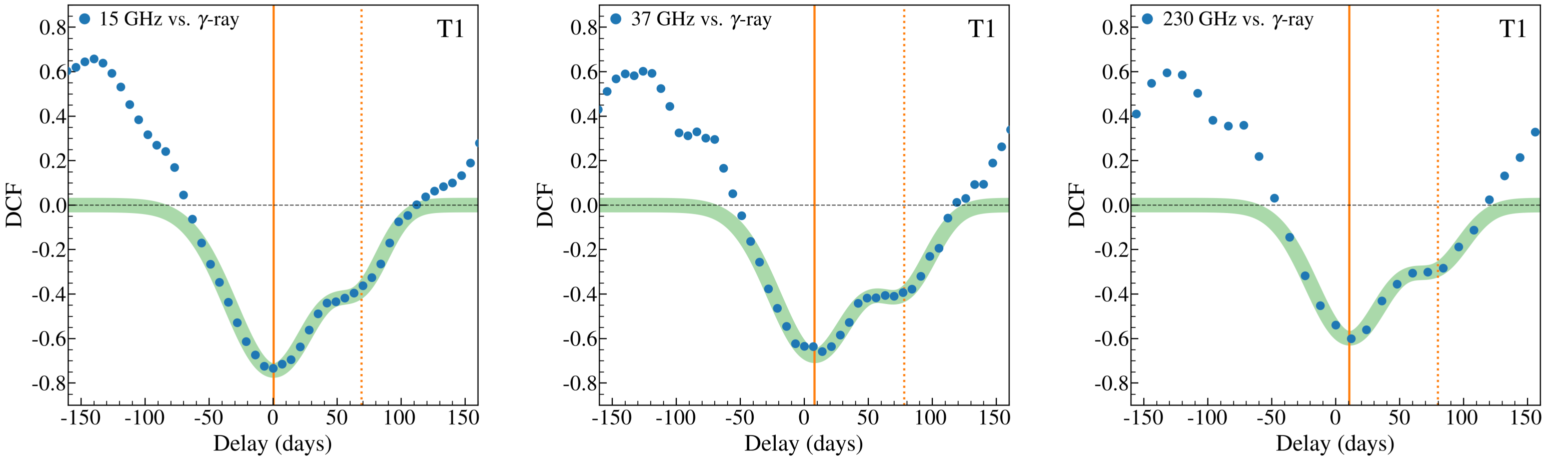

**Figure 5.8.** Gaussian fits to the DCF curves shown in Figure 5.7. The thick green curve indicates the resultant model profile. The identified DCF peaks are marked with the yellow vertical lines: the significant peaks (*solid*) and side-lobe peaks (*dotted*). The fits were performed using a partial DCF curve exceeding the threshold DCF coefficients (*horizontal black dashed line*).

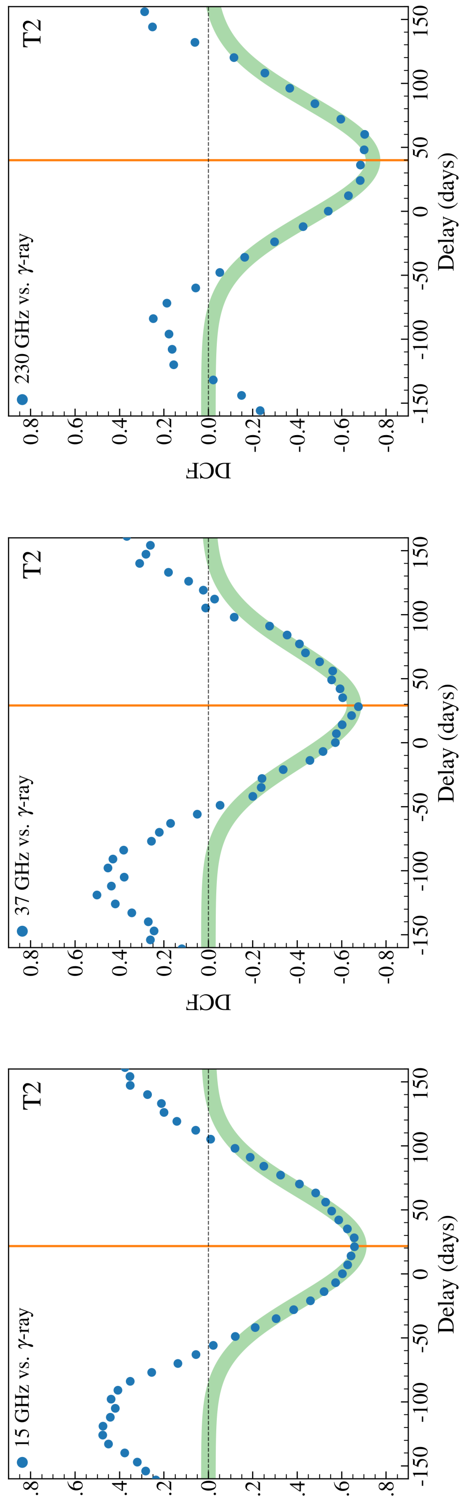

**Figure 5.8.** Continued.

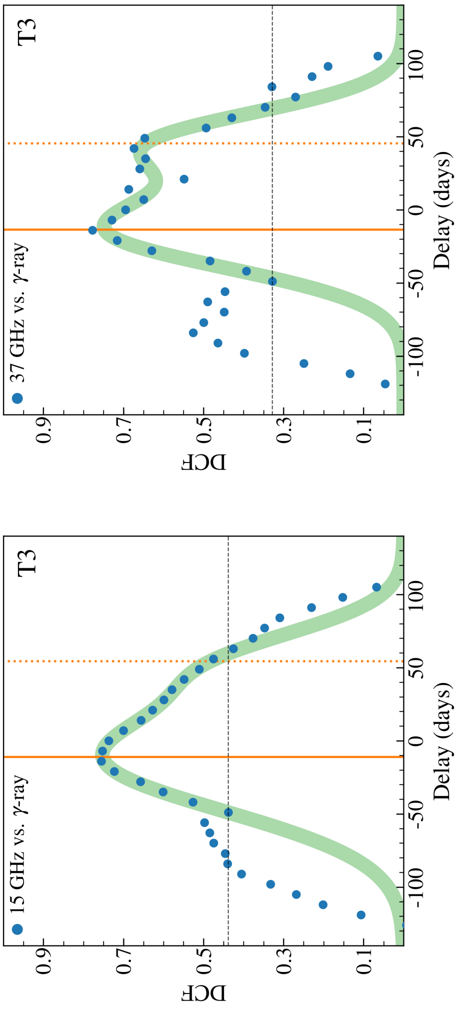

**Figure 5.8.** Continued.

Table 5.2. The best-fit Gaussian parameters found from Figure 5.8.

| Data | $a^1$ | $c^2$ (days) | $\|w\|^3$ (days) |
|---|---|---|---|
| $T1$ at 15 GHz | −0.74 ± 0.01 | 0.4 ± 0.7 | 33.6 ± 0.8 |
| $T1$ at 37 GHz | −0.68 ± 0.01 | 7.9 ± 1.3 | 31.2 ± 1.4 |
| $T1$ at 230 GHz | −0.60 ± 0.01 | 10.7 ± 1.2 | 29.3 ± 1.3 |
| $T2$ at 15 GHz | −0.68 ± 0.01 | 21.8 ± 1.2 | 43.3 ± 1.3 |
| $T2$ at 37 GHz | −0.66 ± 0.02 | 29.0 ± 1.3 | 44.2 ± 1.6 |
| $T2$ at 230 GHz | −0.74 ± 0.02 | 39.9 ± 1.4 | 45.7 ± 1.5 |
| $T3$ at 15 GHz | 0.75 ± 0.01 | −11.0 ± 1.5 | 36.7 ± 1.4 |
| $T3$ at 37 GHz | 0.73 ± 0.03 | −13.5 ± 3.3 | 26.1 ± 2.9 |

Note. — [1] Amplitude of the Gaussian component; [2] Location of the Gaussian component; [3] Width of the Gaussian component.

### 5.3.3 Jet kinematics

The activity in the parsec scale jet of 0716+714 has been monitored at 7 mm (43 GHz) within the VLBA-BU-BLAZAR program. To represent the jet emission structure, we model the sky brightness distribution in the (u,v) visibility domain by a number of two-dimensional Gaussian intensity profiles using the *modelfit* task in the `Difmap` software package (Shepherd 1997). Figure 5.9 shows the radio jet structure of the blazar on 2019 October 19. We designate the 7 mm core as $A0$, which is assumed to be the brightest region at the upstream end of the jet flow. Apart from the core, we identify two stationary features, $A1$ and $A2$, located at average distances of 0.10±0.02 and 0.53±0.10 mas from the core, respectively, and 14 individual moving knots ($B1$–$B14$); here the errors of the mean distances of $A1$ and $A2$ are their mean component sizes. Figure 5.10 shows the knot propagation and the radio and $\gamma$-ray light curves. Comparison of the total and the core 37 GHz light curves shows that the core is nearly always the dominant

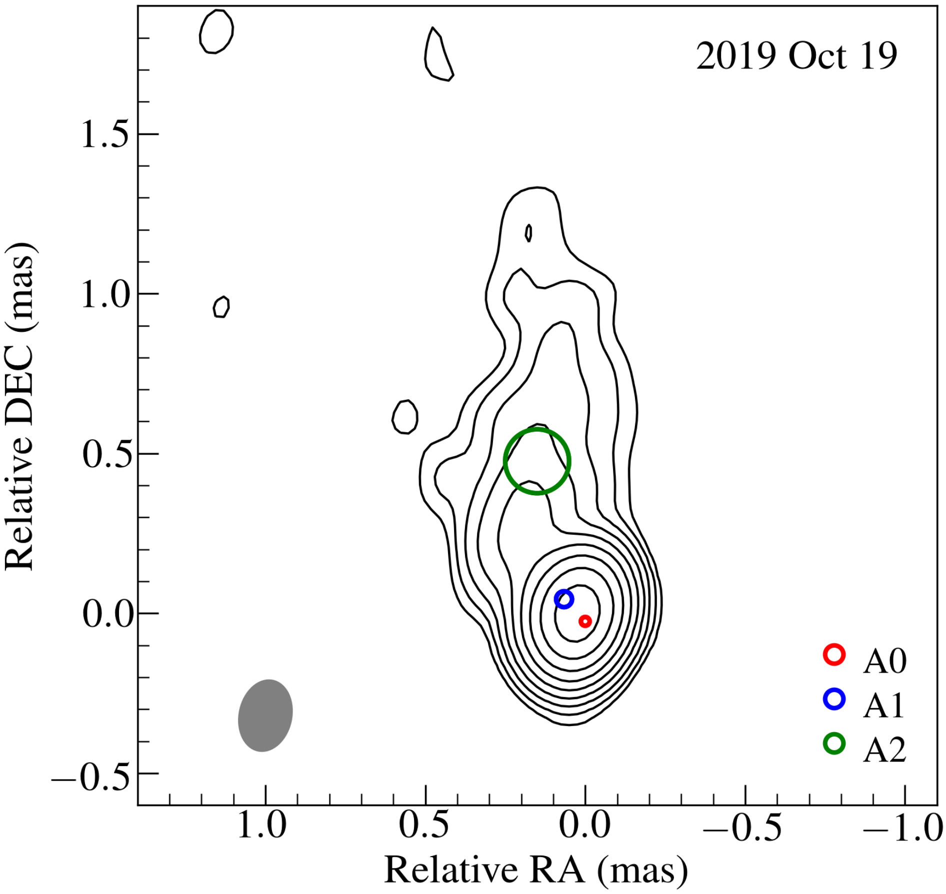

**Figure 5.9.** Total intensity image of the 0716+714 jet observed by the VLBA at 43 GHz on 2019 October 19. The contour levels increase by a factor of 2, from 0.25% to 64% of the peak flux (i.e., 0.55 Jy). The synthesized beam size is shown by ellipse in the *bottom-left* corner. The blue and green circles indicate the mean positions and sizes of $A1$ and $A2$ measured in 2008–2019, respectively. In this map, the red circle ($A0$; the core) is simply described at the location of the map peak with its mean size (i.e., a FWHM of 0.03 mas).

source of the millimeter emission.

The $B1$–$B14$ jet components show a linear motion except for $B7$ which was better fit by a quadratic polynomial. Also, we exclude the $B14$ knot from the further kinematics analysis because it is detected only at three epochs. The ejection epoch $T_0$ for each of the components

$B1$–$B13$ was calculated from fits to the RA and DEC coordinate using a linear regression. Due to large errors in $T_0$ exceeding 0.5 years for the $B3$, $B5$, $B7$, and $B10$ knots, we calculated the ejection epoch from a linear fit to the R-coordinate (i.e., the radial distance from the core versus time). A complete description and data will be provided in Weaver et al. in prep. The kinematics of the knots are summarized in Table 5.3.

For the knots $B1$–$B13$, the apparent velocity ($\beta_{\rm app}$) is estimated in the range from 6 to 26 $c$. The direction of the motion varies between −9° (Western) and 34° (Eastern) as measured from North. On average, the knots were ejected from the core every 0.8 years. This is a bit higher than what Jorstad et al. (2017) expected. However, if we exclude the large empty period between $B10$ and $B11$ (i.e., 893 days), the ejection interval becomes 0.6 years. Two knots were found in each of the $T1$, $T2$, and $T3$ periods: $B2$–$B3$ in $T1$, $B8$–$B9$ in $T2$, and $B11$–$B12$ in $T3$. This suggests a link of the propagation of the knots and the significant correlation between the radio and $\gamma$-ray emission.

By checking the 43 GHz core fluxes, however, we find that the overall positions of the ejection times in $T1$, $T2$, and $T3$ are located at the growing stages (e.g., onset/rising/peaking) of the radio flares. In particular, a consistent behavior can be seen in $T2$. The ejection times coincide with the $\gamma$-ray flares decaying and the radio flares rising. In the case of $T3$, the ejection of component $B11$ seems not to be correlated with any significant events at both radio and $\gamma$-rays. However, we noticed that strong radio and $\gamma$-ray flares started rising just after the ejection of $B12$ almost contemporaneously.

We further investigated the global kinematic properties of the 0716+714 jet. The overall variations of the parameters in the radial distance domain ($r$) show complex behavior with large scatter, except the DEC motion (see the top panel of Figure 5.11). In this study, we employed simple linear trends to approximate the global behaviors of the parameters of the knots. As was shown above, there is a stationary feature $A2$ at about ~0.53 mas from the core. This feature could be a transition region or a shock which leads to a difference in the observed patterns of the jet physical conditions (e.g., Kadler et al. 2008; Larionov et al. 2013; Beuchert et al. 2018). Thus, we performed the analysis for two groups separately: one with $r < 0.53$ mas and the other with $r \geq 0.53$ mas. The angular resolution of our data is insufficient to apply the analysis

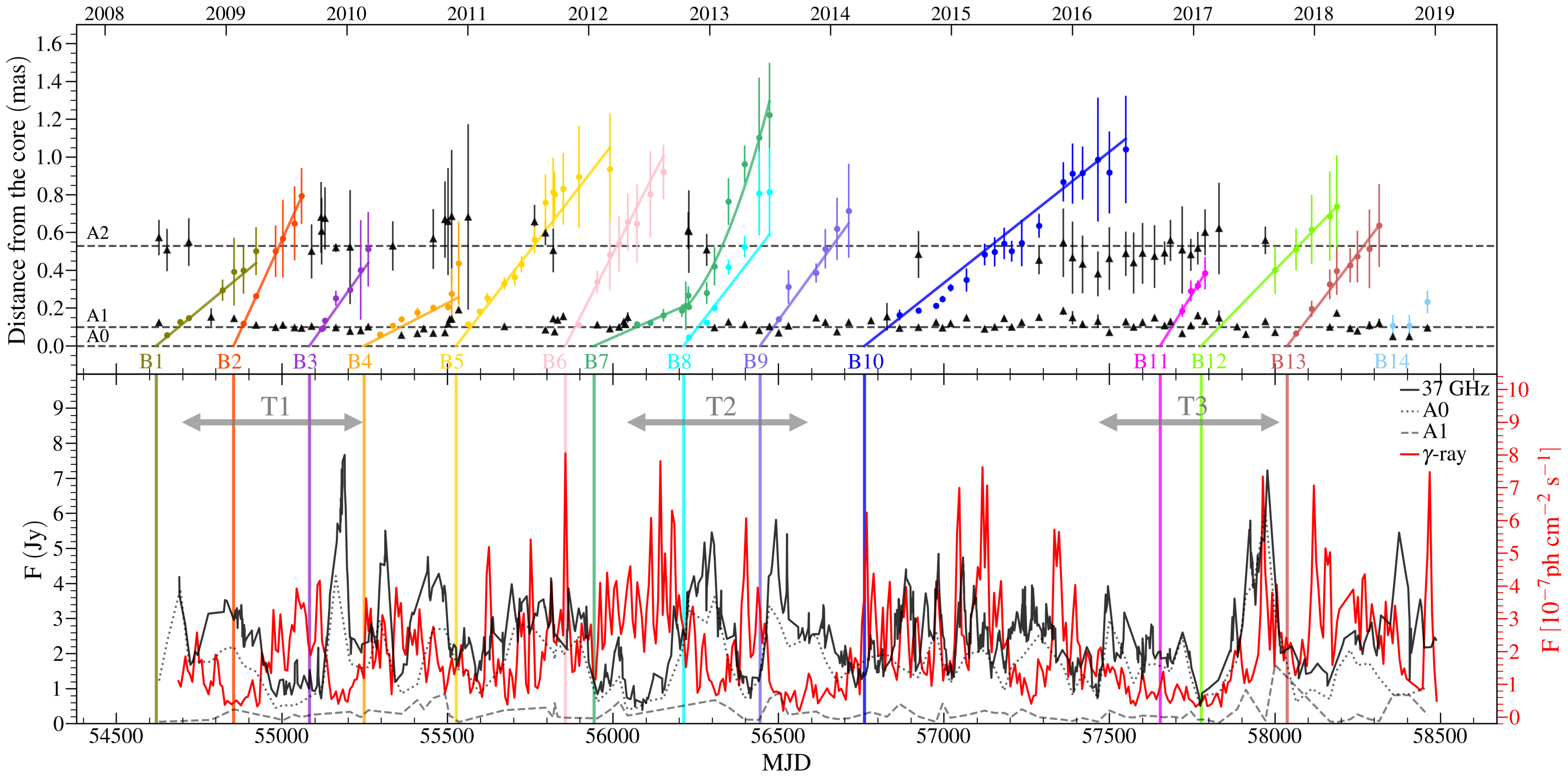

**Figure 5.10.** Top: separation of jet components from the core in 0716+714. The solid lines represent linear fit to the motion, while dashed lines indicate the position of the core *A*0, and stationary features *A*1 and *A*2. Bottom: the 43 GHz light curves of *A*0 and *A*1 components overlaid on the 37 GHz and gamma-ray light curves of the entire source. The component *A*2 is omitted due to its weak emission. Vertical solid lines mark the epochs of ejection of the newborn jet components.

Table 5.3. Newborn jet components in 2008–2019.

| ID | $T_0^1$ (MJD) | $\mu^2$ (mas/year) | $\phi^3$ (°) | $\beta_{\rm app}^4$ ($c$) |
|---|---|---|---|---|
| B1 | 54620 ± 15 | 0.53 ± 0.04 | 21 ± 22 | 10.0 ± 0.3 |
| B2 | 54854 ± 2 | 1.40 ± 0.03 | −3 ± 6 | 26.4 ± 0.2 |
| B3 | 55083 ± 10 | 1.04 ± 0.05 | −9 ± 4 | 19.6 ± 0.3 |
| B4 | 55248 ± 52 | 0.33 ± 0.04 | 26 ± 5 | 6.2 ± 0.2 |
| B5 | 55526 ± 32 | 0.82 ± 0.03 | 23 ± 2 | 15.6 ± 0.2 |
| B6 | 55856 ± 8 | 1.24 ± 0.05 | 23.3 ± 1.2 | 23.4 ± 0.3 |
| B7 | 55943 ± 79 | 1.07 ± 0.11 | 30 ± 8 | 20.1 ± 0.6 |
| B8 | 56213 ± 2 | 0.83 ± 0.13 | 34 ± 6 | 15.6 ± 0.7 |
| B9 | 56444 ± 6 | 0.88 ± 0.07 | 5 ± 5 | 16.7 ± 0.4 |
| B10 | 56760 ± 61 | 0.51 ± 0.03 | 25 ± 2 | 9.6 ± 0.2 |
| B11 | 57653 ± 1 | 1.04 ± 0.12 | 8 ± 12 | 19.6 ± 0.7 |
| B12 | 57777 ± 4 | 0.66 ± 0.03 | 5 ± 8 | 12.4 ± 0.2 |
| B13 | 58037 ± 2 | 0.84 ± 0.03 | 27 ± 4 | 15.8 ± 0.2 |

Note. — [1] Ejection time; [2] Proper motion; [3] Direction of motion (North through East); [4] Apparent velocity.

on smaller scales (e.g., less than 0.2 mas). Thus, the stationary feature $A1$ was excluded from this analysis.

Figure 5.11 shows the results of the analysis on the jet parameters: the DEC and RA motions, component sizes (FWHM), and position angles. We find a clear and straight motion in the northern direction, considering the following dependence: $d_{xy} \propto kr$, where $d_{xy}$ is either the relative RA ($x$) or DEC ($y$) of the knots, $r$ is the radial distance from the core, and $k$ is the slope. The linear slope of the motion in the $y$ direction is $k$ ~0.9 which means almost one-to-one match with the radial distance. However, the slope of the motion in the $x$-axis which is assumed to be perpendicular to the jet axis, is much smaller. It means that the motion is pri-

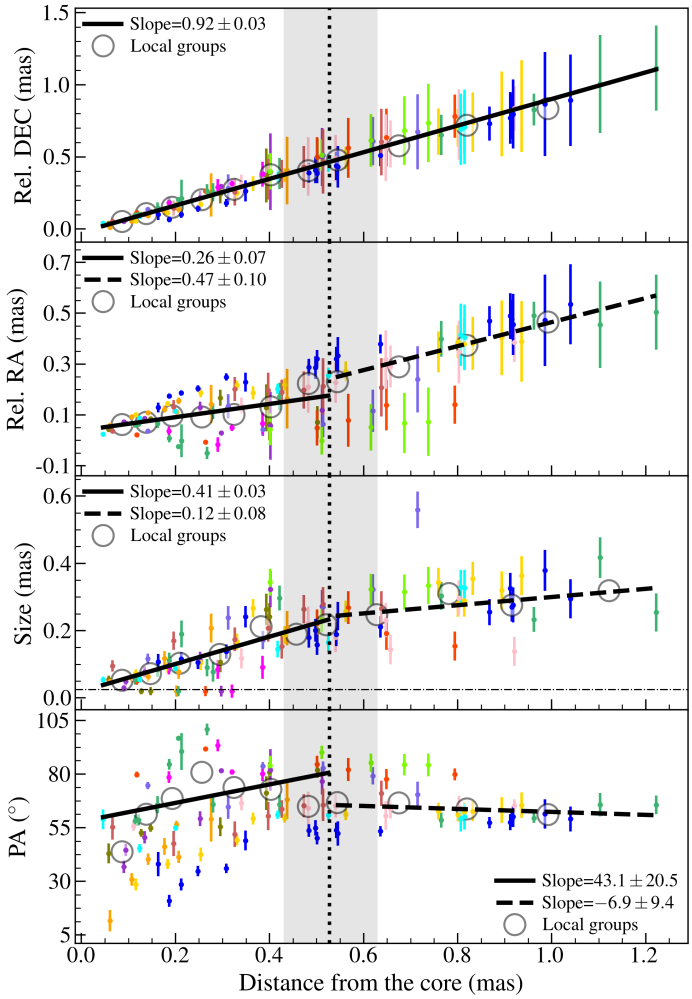

**Figure 5.11.** From top to bottom: the variations of relative DEC and RA, size, and position angle (PA; CW from East) as a function of the distance from the core for the knots *B*1–*B*13 obtained from the model-fits in the VLBA images. For the knots, the color marks are the same as in Figure 5.10. The black solid/dashed lines indicate a linear regression. The linear trends were divided by the mean position of *A*2 (i.e., 0.53 mas) which is denoted by the vertical black dotted line, except for the vertical motion. The shaded gray color region represents the mean FWHM of *A*2 (i.e., 0.2 mas) which shows the overall size of the region. The empty gray circles show the mean variations of the parameters by averaging 10 consecutive points each. In the size panel, lower limits are indicated by the horizontal dot-dashed line.

marily in the $y$ direction. Interestingly, our knots showed at least more than one curve in their trajectories which indicates a bend in the jet (see also Larionov et al. 2013; Rani et al. 2015). From the linear fits, we found that there are two linear trends in this transverse motion: the linear slopes of ~0.26 over $r < 0.53$ mas and ~0.47 over $r \geq 0.53$ mas. This indicates there is a change in the jet direction at $A2$. The component sizes also show different slopes.

In this case, however, the first slope is higher than the second one suggesting that the jet becomes more confined beyond $r \sim 0.53$ mas. Lastly, the position angle shows large variations in the inner region, before $A2$. This directly indicates the presence of a strong bending structure in the jet. Due to the large scatter, the first linear trend does not well fit the data. However, the outer region (i.e., downstream $A2$) shows a more obvious linear trend. It should be noted that the uncertainties of the slopes in the position angle are quite large. This means that the angle variations are very complicated and the linear trends cannot fully describe the variations. We form groups by averaging over 10 consecutive points (total 110 model jet components) in the $r$ domain; in the case of the component size, seven lower limits on the size were rejected from the analysis, and the last bin contains three data points. The groups of the position angle indicate that the jet axis moves from East (e.g., ~40°) to North (e.g., ~80°) up to a radial distance of ~0.3 mas, then the jet bends back toward the eastern direction. However, the variation in the position angle is relatively weak beyond ~0.3 mas from the core before converging at about 64°.

Figure 5.12 shows the distribution of the observed brightness temperatures versus radial distance (Kovalev et al. 2005; Jorstad et al. 2017). Seven outliers which correspond to the unresolved jet components shown in Figure 5.11, were excluded from the analysis. We fit a simple power-law model (i.e., $\mathrm{T_b} \propto r^{\epsilon}$) to analyze the brightness temperature gradient along the jet. To investigate any transition at the position of $A2$, we again divided the distribution in the same manner as Figure 5.11. The resultant power-law indices are estimated of $\epsilon = -2.7 \pm 0.2$ and $\epsilon = -1.5 \pm 0.5$ in the inner and outer regions, respectively. The power-law dependence of 0716+714 within the inner region is consistent with the values obtained from the parsec-scale jets of other blazars (e.g., Kadler et al. 2008; Rani et al. 2015; Kravchenko et al. 2016). The notable change in the brightness temperature gradient is an indication of a sudden change in

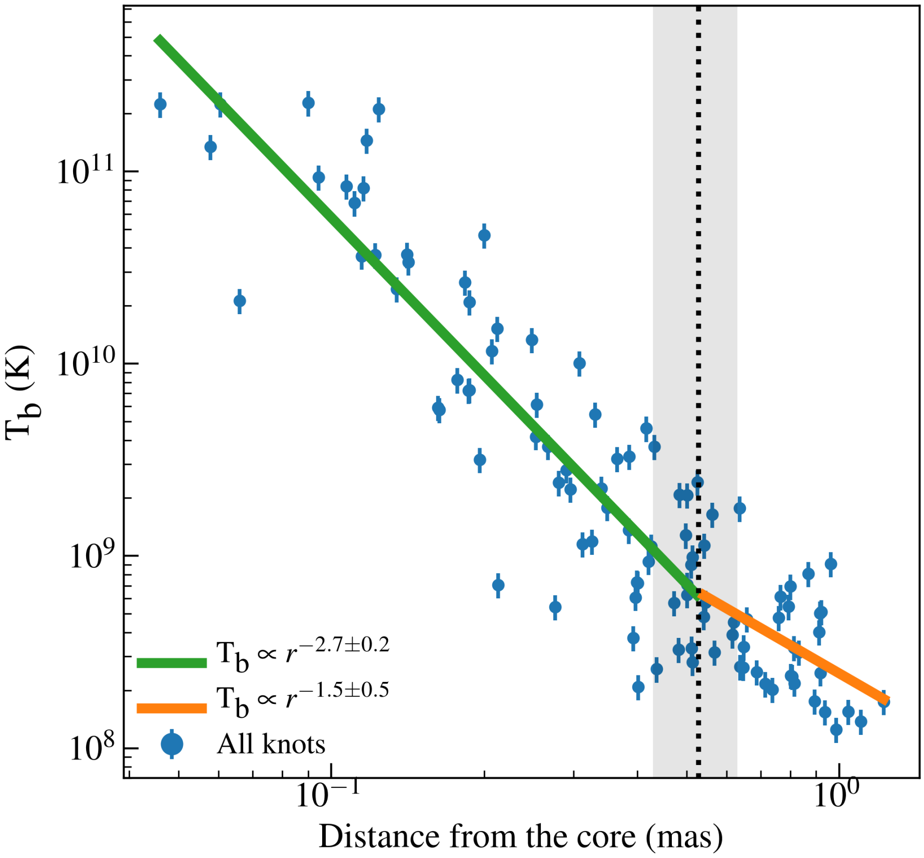

**Figure 5.12.** Observed brightness temperatures of all the knots ($B1$–$B13$) as a function of the distance from the core. The analysis is the same as Figure 5.11, but using a power-law ($T_b \propto r^{\epsilon}$). The uncertainties of the brightness temperatures were assumed to be 15% (Beuchert et al. 2018).

the physical properties of the jet (e.g., Böttcher et al. 2005; Fromm et al. 2013; Beuchert et al. 2018).

Rani et al. (2014) suggested a connection between the $\gamma$-rays and the inner jet position angle (near the core). We investigated the variations in the mean position angle of the knots, that are shown in Figure 5.13. Interestingly, the three periods with the significant radio-to-$\gamma$-ray correlations (i.e., $T1$, $T2$, and $T3$) overlap with the larger mean position angles (e.g., above 70°). This indicates that the global jet direction was more aligned toward North during those

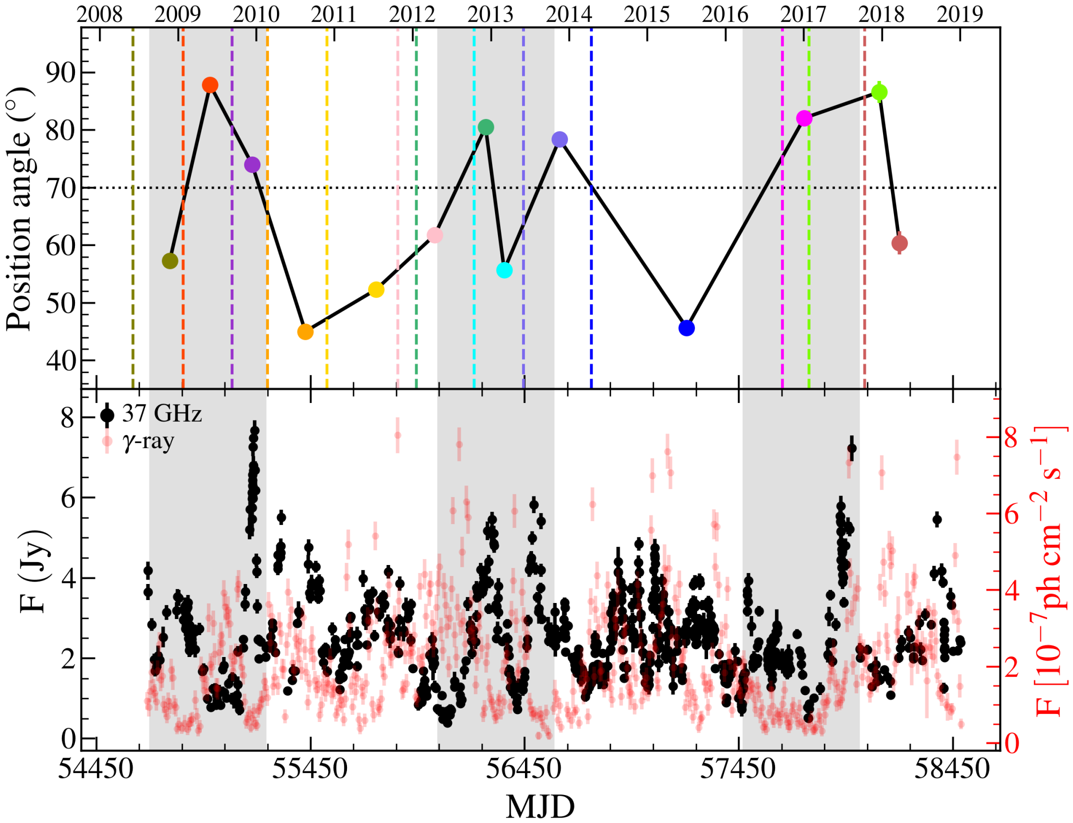

**Figure 5.13.** *Top*: mean position angle of the jet knots marked at their mean epochs. The color marks are the same as in Figure 5.10. The vertical dashed lines indicate the ejection times of the knots. The horizontal dotted line refers to 70°. The gray shaded regions show $T1$, $T2$, and $T3$, respectively. *Bottom*: the observed radio and $\gamma$-ray light curves.

periods. Changes in the jet orientation can be due to propagation of jet components at different position angles (Gómez et al. 2011; Casadio et al. 2015b; Pushkarev et al. 2017). This might determine the association of the knot with a $\gamma$-ray flare by changing Doppler factor and viewing angle of the jet (e.g., Casadio et al. 2015a). Thus, we suggest that the northerly position angle corresponds to closer alignment of the jet with the line of sight, and then beaming effects lead to the correlated flares (see also Jorstad et al. 2001a; Rani et al. 2014; Liodakis et al. 2018a, for discussions of different beaming effects between the radio and $\gamma$-ray emitting regions).

## 5.4 Discussion

### 5.4.1 Internal shock interactions

The occasional occurrence of a significant correlation or anti-correlation between the 37 GHz radio and *Fermi*-LAT $\gamma$-ray activity might indicate that variability in these bands is initiated by the same physical process. However, as the $\gamma$-ray emitting region has to be compact, it is generally found to be optically thick to synchrotron self-absorption (SSA) at radio wavelengths. In other words, the $\gamma$-ray emission is likely to be produced up-stream from the 37 GHz radio core. The delay between radio and $\gamma$-ray variability was found to be of the order of a few – $\sim$ 29 days. We therefore parameterize this delay as $\Delta t_{\mathrm{r}\gamma} \equiv 20\, t_{20}$ days. For a jet moving with a Lorentz factor $\Gamma \equiv 10\Gamma_1$ with a viewing angle of $\theta_{\mathrm{obs}} \approx 1/\Gamma \approx 5.7^o$ (leading to a Doppler factor of $\delta = \Gamma = 10\delta_1$), the time delay corresponds to a jet propagation distance of $d_{\mathrm{r}\gamma} \approx 1.7\,\Gamma_1\,\delta_1\,t_{20}$ pc. With the above-mentioned viewing angle and the angular-scale (see Section 5.1), this corresponds to a projected angular distance of

$$\theta_{\mathrm{r}\gamma,\mathrm{proj}} \approx 37\,\Gamma_1\,\delta_1\,t_{20}\,(\theta_{\mathrm{obs}}/5.7^o)\;\mu\mathrm{as} \tag{5.1}$$

The time delay $\Delta t_{\mathrm{r}\gamma}$ corresponds to a co-moving time (in the rest-frame of the $\gamma$-ray emission region) of $\Delta t'_{\mathrm{r}\gamma} = 200\,\delta_1\,t_{20}$ days. Here, and in the following, primed quantities refer to the co-moving frame of the emission region. This co-moving time delay is significantly shorter than the radiative cooling time scale of electrons radiating synchrotron emission at 37 GHz in a magnetic field of $B' = 0.1\,B_{-1}$ G, which is $t'_{\mathrm{rad}} \approx 9.5 \times 10^3\,B_{-1}^{-3/2}\,\delta_1^{-1/2}\,(1 + C)^{-1}$ days, where $C \equiv \nu F_\nu^C/\nu F_\nu^{sy} \sim 1$ is the Compton dominance parameter. This means that 37-GHz-radio-emitting electrons (with Lorentz factor $\gamma'_{37} \approx 94\,B_{-1}^{-1/2}\,\delta_1^{-1/2}$) that may have been co-accelerated with the $\gamma$-ray emitting electrons in the $\gamma$-ray emission region, will not have had time to cool significantly by the time they reach the radio emitting zone. Hence, if a $\gamma$-ray flaring event produces excess electrons both at low (radio emitting: $\gamma' \sim 100$) and high (GeV $\gamma$-ray emitting: $\gamma' \sim 10^4 - 10^5$) energies simultaneously, these excess radio emitting electrons will not have been affected by radiative cooling by the time the emission region reaches the radio core (becoming optically thin to SSA), thus leading to positively correlated variability among the radio and $\gamma$-ray bands. In contrast, $\gamma$-ray emitting electrons will cool on a co-moving time scale of a few days – weeks (corresponding to observed time scales of $\sim$ a few hours – days) and will have cooled away when reaching the radio emitting region.

Assuming the internal shock interaction, we further estimate the propagation distance ($d_{\rm r\gamma}$; see above) in terms of $\beta_{\rm app}$ for each period and frequency. For $\beta_{\rm app}$, the measurements in Table 5.3 were used. We considered the mean $\beta_{\rm app}$ values of the knots ejected in the $T1$ and $T2$ periods, separately: $B2$–$B3$ for $T1$ and $B8$–$B9$ for $T2$. In the case of $T3$ ($B11$–$B12$), $B13$ was used instead of $B11$ due to its closer timing to the flares. Using the relation $\Gamma \approx (1+\beta_{\rm app}^2)^{1/2}$ (e.g., Pushkarev et al. 2012; Karamanavis et al. 2016b), we obtained the following set of parameters: $\beta_{\rm app} = 23$ and $\theta_{\rm obs} = 2.5°$ for $T1$, $\beta_{\rm app} = 16$ and $\theta_{\rm obs} = 3.6°$ for $T2$, and $\beta_{\rm app} = 14$ and $\theta_{\rm obs} = 4.1°$ for $T3$. With these estimates, we calculated the $d_{\rm r\gamma}$ values (see Table 5.4).

As elaborated above, a positive correlation (with time delay) between the $\gamma$-ray and radio light curves indicates the simultaneous production of excess electrons at low and high energies. This is expected in many shock-acceleration scenarios, where a flaring event is plausibly explained by an over-dense region in the jet interacting with obstacles or other (slower) jet components (e.g., Spada et al. 2001; Sokolov et al. 2004; Sokolov & Marscher 2005; Graff et al. 2008; Böttcher & Dermer 2010; Chen et al. 2011; Joshi & Böttcher 2011; Zhang et al. 2015; Baring et al. 2017; Böttcher & Baring 2019). Internal-shock interactions may, however, plausibly also significantly change the amplitude and spectral characteristics of magneto-hydrodynamic turbulence in the emission region, which could harden the shock-accelerated particle distribution. Such a scenario has been investigated, e.g., by Böttcher & Baring (2019) in an attempt to model an orphan GeV $\gamma$-ray flare of the blazar 3C 279 that exhibited significant spectral hardening in the GeV regime during the flare. Such a scenario actually predicted an anti-correlation between the $\gamma$-ray and radio light curves since the spectral hardening of the non-thermal electron distribution led to a depletion of lower-energy electrons at the expense of a significantly larger power in high-energy electrons. While such a scenario may predict anti-correlated behavior between gamma-ray and radio emission, one would expect the gamma-ray flare to lead the radio decline. Furthermore, the delay would be expected to increase with decreasing frequency, also opposite to the observed trend. It therefore seems that such a scenario is not compatible with the observed anti-correlations found here.

Table 5.4. The $d_{r\gamma}$ values obtained from the delays of the significant correlations in $T1$, $T2$, and $T3$.

| | $T1^1$ | $T2^1$ | $T3^2$ |
|---|---|---|---|
| $d_{\gamma,\mathrm{15GHz}}$ (pc) | 0.1 ± 0.2 | 3.6 ± 0.2 | 1.4 ± 0.2 |
| $d_{\gamma,\mathrm{37GHz}}$ (pc) | 2.7 ± 0.4 | 4.7 ± 0.2 | 1.7 ± 0.4 |
| $d_{\gamma,\mathrm{230GHz}}$ (pc) | 3.6 ± 0.4 | $< 6.5^3$ | - |

Note. — $^1$ Negative correlation with the radio leading feature; $^2$ Positive correlation with the $\gamma$-ray leading feature; $^3$ considered to be overestimated due to the sparse sampling.

### 5.4.2 Frequency dependence in the time lags

Previous observations of $\gamma$-ray bright blazars suggested that a time lag between the $\gamma$-ray and radio emission is due to opacity effect (Pushkarev et al. 2010; Rani et al. 2013a; Ramakrishnan et al. 2016; Liodakis et al. 2018b). In general, the $\gamma$-rays precede the radio emission, thus suggesting an upstream production of the $\gamma$-rays with respect to the radio emitting site (Fuhrmann et al. 2014; Max-Moerbeck et al. 2014a).

For the anti-correlated variabilities, the distance ($d_{r\gamma}$) increases with higher radio frequencies. This is contrary to the well-known peak-to-peak based expectation: smaller distance with higher radio frequencies (e.g., Pushkarev et al. 2010). We note that the $\gamma$-ray flares (two episodes of enhanced $\gamma$-ray emission in each of the $T1$ and $T2$ periods) lead the radio flares, while the measured delays indicate that the radio variability patterns lead the $\gamma$-ray ones. The former is in agreement with our expectation, whereas the latter is not. As we mentioned in Section 5.3.2.3, however, the $\gamma$-ray delays correspond to a negative correlation, indicating inverse patterns between the light curves (see also Rani et al. 2014). The discrepancy can be resolved if one considers the delay as the distance between the radio flares and the $\gamma$-ray valleys. This suggests that the radio variation, thus the onset of a radio flare precede the $\gamma$-ray peak that is about to decay. Indeed, this can be seen from the comparison between the $\gamma$-rays and the 43 GHz VLBA core fluxes (see Figure 5.10). León-Tavares et al. (2011) decomposed the longer-lasting and broader radio flares into exponential subcomponents using the method initially introduced by Valtaoja et al. (1999). They also found that the gamma-ray peaks tend to coincide with the initial stages of a growing radio flare, and this sometimes happens when the peak of the radio flare is still far away in time from the gamma-ray peak.

In this circumstance, we suggest the following scenario: a strong moving disturbance (or shock) moves from the jet base through the radio cores. It initially produces a $\gamma$-ray flare, where the region is still optically thick to SSA. The $\gamma$-ray flare subsides quickly, and radio flares appear as the disturbance reaches the $\tau_{\mathrm{SSA}} = 1$ regions for the different radio frequencies. Given the long travel delays (around 110–140 days) and variability signatures from other events during that time, the resulting positive correlation with $\gamma$-ray lead may not be very significant. Possibly caused by the shock-compressed, stronger magnetic field, the relativistic electrons lose energy more efficiently via synchrotron emission at the expense of IC scattering. This could lead to a suppression of the $\gamma$-ray emission after the radio flares peak, and thus, an anti-correlation with leading radio flares and delayed $\gamma$-ray valleys. In such a scenario, however, the observed time delays are difficult to explain. The delay between the radio flares and the gamma-ray dips could possibly originate from synchrotron self-Compton (SSC) cooling on the light crossing time scale through the radio core: as the radio flare evolves, the synchrotron photon field in the radio core builds up, leading to SSC emission (and cooling) of the high-energy electrons. The resulting SSC emission is expected to emerge in X-rays, so this scenario would predict that the radio flare(s) should be correlated with X-ray flares. There have been a number of previous studies (e.g., Vittorini et al. 2009; Liao et al. 2014; Rani et al. 2015; MAGIC Collaboration et al. 2018) that report correlated radio/X-ray emission in 0716+714. Given sparse sampling of the X-rays (e.g., Rani et al. 2013a; Wierzcholska & Siejkowski 2015) and the concave X-ray spectrum generated by both synchrotron and IC (e.g., Liao et al. 2014; MAGIC Collaboration et al. 2018), however, more detailed hard X-ray observations would be necessary for clarity. It is worth noting that the 230 GHz data suffers relatively sparse sampling in $T2$. This prevents us from measuring the delay of the anti-correlation accurately in this period. Thus, we consider that the $d_{\gamma,230\mathrm{GHz}}$ of $T2$ is significantly overestimated, and might actually be smaller (e.g., around 5.0–5.5 pc) given the opacity effect in the jet.

The positively correlated variability in $T3$ consists of one huge $\gamma$-ray flare and several minor ones. For this positive correlation, we expect that the time delays came from the peak-to-peak based distance. The calculated $d_{\mathrm{r}\gamma}$ values at 15 and 37 GHz are relatively small and consistent with each other within errorbars. This indicates that the major $\gamma$-ray flare was produced at a region upstream of the radio cores by about 1.5–2.0 pc. We also found that the two radio flares are almost simultaneous. The distance between the radio cores (i.e., the core shift) is variable with time (e.g., Kudryavtseva et al. 2011; Plavin et al. 2019). Thus, the core shift might be less pronounced during the flaring period which leads to such radio flares peaking contemporaneously. We consider that the passage of the knot $B12$ triggered the notable radio to $\gamma$-ray events in the radio core region (i.e., standing shock); but it could be linked with $B13$ if the knot suffered significant velocity changes (see Section 5.4.3). After the escape of $B12$ from the standing shocks, the 43 GHz core seems to grow continuously and produce the strong radio and $\gamma$-ray flares almost contemporaneously. This acceleration could be caused by either the consecutive injection of new relativistic shells into the radio core (e.g., Böttcher & Dermer 2010), magnetic reconnection (e.g., Jorstad et al. 2013), or the extended structure of the moving knot (e.g., Agudo et al. 2011b; Kim et al. 2018b; MAGIC Collaboration et al. 2018; Weaver et al. 2019).

### 5.4.3 Timing of the knot ejections in $T1$ and $T2$

By using the VLBA observations, we found that all the $\gamma$-ray flares are correlated with the radio emission, were accompanied by an ejection of a VLBI jet component: $B2$ and $B3$ in $T1$, $B8$ and $B9$ in $T2$, and $B12$ (or $B13$) in $T3$. These findings further support the internal shock scenario/interpretation. The calculated ejection epochs ($T_0$) are expected to coincide with the timing when the knot passes through the radio core. Thus, this could be explaining the estimated $T_0$ locations of the knots relative to the evolutionary stages of the 43 GHz core flares. We find that the ejection times of $B3$, $B8$, and $B9$ are located at a rising stage of a radio flare, whereas that of $B2$ is near the peak of a radio flare. However, the actual peaks of the radio flares can be a product of superposed underlying components (e.g., León-Tavares et al. 2011), and thus care should be taken in the comparison.

The position of $T_0$ in the radio light curves, might be affected by variable beaming effects (e.g., Liodakis et al. 2018a) and/or complex trajectories of the knots. Larionov et al. (2013) suggested that a shock wave moving down a helical path along the jet can explain the observed flaring features in 0716+714. This might play a crucial role for the individual knots, thus resulting in less accurate estimates of $T_0$ or distortion of the observed flaring features (see also Kravchenko et al. 2020, for the significantly bent structure even at $\mu$as scales). Furthermore, there could be a substantial change in the velocity of the knots due to the interaction with the standing shocks (e.g., Schinzel et al. 2012; Liodakis 2018) or a bent-jet structure (e.g., Rani et al. 2015). This suggests a transition from smaller velocities in a region near the radio core to higher velocities beyond this region. The knot $B2$ has the highest apparent velocity ($26\,c$) in our observations, and this might affect the estimation of its $T_0$ making it appear further downstream from its true ejection epoch. Given the overall trend in $T_0$ of the knots (i.e., a position between the $\gamma$-ray and radio flares), however, we consider that these knots likely caused the notable radio flares in $T1$ and $T2$ by interacting with the radio core.

### 5.4.4 Location of the $\gamma$-ray production site

Our results suggest that a region upstream of the radio core is the origin of the observed notable $\gamma$-ray flares in the $T1$, $T2$, and $T3$ periods. For the one in $T3$, we can define the $\gamma$-ray production site by assuming the location of the 15 GHz radio core from the central engine to be 7–8 pc as reported by Pushkarev et al. (2012) and Butuzova (2018). With the $d_{\gamma,15\mathrm{GHz}}$ value of 1.5 pc, the $\gamma$-ray site can be estimated as 5.5–6.5 pc from the central engine. Rani et al. (2015) reported the location of the 43 GHz core to be ~6.5 pc. This might be explaining the occurrence of the radio and $\gamma$-ray flares in close proximity to each other in $T3$. For $T1$ and $T2$, the delays of the positive correlations with $\gamma$-ray lead, decrease with higher frequencies as expected. The delays in $T1$ and $T2$ at 15 GHz are roughly $-140$ and $-120$ days, respectively. Interestingly, $d_{\mathrm{r}\gamma}$ of these delays can be estimated as 47 and 20 pc for $T1$ and $T2$, respectively. Given the locations of the 15 and 43 GHz cores suggested by previous studies (i.e., 6–8 pc), such large values seem to be highly overestimated.

We consider that this could be attributed to a complicated path (e.g., helices) of the moving disturbances and/or significant changes in $\beta_{\rm app}$ of the knots. Assuming the viewing angles found in Section 5.4.1, we found that the $d_{\rm r\gamma}$ values are comparable to the expected locations of the radio cores with the $\beta_{\rm app}$ values around 3.5 for $T1$ and 6.0 for $T2$. Thus, we suggest that strong moving disturbances produce the $\gamma$-ray flares in $T1$ and $T2$ at subparsec scales from the jet apex and undergo significant velocity changes (possibly with variable viewing angles) in their motions by the time they reach the radio cores (see also Geng et al. 2020, for a subparsec-scale origin of $\gamma$-rays in 0716+714).

### 5.4.5 Evolution of the parsec scale jet

Considering the three primary evolutionary stages in the energy losses of the travelling shocks: Compton, synchrotron, and adiabatic (Marscher et al. 1992), Rani et al. (2015) derived the three power-law dependencies of the brightness temperature on the radial distance from the core (Lobanov & Zensus 1999) in the 0716+714 jet: $\epsilon_c = [11-s-a\,(s+1)]/8 + [b\,(s+3)]/2 - 2$ for Compton loss, $\epsilon_s = -[4\,(s-1) + 3\,a\,(s+1)]/6 + [b\,(s+3)]/2 - 2$ for synchrotron loss, and $\epsilon_a = [2\,(5-2\,s) - 3\,a\,(s+1)]/6 + [b\,(s+3)]/2 - 2$ for adiabatic loss, where $a$, $b$, and $s$ are the power-law scaling indices of the magnetic field $B \propto r^{-a}$, Doppler factor $\delta \propto r^{b}$, and electron distribution $N(\gamma) \propto \gamma^{-s}$, respectively (see also Schinzel et al. 2012, for the case of the quasar 3C 345). We employed this approach to interpret our results on the observed brightness temperature. $a$ can be set to be 1 or 2 for toroidal and poloidal magnetic fields, accordingly. However, we also considered an intermediate value of 1.5 for $s$ (Lobanov & Zensus 1999). Given the possible variations in Doppler factor (e.g., Schinzel et al. 2012; Rani et al. 2015), we used $b$ with values between 0 and 1. Figure 5.14 shows the calculated $\epsilon$ with the typical value of $s = 2$ (optically thin spectral index $\alpha \sim -0.5$ from $S_\nu \propto \nu^{\alpha}$). We find that the combination of $a = 1$ and $b = 0.6$ nicely corresponds to our observed power-law dependencies: $\epsilon_s = -2.7$ and $\epsilon_a = -1.7$ for the inner and outer regions, respectively. This implies that the propagating shocks suffer strong radiative cooling via synchrotron losses at first, then adiabatic losses become

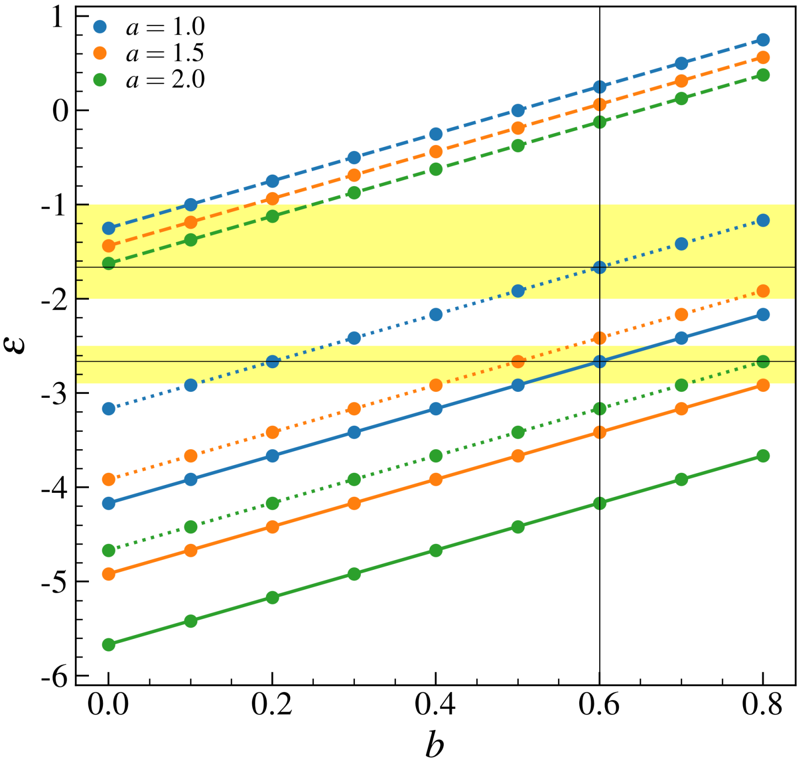

**Figure 5.14.** Calculated $\epsilon$ as a function of $b$. $a$ depends on the dominant magnetic field component: from 1 (toroidal) to 2 (poloidal). The dashed, dotted, and solid lines indicate $\epsilon_c$, $\epsilon_a$, and $\epsilon_s$ respectively. The yellow regions denote the power-law dependencies of the inner and outer regions with their uncertainties. The most probable estimates ($\epsilon_s = -2.7$ and $\epsilon_a = -1.7$) are marked by the vertical and horizontal lines.

prominent as the shocks passes the standing shock $A2$.

Such changes in the brightness temperature gradient could be caused by a recollimation shock (RCS) and compression of the plasma flow, thus suggesting the stationary feature $A2$ being a RCS (Kadler et al. 2008). One can expect an increase in the expansion rate of the propagating blobs beyond the RCS, which is supposed to be an overpressured region with respect to the nearby environment (e.g., Beuchert et al. 2018). This is consistent with our estimation above: $\epsilon \sim \epsilon_a$, after the $A2$ region. The variations in the component size shown in Figure 5.11, however, indicate that the expansion became less pronounced after $A2$. This might be indicating that $A2$ is a standing feature induced by a bend, rather than recollimation (e.g., Jorstad et al. 2001a; Rani et al. 2015). The notable changes in the transverse motion and position angle beyond $A2$ in Figure 5.11, support such a standing oblique shock scenario (see Jorstad et al. 2001a; Ramakrishnan et al. 2014). Larionov et al. (2013) also concluded the stationary feature (their knot $K2$) belongs to a bending point accompanied by kinematic changes of a moving knot around the standing component. We suggest that collision with the ambient medium or magneto-hydrodynamical instabilities resulted in the formation of the structure.

## 5.5 Summary

We have analyzed the long-term cm- and mm-radio and $\gamma$-ray light curves of the blazar 0716+714 to explore the connection between these two bands and to pinpoint the site where high-energy emission is produced. Using the monitoring VLBA data allowed us to reveal the parsec-scale jet activity throughout our observations in detail. Our primary conclusions are the following:

1. We found three significant correlations between the radio (15, 37, and 230 GHz) and $\gamma$-ray light curves in 2008–2019. To identify the probable time ranges of these correlated behaviors in the rapid radio and $\gamma$-ray variabilities, we split the light curves into several sections and found three 1.5 yr-periods: two ($T1$ and $T2$) with an anti-correlation and one ($T3$) with a positive correlation. All these correlations exceed the significance level of 99.9% and peaked at the time delays within 40 days (radio-leading feature) for the anti-correlations and $-14$ days ($\gamma$-ray-leading feature) for the positive correlation.

2. Using the VLBA monitoring observations, we found three stationary jet features including the core, which dominates in the radio emission. The kinematic analysis revealed 14 jet components moving downstream the jet. Their apparent velocities range from 6 to 26 $c$, and the average ejection rate is estimated of ~0.8 years. Each of the three significant radio/$\gamma$-ray correlations was accompanied by two (for $T1$ and $T2$) or one (for $T3$) moving jet components. We found that these components were emerged from the core when radio flares were in the growing stage (i.e., onset/rising/peaking).

3. We consider that the significant positive or negative correlation between the radio and

$\gamma$-ray bands, are attributed to the same physical process which is initiated by the shock interactions between an over-dense region (e.g., the radio core) and a moving disturbance (e.g., the jet components). We conclude that the observed radio/$\gamma$-ray anti-correlations in $T1$ and $T2$ are attributed to the inverse pattern (i.e., leading radio flares and delayed $\gamma$-ray dips). This unusual phenomenon could be generated due to highly efficient synchrotron at the expense of IC process caused by possibly shock-compressed, stronger magnetic field in the emission region. In this picture, the delays of the anti-correlations can be interpreted as the distances between the radio cores and a region downstream of the radio cores where the propagating disturbances (or its shock front) reached.

4. The positive radio/$\gamma$-ray correlations in $T1$ and $T2$ were located at the delays of about 110–140 days. These correlations seem to be less significant due to the long travel times and underlying short-term variability (possibly from other jet regions). Considering the known positions of the 15 and 43 GHz radio cores in the 0716+714 jet (i.e., 6–8 pc from the jet apex), the calculated $d_{\mathrm{r}\gamma}$ values of those large delays are overestimated (i.e., 20–50 pc). We suggest that the complex inner jet kinematics (e.g., helices and/or significant velocity changes probably with variable viewing angles) could be responsible for the discrepancy. In the case of the one in $T3$, our estimates point the $\gamma$-ray production site at 5.5–6.5 pc from the jet apex.

5. The overall motions of the jet components are complicated with highly variable position angles, particularly within ~0.4 mas from the core. The observed brightness temperature decreases along the jet following a power-law. The power-law index is estimated as $-2.7 \pm 0.2$, which changes to $-1.5 \pm 0.5$ at the position of the stationary feature $A2$ (~0.53 mas from the core). This indicates a change in the energy losses from being synchrotron-dominated to adiabatically-dominated.

6. We found that the significant radio/$\gamma$-ray correlations (i.e., $T1/T2/T3$) overlap with the timing when the average position angle of the jet components was higher than about 70°. This indicates that the global jet direction was mostly pointed toward the north direction in the image plane during the three periods. Thus, we consider that there might be a

preference in the jet direction causing the radio/$\gamma$-ray correlated behavior. This could be explained by a closer alignment of the jet with the line of sight, leading to an enhancement of the beaming effects.

# Chapter 6

# Conclusion

We have studied the relativistic jets of blazars, which is arguably the most powerful persistent objects in the Universe. Their extreme physical conditions cause various remarkable phenomena in the sky and draw our attention. Strong, variable $\gamma$-ray emission is one of the most interesting characteristics of blazar jets and is definitely linked with the jet activities. The goal of our works is to broaden our understanding of how the $\gamma$-ray flares are produced, where they originated, and its connection with the radio jet. Detailed observations of individual objects of the jets are essential to shed light on the questions. By monitoring their structures and fluxes when they are flaring at $\gamma$-rays, one can obtain the details and clues of the sources and supply a wealth of information as well. In this thesis, we tried to understand the physics of the $\gamma$-ray bright blazars (i.e., the radio/$\gamma$-ray connection) by studying four individual blazar jets (BL Lacertae, 1749+096, 3C 273, and 0716+714) with multi-waveband data including high-resolution VLBI datasets.

The common view is that the jet radio emission is produced via synchrotron process with energetic electrons, while the high energy ($\gamma$-ray) emission can either be generated through the IC process of low energy (e.g., infrared) seed photons or by hadronic processes (e.g., proton synchrotron). At present, the leptonic models became the most plausible scenario that the bulk of the gamma-ray emission is produced within the parsec-scale jet where the stationary structures (e.g., standing shocks) play an important role in the jet physics, rather than the hadronic models. Overall, our observational results support such leptonic models and can be explained by the presence of moving shocks and the radio core (the VLBI core). In the following, we list the details of our findings obtained from the four blazar jets.

In Chapter 2, multi-frequency radio observations of the KVN provided light curves and spectra of the jet of BL Lacertae at 22/43/86/129 GHz. The KVN data spanned three years (2013–2016) which overlap with two $\gamma$-ray flares occurred November 2013 and March 2015. During this period, radio emission of the jet decayed consistently as there was a huge radio flare in 2012. The decays were exponential with the timescales of 411±85 days at 22 GHz, 352±79 days at 43 GHz, 310±57 days at 86 GHz, and 283±55 days at 129 GHz. Using a synchrotron cooling mechanism, we found magnetic field strength of $B \sim 2\,\mu$T and electron Lorentz factors of $\gamma \sim 10\,000$. The frequency dependence of the observed decay timescales follows a power-law form. The estimated scale (i.e., $\tau \propto \nu^{-0.2}$) is in agreement with the concept of a standing recollimation which is supported by recent astrometric observations: a rapid decrease in the core shift at mm-wavelengths. As the major radio flare decays, spectrum of the KVN core changed from a flat feature ($\alpha \approx 0$) to a steep feature $\alpha \approx -0.5$. Such phenomenon can be explained by the generalized shock model that predicts the transition as the shock evolves. Interestingly, we do not find notable radio counterpart to the two $\gamma$-ray flares throughout the observations. This might be due to (1) the presence of different radio/$\gamma$-ray origins, (2) the complex intrinsic red-noise type variability at the observing radio frequencies, (3) variations in the viewing angle of the jet, and (4) the orphan $\gamma$-ray flares. Overall, the activities of BL Lacertae were normal during the $\gamma$-ray flares, but without a notable radio/$\gamma$-ray connection.

In Chapter 3, the blazar 1749+096 was investigated using multi-waveband (radio, optical, X-ray, and $\gamma$-ray) light curves and VLBA datasets to explore the physical backgrounds of two $\gamma$-ray flares in 2016: the first event in July and the second one in October. In particular, the first $\gamma$-ray flare was the historically huge event ($\sim 3 \times 10^{-6}\,\mathrm{ph\,cm^{-2}\,s^{-1}}$) in this source since the *Fermi*-LAT operated in 2008. This remarkable event accompanied by a notable spectral hardening on the plane of $\gamma$-ray photon index vs. time, which is rare to be observed. We consider a surge of $\gamma$-rays at higher $\gamma$-ray bands (energies) caused by strong shock acceleration, as the behind mechanism of the phenomenon. There is a hint of the $\gamma$-ray transition between the softer-when-brighter and harder-when-brighter trends around a flux value of $1.7 \times 10^{-7}\,\mathrm{ph\,cm^{-2}\,s^{-1}}$. The probable causes of this behavior can be either different emitting mechanisms or electron cooling timescale. A conventional picture of the radio/$\gamma$-ray connection is that a $\gamma$-ray flare precedes a radio counterpart (i.e., a flare). Interestingly, the first $\gamma$-ray flare was simultaneous with the flares at longer wavelengths (radio to X-rays). This directly indicates that the flares at all these wavebands originate from a same jet region and are physically correlated with each other. Radio observations are crucial to constrain the $\gamma$-ray production site as blazar jets become transparent at longer distances from the central engine with longer radio wavelengths (e.g., $> 10^4\ R_\mathrm{s}$ at radio frequencies, with $R_\mathrm{s}$ being the Schwarzschild radius). Thus, the contemporaneous radio-to-$\gamma$-ray flares imply that the $\gamma$-ray origin is the radio core. In addition, the emergence of the propagating polarized knot from the core suggests the presence of a moving disturbance (i.e., a new jet component). The polarized emission reached 230 mJy/beam with a notable EVPA swing by about $\sim 32^\circ$ in the radio core during the $\gamma$-ray flaring period. This further support a moving shock that passes through the core region. The second $\gamma$-ray flare is rather weak, compared to the first $\gamma$-ray event. During the flaring period, we found only an optical counterpart to it and a weak polarized knot moving down the jet through the core. Thus, we suggest the same scenario as the case for the first $\gamma$-ray flare, but with less pronounced Doppler boosting and energization.

In Chapter 4, jet activities of the blazar 3C 273 seen by the ALMA at 3 mm (100 GHz) and VLBA at 7 mm (43 GHz) were presented. We reported how the radio jet behaves during $\gamma$-ray flaring periods and a complicated inner structure of the jet (i.e., multiple recollimation shocks). By checking daily-binned $\gamma$-ray light curves, we found two notable $\gamma$-ray flares in 2015–2019. Overall, the $\gamma$-ray photon indices do not show a clear trend quantitatively. Owing to the jet opacity effects, observations at higher radio frequencies are important as the emission comes from more inner regions of the jet. The ALMA data meets this requirement. The DCF analysis revealed a highly correlated (i.e., a coefficient value of $\sim 0.7$) behavior between the 100 GHz radio emission and the $\gamma$-rays detected around 2016. From the VLBA observations, we found three stationary features including the core: $S1$ and $S2$ at about 0.16 and 0.33 mas from the core, respectively. These compact components were the major source of the observed radio emission throughout the observations. Given the strong polarized knots appeared at the jet upstream region and the evolution of the three emitting structures, we consider $S1$ and the core as the origin of the 2016 and 2017 $\gamma$-ray flares, respectively. As a powerful disturbance passes through these standing structures, freshly accelerated electrons produce enhanced $\gamma$-rays via the IC process. The observed brightness temperatures further support the idea. It peaked (e.g., up to $\sim\ 10^{12}\ K$) at $S1$ and the core for each of the $\gamma$-ray flares, thus meaning enhanced particle energy during the events. In particular, the 2017 $\gamma$-ray flare was lasted for a short duration (e.g., less than one day). For this flare, we rather compared it to the profile of the ALMA fluxes by modelling them in a exponential form. The simultaneous radio and $\gamma$-ray peaks further support the mm-wave core for the origin of the 2017 $\gamma$-ray flare. We also observed spatial displacements of the stationary components (i.e., $S2$). This phenomenon seems to be caused by changes in the physical conditions (e.g., variable opacity, core shuttling, and the RCS breakout) of the standing shocked regions as a propagating jet component enters these regions.

In Chapter 5, the radio/$\gamma$-ray connection was explored in the blazar 0716+714 with extensive radio data over a wide frequency range (centimeter to millimeter), including VLBA datasets. Many $\gamma$-ray flares appeared in the jet throughout our observations (2008–2019) and various phenomena that might be linked to the flares were reported. Our long-term data (10.5 yrs) clearly show that the observed radio emission of the source originated from the jet. 0716+714 is known to have rapid variability at the entire electromagnetic spectrum. Interestingly, the variability is severe even at radio frequencies (e.g., a few months). By using a reasonable approach, we identified three 1.5 yr periods ($T1/T2/T3$) that show significant radio/$\gamma$-ray correlations (i.e., two anti-correlations and one positive correlation) between the observed radio and $\gamma$-ray emission at the confidence level of 99%. Kinematic analysis with the 7 mm VLBA data revealed 14 moving jet components and three stationary features including the radio core. The superluminal motions of the moving knots range from 6 to 26 $c$ and the ejection rate was about 0.8 years. The three 1.5 yr periods coincided with the emergence of one or two moving jet components from the core. Hence, internal shock interaction between the over-dense regions (e.g., the RCS) and moving shocks, is considered to be the most likely physical process for the radio/$\gamma$-ray correlations in this study. The observed anti-correlation, such unusual phenomenon is tricky to understand its physical background, given the radio-leading feature and the unexpected frequency dependence in the delays (i.e., larger delays with higher frequencies). We consider that this behavior is caused by the combination of leading radio flares and delayed $\gamma$-ray dips. The $\gamma$-ray dips can be produced by efficient synchrotron with stronger magnetic field in the emitting regions. The $\gamma$-ray dissipation zone is assumed to be linked with the delays of the positive correlations in each of the three periods. In the case of $T1$ and $T2$, we suspect that the observed delays are overestimated due to the complicated kinematics in the inner jet regions (e.g., velocity changes and helices). For $T3$, the delay of the correlation indicates 5.5–6.5 pc from the central black hole for the production site of the $\gamma$-ray flare. Interestingly, the global jet direction pointed toward the north direction in the sky during the radio/$\gamma$-ray correlated periods. We suggest that the jet alignment toward out line of sight becomes closer with smaller viewing angle when the jet position angle is high enough ($\leq$ 70°). This would enhance the beaming effects.

In short, we conclude that the radio/$\gamma$-ray connection is tightly linked with the propagation of a strong disturbance in the jet. As moving shocks pass through a standing, shocked region with dense magnetic field and/or particle density (e.g., the radio core or other standing shocks), the shock-shock interactions accelerate the relativistic electrons and produce enhanced $\gamma$-ray emission via the IC process at parsec-scale distances from the jet apex. With the passage of a propagating knot, the random and turbulent magnetic fields in the emitting region can be compressed, thus resulting in variations in the polarized intensity and EVPA. This will appear in VLBI images with a strong, moving polarized knot as we observed.

As evident from the above results, investigation of the emission properties, multi-waveband correlation, and VLBI images play a key role in exploring the emission processes and physical conditions of the jets. For better understanding of the $\gamma$-ray flares (e.g., orphan $\gamma$-ray flares), however, it is strongly required to improve the observational techniques for better angular resolution, cadence (i.e., sampling interval), and sensitivity. These will be achieved by increasing length of the maximum baseline (e.g., space-VLBI arrays; e.g., RadioAstron or Millimetron), the number of radio antennas (e.g., ALMA or ngVLA), and the observing frequency (e.g., EHT; ~230 GHz). Theoretical approaches are also important as recent studies/observations have pointed out significant detections of neutrinos from blazars, geometrical effects (i.e., changes in the viewing angle), and the role of different mechanisms for particle acceleration (e.g., magnetic reconnection/turbulence). Thus, the corresponding models (e.g., lepto-hadronic models/turbulent multi-zone model) should be studied and developed with relevant observations.

# Bibliography

Abdo, A. A., Ackermann, M., Ajello, M., et al. 2009, ApJ, 700, 597

Abdo, A. A., Ackermann, M., Ajello, M., et al. 2010a, ApJ, 710, 1271

Abdo, A. A., Ackermann, M., Agudo, I., et al. 2010b, ApJ, 721, 1425

Abdo, A. A., Ackermann, M., Ajello, M., et al. 2010c, ApJ, 722, 520

Abdo, A. A., Ackermann, M., Ajello, M., et al. 2011, ApJ, 730, 101

Abeysekara, A. U., Benbow, W., Bird, R., et al. 2018, ApJ, 856, 95

Acero, F., Ackermann, M., Ajello, M., et al. 2015, ApJS, 218, 23

Agarwal, A., Mohan, P., Gupta, Alok C., et al. 2017, MNRAS, 469, 813

Agudo, I., Jorstad, S. G., Marscher, A. P., et al. 2011a, ApJL, 726, L13

Agudo, I., Marscher, A. P., Jorstad, S. G., et al. 2011b, ApJL, 735, L10

Ajello, M., Atwood, W. B., Baldini, L., et al. 2017, ApJS, 232, 18

Albert, J., Aliu, E., Anderhub, H., et al. 2007, ApJ, 666, L17

Algaba, J. -C., Zhao, G. -Y., Lee, S. -S., et al. 2015, JKAS, 48, 237

Algaba, J. -C., Lee, S. -S., Kim, D. -W., et al. 2018, ApJ, 852, 30

Angelakis, E., Fuhrmann, L., Myserlis, I., et al. 2019, A&A, 626, A60

Arlen, T., Aune, T., Beilicke, M., et al. 2013, ApJ, 762, 92

Asada, K., & Nakamura, M. 2012, ApJL, 745, L28

Asano, K., Takahara, F., Kusunose, M., et al. 2014, ApJ, 780, 64

Attridge, J. M., Wardle, J. F. C., & Homan, D. C. 2005, ApJ, 633, L85

Atwood, W. B., Abdo, A. A., Ackermann, M., et al. 2009, ApJ, 697, 1071

Bach, U., Krichbaum, T. P., Ros, E., et al. 2005, A&A, 433, 815

Bach, U., Krichbaum, T. P., Kraus, A., et al. 2006, A&A, 452, 83

Banasiński, P., Bednarek, W., & Sitarek, J. 2016, MNRAS, 463, L26

Banasiński, P., & Bednarek, W. 2018, ApJ, 864, 128

Baring, M. G., Böttcher, M., & Summerlin, E. J. 2017, MNRAS, 464, 4875

Bennett, C. L., Larson, D., Weiland, J. L., & Hinshaw, G. 2014, ApJ, 794, 135

Berton, M., Liao, N. H., La Mura, G., et al. 2018, A&A, 614, A148

Beuchert, T., Kadler, M., Perucho, M., et al. 2018, A&A, 610, A32

Blandford, R. D. & Znajek, R. L. 1977, MNRAS, 179, 433

Blandford, R. D. & Königl, A. 1979, ApJ, 232, 34

Blandford, R. D. & Payne, D. G. 1982, MNRAS, 199, 883

Blandford, R., Meier, D., & Readhead, A. 2019, ARA&A, 57, 467

Bloom, S. D., Bertsch, D. L., Hartman, R. C., et al. 1997, ApJ, 490, L145

Blumenthal, G. R., & Gould, R. J. 1970, RvMP, 42, 237

Boccardi, B., Krichbaum, T. P., Ros, E., & Zensus, J. A. 2017, A&ARv, 25, 4

Bonato, M., Liuzzo, E., Giannetti, A., et al. 2018, MNRAS, 478, 1512

Böttcher, M., & Chiang, J. 2002, ApJ, 581, 127

Böttcher, M., Marscher, A. P., Ravasio, M., et al. 2003, ApJ, 596, 847

Böttcher, M. 2005, ApJ, 621, 176

Böttcher, M., Harvey, J., Joshi, M., et al. 2005, ApJ, 631, 169

Böttcher, M., & Dermer, C. D. 2010, ApJ, 711, 445

Böttcher, M., Reimer, A., Sweeney, K., & Prakash, A. 2013, ApJ, 768, 54

Böttcher, M. 2019, Galaxies, 7, 20

Böttcher, M., & Baring, M. G. 2019, ApJ, 887, 133

Bouman, K. L., Johnson, M. D., Zoran, D., et al. 2016, arXiv:1512.01413

Bruni, G., Gómez, J. L., Casadio, C., et al. 2017, A&A, 604, A111

Butuzova, M. S. 2018, ARep, 62, 654

Casadio, C., Gómez, J. L., Jorstad, S. G., et al. 2015a, ApJ, 813, 51

Casadio, C., Gómez, J. L., Grandi, P., et al. 2015b, ApJ, 808, 162

Catanese, M., Akerlof, C. W., Biller, S. D., et al. 1997, ApJ, 480, 562

Cawthorne, T. V., Jorstad, S. G., & Marscher, A. P. 2013, ApJ, 772, 14

Cerruti, M., Zech, A., Boisson, C., & Inoue, S. 2015, MNRAS, 448, 910

Chatterjee, R., Bailyn, C. D., Bonning, E. W., et al. 2012, ApJ, 749, 191

Chen, X., Fossati, G., Liang, E. P., & Böttcher, M. 2011, MNRAS, 416, 2368

Chen, L. 2018, ApJS, 235, 39

Chidiac, C., Rani, B., Krichbaum, T. P., et al. 2016, A&A, 590, A61

Coogan, R. T., Brown, A. M., & Chadwick, P. M. 2016, MNRAS, 458, 354

Coppejans, D. L., Margutti, R., Guidorzi, C., et al. 2018, ApJ, 856, 56

Costamante, L., Cutini, S., Tosti, G., et al. 2018, MNRAS, 477, 4749

D'Ammando, F., Orienti, M., Larsson, J., & Giroletti, M. 2015, MNRAS, 452, 520

Danforth, C. W., Nalewajko, K., France, K., & Keeney, B. A. 2013, ApJ, 764, 57

Davis, S. W., & Tchekhovskoy, A. 2020, ARA&A, 58, 407

Del Zanna, L., Papini, E., Landi, S., et al. 2016, MNRAS, 460, 3753

Denn, G. R., Mutel, R. L., & Marscher, A. P. 2000, ApJS, 129, 61

Ding, N., Gu, Q. S., Geng, X. F., et al. 2019, ApJ, 881, 125

Dodson, R., Rioja, M. J., Molina, S. N., & Gómez, J. L. 2017, ApJ, 834, 177

Dotson, A., Georganopoulos, M., Kazanas, D., & Perlman, E. S. 2012, ApJL, 758, L15

Dotson, A., Georganopoulos, M., Meyer, E. T., & McCann, K. 2015, ApJ, 809, 164

Edelson, R. A., & Krolik, J. H. 1988, ApJ, 333, 646

Emmanoulopoulos, D., McHardy, I. M., & Papadakis, I. E. 2013, MNRAS, 433, 907

Ertley, C. 2014, AAS, 223, 118.03

Evans, P. A., Beardmore, A. P., Page, K. L., et al. 2007, A&A, 469, 379

Event Horizon Telescope Collaboration 2019, ApJL, 875, L1

Fanaroff, B. L., & Riley, J. M. 1974, MNRAS, 167, 31

Fath, E. A. 1909, PA, 17, 504

Formalont, E. B. 1999, Image Analysis, in: Taylor, G. B., Carilli, C. L., & Perley, R. A. (eds.), Synthesis Imaging in Radio Astronomy II, ASP Conf. Ser., 180, 301

Foschini, L., Ghisellini, G., Kovalev, Y. Y., et al. 2011, MNRAS, 413, 1671

Fossati, G., Maraschi, L., Celotti, A., et al. 1998, MNRAS, 299, 433

Fromm, C. M., Ros, E., Perucho, M., et al. 2013, A&A, 551, A32

Fuhrmann, L., Larsson, S., Chiang, J., et al. 2014, MNRAS, 441, 1899

Gabuzda, D. C., Sitko, M. L., & Smith, P. S. 1996, AJ, 112, 1877

Gaur, H., Gupta, A. C., Bachev, R., et al. 2015, A&A, 582, A103

Gehrels, N., Chincarini, G., Giommi, P., et al. 2004, ApJ, 611, 1005

Geng, X., Zeng, W., Rani, B., et al. 2020, ApJ, 904, 67

Ghisellini, G., Celotti, A., & Costamante, L. 2002, A&A, 386, 833

Ghisellini, G., Tavecchio, F., Foschini, L., & Ghirlanda, G. 2011, MNRAS, 414, 2674

Ghisellini, G., Tavecchio, F., Maraschi, L., et al. 2014, Nature, 515, 376

Giommi, P., Padovani, P., Polenta, G., et al. 2012, MNRAS, 420, 2899

Gómez, J. L., Martí, J. M., Marscher, A. P., et al. 1995, ApJ, 449, L19

Gómez, J. L., Martí, J. M., Marscher, A. P., et al. 1997, ApJ, 482, L33

Gómez, J. L., Roca-Sogorb, M., Agudo, I., et al. 2011, ApJ, 733, 11

Gómez, J. L., Lobanov, A. P., Bruni, G., et al. 2016, ApJ, 817, 96

Graff, P. B., Georganopoulos, M., Perlman, E. S., & Kazanas, D. 2008, ApJ, 689, 68

Guo, Y. C., Hu, S. M., Li, Y. T., & Chen, X. 2016, MNRAS, 460, 1790

Gurwell, M. A., Peck, A. B., Hostler, S. R., et al. 2007, ASPC, 375, 234

Hardcastle, M. J., & Croston, J. H. 2020, NewAR, 88, 101539

Harris, J., Daniel, M. K., & Chadwick, P. M. 2012, ApJ, 761, 2

Hazard, C., Mackey, M. B., & Shimmins, A. J. 1963, Nature, 197, 1037

Hervet, O., Boisson, C., & Sol, H. 2016, A&A, 592, A22

H.E.S.S Collaboration, Abdalla, H., Abramowski, A., et al. 2018, A&A, 619, A71

H.E.S.S Collaboration, Abdalla, H., Adam, R., et al. 2019, A&A, 627, A159

Hjorth, J. 2013, RSPTA, 371, 20120275

Hodgson, J. A., 2015, Ultra-high resolution observations of selected blazars, Ph.D. Thesis, Universität zu Köln

Hodgson, J. A., Lee, S. -S., Zhao, G. -Y., et al. 2016, JKAS, 49, 137

Hodgson, J. A., Krichbaum, T. P., Marscher, A. P., et al. 2017, A&A, 597, A80

Hodgson, J. A., Rani, B., Lee, S. -S., et al. 2018, MNRAS, 475, 368

Högbom, J. A. 1974, A&AS, 15, 417H

Homan, D. C., Ojha, R., Wardle, J. F. C., et al. 2002, ApJ, 568, 99

Hovatta, T., Tornikoski, M., Lainela, M., et al. 2007, A&A, 469, 899

Hovatta, T., Nieppola, E., Tornikoski, M., et al. 2008a, A&A, 485, 51

Hovatta, T., Lehto, H. J., & Tornikoski, M. 2008b, A&A, 488, 897

Hovatta, T., Valtaoja, E., Tornikoski, M., & Lähteenmäki, A. 2009, A&A, 494, 527

Hughes, P. A., Aller, H. D., & Aller, M. F. 1985, ApJ, 298, 301

Hughes, P. A., Aller, H. D., & Aller, M. F. 1991, ApJ, 374, 57

Hughes, P. A. 2005, ApJ, 621, 635

Hughes, P. A., Aller, M. F., & Aller, H. D. 2011, ApJ, 735, 81

Irwin J. A., 2007, Astrophysics: Decoding the Cosmos. Wiley-VCH Verlag, Wenheim, Germany

Jimenez-Gallardo, A., Massaro, F., Prieto, M. A., et al. 2020, ApJS, 250, 7

Jorstad, S. G., Marscher, A. P., Mattox, J. R., et al. 2001a, ApJS, 134, 181

Jorstad, S. G., Marscher, A. P., Mattox, J. R., et al. 2001b, ApJ, 556, 738

Jorstad, S. G., Marscher, A. P., Lister, M. L., et al. 2005, AJ, 130, 1418

Jorstad, S. G., Marscher, A. P., Smith, P. S., et al. 2013, ApJ, 773, 147

Jorstad, S. G., & Marscher, A. P. 2016, Galaxies, 4, 47

Jorstad, S. G., Marscher, A. P., Morozova, D. A., et al. 2017, ApJ, 846, 98

Joshi, M., & Böttcher, M. 2011, ApJ, 727, 21

Kadler, M., Ros, E., Perucho, M., et al. 2008, ApJ, 680, 867

Kaiser, C. R. 2006, MNRAS, 367, 1083

Karamanavis, V., Fuhrmann, L., Angelakis, E., et al. 2016a, A&A, 590, A48

Karamanavis, V., Fuhrmann, L., Krichbaum, T. P., et al. 2016b, A&A, 586, A60

Kardashev, N. S., Khartov, V. V., Abramov, V. V., et al. 2013, ARep, 57, 153

Kim, J. -Y., Trippe, S., Sohn, B. -W., et al. 2015, JKAS, 48, 285

Kim, D. -W., Trippe, S., Lee, S. -S., et al. 2017, JKAS, 50, 167

Kim, J. -Y., Krichbaum, T. P., Lu, R. -S., et al. 2018a, A&A, 616, A188

Kim, D. -W., Trippe, S., Lee, S. -S., et al. 2018b, MNRAS, 480, 2324

Kim, D. -W., Trippe, S., & Kravchenko, E. V. 2020, A&A, 636, A62

Koay, J. Y., Jauncey, D. L., Hovatta, T., et al. 2019, MNRAS, 489, 5365

Kochanek, C. S., Shappee, B. J., Stanek, K. Z., et al. 2017, PASP, 129, 104502

Kovalev, Y. Y., Kellermann, K. I., Lister, M. L., et al. 2005, AJ, 130, 2473

Kovalev, Y. Y., Lobanov, A. P., Pushkarev, A. B., & Zensus, J. A. 2008, A&A, 483, 759

Kravchenko, E. V., Kovalev, Y. Y., Hovatta, T., & Ramakrishnan, V. 2016, MNRAS, 462, 2747

Kravchenko, E. V., Gómez, J. L., Kovalev, Y. Y., et al. 2020, ApJ, 893, 68

Krawczynski, H., Hughes, S. B., Horan, D., et al. 2004, ApJ, 601, 151

Kudryavtseva, N. A., Gabuzda, D. C., Aller, M. F., & Aller, H. D. 2011, MNRAS, 415, 1631

Kushwaha, P., Singh, K. P., & Sahayanathan, S. 2014, ApJ, 796, 61

Kusunose, M., Takahara, F., & Li, H. 2000, ApJ, 536, 299

Laing, R. A. 1980, MNRAS, 193, 439

Lara, L., Giovannini, G., Cotton, W. D., et al. 2004, A&A, 415, 905

Larionov, V. M., Jorstad, S. G., Marscher, A. P., et al. 2013, ApJ, 768, 40

Lee, S. -S., Lobanov, A. P., Krichbaum, T. P., et al. 2008, AJ, 136, 159

Lee, S. -S., Han, M., Kang, S., et al. 2013, EPJWC, 61, 07007

Lee, S. -S., Petrov, L., Byun, D. -Y., et al. 2014, AJ, 147, 77

Lee, S. -S., Byun, D. -Y., Oh, C. -S., et al. 2015, JKAS, 48, 229

Lee, S. -S., Lobanov, A. P., Krichbaum, T. P., & Zensus, J. A. 2016a, ApJ, 826, 135

Lee, S. -S., Wajima, K., Algaba, J. -C., et al. 2016b, ApJS, 227, 8

Lee, J. W., Lee, S. -S., Hodgson, J. A., et al. 2017, ApJ, 841, 119

León-Tavares, J., Valtaoja, E., Tornikoski, M., et al. 2011, A&A, 532, A146

León-Tavares, J., Valtaoja, E., Giommi, P., et al. 2012, ApJ, 754, 23

León-Tavares, J., Chavushyan, V., Patiño-Álvarez, V., et al. 2013, ApJL, 763, L36

Leung, G. K., Takata, J., Ng, C. W., et al. 2014, ApJL, 797, L13

Lewis, T. R., Becker, P. A., & Finke, J. D. 2016, ApJ, 824, 108

Lewis, T. R., Finke, J. D., & Becker, P. A. 2018, ApJ, 853, 6

Li, H., & Kusunose, M. 2000, ApJ, 536, 729

Liao, N. H., Bai, J. M., Liu, H. T., et al. 2014, ApJ, 783, 83

Lico, R., Giroletti, M., Orienti, M., et al. 2014, A&A, 571, A54

Lico, R., Giroletti, M., Orienti, M., et al. 2017, A&A, 606, A138

Linford, J. D., Taylor, G. B., & Schinzel, F. K. 2012, ApJ, 757, 25

Liodakis, I. 2018, A&A, 616, A93

Liodakis, I., Hovatta, T., Huppenkothen, D., et al. 2018a, 866, 137

Liodakis, I., Romani, R. W., Filippenko, A. V., et al. 2018b, MNRAS, 480, 5517

Liodakis, I., Romani, R. W., Filippenko, A. V., et al. 2019, ApJ, 880, 32

Lisakov, M. M., Kovalev, Y. Y., Savolainen, T., et al. 2017, MNRAS, 468, 4478

Lister, M. L., Cohen, M. H., Homan, D. C., et al. 2009, AJ, 138, 1874

Lobanov, A. P. 1996, Ph.D. Thesis, New Mexico Institute of Mining and Technology, Socorro, NM, USA

Lobanov, A. P. 1998a, A&A, 330, 79

Lobanov, A. P. 1998b, A&AS, 132, 261

Lobanov, A. P., & Zensus, J. A. 1999, ApJ, 521, 509

Lu, R. S., Shen, Z. Q., Krichbaum, T. P., et al. 2012, A&A, 544, A89

MacDonald, N. R., Marscher, A. P., Jorstad, S. G., & Joshi, M. 2015, ApJ, 804, 111

MAGIC Collaboration, Ahnen, M. L., Ansoldi, S., et al. 2018, A&A, 619, A45

Marscher, A. P., Gear, W. K., & Travis, J. P. 1992, in Variability of Blazars, ed. E. Valtaoja & M. Valtonen, 85

Marscher, A. P. 1995, PNAS, 92, 11439

Marscher, A. P., Jorstad, S. G., D'Arcangelo, F. D., et al. 2008, Nature, 452, 966

Marscher, A. P., Jorstad, S. G., Larionov, V. M., et al. 2010, ApJL, 710, L126

Marscher, A. P., Jorstad, S. G., Larionov, V. M., et al. 2011, JApA, 32, 233

Marscher, A. P. 2012a, IJMPS, 8, 151

Marscher, A. P., Jorstad, S. G., Agudo, I., et al. 2012b, eConf C1111101, Fermi & Jansky: Our Evolving Understanding of AGN, arXiv:1204.6707

Marscher, A. P. 2014, ApJ, 780, 87

Marscher, A. P. 2016, Galaxies, 4, 37

Martí, J. M., Perucho, M., & Gómez, J. L. 2016, ApJ, 831, 163

Martí-Vidal, I., Krichbaum, T. P., Marscher, A., et al. 2012, A&A, 542, A107

Maselli, A., Massaro, E., Nesci, R., et al. 2010, A&A, 512, A74

Massaglia, S., Bodo, G., Rossi, P., et al. 2016, A&A, 596, A12

Massaro, F., Missaglia, V., Stuardi, C., et al. 2018, ApJS, 234, 7

Mastichiadis, A., & Kirk, J. G. 1997, A&A, 320, 19

Mattox, J. R., Bertsch, D. L., Chiang, J., et al. 1996, ApJ, 461, 396

Max-Moerbeck, W., Hovatta, T., Richards, J. L., et al. 2014a, MNRAS, 445, 428

Max-Moerbeck, W., Richards, J. L., Hovatta, T., et al. 2014b, MNRAS, 445, 437

McConnell, N. J., & Ma, C. -P. 2013, ApJ, 764, 184

Meyer, M., Scargle, J. D., & Blandford, R. D. 2019, ApJ, 877, 39

Mizuno, Y., Gómez, J. L., Nishikawa, K. -I., et al. 2015, ApJ, 809, 38

Nakamura, M., Asada, K., Hada, K., et al. 2018, ApJ, 868, 146

Nalewajko, K. 2013, MNRAS, 430, 1324

Nandikotkur, G., Jahoda, K. M., Hartman, R. C., et al. 2007, ApJ, 657, 706

Nemmen, R. S., Georganopoulos, M., Guiriec, S., et al. 2012, Science, 338, 1445

Netzer, H. 2013, The Physics and Evolution of Active Galactic Nuclei (New York: Cambridge)

Nilsson, K., Pursimo, T., Sillanpää, A., et al. 2008, A&A, 487, L29

Oh, J., Trippe, S., Kang, S., et al. 2015, JKAS, 48, 299

Orienti, M., Dallacasa, D., & Stanghellini, C. 2007, A&A, 475, 813

Orienti, M., Koyama, S., D'Ammando, F., et al. 2013, MNRAS, 428, 2418

O'Sullivan, S. P., & Gabuzda, D. C. 2009a, MNRAS, 400, 26

O'Sullivan, S. P., & Gabuzda, D. C. 2009b, MNRAS, 393, 429

Pacholczyk, A. G. 1970, Radio Astrophysics (San Francisco: Freeman)

Paliya, V. S., Sahayanathan, S., & Stalin, C. S. 2015, ApJ, 803, 15

Paliya, V. S. 2015, ApJL, 808, L48

Paliya, V. S., Zhang, H., Böttcher, M., et al. 2018, ApJ, 863, 98

Park, J., & Trippe, S. 2017, ApJ, 834, 157

Park, J., Hada, K., Kino, M., et al. 2019a, ApJ, 871, 257

Park, J., Lee, S. -S., Kim, J. -Y., et al. 2019b, ApJ, 877, 106

Park, J., Hada, K., Nakamura, M., et al. 2021, ApJ, 909, 76

Perucho, M., Martí, J. M., Cela, J. M., et al. 2010, A&A, 519, A41

Petropoulou, M., & Dimitrakoudis, S. 2015, MNRAS, 452, 1303

Piano, G., Munar-Adrover, P., Pacciani, L., et al. 2018, A&A, 616, A65

Planck Collaboration, Ade, P. A. R., Aghanim, N., et al. 2016, A&A, 594, A13

Plavin, A. V., Kovalev, Y. Y., Pushkarev, A. B., & Lobanov, A. P. 2019, MNRAS, 485, 1822

Potter, W. J., & Cotter, G. 2013, MNRAS, 431, 1840

Press, W. H. 1978, Flicker Noises in Astronomy and Elsewhere, Comments Astrophys., 7, 103

Prince, R., Majumdar, P., & Gupta, N. 2017, ApJ, 844, 62

Prince, R. 2019, ApJ, 871, 101

Pushkarev, A. B. 2001, Astron. Rep., 45, 667

Pushkarev, A. B., Kovalev, Y. Y., & Lobanov, A. P. 2008, in Proc. of The 9th European VLBI Network Symposium on The role of VLBI in the Golden Age for Radio Astronomy and EVN Users Meeting Conf. [arXiv:0812.4617]

Pushkarev, A. B., Kovalev, Y. Y., & Lister, M. L. 2010, ApJL, 722, L7

Pushkarev, A. B., Hovatta, T., Kovalev, Y. Y., et al. 2012, A&A, 545, A113

Pushkarev, A. B., Kovalev, Y. Y., Lister, M. L., & Savolainen, T. 2017, MNRAS, 468, 4992

Pushkarev, A. B., Butuzova, M. S., Kovalev, Y. Y., & Hovatta, T. 2019, MNRAS, 482, 2336

Raiteri, C. M., Villata, M., D'Ammando, F., et al. 2013, MNRAS, 436, 1530

Raiteri, C. M., Villata, M., Acosta-Pulido, J. A., et al. 2017, Nature, 552, 374

Ramakrishnan, V., León-Tavares, J., Rastorgueva-Foi, E. A., et al. 2014, MNRAS, 445, 1636

Ramakrishnan, V., Hovatta, T., Nieppola, E., et al. 2015, MNRAS, 452, 1280

Ramakrishnan, V., Hovatta, T., Tornikoski, M., et al. 2016, MNRAS, 456, 171

Rani, B., Gupta, A. C., Bachev, R., et al. 2011, MNRAS, 417, 1881

Rani, B., Krichbaum, T. P., Fuhrmann, L., et al. 2013a, A&A, 552, A11

Rani, B., Lott, B., Krichbaum, T. P., et al. 2013b, A&A, 557, A71

Rani, B., Krichbaum, T. P., Marscher, A. P., et al. 2014, A&A, 571, L2

Rani, B., Krichbaum, T. P., Marscher, A. P., et al. 2015, A&A, 578, A123

Rani, B., Jorstad, S. G., Marscher, A. P., et al. 2018, ApJ, 858, 80

Richards, J. L., Max-Moerbeck, W., Pavlidou, V., et al. 2011, ApJS, 194, 29

Rioja, M. J., & Dodson, R. 2011, AJ, 141, 114

Rioja, M. J., Dodson, R., Jung, T. -H., et al. 2014, AJ, 148, 84

Rioja, M. J., Dodson, R., Jung, T., & Sohn, B. 2015, AJ, 150, 202

Roberts, D. H., Wardle, J. F. C., & Brown, L. F. 1994, ApJ, 427, 718

Robertson, D. R. S., Gallo, L. C., Zoghbi, A., & Fabian, A. C. 2015, MNRAS, 453, 3455

Ros, E., Zensus, J. A., & Lobanov, A. P. 2000, A&A, 354, 55

Russell, H. R., McDonald, M., McNamara, B. R., et al. 2017, ApJ, 836, 130

Rybicki, G. B. & Lightman, A. P. 1997, Radiative Processes in Astrophysics (Weinheim: Wiley-VCH)

Sądowski, A., Narayan, R., Penna, R., & Zhu, Y. 2013, MNRAS, 436, 3856

Sambruna, R. M., Ghisellini, G., Hooper, E., et al. 1999, ApJ, 515, 140

Sandrinelli, A., Covino, S., Treves, A., et al. 2017, A&A, 600, A132

Schinzel, F. K. 2011, Physics and Kinematics of the Parsec Scale Jet of the Quasar 3C 345, Ph.D. Thesis, Universität zu Köln

Schinzel, F. K., Lobanov, A. P., Taylor, G. B., et al. 2012, A&A, 537, A70

Seyfert, C. K. 1943, ApJ, 97, 28

Shah, Z., Jithesh, V., Sahayanathan, S., et al. 2019, MNRAS, 484, 3168

Shappee, B. J., Prieto, J. L., Grupe, D., et al. 2014, ApJ, 788, 48

Shepherd, M. C., Pearson, T. J., & Taylor, G. B. 1994, BAAS, 26, 987

Shepherd, M. C. 1997, ASPC, 125, 77S

Shklovsky, I. S. 1955, AZh, 32, 215

Sikora, M., Begelman, M. C., & Rees, M. J. 1994, ApJ, 421, 153

Sironi, L., & Spitkovsky, A. 2014, ApJL, 783, L21

Sokolov, A., Marscher, A. P., & McHardy, I. M. 2004, ApJ, 613, 725

Sokolov, A., & Marscher, A. P. 2005, ApJ, 629, 52

Spada, M., Ghisellini, G., Lazzati, D., & Celotti, A. 2001, MNRAS, 325, 1559

Stickel, M., Fried, J. W., & Kühr, H. 1988, A&A, 191, L16

Stirling, A. M., Cawthorne, T. V., Stevens, J. A., et al. 2003, MNRAS, 341, 405

Strauss, M. A., Huchra, J. P., Davis, M., et al. 1992, ApJS, 83, 29

Tavecchio, F., Ghisellini, G., Bonnoli, G., & Ghirlanda, G. 2010, MNRAS, 405, L94

Tchekhovskoy, A., & Bromberg, O. 2016, MNRAS, 461, L46

Teraesranta, H., Tornikoski, M., Mujunen, A., et al. 1998, A&AS, 132, 305

The Fermi-LAT Collaboration, Abdollahi, S., Acero, F., et al. 2019, arXiv:1902.10045

The Fermi-LAT Collaboration, Baldini, L., Ballet, J., et al. 2021, arXiv:2106.00100

Trippe, S., Krips, M., Piétu, V., et al. 2011, A&A, 533, A97

Trippe, S., Neri, R., Krips, M., et al. 2012, A&A, 540, A74

Uemura, M., Itoh, R., Liodakis, I., et al. 2017, PASJ, 69, 96

Uttley, P., McHardy, I. M., & Papadakis, I. E. 2002, MNRAS, 332, 231

Valtaoja, E., & Teräsranta, H., Urpo, S., et al. 1992, A&A, 254, 71

Valtaoja, E., & Teräsranta, H. 1995, A&A, 297, L13

Valtaoja, E., Lähteenmäki, A., Teräsranta, H., & Lainela, M. 1999, ApJS, 120, 95

van der Westhuizen, I. P., van Soelen, B., Meintjes, P. J., & Beall, J. H. 2019, MNRAS, 485, 4658

van Moorsel, G., Kemball, A., & Greisen, E. 1996, ASPC, 101, 37

Vercellone, S. 2019, Rendiconti Lincei. Scienze Fisiche e Naturali, 30, S131

Villata, M., Raiteri, C. M., Aller, H. D., et al. 2004, A&A, 424, 497

Vittorini, V., Tavani, M., Paggi, A., et al. 2009, ApJ, 706, 1433

Vol'vach, A. E., Kutkin, A. M., Vol'vach, L. N., et al. 2013, ARep, 57, 34

Weaver, Z. R., Balonek, T. J., Jorstad, S. G., et al. 2019, ApJ, 875, 15

Wehrle, A. E., Marscher, A. P., Jorstad, S. G., et al. 2012, ApJ, 758, 72

Wehrle, A. E., Grupe, D., Jorstad, S. G., et al. 2016, ApJ, 816, 53

Wierzcholska, A., & Siejkowski, H. 2015, MNRAS, 452, L11

Williamson, K. E., Jorstad, S. G., Marscher, A. P., et al. 2014, ApJ, 789, 135

Woosley, S. E., & Bloom, J. S. 2006, ARA&A, 44, 507

Yang, H., Yuan, W., Yao, S., et al. 2018, MNRAS, 477, 5127

Zhang, H., Chen, X., Böttcher, M., et al. 2015, ApJ, 804, 58

Zhang, F., Zhao, C., Han, S., et al. 2021, RemS, 13, 1226

Zhao, G. -Y., Jung, T., Dodson, R., et al. 2015, PKAS, 30, 629

Zhao, G. -Y., Algaba, J. -C., Lee, S. -S., et al. 2018, AJ, 155, 26

# Appendix A

# Appendices for Chapter 4

## A.1 Gaussian model-fit parameters

Parameters of the 43 GHz components obtained from Gaussian model fits.

| Date | MJD | Comp.[a] | Flux<br>(Jy) | Distance[b]<br>(mas) | Angle[c]<br>(°) | Size<br>(mas) | $B^d_{\mathrm{maj}}$<br>(mas) | $B^d_{\mathrm{min}}$<br>(mas) | $B^d_{\mathrm{PA}}$<br>(°) | rms[e]<br>(mJy/beam) | Peak[f]<br>(Jy/beam) |
|---|---|---|---|---|---|---|---|---|---|---|---|
| 2015-12-05 | 57361 | Core | 2.24 | 0.00 | – | 0.09 | 0.45 | 0.15 | −12.70 | 4.80 | 4.16 |
| | | S1 | 3.76 | 0.16 | −145.03 | 0.05 | | | | | |
| | | S2 | 1.19 | 0.36 | −135.78 | 0.16 | | | | | |
| | | J1 | 0.72 | 0.71 | −130.74 | 0.13 | | | | | |
| | | J2 | 0.67 | 0.87 | −139.77 | 0.12 | | | | | |
| | | J3 | 0.70 | 0.91 | −131.31 | 0.08 | | | | | |
| | | J4 | 0.05 | 1.60 | −131.37 | 0.09 | | | | | |
| | | J5 | 0.21 | 3.02 | −139.39 | 0.36 | | | | | |
| | | J6 | 0.12 | 3.12 | −133.67 | 0.12 | | | | | |
| | | J7 | 0.29 | 5.93 | −140.29 | 0.92 | | | | | |
| 2016-01-01 | 57388 | Core | 2.02 | 0.00 | – | 0.08 | 0.43 | 0.17 | −7.84 | 10.76 | 5.31 |
| | | S1 | 4.77 | 0.16 | −145.78 | 0.04 | | | | | |
| | | S2 | 1.09 | 0.37 | −135.58 | 0.15 | | | | | |
| | | J1 | 1.76 | 0.87 | −134.01 | 0.22 | | | | | |
| | | J2 | 0.08 | 1.31 | −139.52 | 0.13 | | | | | |
| | | J3 | 0.29 | 3.10 | −136.72 | 0.48 | | | | | |
| | | J4 | 0.22 | 5.95 | −140.31 | 0.82 | | | | | |

**Table A.1.** [a] Higher Jx numbers correspond to larger downstream distances from the core; [b] Distance from the core; [c] Position angle relative to the core component; [d] FWHM of the elliptical beam: the major and minor axis, and the inclination angle of the major axis with respect to north; [e] rms noise of the residual map; [f] Map peak of the CLEAN map.

Parameters of the 43 GHz components obtained from Gaussian model fits.

| Date | MJD | Comp.[a] | Flux (Jy) | Distance[b] (mas) | Angle[c] (°) | Size (mas) | $B^d_{\mathrm{maj}}$ (mas) | $B^d_{\mathrm{min}}$ (mas) | $B^d_{\mathrm{PA}}$ (°) | rms[e] (mJy/beam) | Peak[f] (Jy/beam) |
|---|---|---|---|---|---|---|---|---|---|---|---|
| 2016-02-01 | 57419 | Core | 1.74 | 0.00 | – | 0.04 | 0.39 | 0.14 | −12.80 | 17.55 | 6.73 |
| | | S1 | 2.44 | 0.15 | −130.03 | 0.02 | | | | | |
| | | S2 | 6.23 | 0.27 | −141.26 | 0.06 | | | | | |
| | | J1 | 1.21 | 0.46 | −133.62 | 0.19 | | | | | |
| | | J2 | 1.56 | 0.95 | −134.40 | 0.15 | | | | | |
| | | J3 | 0.60 | 1.08 | −130.51 | 0.07 | | | | | |
| | | J4 | 0.08 | 1.34 | −140.46 | 0.11 | | | | | |
| | | J5 | 0.47 | 3.24 | −135.71 | 0.59 | | | | | |
| 2016-03-19 | 57466 | Core | 1.82 | 0.00 | – | 0.07 | 0.42 | 0.17 | −6.95 | 7.95 | 8.39 |
| | | S1 | 1.61 | 0.15 | −132.52 | 0.07 | | | | | |
| | | S2 | 8.50 | 0.32 | −140.96 | 0.07 | | | | | |
| | | J1 | 0.38 | 0.44 | −127.67 | 0.10 | | | | | |
| | | J2 | 0.19 | 0.72 | −133.32 | 0.06 | | | | | |
| | | J3 | 0.43 | 0.90 | −128.88 | 0.18 | | | | | |
| | | J4 | 1.99 | 1.12 | −133.70 | 0.20 | | | | | |
| | | J5 | 0.26 | 3.39 | −136.05 | 0.40 | | | | | |
| | | J6 | 0.26 | 6.18 | −140.76 | 0.84 | | | | | |

**Table A.1.** Continued.

Parameters of the 43 GHz components obtained from Gaussian model fits.

| Date | MJD | Comp.[a] | Flux<br>(Jy) | Distance[b]<br>(mas) | Angle[c]<br>(°) | Size<br>(mas) | $B^d_{maj}$<br>(mas) | $B^d_{min}$<br>(mas) | $B^d_{PA}$<br>(°) | rms[e]<br>(mJy/beam) | Peak[f]<br>(Jy/beam) |
|---|---|---|---|---|---|---|---|---|---|---|---|
| 2016-04-23 | 57501 | Core | 1.86 | 0.00 | – | 0.03 | 0.37 | 0.15 | −3.62 | 17.22 | 9.10 |
| | | S1 | 1.54 | 0.15 | −132.81 | 0.08 | | | | | |
| | | S2 | 10.49 | 0.37 | −139.47 | 0.09 | | | | | |
| | | J1 | 0.61 | 0.62 | −129.17 | 0.29 | | | | | |
| | | J2 | 0.61 | 0.99 | −131.57 | 0.14 | | | | | |
| | | J3 | 2.06 | 1.22 | −132.81 | 0.20 | | | | | |
| | | J4 | 0.18 | 3.49 | −136.15 | 0.45 | | | | | |
| 2017-04-16 | 57859 | Core | 2.05 | 0.00 | – | 0.07 | 0.40 | 0.15 | −8.33 | 7.04 | 1.93 |
| | | S1 | 1.11 | 0.20 | −135.43 | 0.09 | | | | | |
| | | S2 | 0.25 | 0.40 | −141.68 | 0.12 | | | | | |
| | | J1 | 1.07 | 0.81 | −139.24 | 0.23 | | | | | |
| | | J2 | 0.03 | 1.06 | −141.93 | 0.12 | | | | | |
| | | J3 | 0.72 | 1.28 | −130.05 | 0.26 | | | | | |
| | | J4 | 0.26 | 1.75 | −137.87 | 0.18 | | | | | |
| | | J5 | 0.52 | 2.00 | −132.47 | 0.25 | | | | | |

**Table A.1.** Continued.

Parameters of the 43 GHz components obtained from Gaussian model fits.

| Date | MJD | Comp.[a] | Flux (Jy) | Distance[b] (mas) | Angle[c] (°) | Size (mas) | $B^d_{\mathrm{maj}}$ (mas) | $B^d_{\mathrm{min}}$ (mas) | $B^d_{\mathrm{PA}}$ (°) | rms[e] (mJy/beam) | Peak[f] (Jy/beam) |
|---|---|---|---|---|---|---|---|---|---|---|---|
| 2017-05-13 | 57886 | Core | 2.32 | 0.00 | – | 0.04 | 0.35 | 0.15 | −4.92 | 15.88 | 3.34 |
| | | S1 | 2.55 | 0.14 | −144.45 | 0.06 | | | | | |
| | | S2 | 0.99 | 0.34 | −138.72 | 0.12 | | | | | |
| | | J1 | 1.09 | 0.77 | −139.49 | 0.27 | | | | | |
| | | J2 | 0.83 | 1.03 | −140.71 | 0.25 | | | | | |
| | | J3 | 0.62 | 1.27 | −129.14 | 0.16 | | | | | |
| | | J4 | 0.88 | 1.78 | −134.10 | 0.37 | | | | | |
| | | J5 | 0.48 | 2.19 | −133.86 | 0.18 | | | | | |
| 2017-06-08 | 57912 | Core | 3.72 | 0.00 | – | 0.07 | 0.38 | 0.16 | −2.67 | 13.40 | 5.04 |
| | | S1 | 3.60 | 0.15 | −142.58 | 0.05 | | | | | |
| | | S2 | 1.26 | 0.32 | −137.83 | 0.13 | | | | | |
| | | J1 | 0.63 | 0.78 | −142.68 | 0.14 | | | | | |
| | | J2 | 1.01 | 0.97 | −138.03 | 0.21 | | | | | |
| | | J3 | 0.67 | 1.26 | −129.38 | 0.23 | | | | | |
| | | J4 | 0.66 | 1.54 | −131.76 | 0.20 | | | | | |
| | | J5 | 0.32 | 1.92 | −139.27 | 0.11 | | | | | |
| | | J6 | 0.76 | 2.12 | −133.16 | 0.25 | | | | | |

**Table A.1.** Continued.

Parameters of the 43 GHz components obtained from Gaussian model fits.

| Date | MJD | Comp.[a] | Flux | Distance[b] | Angle[c] | Size | $B^d_{\mathrm{maj}}$ | $B^d_{\mathrm{min}}$ | $B^d_{\mathrm{PA}}$ | rms[e] | Peak[f] |
|---|---|---|---|---|---|---|---|---|---|---|---|
|  |  |  | (Jy) | (mas) | (°) | (mas) | (mas) | (mas) | (°) | (mJy/beam) | (Jy/beam) |
| 2017-07-03 | 57937 | Core | 4.41 | 0.00 | – | 0.10 | 0.44 | 0.15 | −12.60 | 11.50 | 4.87 |
|  |  | S1 | 3.67 | 0.17 | −145.42 | 0.05 |  |  |  |  |  |
|  |  | S2 | 0.93 | 0.32 | −140.05 | 0.12 |  |  |  |  |  |
|  |  | J1 | 0.08 | 0.59 | −147.08 | 0.09 |  |  |  |  |  |
|  |  | J2 | 0.71 | 0.83 | −141.58 | 0.15 |  |  |  |  |  |
|  |  | J3 | 0.53 | 1.02 | −138.43 | 0.14 |  |  |  |  |  |
|  |  | J4 | 0.54 | 1.20 | −129.23 | 0.25 |  |  |  |  |  |
|  |  | J5 | 0.76 | 1.55 | −132.29 | 0.28 |  |  |  |  |  |
|  |  | J6 | 0.36 | 1.95 | −138.81 | 0.24 |  |  |  |  |  |
|  |  | J7 | 0.56 | 2.18 | −133.08 | 0.23 |  |  |  |  |  |
| 2017-08-06 | 57971 | Core | 1.59 | 0.00 | – | 0.04 | 0.36 | 0.13 | −10.5 | 9.36 | 2.91 |
|  |  | S1 | 2.37 | 0.12 | −127.25 | 0.06 |  |  |  |  |  |
|  |  | S2 | 2.00 | 0.26 | −139.42 | 0.04 |  |  |  |  |  |
|  |  | J1 | 0.26 | 0.41 | −137.03 | 0.05 |  |  |  |  |  |
|  |  | J2 | 0.56 | 0.90 | −140.27 | 0.19 |  |  |  |  |  |
|  |  | J3 | 0.61 | 1.19 | −134.08 | 0.30 |  |  |  |  |  |
|  |  | J4 | 0.29 | 1.47 | −128.01 | 0.24 |  |  |  |  |  |
|  |  | J5 | 0.52 | 1.87 | −135.26 | 0.34 |  |  |  |  |  |
|  |  | J6 | 0.33 | 2.31 | −133.10 | 0.29 |  |  |  |  |  |

**Table A.1.** Continued.

# 요 약

활동성은하핵 (AGN)들의 상대론적 제트는 우주에서 가장 강력하며 영속적인 에너지 소스들 중에 하나이다. 고에너지 천체물리분야 뿐만 아니라 은하와 성단의 진화에 중요한 역할을 함에 따라, AGN 제트들에 대한 연구는 가치있으며 전도유망하다. 전파에서 밝은 AGN (radio-loud AGN)들 중, 그들의 제트가 뻗어나가는 축과 우리의 시선방향 사이의 각도가 매우 작은 (약 5도 이내) AGN들은 블레이저 (Blazar)로써 분류된다. Blazar들의 대표적인 특징 중 하나는 그들의 제트로부터 나오는 강력한 감마선 방출이다. 하지만 고에너지 망원경들의 공간분해능이 충분하지 못하기 때문에, 그러한 고에너지 빛 방출에 대한 우리의 이해는 제한되어 있고, 이에 따라 Blazar 감마선 폭발의 기원은 현재 활발한 논쟁 중에 있다. 그러한 고에너지 빛의 방출기작과 기원을 탐구하기 위해서, 본 저자는 최근 강한 감마선 방출을 보인 몇 개의 개별 Blazar들을 연구하였다: BL Lacertae, OT 081 (1749+096), 3C 273, 그리고 0716+714. 이 연구들에서 본 저자는 감마선 폭발 기간 동안에 제트들의 빛, 구조, 그리고 운동학이 어떻게 변화하는지를 조사하였으며, 이를 위해 그들의 다파장 (전파–감마선) 변광곡선 및 최장기선 간섭계 (VLBI) 데이터들을 시간도메인과 이미지면 위에서 분석하였다.

Blazar의 한 유형인 BL Lac object에 속하며, 또한 해당 타입의 원형이기도 한 BL Lacertae가 한국 VLBI 관측기인 KVN를 이용해 연구되어졌다. 22, 43, 86, 그리고 129 GHz에서 얻어진 전파코어의 변광곡선을 이용하여 얻어진 제트의 특성들이 나타내어졌다. 우리의 관측데이터는 하나의 강력한 전파 폭발의 감쇄 부분을 포함한다. 지수함수적 감쇄의 시간규모 ($\tau$) 들은 다음의 관계식을 따른다: $\tau \propto \nu^{-0.2}$, $\nu$는 관측주파수를 나타낸다. 이는 불투명도 효과 (Core shift)로부터 예상되는 결과에 비해 매우 얕다. KVN의 다주파수 동시관측은 전파 방출 빛에 대한 분광학적 분석을 가능하게 해준다. 시간과 전파 주파수에 대한 분광지수 (Spectral index)의 변화는 Recollimation shock 모델과 Generalized shock 모델들을 지지한다.

OT 081은 조밀하고 소형인 제트를 지닌 Blazar이다. 많은 VLBI 이미지들에서 해당 제트는 바깥쪽으로 연장된 눈에 띄는 구조들 없이 단순한 포인트와 같은 형태의 구조를 보여준다. 이 소스는 주목할 만한 감마선 폭발없이 전파에서 지속적으로 밝아왔었다. 그러나 2016년도에 이 타겟소스에 대해서 역사적으로 강력한 감마선 폭발이 발생하였

었다. 이 현상을 조사하기 위해, 다파장 데이터들이 사용되었다: KVN과 OVRO (전파), ASAS-SN (광학), Swift-XRT (엑스선), 그리고 *Fermi*-LAT (감마선). 2016 감마선 폭발이 낮은 주파수대 (전파부터 엑스선까지)의 방출 빛들과 상당한 상관관계를 가지고 있음이 드러났다. VLBA 관측데이터를 이용함으로써, 우리는 또한 이 감마선 폭발이 전파코어로부터 나와 제트의 하류로 전파/이동해나가는 편광 컴포넌트 (Knot)의 출현을 수반했었음을 찾았다. 이러한 모든 증거들을 조합해봄으로써, 우리는 전파코어가 감마선 폭발의 기원이라 결론지었다.

Blazar들은 두 가지 유형으로 나뉘어 질 수 있다: 넓은 광학 방출선의 존재/부재에 따라, Flat-Spectrum Radio Quasar (FSRQ) 그리고 BL Lac object. 근래의 연구결과들은 FSRQ들로부터 나오는 감마선들이 Broad-Line Region (BLR) 너머의 지역에서 기원함을 시사했었다. 이는 전파코어가 위치해 있을 것으로 여겨지는, 중앙의 블랙홀로부터 몇 파섹 (parsec) 떨어진 거리를 암시한다. 이러한 아이디어에 착안하여, 본 저자는 가장 강하며 유명한 Blazar들 중 하나인 3C 273 (FSRQ)로부터 발생한 최근의 두 감마선 폭발들을 조사하였다. 분석은 ALMA, VLBA, 그리고 *Fermi*-LAT 데이터들을 이용하여 수행되어졌다. 전파와 감마선 변광곡선 사이의 상관관계를 알아보기 위해, Discrete Correlation Function (DCF)가 사용되었다. 우리의 결과들은 매우 조밀한 Multiple standing shock들이 3C 273의 제트 안에서 관측된 감마선 폭발들의 기원임을 나타낸다.

0716+714는 모든 전자기파 영역에서 극적인 변광성을 보이는 것으로 알려져 있다. 우리의 사전조사결과로 밝혀진 해당 소스에서의 전파와 감마선 방출 빛 사이의 역상관관계 (anti-correlation)는 우리가 0716+714 제트 안에서 전파/감마선 연관성에 대한 자세한 연구를 개시하게 되는 동기가 되었다. 기록 보관된 (archival) 다파장 데이터들 (SMA, Metsähovi, OVRO, *Fermi*-LAT, 그리고 VLBA)이 사용되었으며, 데이터들 간의 상관관계 분석은 변광곡선들의 모델링과 시뮬레이션을 이용해 수행되어졌다. 그 결과, 우리는 세 개의 중대한 전파/감마선 상관관계를 찾았다: 두 개의 역상관관계들과 하나의 양적 상관관계. 우리는 또한 감마선 폭발들이 발생하는 동안 파섹 규모에서의 제트가 어떠한 활동성을 보이는지를 알아보기 위해 VLBA 데이터를 분석하였다. 결과들로부터 얻어진 모든 증거를 토대로 우리는 제트 내에서 감마선 폭발들의 기원을 한정하고, 관측된 상관관계들의 배경기작으로써 이동하는 섭동이 전파코어를 지나면서 유발되는 Internal-shock interaction을 제안한다.

극적인 물리적 상태와 다양한 시나리오 및 가능성들 때문에, Blazar의 상대론적 제트들에 대한 물리는 복잡하며 까다롭다. 고분해능 VLBI 어레이들을 통한 제트의 자세한 관측은 현재 제트물리에서의 쟁점들을 해결할 가장 좋은 방법이다. 본 학위논문은 Blazar 감마선 폭발들의 특성에 대한 새로운 관측적 데이터와 결과들을 보여주며, 4개의 주목할 만한 Blazar들의 경우들에 대하여 풍부한 정보를 제공함으로써 학계에 기여한다. 본 학위논문에 수록된 개별 연구들은 다음과 같은 결론을 내린다: (1) Blazar의 감마선 폭발들은 제트 내에서 다중 방출 영역을 가진다 (중앙 블랙홀로부터 subpc/pc 규모의 거리) 그리고 (2) subpc/pc 규모의 거리에서 제트의 하류를 따라 전파해나가는 Shock/섭동들의 이동이 감마선 폭발을 유발한다 (특별히 그들이 Standing shock 구조들을 지나갈 때).

**주요어:** 은하: 활동성 – 은하: 제트 – 전파 연속 방출선: 은하 – 개별: BL Lacertae, 1749+096, 3C 273, 0716+714 – 기술: 빛의 간섭현상 – 기기: 전파간섭계 – 감마선: 은하

**학번:** 2014-21383

# 감사의 글

2014년 3월, 입학한 후로 벌써 7년 하고도 6개월의 시간이 흘렀습니다. 매년 졸업하는 선배님들의 졸업축하연을 3층 휴게실에서 보며 “나도 언젠가는 졸업할 수 있을까?” 하는 생각을 늘 했던 기억이 납니다. 결국 저에게도 이렇게 졸업이라는 영예로운 시간이 찾아왔네요. 초등학교를 입학한 이후로 군복무 기간 2년을 제외하면 늘 항상 학생 신분이었는데, 이제 정말로 학교라는 곳을 떠나 진정한 사회인으로써 밖으로 나간다고 생각하니 속시원하면서도 뿌듯하고, 감격스럽기도 하네요. 우선은 오늘날 제가 박사졸업이라는 성취를 얻기까지 많은 고마운 분들이 있었습니다.

먼저 저의 지도교수님이신 Sascha Trippe 교수님께 감사드립니다; Professor, I really appreciate your continuous support and guidance for me. It was my great pleasure doing my PhD work under your supervision. You have always been nice to me :) I hope we can work together again in the future. 저의 박사학위논문 심사위원을 맡아주신 구본철, 임명신 교수님과 이상성, 변도영 박사님께도 깊은 감사의 말씀을 전하고 싶습니다. 입학하고 구본철 교수님의 수업을 많이 듣기도 했고, 교수님 수업의 조교를 자주 맡기도 했었습니다. 학자로써, 교육자로써 늘 흠모해왔던 교수님께서 2014년도 2학기 종강할 무렵 제게 해주셨던, 점점 나아지고 있다는 칭찬의 말씀이 저에게 얼마나 큰 기쁨과 격려가 되었는지 모릅니다. 학위 과정 동안 교수님께 들었던 그 칭찬의 말씀이 이따금 떠오르며 저에게 참 많은 힘이 되었었습니다. 감사합니다 교수님. 항상 학생들을 존중하고 따뜻하게 대해 주셨던 임명신 교수님 또한 기억에 많이 남습니다. 저도 훗날 교수님처럼 주위에 존경을 받는 따뜻하고 인자한 학자가 될 수 있도록 노력하겠습니다. 연구를 시작한 처음 시기에 저를 많은 부분 이끌어 주시고 가르침을 주신 이상성 박사님께 감사드립니다. 박사님은 저에게 어찌 보면 또 다른 지도교수님과도 같은 분이십니다. 항상 박사님께 받은 도움과 응원 잊지 않고 더 열심히 정진해 나아가겠습니다. 한때 KVN 관측과 관련하여 저와 저희팀 멤버들이 늦은 저녁 혹은 새벽에 연락드릴 일이 잦았었던 변도영 박사님께도 감사드립니다. KVN의 아버지라 불리우는 박사님의 헌신과 노력 덕분에 저희들이 KVN을 가지고 연구해나갈 수 있었습니다. 감사드립니다 박사님. 저의 학위 과정 후반부에서 가장 큰 도움과 힘이 되어주신 Evgeniya V. Kravchenko 박사님께도 깊

은 감사의 말씀을 드립니다 (Jenny, I am grateful for your support and encouraging me. Let's stay in touch!).

19동에 있으면서 참 많은 분들을 만났었습니다. 함께하여 주신 학과 선후배/동기 여러분과 행정실 선생님들, 그리고 모든 천문학과 교수님들께도 감사의 말씀을 드립니다. 특별히 많은 시간을 보낸 저희 팀 동료들에게 깊은 감사의 말씀을 전합니다. 정환이형과 태석이형, 늘 저희들의 큰 형님으로써 든든하게 이끌어 주시고 함께 해주셔서 감사합니다. 선배이면서도 동시에 동생으로써 저와 많은 시간 함께해주고 격려해 준 종호에게도 감사의 말을 전하고 싶습니다. 종호야 너를 통해 참 많은 것을 느끼고 배웠어. 덕분에 나 또한 많은 부분 발전할 수 있었던 것 같다. 함께 할 수 있어서 기뻤고 고마웠다. 저에게는 팀 후배이자 동생들이기도 한 민철, 건우, 나은에게도 감사의 말과 격려의 말을 전하고 싶습니다. 모두 각자의 자리에서 열심히 해서 꼭 좋은 결과 얻길 바라며 늘 응원할게. 힘든 대학원 생활 중에 팀원들과 함께했던 술 한잔이 특히나 많이 그리울 것 같습니다 (Zoom으로라도 그런 자리가 종종 있길..). 그 외에도 여러 고마운 사람들이 있습니다. 특별히 친구로써 저의 학위 초반 과정을 함께 해줬고 저에게 큰 의지가 되었던 재영이와 국섭이에게 감사의 말을 전하고 싶습니다. 재영아 2014년도 이제 막 연구를 시작했을 때 아무것도 모르던 나에게 많은 도움을 주어서 정말 고맙다. 너와 함께 했던 재미난 추억들이 이래저래 참 많은 것 같구나. 함께 해줘서 고마웠고, 천문연에서 앞으로도 멋지게 잘 해내어 가길 늘 응원할게. 국섭아 너와 참 많은 이야기를 나누며 서로에게 위로와 격려가 되었던 시간들이 그립고 또 귀하다. 언제나 편한 친구로써 너에게 작게 나마 마음의 위안과 힘을 줄 수 있는 내가 될 수 있다면 좋겠구나. 앞으로도 건강하고 건승하길 바랄게. 가끔 19동에서 마주칠 때마다 늘 반갑게 안부 물어주고, 한때 연구실 옆자리에 붙어지내면서 자주 밥도 같이 먹었던 헌철이에게도 고마움을 표하고 싶습니다. 고맙다 헌철아, 항상 건강하고 뜻하는 바 꼭 이루길 바랄게. 저와 같이 2014년도에 대학원에 입학하고 많은 시간을 함께했던 동기들 또한 생각납니다. 창우, 은총, 한울, 준구, 성원, 관호, 명재 모두 고맙구나. 다들 각자의 자리에서 행복한 삶을 누리길 기원한다. 특별히 저와 함께 19동에 남아 학문의 길을 계속 갔던 준구와 함께 한 시간들이 많습니다. 덕분에 더욱 즐겁게 학교 생활을 할 수 있었던 것 같습니다. 고맙다 준구야. 이제 사회에 나가서 하고 싶은 일들 맘껏하며 즐겁게 지내길 바랄게. 이 외에도 부족한 저의 사교력 탓에 친해지지 못한 많은 선후배님들이 계십니다. 늘 따뜻하게 말 한마디 건네지 못하

고, 친해지고 싶으면서도 부끄러움때문에 다가가지 못했지만, 천문학을 하는 학도로써 동지로써 늘 19동에 함께 계셔주셔서 고마운 마음을 가지고 있습니다. 다들 꼭 뜻하시는 바 이루시고 무엇보다 건강하게 대학원 생활, 직장 생활 잘 하시길 늘 응원하고 기원하겠습니다.

학부시절 충북대에서 수학하면서 참 좋은 인연들을 많이 만났었습니다. 인생에서 가장 빛났던 20대 초중반의 시기를 함께했던 천문우주학과 07학번 동기들 모두에게 감사합니다. 그 시절이 그리울 때가 참 많습니다. 앞으로도 서로를 응원하고 의지하며 험난한 인생의 길을 함께 이겨나갈 수 있으면 좋겠습니다. 특별히 종수, 거성 (재현), 병석이에게 고마운 마음 전하고 싶습니다. 너희들과 종종 모여서 그 시절 그때처럼 신나게 놀았던 시간들이 학위과정 속에서 나에게 큰 힘이 되었다. 앞으로도 즐겁게, 그리고 서로를 응원하며 열심히 살아보자. 고려대와 연세대, 미국에서 수학하고 있는 상환, 성식이형, 경호에게도 감사합니다. 학문에 대한 여러분의 열정과 진지함을 보며 많은 것을 배웠습니다. 모두 건강하고 꼭 뜻하는 바 이루시길 기원하겠습니다. 학부시절을 통틀어 가장 기억에 남는 교수님이 한 분 계십니다. 바로 물리학과의 강병원 교수님이십니다. 교수님의 수업들을 들으며 늘 진정한 참 교육자이시다라는 생각을 해왔었습니다. 이곳 서울대에서의 학업이 바빠지면서 찾아뵙지 못한 것이 벌써 3~4년 정도 된 것 같습니다. 이제 이 학위논문을 가지고 교수님을 뵈러 곧 내려가겠습니다. 늘 존경하며 감사드립니다 교수님. 서울대에서 만난 오랜 친구 정민에게도 고마운 마음 전하고 싶습니다. 고된 대학원 생활 함께 할 수 있어서 즐거웠고, 한결같은 응원과 격려를 주어 고맙다. 훌륭한 학자가 될 것이라 믿어 의심치 않고, 우리 모두 각자의 자리에서 앞으로도 최선을 다해 정진하자.

마지막으로 부모님과 형에게 깊은 감사의 말씀을 전합니다. 언제나 저의 선택과 결정을 묵묵히 지켜봐 주시고 늘 격려와 사랑으로 품어주심에 대한 감사한 마음, 글로 이루 다 표현할 길이 없습니다. 가족이 늘 곁에 든든하게 있어주었기 때문에 이 길고 어려웠던 학위과정에서 끝까지 힘을 낼 수 있었습니다. 점점 나이가 한살 한살 들어감에 따라 가족에 대한 마음, 그 소중함이 더욱 커지는 것 같습니다. 형수님과 두 조카, 예찬 은찬에게도 감사의 마음을 전합니다. 가족으로써 항상 함께 해주셔서 고맙습니다. 우리 가족 모두 너무나 감사하고 항상 건강하길 바랍니다. 저 또한 가족에게 힘과 위로와 격려가 될 수 있는 사람이 되기 위해 앞으로도 더욱 노력해 나가겠습니다. 부끄러워 사랑

한다는 말을 항상 하지 못했었는데, 이곳에서나마 하게 되어 참 기쁩니다. 엄마 아빠 그리고 형! 언제나 사랑해왔고 지금도, 앞으로도 늘 사랑합니다.

이 학위과정의 끝이 곧 새로운 시작임을 알고 있습니다. 저를 응원해주고 지켜봐주시는 모든 고마운 분들을 생각하며 앞으로도 어디를 가서든 항상 열심히, 그리고 겸손하게 주어진 일에 최선을 다하며 살아가겠습니다. 2013년 가을, 대학원 입학면접 마지막 순간에 구본철 교수님께서 마지막으로 하고 싶은 말 있냐며 제게 물으신 질문에 했던 답을 끝으로 글을 마치려 합니다. 남은 청춘과 열정을 다해 꾸준히 정진해 나가는 아름다운 천문학도의 모습을 보여드릴 수 있도록 항상 최선을 다하겠습니다. 감사합니다.

2021년 7월 30일 해 질 무렵 관악산에서,
김 대 원 올림